MANCHESTER 1824
The University of Manchester

X-ray Micro-Tomography and Volumetric Strain Measurement in the Intervertebral Disc

A thesis submitted to The University of Manchester for the degree of

Doctor of Philosophy

in the Faculty of Biology Medicine and Health

2018

Catherine M. Disney

School of Biological Sciences

Division of Cell Matrix and Regenerative Medicine

Contents

Contents 2

List of Figures 8

List of Tables 14

List of Abbreviations 15

Abstract 16

Declaration 17

Copyright Statement 18

List of Publications 19

Acknowledgements 20

Rationale for Thesis in Journal Format 21

1 Introduction 22

1.1 Outline of Thesis 23

2 Literature review 25

2.1 The intervertebral disc 25

2.1.1 Degeneration 27

2.1.2 Microstructure 29

2.1.2.1 Nucleus pulposus 30

2.1.2.2 Annulus fibrosus 31

2.1.2.3 Endplate 36

2.1.3 Load mechanics and tissue properties 37

2.1.3.1 Loading during function 37

2.1.3.2 Mechanical characterisation of the disc 38

2.1.4 Animal models 40

2.2 Review of imaging techniques for soft tissue visualisation and deformation under load 41

2.2.1 Imaging soft tissue microstructure 41

2.2.2 *In situ* imaging to observe microstructural deformation mechanisms 42

2.2.2.1 Intervertebral disc 43

2.2.2.2 Tendon 44

2.2.2.3 Vascular 45
2.3 X-ray and micro-computed tomography 46
2.3.1 Generation of X-rays 46
2.3.1.1 Microfocus laboratory source 46
2.3.1.2 Synchrotron source 47
2.3.2 Interactions of X-rays with matter 48
2.3.3 X-ray transmission contrast acquisition 51
2.3.4 Phase contrast acquisition 53
2.3.5 Reconstruction 53
2.3.6 Image artefacts 54
2.4 MicroCT of soft tissues 55
2.4.1 Heavy metal stains for collagenous tissues 56
2.4.2 In-line phase contrast imaging 57
2.5 Image correlation for strain measurement in soft tissue 60
2.5.1 Digital image correlation (2D-DIC & 3D-DIC) 60
2.5.2 Digital volume correlation (DVC) 64
2.6 Summary and hypotheses 66
3 Visualising the 3D microstructure of stained and native intervertebral discs using X-ray micro tomography 72
3.1 Author contribution statement: 73
3.2 Abstract 74
3.3 Introduction 75
3.4 Methods 77
3.4.1 Tissues and materials 77
3.4.2 MicroCT of chemically-fixed and stained disc segments and whole discs ... 77
3.4.3 Laboratory and synchrotron phase contrast microCT of unstained IVD tissue 78
3.5 Results 79
3.5.1 Laboratory microCT of stained IVD segments 80
3.5.2 Laboratory microCT of whole IVD stained with PMA 83

3.5.3 Laboratory and synchrotron source in-line phase contrast microCT of chemically fixed tissue segments 85
3.5.4 Synchrotron source in-line phase contrast microCT of native tissue segments 87
3.6 Discussion 88
3.7 Supplementary 94
4 Synchrotron tomographic measurement of strain in soft tissue: native intervertebral disc deformation at histological resolution 95
4.1 Author contribution statement: 96
4.2 Abstract 97
4.3 Introduction 98
4.4 Materials and methods 99
4.4.1 Tissue and materials 99
4.4.2 Equipment and testing 100
4.4.3 In-line phase contrast synchrotron microCT 100
4.4.4 Image processing and DVC analysis 101
4.4.5 Transformation to local coordinates and strain calculation 102
4.5 Results 102
4.5.1 Synchrotron micro-tomography of native IVD within the spine segment 102
4.5.2 *In situ* loading; tomography after stress relaxation 104
4.5.3 Lamellae bundle angle 105
4.5.4 Digital volume correlation; displacement of structures can be tracked and mapped as strain 108
4.6 Discussion 112
4.6.1 Novel 3D imaging of intact native IVD microstructure 112
4.6.2 Lamellae bundle angle depends on anatomical position 112
4.6.3 Maximum principle strain 113
4.6.4 Study limitations and future directions 115
4.7 Conclusions 116

4.8 Supplementary 117
5 An update on high resolution synchrotron micro-computed tomography of the native intact intervertebral disc 126
5.1 Author contribution statement: 127
5.2 Abstract 128
5.3 Introduction 129
5.4 Materials and methods 129
5.4.1 Tissue and materials 129
5.4.2 Equipment and testing 130
5.4.3 In-line phase contrast synchrotron microCT 132
5.5 Results and discussion 132
5.6 Conclusions 137
6 Summary and conclusion 138
6.1 Workflow for imaging microstructure deformation and strain measurement in intact soft tissues 139
6.1.1 Sample preparation and loading conditions 139
6.1.1.1 Precise and consistent sample dissection 139
6.1.1.2 Effect of sample preparation on tissue mechanics 139
6.1.1.3 Physiologically relevant loading regimes are limited by imaging capabilities 139
6.1.2 Imaging microstructure; towards 3D imaging of native samples using microCT 140
6.1.2.1 Balancing contrast, resolution and field of view 140
6.1.2.2 Compromise between image quality and radiation dose 141
6.1.2.3 Data handling and image processing 141
6.1.3 Tracking displacement of features using image correlation 141
6.1.3.1 Sufficient features to track 141
6.1.3.2 Tracking reliability depends on correlation parameters 141
6.1.3.3 Correlation is inclusive of image noise and artefacts 142
6.1.4 Strain calculation and interpretation 142
6.2 Advances in IVD structure and mechanical characterisation and future studies 144
6.2.1 Studying the effects of IVD degeneration and needle injury on microstructure deformation 144

6.3 Conclusion 148
7 References 149
A. A Review of Techniques for Visualising Soft Tissue Microstructure Deformation and Quantifying Strain *Ex vivo* 169
A.1 Author contribution statement: 170
A.2 Abstract 171
A.3 Introduction 172
A.4 Imaging soft tissue microstructure to observe mechanical function 174
A.4.1 Imaging soft tissue microstructure 174
A.4.2 *In situ* imaging to observe microstructural deformation mechanisms 178
A.4.2.1 Tendon 178
A.4.2.2 Intervertebral disc 179
A.4.2.3 Vascular 180
A.5 Tracking microstructure to map local strain 181
A.5.1 Discrete strain measurement 181
A.5.2 Full-field strain measurement 181
A.5.2.1 Digital image correlation 181
A.5.2.2 Digital volume correlation 184
A.6 Outlook: volumetric strain measurement in soft tissue 185
A.6.1 Sample preparation and loading conditions 185
A.6.1.1 Precise and consistent sample dissection 185
A.6.1.2 Effect of sample preparation on tissue mechanics 185
A.6.1.3 Physiologically relevant loading regimes are limited by imaging capabilities 186
A.6.2 Imaging microstructure; towards 3D imaging of native samples using microCT 186
A.6.2.1 Balancing contrast, resolution and field of view 186
A.6.2.2 Compromise between image quality and radiation dose 187
A.6.2.3 Data handling and image processing 187
A.6.3 Tracking displacement of features using image correlation 187
A.6.3.1 Sufficient features to track 187
A.6.3.2 Tracking reliability depends on correlation parameters 187
A.6.3.3 Correlation is inclusive of image noise and artefacts 188
A.6.4 Strain calculation and interpretation 188

A.7 Conclusion 189

B. Diamond Light Source proposal 15444 Manchester Collaboration: Structural and mechanical characterisation intervertebral discs loaded *in situ* 191

B.1 Abstract 192

B.2 Scientific background and aims 193

B.3 Experimental methods 194

B.4 Beamline and beamtime justification 195

B.5 Expected results and impact 196

C. Diamond Light Source proposal 19322: Structural and mechanical characterisation of the intervertebral disc and degeneration 197

C.1 Abstract 198

C.2 Scientific background and aims 199

C.3 Experimental methods 201

C.4 Beamline and beamtime justification 201

C.5 Expected results and impact 201

D. EPSRC Doctoral Prize Fellowship proposal 203

D.1 Project proposal 204

D.2 Expected outputs from proposed research programme 207

Word count: 27,808

List of Figures

Figure 2.1 a) Spine regions and b) section of the spine showing location and macrostructure of the IVD (Naish and Court, 2014). 26

Figure 2.2 Structure of the IVD. A cut out shows the central nucleus pulposus and lamella architecture of the annulus fibrosus with alternating orientation of collagen bundles (Chapter 4, unpublished). 27

Figure 2.3 Example MRI of the lumbar spine. Advanced degeneration of L1-L2 disc with relative preservation of other IVDs (Sharma et al., 2014). 28

Figure 2.4 MRI images illustrating early and advanced degeneration in human lumbar IVD. 200 µm isotropic voxel resolution (Smith et al., 2011). 29

Figure 2.5 Histology section of murine IVD showing two phenotypically different populations. Thick arrow shows the border with the AF where elongated fibroblast-like cells are located and the thin arrow indicates border with the NP region where oval chondrocyte-like cells can be found. (Walsh and Lotz, 2004). 30

Figure 2.6 An early study of NP collagen framework structure using scanning electron microscopy (30,000X) (Inoue, 1981). 31

Figure 2.7 Ovine AF histology sections showing large elastic bridging structures spanning several lamellae (indicated by black and white arrows). a) toluidine blue/fast green b) & c) stained with picrosirus red and imaged with polarised light where white arrows mark the TLCBs (Melrose et al., 2008). 32

Figure 2.8 Differential interference contrast of ovine AF and 3D reconstruction of translamellar bridging from serial sections. (Schollum et al., 2009b). 33

Figure 2.9 OCT of anterior ovine AF with cross bridges marked with red arrows (resolution 5.6µm). Field of view 6 × 6 × 1.89 mm but effective image depth was limited to ~1 mm (not 1.89 mm due to scattering) (Han et al., 2015). 34

Figure 2.10 Immunostained bovine microfibrils showing a continuous elastic network across several lamellae. CS: cross sectioned lamellae. nIP: nearly in-plane lamellae. Collagen bundles are encircled by the elastic network (white arrows) which continues through lamellae boundaries (Yu et al., 2015). 35

Figure 2.11 Orientation of elastic fibres in sheep AF, given relative to the tangential to circumferential direction (marked as TCD in figure). Inter- lamellar orientation is given as percentage to intra-lamellar fibre count. Upper right; SEM of inter- lamellae elastic fibres (Tavakoli et al., 2017). 36

Figure 2.12 Non-linear viscoelastic mechanical behaviour. a) J-stress-strain during loading and unloading b) Stress relaxation c) Creep. 39

Figure 2.13 Schematics showing the microstructure of different organs. Tendon (a) (Screen et al., 2015), intervertebral disc (b) (Disney et al., 2017) and artery (c) (Gasser et al., 2006) are given as examples. All panels adapted with permission. (Disney et al., 2018). 43

Figure 2.14 Generation of X-rays. a) Schematic of an X-ray tube showing electrons emitted from a heated element are accelerated to hit a target where X-rays are generated. The source can be open or closed. The advantage of having an open source is that it allows for the filament to be replaced. b) An example Bremsstrahlung spectrum with characteristic radiation emitted from an

X-ray tube with tungsten target at 80, 100, 120 and 140 kVp. Adapted from Seibert et al. (2004). 46

Figure 2.15 Schematic of synchrotron components. Electrons are emitted (e-gun) and accelerated (linear accelerator: LINAC) into a booster ring where they build momentum and are then injected into a storage ring. The storage ring is closed loop where bending magnets change the path of the electron beam. Beamlines, positioned tangentially to the main storage ring, are supplied by radiation from insertion devices (series of magnets) or bending magnets. A radio frequency supply (RF) replenishes energy in the storage ring lost to the beamline (Willmott, 2011). 48

Figure 2.16 Interaction of X-rays with matter. X-rays are either elastically or ineastically scattered at material boundaries, absorbed or transmitted through the sample. If absorbed by the material, lower energy photons or electrons (Auger) are emitted. Refraction occurs when radiation enters a material and, due to a change in velocity, the resulting wave is phase-shifted. 49

Figure 2.17 Attenuation is proportional to the incident X-ray energy and depends on atomic number. Absorption edges (k-edges) specific to the element and are related to the minimum energy required to ionise the atom. (Willmott, 2011) 50

Figure 2.18 Laboratory microCT system. An X-ray beam, originating from an X-ray tube, passes through a sample placed on the rotation stage. The transmitted signal is detected using a scintillator and CCD array. 51

Figure 2.19 Tomography acquisition example. Transmission profiles are taken at multiple different angles through the sample (a) which can represented with respect to the sample rotation angle as a sinogram (b). Adapted from (Iwaguchi et al., 2016) 52

Figure 2.20 Phase shift (refractive index decrement) index (δ) can be a thousand times larger than the absorption index (β). Based on calculations for flesh transmission through 1 mm ($C_{12}H_{60}O_{25}N_5$, density as 1.071 gcm^{-3}) (Willmott, 2011). 58

Figure 2.21 In-line phase contrast microCT of rat IVD. Lamellae are indicated by black arrows and bridging by white arrows. Non-lamellar fibrillar NP structure is marked by an asterisk. (Naveh et al., 2014). 59

Figure 2.22 Example of a subset before and after deformation. Adapted from Pan et al., 2009. 61

Figure 2.23 The two different approaches taken for DVC. Local correlates independent sub-volumes whereas global uses a mesh and a model of system mechanics to constrain displacements. Global methods have a smoothing effect on displacement results, whilst local approaches retain measurement variability. This variability could be important to learn something new about a systems mechanics. Adapted from Disney et al., 2018. 64

Figure 2.24 In situ imaging to quantify tissue mechanics. The top arrow (sample interaction) describes the sample preparation required for each different imaging technique and their limitations. Tissue mechanics ranging from volumetric strain to discrete strain and observational mechanics can be related to the above imaging techniques (Disney et al., 2018). 66

Figure 3.1 Anatomy of the intervertebral disc. Schematic of the IVD (a). IVDs are situated between the vertebral bodies in the spine. They provide flexibility and bear load caused by body weight and physical activity. A portion is cut out to show the central gelatinous NP and the alternating orientation of collagen bundles between adjacent AF lamellae. Yellow arrows indicate the load

path. Bovine tail intervertebral disc stained with PMA and stored in membrane box for scanning (b). 76

Figure 3.2 Summary of methods. Note: Figure 3 refers to Figure 3.3, Figure 4 refers to Figure 3.4 etc. in this figure. 80

Figure 3.3. Quarter fixed and stained bovine IVD segments. Three heavy metal stains, I_2KI (a, d, g), PMA (b, e, h) and PTA (c, f, i), have been evaluated for enhancing contrast after 2 weeks incubation. Tomogram renders show unstained regions in red (a-c). Radial slices (d-f) showing large unstained regions using PMA and PTA (e, f). Magnified radial slices (g-i) show oblique collagen arrangement in the AF. I_2KI only provides enough contrast to resolve lamella structures in the outer AF region whereas PMA and PTA allow some internal structure of collagen bundles to be resolved. 82

Figure 3.4 Fixing and staining with PMA increases X-ray contrast but fails to fully penetrate a whole bovine disc and causes major structural changes. Whole intervertebral disc unstained (a, c, e) and stained with PMA for 2 months (b, d, f). Radiograph (a), tomography slice (c) and associated line profile (e) show that X-ray attenuation is low and no structural features resolved in unstained IVDs. Attenuation and contrast are improved with PMA staining (b, d, f) although there are still some unstained regions shown in red (g-i). Rendered tomogram (g) clipped to show radial slice (i). Fixing and staining caused visible structural changes (j). 84

Figure 3.5 In-line phase contrast microCT of unstained bovine IVD segments. Samples scanned using Carl Zeiss Xradia Versa (MXIF) (a) and synchrotron (b-g). Samples have been fixed, through an ethanol dehydration series and embedded in paraffin wax (a-f), or fixed only (g). Overview of IVD structure (c-e) using images taken from one slice (b). Collagen fibres (f) and AF lamella structure (g) were resolved. 86

Figure 3.6 Synchrotron source in-line phase contrast microCT resolves bovine IVD microstructure. Scans taken at I13-2 are capable of resolving native tissue structure at histological resolution. A single slice shows AF collagen bundle alignment (a) with 3D render of same region (b) (volume size panel b: 4500 × 1500 × 160 µm). Elastic network of AF (c, d) where orange arrows indicate compartments and green arrows show inter-lamella bridging (volume size panel c: 2540 × 1400 × 500 µm). 88

Figure 3.7 Fibre analysis of native bovine annulus fibrosus. Collagen bundles in a cropped volume (1460 x 1030 x 1140 µm) of AF (a) can be correlated to cylinder template (b) and individual fibres traced (c). The 3D orientation of each fibre is calculated and plotted (d). The angle relative to the z axis (θ) is displayed using a colour map and the angle in the x-y plane (φ, 0-360) is shown on the orientation sphere (d) where bar height is frequency. 93

Figure 4.1 Structure of native intervertebral disc; a) schematic of the IVD, b) rendered tomogram, c) virtual slices taken from three anatomical positions, d) sagittal, e) transverse and f) radial. 103

Figure 4.2 In situ loading; a) force reading from sequential compression, b) sequence of 3D renders of the disc being compressed from the lower endplate. 104

Figure 4.3 Volumes of interest selected for analysis and defining a local coordinate system; a) transverse slice showing position of medial and lateral cube volumes b) rendered medial cube c) rendered lateral cube d) global and local lamella coordinate system. 105

Figure 4.4 Bundle orientation varies with anatomical location; a) d) two alternating orientations of collagen bundles shown by clipping in the lamella plane b) e) all traced bundles are shown with view in lamella plane c) f) bundle orientation for L0 and L4 after rotation transformation to lamella local coordinate system where phi φ is in-plane angle. a-c) medial volume of interest d-f) lateral volume of interest. Cube volumes have 320 µm dimensions. 107

Figure 4.5 Tracking displacement using DVC; a) sub-volume used for tracking was a 20 pixel (32 µm) cube shown by the orange box on the image data b) tracking points had a 4 pixel (6.4 µm) spacing c) mean tracking residual for all compression steps d) median and interquartile range for displacement values in the local lamella coordinate system. 109

Figure 4.6 Medial cube maximum principle strain; a) maximum principle strain vector components defined in local lamella coordinate system b,c,e) maximum principle strain plotted with image data, clipped across lamella (b) and clipped in the lamella plane (c & e) d & f) shows principle strain vectors in the lamella plane plotted with image data. 110

Figure 4.7 Lateral cube maximum principle strain; a) maximum principle strain vector components defined in local lamella coordinate system b,c,e) maximum principle strain plotted with image data, clipped across lamella (b) and clipped in the lamella plane (c & e) d & f) shows principle strain vectors in the lamella plane plotted with image data. 111

Supplementary figure 4.8 Angle of maximum principle strain in the lamellae plane. Strain magnitude is thresholded to only include values above the 0.25 quantile. a) Strains in the medial cube are directed more vertically (>50° and <-50°), matching the steeper inclination of the bundle angle, whereas b) strains in the lateral cube are closer to horizontal, tending towards the shallow bundle angle. 117

Supplementary figure 4.9 Maximum principle strain magnitudes for all load steps. Histograms and boxplots of interquartile range show the distribution of strain magnitudes for a) & b) the medial cube and c) & d) the lateral cube. A progression of increasing strain with increasing load is shown for both cubes. It is expected that the maximum principle strain distribution is skewed toward higher values and becomes more skewed with higher applied loads. 118

Supplementary figure 4.10 Medial cube maximum principle strain for the repeat scan at L0; a) maximum principle strain vector components defined in local lamella coordinate system b,c,e) maximum principle strain plotted with image data, clipped across lamella (b) and clipped in the lamella plane (c & e) d & f) shows principle strain vectors in the lamella plane plotted with image data. 119

Supplementary figure 4.11 Lateral cube maximum principle strain for the repeat scan at L0; a) maximum principle strain vector components defined in local lamella coordinate system b,c,e) maximum principle strain plotted with image data, clipped across lamella (b) and clipped in the lamella plane (c & e) d & f) shows principle strain vectors in the lamella plane plotted with image data. 120

Figure 5.1 Sample preparation and Diamond-Manchester beamline (I13-2); a) Radiograph of spine segment. Orange lines shows position of cuts made for sample preparation. b) Sample preparation steps. c) Diamond-Manchester beamline set-up with Deben rig (open) and sample in place. 131

Figure 5.2 MicroCT of native intact rat IVD a) all lamellae from inner to outer AF can be resolved, b) & c) a virtual transverse slice shows that results have histological resolution. Histology courtesy of Amie Kilkenny: rat IVD section stained with haematoxylin and eosin. 133

Figure 5.3 Virtual slices of NP. a) Transverse and b) longitudinal slices show NP cells in the centre of the IVD surrounded by radially arranged fibres (orange arrows), c) higher magnification (4x objective) resolved individual cells of 8-10 µm diameter (yellow box). 134

Figure 5.4 a) Transverse slice showing lamellae and individual AF bundles in the anterior portion of the disc, b) the bundles change orientation as they approach the endplate where cells have been resolved. 135

Figure 5.5 NP is resolved throughout the in situ compression sequence. Transverse slices taken from a) first scan and b) last (fifth) scan in the compression sequence. 136

Figure 6.1 Proposed workflow for soft tissue microCT-DVC studies (Disney et al., 2018). 143

Figure 6.2 Ex vivo IVD degeneration study a) control sample b) sample with trypsin digested NP. 145

Figure 6.3 Needle injury study a) radiograph of 27 gauge needle inserted into posterior of the IVD b) radiograph of smaller 33 gauge needle inserted into posterior of the IVD c) & d) comparison of needle injuries e) buckling of lamellae (yellow arrow) positioned laterally to the need injury (yellow dashed line) f) Inter-lamella fibres (yellow arrows). 147

Figure 7.1 In situ imaging studies are essential to characterise biological tissue structure during function, ageing and to develop regenerative treatments. 173

Figure 7.2 MicroCT imaging of soft tissue. Individual fascicles have been resolved in tendon stained with iodine potassium iodide (a) (Shearer et al., 2016). Paraffin embedded unpressurised and pressurised aorta imaged using in-line phase contrast microCT (b) (Walton et al., 2015). Native annulus fibrosus of the intervertebral disc imaged using in-line phase contrast synchrotron microCT (c) (Disney et al., 2017). All panels adapted with permission. 176

Figure 7.3 In situ imaging to quantify tissue mechanics. The top arrow (sample interaction) describes the sample preparation required for each different imaging technique and their limitations. Tissue mechanics ranging from volumetric strain to discrete strain and observational mechanics can be related to the above imaging techniques. 177

Figure 7.4 Schematics showing the microstructure of different organs. Tendon (a) (Screen et al., 2015), intervertebral disc (b) (Disney et al., 2017) and artery (c) (Gasser et al., 2006) are given as examples. All panels adapted with permission. 178

Figure 7.5 Proposed workflow for soft tissue microCT-DVC studies. 189

Figure 7.6 Intervertebral disc: structure and pathology. a) Schematic of IVD. Cartilaginous endplates transmit compressive force from the vertebrae to the inner collagen II- and aggrecan-rich nucleus pulposus and the outer collagen-I rich annulus fibrosus. b) histological structure of a healthy, decalcified, sectioned and H&E stained vertebral unit comprising vertebrae (V) and annulus fibrosus (AF) and nucleus pulposus (NP) regions of the intervertebral disc. c) the degenerate disc is characterised by fissures (F) within the NP. 193

Figure 7.7 MicroCT of fresh IVD tissue using phase contrast imaging at the Diamond-Manchester Beamline. a) Longitudinal slice where lines mark lamella boundaries and arrows indicate bridging structures. b) Radial slice showing collagen bundle organisation. c) 3D render of

collagen bundles. d-f) radial slices with orientation analysis showing compression of IVD tissue. 195

Figure 7.8 a) tomogram of native AF, b) individual collagen bundles have been traced and their orientation displayed. 199

Figure 7.9 a) In situ compression of rat spine segment, b) rendered tomogram of the IVD, c) tranverse slice showing AF, d) principle strain in the AF. 200

List of Tables

Table 2.1 Soft tissue DIC studies for mapping surface strain. Studies are organised by sample into tissue groups (indicated by shading). Imaging and DIC method are given as well as further information about the features used for correlation (applied speckle or natural image texture). 63

Table 2.2 Summary of imaging techniques and IVD structures resolved **67**

Table 4.1 Lamella bundle angle from transverse plane has been shown to vary circumferentially. Most studies used dissection or lamella peeling and observation to measure bundle angle. 113

Table A.1 Soft tissue DIC studies for mapping surface strain. Studies are organised by sample into tissue groups. Imaging and DIC method are given as well as further information about the features used for correlation (applied speckle or natural image texture). 182

List of Abbreviations

AF	Annulus fibrosus
CCD	Charge-coupled device
CT	(X-ray) Computed tomography
DIC	Differential interference contrast
DIC	Digital image correlation
DLS	Diamond Light Source
DTAF	(4,6-dichlorotriazinyl)aminofluorescein
DVC	Digital volume correlation
ECM	Extracellular matrix
I_2KI	Iodine potassium iodide
IVD	Intervertebral disc
IVDD	Intervertebral disc degeneration
LBP	Low back pain
microCT	(X-ray) Micro-computed tomography
MRI	Magnetic resonance imaging
MXIF	Manchester X-ray imaging facility
NP	Nucleus pulposus
OCT	Optical coherence tomography
PBS	Phosphate buffered saline
PCXMT	In-line phase contrast X-ray micro tomography
PMA	Phosphomolybdic acid
PTA	Phosphotungstic acid
SHG	Second harmonic generation
TLCB	Translamellar cross bridge

Abstract

The majority of the population suffers from low back pain at some point in their life. Of which, around 40% of cases are caused by intervertebral degeneration (IVDD). The degeneration process is complex, with mechanics and biology interrelated where mechanical overloading causes a cell response resulting in degeneration of extracellular matrix. However, the native IVD micro- structural and mechanical environment is poorly understood. This thesis presents a method to visualise and quantify microstructural deformation of the intact native IVD under load using X-ray micro-computed tomography (microCT). X-ray transmission contrast in soft tissues is weak but can be enhanced using heavy metal stains or in-line phase contrast imaging. The first objective was to image IVD microstructure using microCT with either 'laboratory' (microfocus tube) or synchrotron X-ray sources. Staining of discs improved contrast but there was uneven penetration and it relied on chemical fixation which influenced tissue structure. Native IVD microstructure was successfully resolved in tissue segments using in-line phase contrast synchrotron microCT. This imaging modality was then used to image an intact native rat IVD under sequential compression (four cumulative 2% strain steps). Deformation was then measured using digital volume correlation and mapped as strain. The main components (endplates, nucleus pulposus and annulus fibrosus) were resolved with details including individual outer lamellae and collagen-fibre bundles for the first volumetric imaging of intact native IVD at this resolution. Collagen bundles could be traced and their orientation defined before and after compression. Maximum principle strain showed no slipping at lamella boundaries, local strain patterns were at a similar scale and distribution to the elastic network with some heterogeneous areas and maximum strain direction aligned with bundle orientation suggesting bundle stretching and sliding. This method has the potential to bridge the gap between measures of macro-mechanical properties and the local 3D micro-mechanical environment experienced by cells. This is the first evaluation of strain at the micro scale level in the intact IVD. However, analysis was restricted to volumes of interest due to streaking artefacts. Image quality was improved by employing careful sample preparation and alignment of the sample in the beam. Resolved structures are now extended to the full disc with all lamellae visible, cells throughout the disc have been identified and imaging remained consistent in a series of scans where the disc was sequentially compressed. The method developed here provides a quantitative framework for future work including investigating the micro mechanical environment during IVDD and the effects of needle injury required for injecting tissue engineered constructs.

Declaration

The author of this thesis declares that no portion of the work referred to in the thesis has been submitted in support of an application for another degree or qualification of this or any other university or other institute of learning.

Copyright Statement

i. The author of this thesis (including any appendices and/or schedules to this thesis) owns certain copyright or related rights in it (the "Copyright") and s/he has given The University of Manchester certain rights to use such Copyright, including for administrative purposes.

ii. Copies of this thesis, either in full or in extracts and whether in hard or electronic copy, may be made **only** in accordance with the Copyright, Designs and Patents Act 1988 (as amended) and regulations issued under it or, where appropriate, in accordance with licensing agreements which the University has from time to time. This page must form part of any such copies made.

iii. The ownership of certain Copyright, patents, designs, trademarks and other intellectual property (the "Intellectual Property") and any reproductions of copyright works in the thesis, for example graphs and tables ("Reproductions"), which may be described in this thesis, may not be owned by the author and may be owned by third parties. Such Intellectual Property and Reproductions cannot and must not be made available for use without the prior written permission of the owner(s) of the relevant Intellectual Property and/or Reproductions.

iv. Further information on the conditions under which disclosure, publication and commercialisation of this thesis, the Copyright and any Intellectual Property and/or Reproductions described in it may take place is available in the University IP Policy (see http://documents.manchester.ac.uk/DocuInfo.aspx?DocID=24420), in any relevant Thesis restriction declarations deposited in the University Library, The University Library's regulations (see http://www.library.manchester.ac.uk/about/regulations/) and in The University's policy on Presentation of Theses.

List of Publications

The literature review presented in Chapter 2 and summary of workflow in Section 6.1 has been adapted from a published review;

Disney, C.M., Lee, P.D., Hoyland, J.A., Sherratt, M.J. and Bay, B.K., 2018. A review of techniques for visualising soft tissue microstructure deformation and quantifying strain *Ex vivo*. Journal of microscopy.

The full version of this publication can be found in 7.

The research presented in Chapter 3 has been published in Scientific Reports:

Disney, C.M., Madi, K., Bodey, A.J., Lee, P.D., Hoyland, J.A. and Sherratt, M.J., 2017. Visualising the 3D microstructure of stained and native intervertebral discs using X-ray microtomography. Scientific reports, 7(1), p.16279.

Acknowledgements

I wish to thank my supervisory team Dr Michael Sherratt, Professor Judith Hoyland and Professor Peter Lee for their advice and support during this project and making me feel welcome in their research groups.

I am incredibly grateful to Professor Brian Bay for hosting me on a 4-month research placement. Brian's advice and enthusiasm has been vital for this research. I appreciate very much all the time spent working with me, discussing results and helping me to make the next step in my career. Thanks for all the beers and for being a good friend.

I am thankful for the funding I have received. This studentship and a research placement at Oregon State University were funded by the EPSRC and MRC Centre of Doctoral Training in Regenerative Medicine (EP/L014904/1). Data was collected from beam times funded by the Diamond-Manchester collaboration (proposal 15444, Appendix B) and Diamond Light Source (proposal 193222, Appendix C). Preliminary data was collected under Diamond-Manchester collaboration beam time (proposal 12776). I am also grateful for the support of the Research Complex at Harwell, Manchester X-ray Imaging Facility, and Biological Services Facility at Manchester.

Being part of many different research groups has offered expertise from many different people. Thank you to Dr Kamel Madi for his encouragement and training during my first experiments. Beam times were successful due to the fantastic people who gave up their time to help. Many thanks to Alex, James, Hua, Mike, Amie, Jingyi, Brian and the I113 staff particularly Andy and Kaz. You were all super and made the extra-long shifts enjoyable!

Finally, my family have been very important in supporting me. Thanks to my parents for lending me their car for trips to Diamond, visiting me in Oregon, all their encouragement and for all the Stanley weekends. It goes without saying, thank you to my twin Ruth for always being there. A big thank you to Alex for being the kindest person, all the coffee breaks, helping during the beam time, listening to my endless research problems and still telling me everything is going to be great and, of course, for the crazy US road trip.

Rationale for Thesis in Journal Format

This thesis contains chapters and sections which have been peer-reviewed and published. Most of this PhD has been focussed on original research with the aim of publishing manuscripts. This includes drafting whole manuscripts, editing with co-authors, submitting to the requirements of journal regulations and dealing with and replying to reviewer's comments in the peer review process. Although each chapter is presented in journal format, all chapters link together and are summarised in the final chapter to form a coherent thesis.

1 Introduction

Low back pain (LBP) is a common health problem with an estimated 84% of the population who suffer at some point in their life (Walker, 2000). LBP has a substantial impact on people socially and financially by limiting mobility and causing work absence (Hoy *et al.*, 2014). The socio-economic cost of LBP was estimated to be £11 billion in the UK in the year 2000 (Maniadakis and Gray, 2000). The Global Burden of Disease 2010 study found that LBP ranked highest, out of 291 conditions, in terms of disability and sixth in overall burden. Prevalence and burden was found to increase with age and peak at roughly 80 years of age (Hoy *et al.*, 2014). Although the aetiology of LBP is complicated, it has been shown that 40% of cases have been linked to structural degeneration of the intervertebral disc (IVD) (Cheung *et al.*, 2009). Treatment of LBP is currently limited to pain management or surgical intervention for the most severe cases of IVD degeneration where the disc has herniated. Complications after surgery result in a 12% reoperation rate, a third of which progress onto lumbar fusion (Heindel *et al.*, 2017, Weinstein *et al.*, 2008).

Imaging the IVD's complex hierarchical structure and relating it to the discs mechanical function is vital to fully characterise degeneration and to design and test the first reparative treatments. Structural imaging is at the heart of understanding the mechanical function of tissues. However, conventional microscopy is typically 2D and destruction of the sample is required for thin tissue sections which often result in structural damage artefacts such as tears and folds (Rastogi *et al.*, 2013, Rolls *et al.*, 2008). X-ray micro-computed tomography (microCT) is a non-destructive 3D imaging method that is capable of microscale resolution. Time lapse imaging of intact *ex vivo* samples enables observation of physiological processes such as mechanical loading of IVDs. Yet, soft tissues such as the IVD, weakly absorb X-rays and so have low transmission contrast. Contrast can be improved using heavy metal stains but staining affinity and protocols are not well defined. In-line phase contrast microCT is capable of resolving unstained non-mineralised tissue but its application has been limited to observational studies where the sample is chemically fixed under load (Walton *et al.*, 2015). Native (fresh) IVD has been resolved using laboratory microCT (Naveh *et al.*, 2014) however scan times are long (hours-days) which makes it unsuitable for time lapse imaging where multiple scans are required. In contrast to laboratory microCT, synchrotron sources have a shorter scan time which is important for imaging native tissues. This thesis evaluates the use of microCT (laboratory and synchrotron source) for structural characterisation and for volumetric strain measurement

in the intact IVD. These techniques will be important to provide an improved understanding of the IVD's micro- structural and mechanical environment during function, degeneration and in reporting efficacy of repair strategies in future studies.

1.1 Outline of Thesis

This thesis contains six chapters which include a general introduction to the research, a literature review to summarise previous findings and provide background to the methods used, three results chapters in journal format and a summary and conclusion chapter. An outline of each chapter is described below:

Chapter 1 introduces the research scope of this thesis. Chapter 2 reviews literature on IVD structure and analyses limitations of current imaging methods for imaging soft tissue microstructure deformation under load. A general background of microCT is given and the potential of microCT for soft tissue is examined for this study. Methods of quantifying deformation using image correlation are discussed. Finally, a summary table of previous IVD imaging studies is given and the research hypotheses are formed.

The literature review concludes that microCT has great potential to characterise 3D microstructure of the IVD but methods of increasing image contrast in IVD tissue had to be tested. Chapter 3 focuses on using microCT to image IVD microstructure with the aim of minimising sample interaction or the effect of preparation on native structure. Three stains were evaluated for contrast enhancement but were found to cause morphological changes. In-line phase contrast microCT was used to image unstained tissue using a laboratory X-ray source for chemically fixed tissue and synchrotron X-ray source for native tissue segments.

After the successful imaging of native IVD tissue, Chapter 4 describes imaging intact native rat IVD using in-line phase contrast synchrotron microCT. The rat spine segment was sequentially compressed and tomography scans taken after each compression. Microstructure was characterised by tracing collagen bundles and finding their orientation. Deformations during the compression sequence are quantified using digital volume correlation and mapped as strain. However, large streaking artefacts obscured large parts of the images which limited structure characterisation and strain measurement.

Even with the previous chapter as a new standard for imaging intact native IVD, a short report in Chapter 5 presents improved quality high-resolution microCT of intact native rat IVD. This chapter describes how the improvements were made by refining sample preparation and careful alignment of the sample in the X-ray beam.

Overall, this thesis develops a methods framework to quantify the micro- structural and mechanical environment in the IVD which will be useful for future degeneration and repair studies. Chapter 6 is a summary drawing all of the thesis results chapters together and sets out aims for future work. The chapter is split into two sections. Firstly, a workflow for imaging soft tissue microstructure deformation and measuring volumetric strain is provided. The second part discusses advances in IVD structural and mechanical characterisation with two future studies focussed on IVD degeneration and needle injury.

Chapter 2

2 Literature review

This chapter provides a general literature review of intervertebral disc (IVD) structure and mechanics, imaging methods and background to methods used in each results chapter. The first section introduces the structure of the disc followed by a general description of degeneration. A detailed review of current microstructural characterisation is given for each tissue region which is followed by an overview of mechanical loading during function and tissue mechanical testing. Having reviewed IVD microstructural and mechanical characterisation, the next section turns to discussing imaging techniques available to visualise soft tissue deformation under load. This section is not limited to the IVD as three case studies (IVD, tendon and vascular) are given to gain a broader insight to mechanical functional imaging. After discussing the challenges of imaging mechanically loaded tissues, the next section considers the use of microCT as a non-destructive imaging technique. Background to how X-rays are generated and a comparison of different sources is given. Brief methodology of transmission contrast acquisition, phase contrast acquisition, reconstruction and possible image artefacts provides necessary information for the results chapters. The fourth section covers microCT of soft tissue, reviewing contrast staining agents and in-line phase contrast imaging studies. The final section reviews strain measurement in soft tissue, initially commenting on 2D- and 3D- digital image correlation and turning to the potential of volumetric strain measurement using microCT-based digital volume correlation. A summary is given and hypotheses are outlined for the rest of the thesis.

2.1 The intervertebral disc

IVDs are the largest avascular organ in the body with 23 discs contributing to 15-20% of the length of the spinal column (Shapiro and Risbud, 2014). The dimensions of the disc are dependent on the spinal region and vary with age and pathology. Figure 2.1 shows different regions in the spine and the positioning of the discs between the vertebral bodies of the spine to form a symphysis joint.

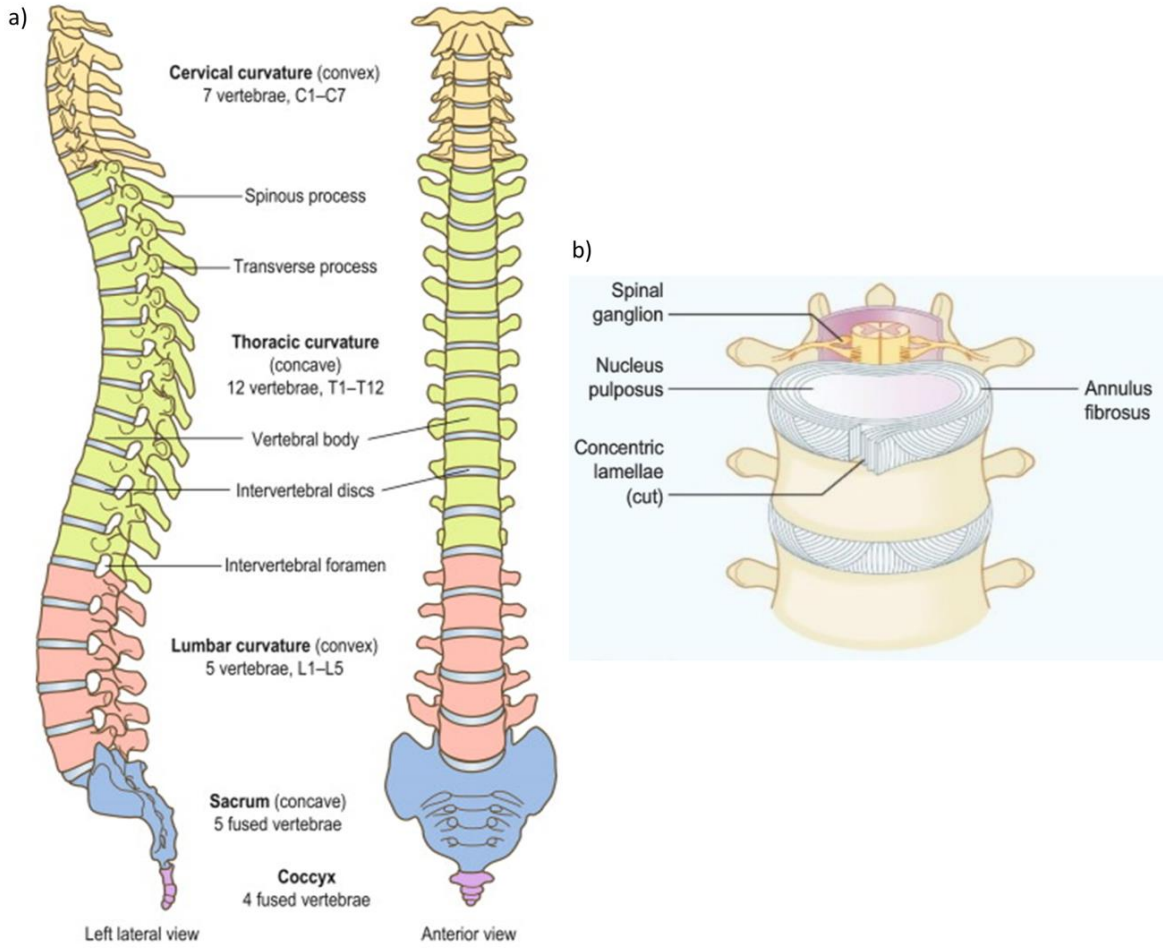

Figure 2.1 a) Spine regions and b) section of the spine showing location and macrostructure of the IVD (Naish and Court, 2014).

IVD function is predominately mechanical and can be classified into three groups; i) the joints provide flexibility by allowing small movements between the vertebrae ii) each disc is capable of transmitting loads caused by body weight and physical activity iii) the discs provide protection to the spine by acting as hydrodynamic shock absorbers when under increased load (Shapiro and Risbud, 2014).

The macrostructure of the IVD shown in Figure 2.2 can be classified into three tissue areas which have different structure and function. The nucleus pulposus (NP), a proteoglycan rich core located in the centre of the disc, is surrounded by an outer circumferential ring of fibrocartilage called the annulus fibrosus (AF). The structure is bounded by cartilage endplates at the vertebra.

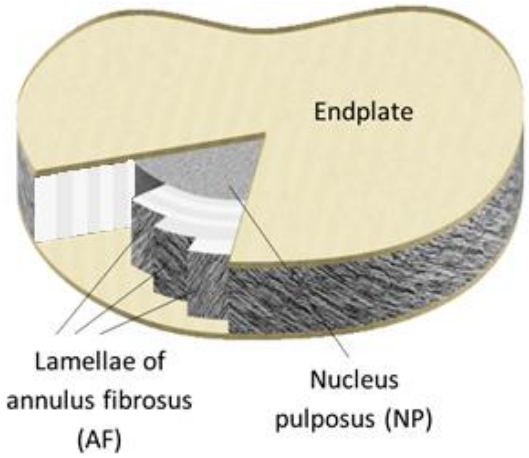

Figure 2.2 Structure of the IVD. A cut out shows the central nucleus pulposus and lamella architecture of the annulus fibrosus with alternating orientation of collagen bundles (Chapter 4, unpublished).

2.1.1 Degeneration

The gold standard for investigating low back pain (LBP) is magnetic resonance imaging (MRI) which enables the assessment of disc damage or degeneration. Gross morphology, such as disc height, or MRI grading schemes are used to evaluate degeneration. Previously, Sharma *et al.* (2014) reviewed clinical MRI scans for disc degeneration cases in 87 patients. Disc degeneration is most prevalent in the lumbar region where there is the highest load and motion (Muriuki *et al.*, 2016, Miller *et al.*, 1988). Figure 2.3 gives an example of a patient's spine with advanced degeneration at L1-L2 level. The centres of healthy discs are clearly visible in MRI due to high water content.

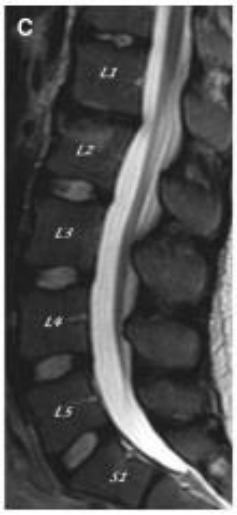

Figure 2.3 Example MRI of the lumbar spine. Advanced degeneration of L1-L2 disc with relative preservation of other IVDs (Sharma et al., 2014).

During early stages of degeneration there is a slight height reduction due to decreasing aggrecan content which leads to less water content in the NP (Roughley, 2004, Sztrolovics *et al.*, 1997). Dehydration could be linked to the observed decrease in NP collagen fibril diameter (Yee *et al.*, 2016). Biochemical analysis has shown that there is also a decrease in collagen I and elastin with increasing degeneration (Kobielarz *et al.*, 2016). Higher resolution MRI can reveal some structural changes in the IVD during different stages of degeneration. The asterisk in Figure 2.4B marks AF lamellae buckling towards the centre and lower water content identified by a decrease in NP signal intensity from the MRI scan. As disc degeneration progresses, height is greatly reduced and disc mechanical function deteriorates as the NP no longer distributes the compressive load evenly to the AF (Chan *et al.*, 2011, Adams and Roughley, 2006). Stress concentrations mean that there is an increased probability for severe structural degeneration such as AF delamination or formation of circumferential radial fissures which can progress to NP herniation or bulge (Smith *et al.*, 2011).

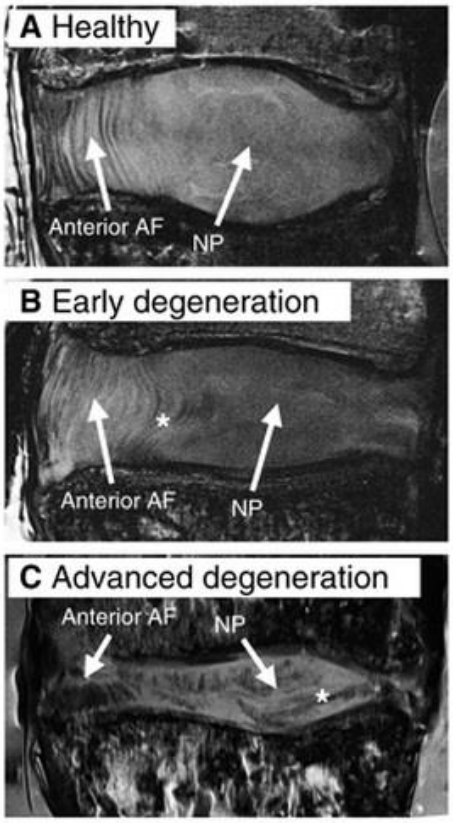

Figure 2.4 MRI images illustrating early and advanced degeneration in human lumbar IVD. 200 µm isotropic voxel resolution (Smith et al., 2011).

2.1.2 Microstructure

The microstructure of the IVD consists of a large amount of extracellular matrix (ECM) with a small number of cells (typically 1% cells of total volume) (Roberts *et al.*, 2006). Figure 2.5 of a histology section demonstrates that IVD cells can be distinguished by morphology into two phenotypically different populations. AF and endplate cells are elongated and fibroblast-like whereas NP cells are more rounded and chondrocyte-like (Roberts *et al.*, 2006).

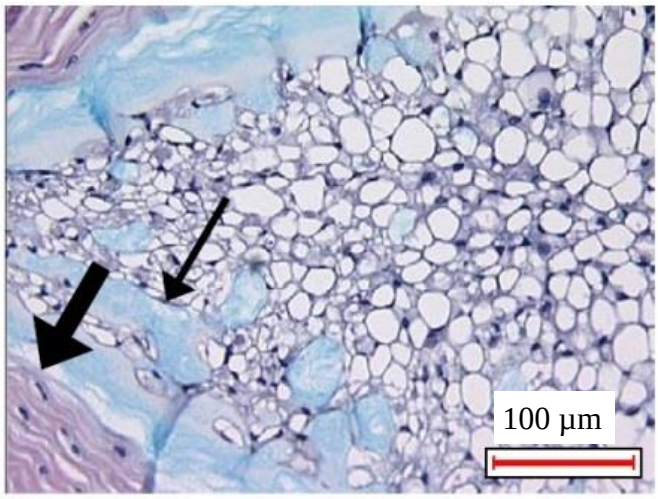

Figure 2.5 Histology section of murine IVD showing two phenotypically different populations. Thick arrow shows the border with the AF where elongated fibroblast-like cells are located and the thin arrow indicates border with the NP region where oval chondrocyte-like cells can be found. (Walsh and Lotz, 2004).

2.1.2.1 Nucleus pulposus

Large rounded NP cells are found arranged in clusters and separated by amorphous fibrillar proteoglycan-collagen matrix. An early study used scanning electron microscopy (Figure 2.6, Inoue, 1981) but more recently the NP fibrous collagen has been resolved using microCT (Figure 2.21, Naveh *et al.*, 2014). Besides the principle, unstructured collagen II framework, an organised elastic network has been reported where long straight elastic fibres are arranged radially (Yu *et al.*, 2002). The ECM of the NP tissue is predominantly collagen II (Eyre and Muir, 1977) along with a high content of polyanionic proteoglycans (mainly aggrecan) (Melrose *et al.*, 2001, Johnstone and Bayliss, 1995, Buckwalter *et al.*, 1985). These proteoglycans' high negative charge attracts counter ions (Chandran and Horkay, 2012, Nap and Szleifer, 2008) causing an influx of water creating a high osmotic pressure (Comper and Laurent, 1978). It is this osmotic pressure that provides resistance against compression.

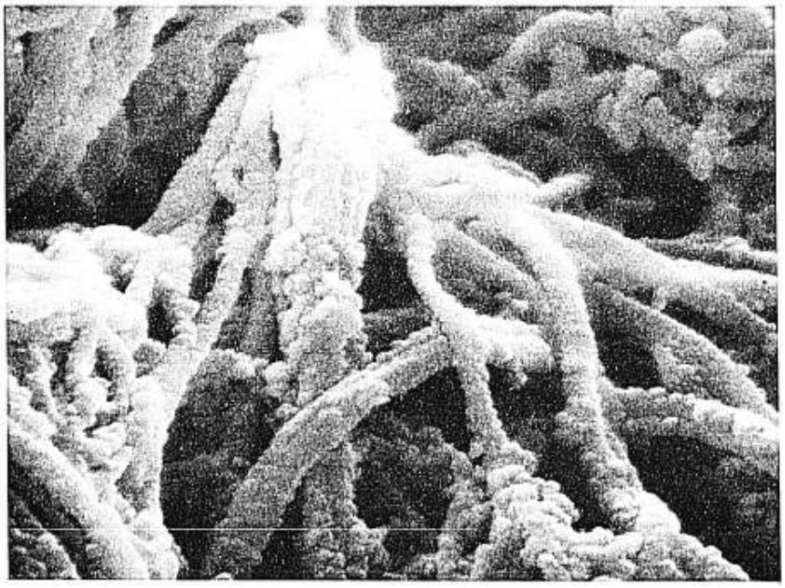

Figure 2.6 An early study of NP collagen framework structure using scanning electron microscopy (30,000X) (Inoue, 1981).

2.1.2.2 Annulus fibrosus

The AF ECM has aligned collagen I fibres which bundle to form long parallel concentric lamellae architecture (Figure 2.2). The orientation of these collagen bundles alternates between adjacent lamellae (Marchand and Ahmed, 1990). Some of the earliest studies on AF structure noted that bundles were orientated at ~50-60° (Inoue, 1973, Horton, 1958). However, later work found that there are regional changes in bundle angle. Cassidy *et al.* (1989) reported that the bundle angle varied radially from 28° to 45° from the outer lamella towards the nucleus. In contrast, more recent studies failed to identify a significant dependency of the fibre angle with radial distance from NP but a strong dependency with respect to the circumferential position (Zhu *et al.*, 2008, Holzapfel *et al.*, 2005, Eberlein *et al.*, 2001, Marchand and Ahmed, 1990). Such studies used careful surface observation at point locations to measure the bundle angle (generally at 3-5 depths and at 6 circumferential locations). However, the layer-by-layer peeling methods or tissue sectioning causes destruction and disruption to the tissue structure. Furthermore, the IVD has large residual strains in the unloaded state (Michalek *et al.*, 2012) and so the act itself of sectioning likely leads to microstructural remodelling. Only a single study has attempted to measure bundle orientation in an intact joint. Stadelmann *et al.* (2018a) found that AF structure orientation ranged between 25° to 50° in an intact joint using magnetic resonance diffusion. However, none of the above studies quantify local variations in bundle structure orientation obtained by 3D microstructural imaging.

Although collagen I forms the main structure of the AF, the elastic network is considered to play a vital role in providing resilience, in terms of solid mechanics, enabling the disc to deform and recover (Smith *et al.*, 2008, Pezowicz *et al.*, 2006). Elastic fibres, composed of elastin and fibrillin microfibrils (Rock *et al.*, 2004), have been found throughout the IVD (Yu *et al.*, 2002, Hickey and Hukins, 1979, Buckwalter *et al.*, 1976). The density of fibres has been found to vary between different regions of the AF (Smith and Fazzalari, 2006) and vary locally with the highest concentration of elastic fibres in the inter-lamellar space and in bridging elements between adjacent lamellae (Yu *et al.*, 2007). AF tissue sections stained with toluidine blue/fast green reveals the translamellar cross bridges (TLCBs) as seen by Melrose *et al.* (2008) (Figure 2.7a). The TLCBs are highly refractile and easy to identify by staining with picrosirus red viewed using polarised light (Figure 2.7b,c). The TLCBs were observed to extend across as many as eight lamella layers. However, the 2D images may not capture the true length of the TLCBs as they could continue out of the plane of view.

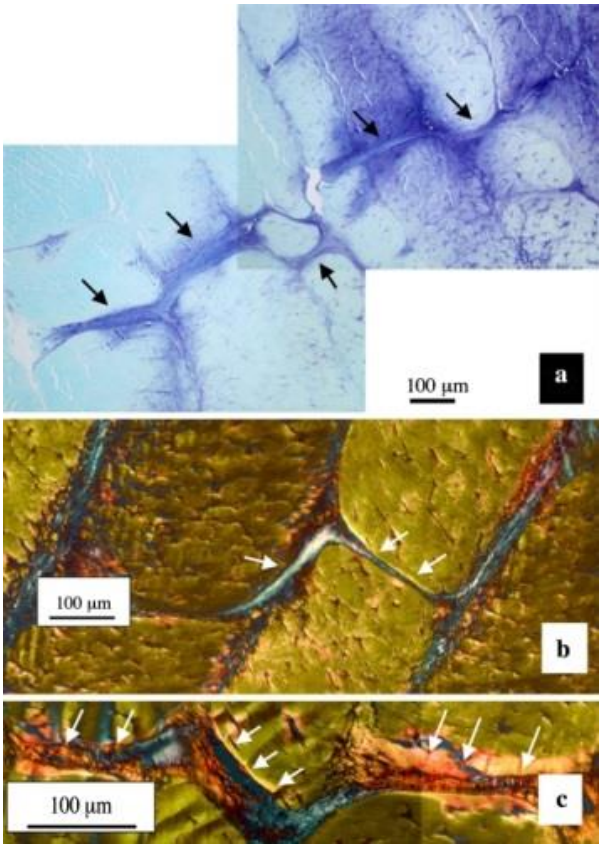

Figure 2.7 Ovine AF histology sections showing large elastic bridging structures spanning several lamellae (indicated by black and white arrows). a) toluidine blue/fast green b) & c) stained with picrosirus red and imaged with polarised light where white arrows mark the TLCBs (Melrose et al., 2008).

Schollum *et al.* (2009b) used differential interference contrast optics (DIC) of serial sectioned AF along the oblique fibre orientation. The stack of serial sectioned 2D images is reconstructed to create a 3D view (Figure 2.8). This serial section reconstruction clearly demonstrated the need to visualise microstructure in 3D; it was found that AF bridging elements have far greater structural complexity than previously thought from 2D studies. The TLCBs were shown to have substantial connections spanning many lamellae (Z in Figure 2.8) and a finer subsidiary branching network (across lamellae 11 and 13 in Figure 2.8).

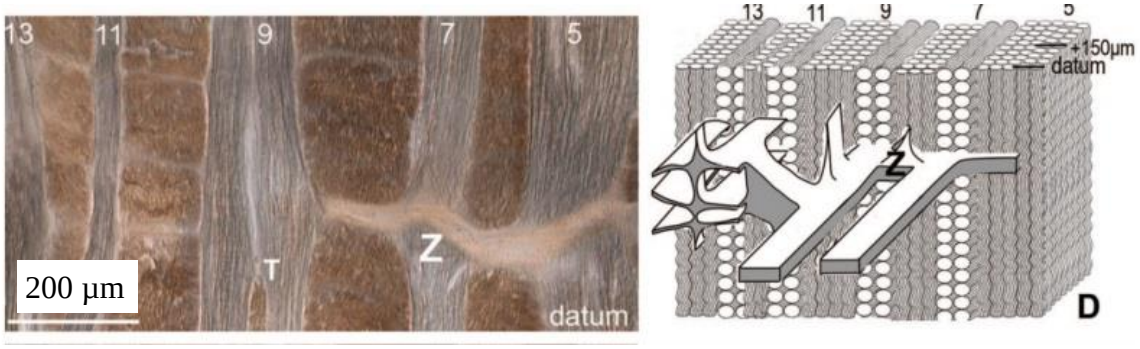

Figure 2.8 Differential interference contrast of ovine AF and 3D reconstruction of translamellar bridging from serial sections. (Schollum et al., 2009b).

A more recent study by Han *et al.* (2015) measured the length of the TLCBs using optical coherence tomography (OCT) (Figure 2.9). This method used a mesoscale volumetric section of AF tissue for intact visualisation of the TLCB network. They concluded that the length of TLCBs has greater variation and is longer when measured using 3D imaging compared to 2D imaging (0.8-1.4 mm measured using 3D OCT compared to 0.3-0.6 mm from 2D sections). OCT is minimally invasive as tissue sectioning is not required allowing for accurate quantification of the AF microstructure. However, imaging depth of the AF using OCT was limited to 1 mm due to scattering.

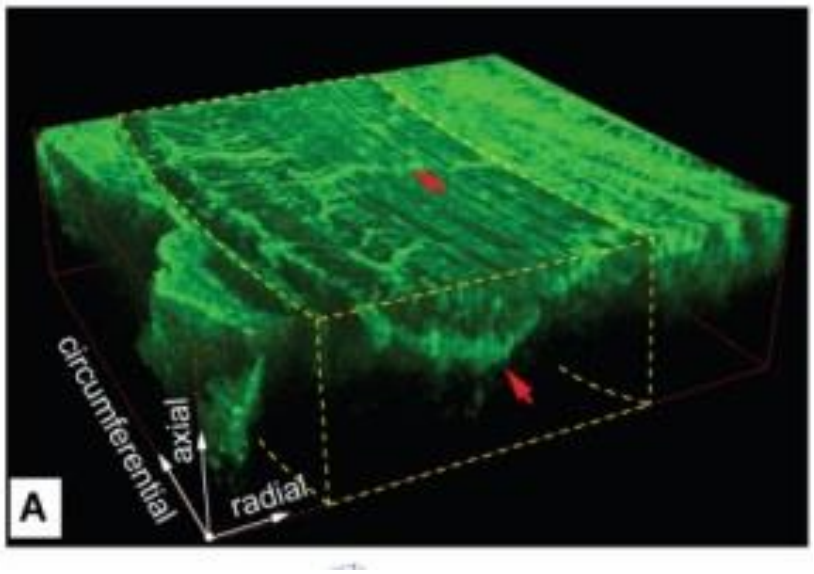

Figure 2.9 OCT of anterior ovine AF with cross bridges marked with red arrows (resolution 5.6µm). Field of view 6 × 6 × 1.89 mm but effective image depth was limited to ~1 mm (not 1.89 mm due to scattering) (Han et al., 2015).

Immunohistochemistry revealed a continuous elastic network across the AF surrounding compartments and connecting collagen bundles within lamellae and adjacent lamella (Figure 2.10) (Yu *et al.*, 2015). The observed elastic network in the AF as visualised by immumnohistochemistry, is more extensive and constitutes a highly integrated structure when compared to observations from DIC (Schollum *et al.*, 2009b) and OCT imaging (Han *et al.*, 2015). This is most likely due to higher resolution and fluorescent antibody markers which aid in the identification of finer elastic structures within the lamellae.

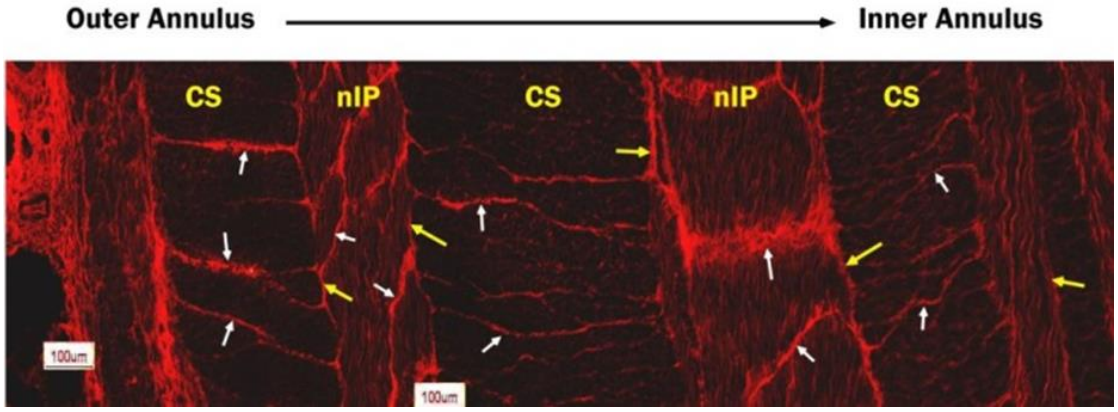

Figure 2.10 Immunostained bovine microfibrils showing a continuous elastic network across several lamellae. CS: cross sectioned lamellae. nIP: nearly in-plane lamellae. Collagen bundles are encircled by the elastic network (white arrows) which continues through lamellae boundaries (Yu et al., 2015).

There is a growing body of AF elastic network characterisation research with the most recent using scanning electron microscopy to visualise inter- and intra- lamellae elastic fibres (Tavakoli *et al.*, 2017) and fibres between collagen bundles (Tavakoli and Costi, 2018b). The inter- lamellae network had fibres of varying shape and size (2-0.1 µm diameter) whilst intra- lamellae fibres had a network of fine parallel and interconnecting fibres (0.3-0.5 µm diameter). The fibre organisation was the same for inter- and intra- networks with 0° orientation to the tangential to circumferential direction and minor ±45° orientations (Figure 2.11). A higher resolution SEM study confirmed that the elastic network is continuous and surrounds and connects collagen bundles (as noted by Yu *et al.* (2015)) with a similar, although less dense, ultra- structure as the inter- and intra- lamellae fibre organisation (Tavakoli and Costi, 2018b).

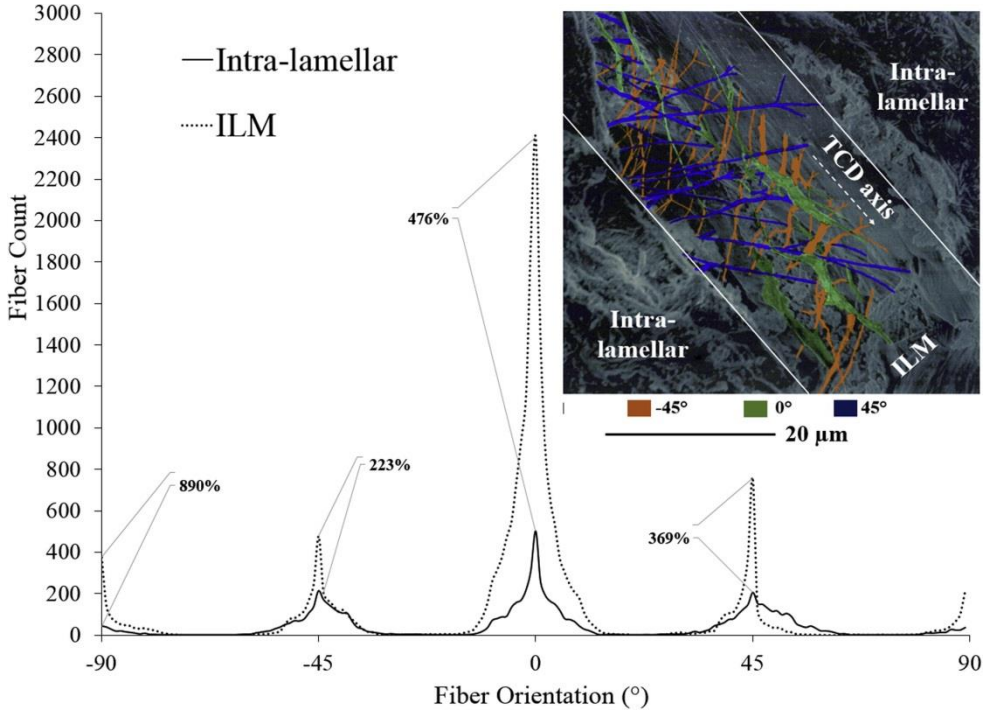

Figure 2.11 Orientation of elastic fibres in sheep AF, given relative to the tangential to circumferential direction (marked as TCD in figure). Inter- lamellar orientation is given as percentage to intra- lamellar fibre count. Upper right; SEM of inter- lamellae elastic fibres (Tavakoli et al., 2017).

2.1.2.3 Endplate

The endplates are thin layers of hyaline cartilage which provides a physical barrier between the IVD and vertebral bodies. Since the disc is avascular, the endplates are semipermeable for nutrient and fluid diffusion, transferred from the vertebrae by advective or diffusive mechanisms (Ferguson *et al.*, 2004, Urban *et al.*, 2004, Nachemson *et al.*, 1970). As a result, calcification and structural changes are detrimental to this function and also as a consequence of the IVD's low capacity for repair (Adams, 2015, Roberts *et al.*, 1996).

Fluid flow in the disc is not only vital for nutrient transfer but also for mechanical function (Section 2.1.3). Therefore, it is important to characterise endplate porosity for insights into fluid flow. Endplate morphology and porosity has been characterised in 3D using microCT. A complex 3D canal network (Gruber *et al.*, 2005) was reported and, interestingly, porosity was found to increase with IVD degeneration (Rodriguez *et al.*, 2012). Porosity is inversely proportional to endplate thickness and also inversely related to mechanical loading (measured using a pressure transducer) (Zehra *et al.*, 2015).

AF fibres are anchored directly into the endplate where AF collagen bundles split into sub-bundles which increase the anchoring surface area to the calcified cartilage (Rodrigues *et al.*, 2017, Rodrigues *et al.*, 2015). Sub-bundle insertion depth varies with thickness of cartilaginous endplate (Rodrigues *et al.*, 2012). AF and NP elastic fibres are also anchored into the endplate (Yu *et al.*, 2002, Roberts *et al.*, 1989, Johnson *et al.*, 1982).

2.1.3 Load mechanics and tissue properties

2.1.3.1 Loading during function

In a healthy disc, the AF and NP regions act together to safely distribute and transmit the loads between the vertebrae (Nachemson, 1963). The endplate absorbs and distributes some of the load induced pressure in the vertebral column (Ludwinski *et al.*, 2013). When a disc is under an increased loading regime, the hydrostatic pressure generated by the loaded NP tissue is conducted to a circumferential stress in the (outer) AF collagen lamellar architecture (O'Connell *et al.*, 2011b, McNally and Adams, 1992). The inner AF, with a high proteoglycan content, serves as a damper which slows the load transmission between the NP and AF (Roughley *et al.*, 2006). The AF has a residual strain which plays an important role in the regulation of circumferential stress (Michalek *et al.*, 2012). Several microstructural mechanisms have been reported during the deformation of the AF: oblique collagen fibres reorientate to the direction of loading (Klein and WL, 1982); collagen I fibres un-crimp allowing strains similar to tendons (~10%) (Puxkandl *et al.*, 2002). However, there is some disagreement as to whether lamellae can move relative to one another (discussed in Section 2.2.2.1).

Loading of the IVD is essential for normal physiology and maintenance of structure (Chan *et al.*, 2011). Loading can be classified into two regimes; diurnal or dynamic changes during physical movement. Both loading regimes have different beneficial effects for IVD function. Diurnal loading is variable on day and night postures. A high load is applied to the disc in upright postures and lower loads for lying postures. Diurnal loading causes the water content of the NP to vary by ~20% (Botsford *et al.*, 1994) providing the mechanism for transport of large soluble molecules vital for cell survival and synthesis of ECM (Kraemer, 1985). Whereas dynamic loading regimes provide an increase in oxygen concentration and a decrease in lactate concentration which is beneficial for maintaining matrix homeostasis (Huang and Gu, 2008). Dynamic loading has been shown to aid in stem cell differentiation alongside growth factors for regenerative medicine therapies (Dai *et al.*, 2014, Tsai *et al.*, 2014, Chan *et al.*, 2011).

IVD cells are in a loaded environment dependent on the different tissue region of the disc. As the disc is compressed the NP cells experience changes in compressive and shear stress (Nerurkar *et al.*, 2010). The transmitted circumferential stress in the AF gives rise to tensile and shear stress changes within and between the lamellae (Setton and Chen, 2004). However, studies quantifying the strains in the disc show that the loading mode is more complicated and spine segment-dependent (Sharma *et al.*, 2014); all loading modes can occur in any tissue area simultaneously. MRI strain maps show that cells in the NP could be subjected to tensile and shear stresses and anterior AF cells could be subjected to compressive stress (Yoder *et al.*, 2014).

2.1.3.2 Mechanical characterisation of the disc

The disc can be described as having dynamic non-linear viscoelastic mechanical behaviour. This behaviour is considered to be due to fluid flow through NP, AF and endplate (poroelasticity) (Emanuel *et al.*, 2015, Vergroesen *et al.*, 2014, Argoubi and ShiraziAdl, 1996, Iatridis *et al.*, 1996, Broberg, 1993) and intrinsic solid phase viscoelasticity (Pham *et al.*, 2018, Tavakoli and Costi, 2018a, Holzapfel *et al.*, 2005). This overall mechanical description of the disc is defined below and in Figure 2.12.

The stress-strain curve commonly observed for biological tissues is non-linear. A typical J-stress-strain curve is shown in Figure 2.12a. The initial low stiffness is important for flexibility as it allows large extensions for small increases in stress. Stiffness increases with strain so large extensions require large stresses which is important for stability (O'Connell *et al.*, 2007, Marini *et al.*, 2015). The concave shape of the curve means that these materials have high toughness as the energy released on failure (area under curve) is lowered when compared to linear stress-strain relationship. Increasing stiffness is due to progressive recruitment of strain resistant components for example increasing hydrostatic pressure (Nachemson, 1963) or fibres in a soft matrix (Pham *et al.*, 2018, Holzapfel *et al.*, 2005).

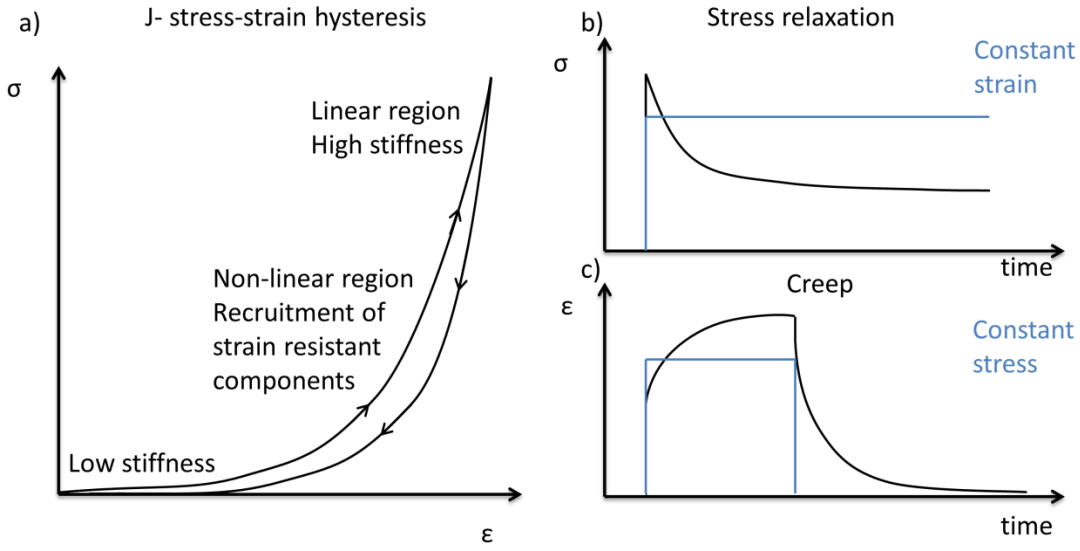

Figure 2.12 Non-linear viscoelastic mechanical behaviour. a) J-stress-strain during loading and unloading b) Stress relaxation c) Creep.

Viscoelastic refers to a time-dependent elastic behaviour with three properties (Figure 2.12). Firstly, as with an elastic material, strain is recoverable however viscous behaviour means that the loading and unloading stress-strain curves do not equate leading to a hysteresis curve. The amount energy absorbed is the area inside the loop, dampening the applied load and increasing structure stability (Gardner-Morse and Stokes, 2003). This curve is also strain rate-dependent (Boxberger *et al.*, 2009, Costi *et al.*, 2008). Secondly, the material displays stress relaxation which is when there is a decrease in stress under constant strain (Périé *et al.*, 2005). Lastly, viscoelastic materials creep (van der Veen *et al.*, 2013, O'Connell *et al.*, 2011a); increasing strain under constant stress can be observed and time-dependent strain recovery after unloading.

The macroscopic response of the disc is reliant on individual constituent tissue properties and microstructure. The disc has functional heterogeneity with anisotropic and regional properties (Tavakoli and Costi, 2018a, Holzapfel *et al.*, 2005, Elliott and Setton, 2001, Iatridis *et al.*, 1998, Skaggs *et al.*, 1994, Cassidy *et al.*, 1989) which must be accounted for when designing a mechanical characterisation study. For example, uniaxial tests reveal that the tensile modulus of the AF when loaded circumferentially is twice that when loaded radially (Guerin and Elliott, 2007, Elliott and Setton, 2001, Iatridis *et al.*, 1998) .

A study by Skaggs *et al.* (1994) examined regional variation in tensile properties of single lamella and found that anterior lamellae were stiffer than posterolateral regions and outer

regions stiffer than inner regions. AF regional variations in stiffness have also been observed in several other studies (Shan *et al.*, 2015, Holzapfel *et al.*, 2005, Elliott and Setton, 2001). Supported by biochemical analysis, Skaggs *et al.* (1994) concluded that the regional stiffness variation was due to structure rather than compositional variation. Only recently, with new imaging and mechanical testing technology, have studies focused on documenting the inter- and intra- lamella mechanics (Tavakoli and Costi, 2018a, Vergari *et al.*, 2016, Mengoni *et al.*, 2015, Pezowicz *et al.*, 2006). However, these initial studies do not compare between different regions of the disc and their imaging was limited to 2D. Furthermore, their act of dissecting samples means residual strain is lost (Michalek *et al.*, 2012). Designing gripping fixtures which consistently apply loads is also challenging.

2.1.4 Animal models

Small (murine) and large (bovine) animal models have similar microstructure and biomechanical properties making them suitable for human studies (Beckstein *et al.*, 2008, O'Connell *et al.*, 2007, Showalter *et al.*, 2012). O'Connell *et al.* (2007) took direct measurements of disc geometry for six commonly used animal models. The percent deviation of the normalised disc height, anteroposterior width and NP area from human geometry was used to compare across models and assess suitability for human studies. Geometric normalisation of the disc has also been used to compare the mechanical properties, glycosaminoglycan and water content of IVDs across animal models. Beckstein *et al.* (2008) concluded that IVD biomechanical properties are largely conserved across animal models including bovine and rat IVDs. Furthermore, Jaumard *et al.* (2015) concluded that rat spine morphology is an appropriate model for axial and shear loading of the human spine. Currently, there is a lack of studies comparing differences in IVD microstructure between animal models instead, literature has focussed on overall geometry as discussed above. However, it is known that the basic hierarchical formation of collagen from molecular to a single fibril appears to be common but there is variation between species, tissues and age of 3D organisation and bundle diameter (Craig *et al.*, 1989, Parry *et al.*, 1978, for information on collagen fibril formation please see a recent review: Holmes *et al.*, 2018). This ultra- to micro- structural variation can be linked to the mechanical system. Holmes et al., 2018 gives the example of comparing between narrow fibrils in cornea to resist hydrodynamic pressure and wide-ranging fibril diameters in tendon to transmit forces. Bearing and transmitting loads in these tissues requires an organised aligned fibrils whereas open networks of fibrils in cartilage and NP resist swelling pressure. Therefore, it is important to consider that there may be micro- structural

and mechanical differences between animal models. Importantly, micro- structural and mechanical characterisation must be from animals of the same age to avoid disparities.

Spontaneous degeneration in small animals does not occur aside for a few exceptions (Moskowitz *et al.*, 1990, Bray and Burbidge, 1998). The presence of notochordal cells, precursors to NP cells, in small animals is considered to be responsible for tissue repair and protecting against degeneration (Aguiar *et al.*, 1999). Interestingly, the sand rat loses notochordal cells and is the only known murine animal model whose IVD degenerates, in a similar manner to human age-related degeneration, based on histological and radiologic evidence (Moskowitz *et al.*, 1990, Gruber *et al.*, 2002), glycosaminoglycan content and resistance to osmotic pressure (Ziv *et al.*, 1992). Due to very limited options of spontaneous age-related degeneration, models for studies of degenerated IVD have been created by AF injury, usually by needle puncture (Michalek *et al.*, 2010, Schollum *et al.*, 2010, Elliott *et al.*, 2008), hyper loading (Paul *et al.*, 2013, Kroeber *et al.*, 2002), or enzymatic degradation (Kalaf *et al.*, 2014, Barbir *et al.*, 2010, Roberts *et al.*, 2008). Recently, a particular mouse strain bred to study low cartilage regeneration has shown potential as a small animal model for IVD degeneration (Choi *et al.*, 2018). Future studies may focus on developing IVD degeneration models through animal breeding or genetic modification such as collagen II mutations (Sahlman *et al.*, 2001).

2.2 Review of imaging techniques for soft tissue visualisation and deformation under load[1]

2.2.1 Imaging soft tissue microstructure

Optical microscopy techniques are commonly used to identify constituent cells and ECM in tissue. Histological visualisation requires micro-spatial resolution and sufficient contrast between cells and ECM structural components. Image contrast between different structures and compositional information can be determined by tissue affinity for various stains. Although serial sectioning and reconstruction can be employed to visualise structures in 3D, the approach is labour intensive and has varied results (Mizutani and Suzuki, 2012). Problematic sections may have to be discarded for a low error reconstruction. Moreover, when viewed by these sectioning techniques, their structure may not be representative as in their natural environment. Sectioning often results in structural damage artefacts such as

[1]Section 2.2 has been taken from Disney, C., Lee, P., Hoyland, J., Sherratt, M. & Bay, B. 2018. A review of techniques for visualising soft tissue microstructure deformation and quantifying strain *Ex vivo*. Journal of microscopy. and adapted for this literature review

tears, fractures, folds and compressions. Ideally imaging should be 3D and non-destructive, leaving the tissue intact in its physiological environment (Walton *et al.*, 2015).

Optical coherence tomography (OCT) uses a relatively longer wavelength light than standard histology and so is capable of penetrating deeper into the tissue (1-2 mm) allowing imaging of mesoscale volumes. Optical clearing of specimens can help to reduce light scattering and hence improve imaging depth. Richardson and Lichtman (2015) review various clearing techniques showing that protocols can range from hours to months and importantly clearing causes changes in tissue morphology. The 3D structural complexity of tissues can be imaged using OCT, for example the connectivity of translamellar cross bridges in the IVD (Han *et al.*, 2015). Furthermore, OCT uses intact native samples allowing for imaging during functional conditions such as artery stiffness changes in pressurised diseased arteries (Adnan *et al.*, 2017). However, caution must be taken when using optical clearing techniques for observing tissues under load. Not only is there a change to the gross mechanical properties but there is a differing effect across tissue types. The differing induced mechanical changes of propylene glycol as an optical clearing agent have been measured using image correlation across tissue layers in artery (Acosta Santamaría *et al.*, 2018). Confocal microscopy has higher resolution than OCT but imaging thickness is limited to a few hundred microns and is only capable of viewing in-plane or nearly in-plane features. The higher resolution, achieved by a focussed high intensity beam and a pinhole to select in focus regions, allows visualisation of microstructures which are responsible for soft tissue mechanical behaviour (Wang *et al.*, 2013, Michalek *et al.*, 2009, Bruehlmann *et al.*, 2004).

2.2.2 *In situ* imaging to observe microstructural deformation mechanisms

Microstructural deformation mechanisms and local strain attenuation is important for native tissue mechanical function. Mechanisms such as collagen fibre sliding, fibre uncrimping, fibre realignment and attenuation by structural heterogeneities have been observed in connective tissue imaging studies. A combination of mechanical testing and imaging, referred to as *in situ* imaging in this thesis, can be a powerful tool to observe microstructural deformation mechanisms. Three case studies of soft tissue *in situ* imaging studies are given below.

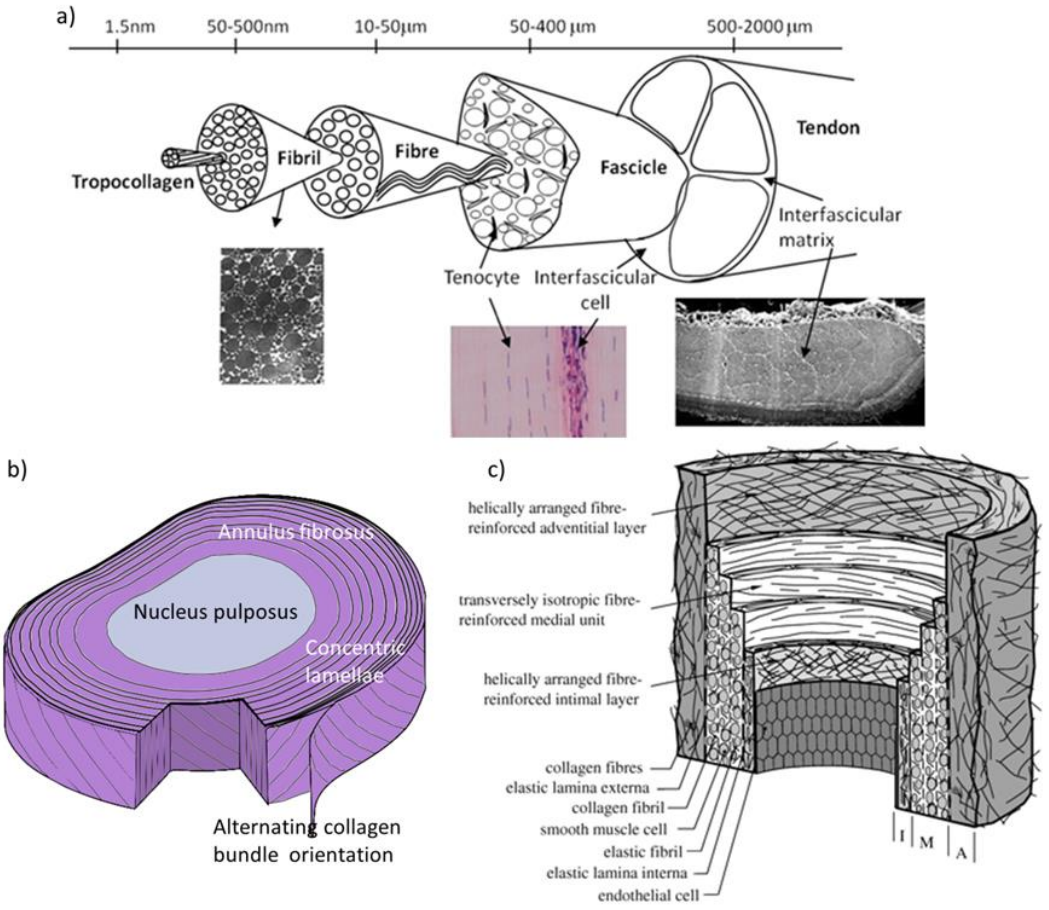

Figure 2.13 Schematics showing the microstructure of different organs. Tendon (a) (Screen et al., 2015), intervertebral disc (b) (Disney et al., 2017) and artery (c) (Gasser et al., 2006) are given as examples. All panels adapted with permission. (Disney et al., 2018).

2.2.2.1 Intervertebral disc

Sections of AF from the IVD have been imaged under load using confocal techniques. Collagen fibrils uncrimped or stretched whilst bundles reoriented and were observed sliding past each other (Vergari *et al.*, 2016, Michalek *et al.*, 2009, Bruehlmann *et al.*, 2004). There's some inconsistency in the observations made at the lamellae boundaries. Bruehlmann *et al.* (2004) reported cells undergo large motions in the interlamellar space suggesting slipping between lamellae. Whereas Michalek *et al.* (2009) and Vergari *et al.* (2016) described no slipping at lamella boundaries. These studies used a 2D imaging technique and different loading conditions of dissected samples for an anisotropic tissue. Cutting samples from the intact structure relieves and disrupts the residual stress state and consequently changing the response to applied loads. The problem is particularly acute

with non-linear materials which shift into different stiffness regimes with the release of residual stress. Further research is required to study IVD microstructural deformation mechanisms in intact samples.

2.2.2.2 Tendon

Tendon is a strong fibrous collagen tissue with a hierarchical structure of fibrils, fibres and fascicles (Figure 2.1a), whose mechanical role is to transmit forces between muscle and bone. The reader can find detailed information on tendon mechanics in a recently published review (Fang and Lake, 2017). Initially tendon fibres uncrimp and realign but the major deformation mechanism is fibre or fascicle sliding under load and during relaxation (Fang and Lake, 2015, Thorpe *et al.*, 2015, Szczesny and Elliott, 2014, Gupta *et al.*, 2010, Screen *et al.*, 2004). This sliding mechanism indicates load is transferred through the tissue by shear as the fibres do not bear load independently (Szczesny and Elliott, 2014). Confocal microscopy has frequently been used where cell nuclei are stained and tissue mechanics inferred by cell movement (Gupta *et al.*, 2010, Screen *et al.*, 2004). Photobleached lines have also been used to visually observe tissue mechanics (Fang and Lake, 2015, Szczesny and Elliott, 2014) but the DTAF stain used has been shown to alter tissue mechanics (Szczesny *et al.*, 2014).

The main challenge in tendon mechanics research is that their shape and loading conditions are extremely varied. The deformation mechanisms depend on loading conditions: for example, shear attenuation is dominated by fibre sliding whereas compression attenuation is dominated by uncrimping and fibre reorganisation in the rotator cuff tendon (Fang and Lake, 2015). To accurately observe and measure microstructure deformation further studies are required using different loading conditions and 3D imaging.

Whilst fascicle sliding is clearly a major microstructural deformation mechanism, the contribution of sliding is dependent on the tendon type (energy storing versus force transmission) and governed by tendon composition, specifically the interfascicular matrix characteristics (Thorpe *et al.*, 2015). Similarly differing composition of fibrocartilage (proteoglycan micro-domains) has been shown to influence overall deformation and the subtle local heterogeneities responsible for the complex deformation mechanisms (Han *et al.*, 2016b). To fully understand this behaviour between tendon types a full-field local strain map is required.

2.2.2.3 Vascular

Arteries carry blood away from the heart and so are required to withstand cyclic changes in pressure. Composed of three concentric layers; collagen fibres make up a connective tissue (tunica adventitia) which surrounds the outside of the vessel, smooth muscle cells and elastic tissue form the central layer (tunica media) and endothelia cells line the inside (tunic intima) (Figure 2.13c). A reduction of waviness in the elastic lamellae of arteries has been seen with increased internal pressure using confocal and electron microscopy (Krasny *et al.*, 2017, Schrauwen *et al.*, 2012, O'Connell *et al.*, 2008, Wolinsky and Glagov, 1964) and more recently using microCT (Walton *et al.*, 2015). In pioneering studies, unfixed arterial tissue was loaded *in situ*, imaged using confocal techniques and uncrimping of collagen fibres was consistently observed (Cavinato *et al.*, 2017, Krasny *et al.*, 2017, Schrauwen *et al.*, 2012). However, there are differing observations regarding the realignment of fibres which may be related to the diverse sample dissection and loading conditions. Cavinato *et al.* (2017) used bulge inflation on segments of tissue (not an intact vessel) and aimed to mimic *in vivo* luminal pressures. Schrauwen *et al.* (2012) used whole-body inflation tests over a range of pressures some of which were not physiological. Krasny *et al.* (2017) applied uniaxial loading in three directions to rectangular strips of tissue. Cavinato *et al.* (2017) states that there was not evident reorientation of collagen fibres under pressurisation, whereas Schrauwen *et al.* (2012) describes fibres aligning to form a symmetrical double helix and Krasny *et al.* (2017) observes realignment of fibres in the applied loading direction. Whilst each study is valuable in characterising structure and mechanical function of arterial tissue, these studies highlight the importance of careful sample preparation and choice of loading mode. The experimental design and conclusions therefore must be interpreted with caution.

The above case studies show how sample preparation required for imaging and choice of loading can affect experimental outcome. Dissecting samples can lead to release of residual strain, and since soft tissue are viscoelastic, this changes their mechanical response to applied loads. Therefore, the desired imaging technique should leave the tissue intact. Furthermore, 2D confocal imaging techniques do not fully capture tissue deformation of an intact sample and so 3D imaging is required. Full-field strain measurement could prove important to investigate deformation mechanisms and how variations in tissue composition, such as proteoglycan content, influence overall and local deformation behaviour.

2.3 X-ray and micro-computed tomography

In comparison to the above imaging modalities, X-rays are more transmissive and less refractile. This means that they can penetrate the specimen with the ability for non-destructive, in terms that an intact sample is used, 3D imaging.

2.3.1 Generation of X-rays

X-rays are a form of electromagnetic radiation with a wavelength of 0.01 to 10 nm and energy between 100 eV and 100 keV.

2.3.1.1 Microfocus laboratory source

Figure 2.14a shows a schematic of an X-ray tube and the generation of X-rays. Briefly, electrons are emitted from a filament (thermionic emission) in a vacuum tube where they are then accelerated by a potential difference (tube voltage) to collide with a target.

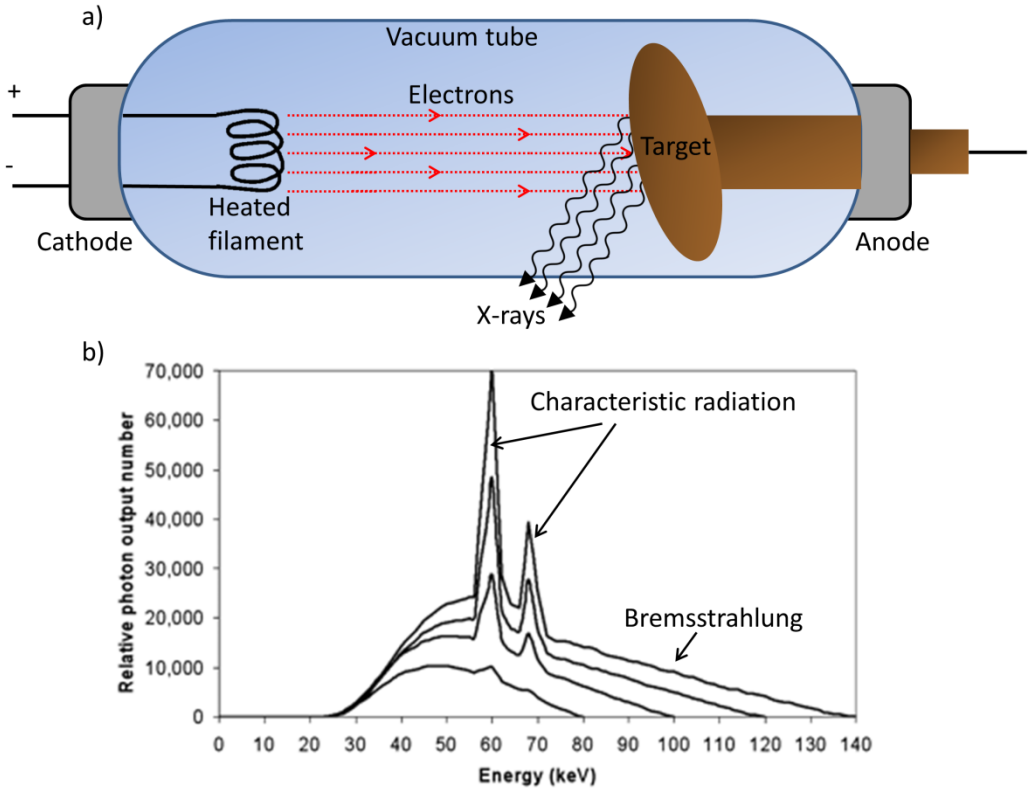

Figure 2.14 Generation of X-rays. a) Schematic of an X-ray tube showing electrons emitted from a heated element are accelerated to hit a target where X-rays are generated. The source can be open or closed. The advantage of having an open source is that it allows for the filament to be replaced. b) An example Bremsstrahlung spectrum with characteristic radiation emitted from an X-ray tube with tungsten target at 80, 100, 120 and 140 kVp. Adapted from Seibert et al. (2004).

Electron collision with the target causes two types of X-ray emission:

i) Bremsstrahlung spectrum emission

Bremsstrahlung interaction causes a continuous polychromatic spectrum (Figure 2.14b). Highly energetic incident electrons decelerate when close a target nucleus. The change in the incident electron's momentum causes emission of X-ray photons. The closer the electron approaches the nucleus, the higher energy of the X-ray emitted and therefore the bremsstrahlung spectrum ranges from zero up to the maximum tube voltage (nucleus collision).

ii) Characteristic X-ray emission

This radiation appears as monochromatic spikes on the bremsstrahlung spectrum and is dependent on the elemental composition of the target (typically tungsten). Electrons emitted from the heated filament knock out an inner shell electron from the target. This means that the atom is now energetically unstable and so an outer shell electron fills the vacancy and photons are emitted equal to the energy difference between the inner and outer shells. Figure 2.14b shows typical spectra emitted from an X-ray tube with characteristic peaks for a tungsten target at different tube voltages. The energy of the spectra therefore depends on the target material and can be changed using downstream filters. This is useful to tune the beam to the sample material absorption profile or filtering to minimise unnecessary absorption or beam hardening (see sections on Interactions of X-rays and Image artefacts).

2.3.1.2 Synchrotron source

Synchrotrons are capable of producing an X-ray beam with high brilliance. Third generation synchrotrons have 10^{10} higher brilliance than laboratory source X-rays (Willmott, 2011). This means that synchrotron source scans can be much shorter than laboratory source scans (minutes compared with hours-days) as there are a higher number of photons per unit area (flux). A parallel and highly coherent beam make synchrotron source X-ray ideal for in-line phase contrast imaging (Section 2.3.4). Electrons are accelerated close to the speed of light and directed using magnets. When the electron beam is influenced by a perpendicular magnetic field (bending magnets or insertion devices), X-rays are emitted to the beamline where optics focus and filter the beam to the experimental hutch. Figure 2.15 shows the major components of a synchrotron.

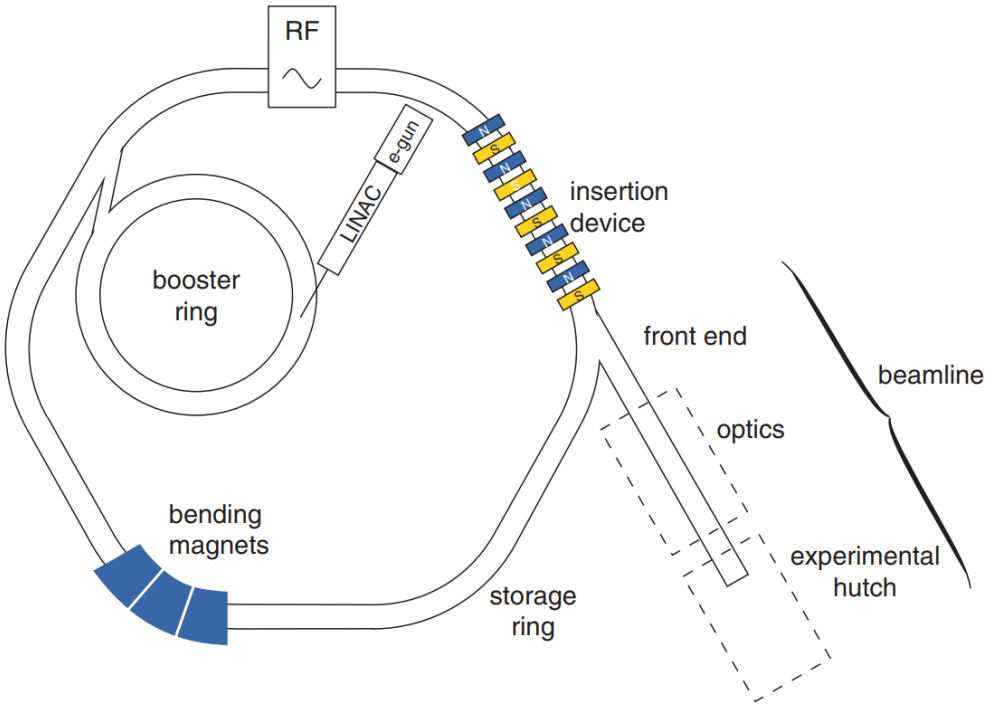

Figure 2.15 Schematic of synchrotron components. Electrons are emitted (e-gun) and accelerated (linear accelerator: LINAC) into a booster ring where they build momentum and are then injected into a storage ring. The storage ring is closed loop where bending magnets change the path of the electron beam. Beamlines, positioned tangentially to the main storage ring, are supplied by radiation from insertion devices (series of magnets) or bending magnets. A radio frequency supply (RF) replenishes energy in the storage ring lost to the beamline (Willmott, 2011).

2.3.2 Interactions of X-rays with matter

The main interactions of X-rays with matter are summarised in Figure 2.16. Thompson (elastic) scattering occurs when the incident radiation accelerates an electron and emits photons at the same frequency. Therefore, the energy of the incident X-rays is the same as the emitted X-rays. Compton (inelastic) scattering is the interaction of the incident photon with an outer shell electron, where energy is transferred to the electron resulting in transmitted X-rays having lower energy. This is a fractional change in energy and therefore can be neglected for X-ray imaging. An important interaction for conventional X-ray imaging is absorption. Incident X-rays are absorbed causing an electron to be ejected. The vacancy is filled by an electron from a shell further out and energy is either emitted as characteristic X-rays (fluorescence) or by the ejection of an outer shell electron (Auger).

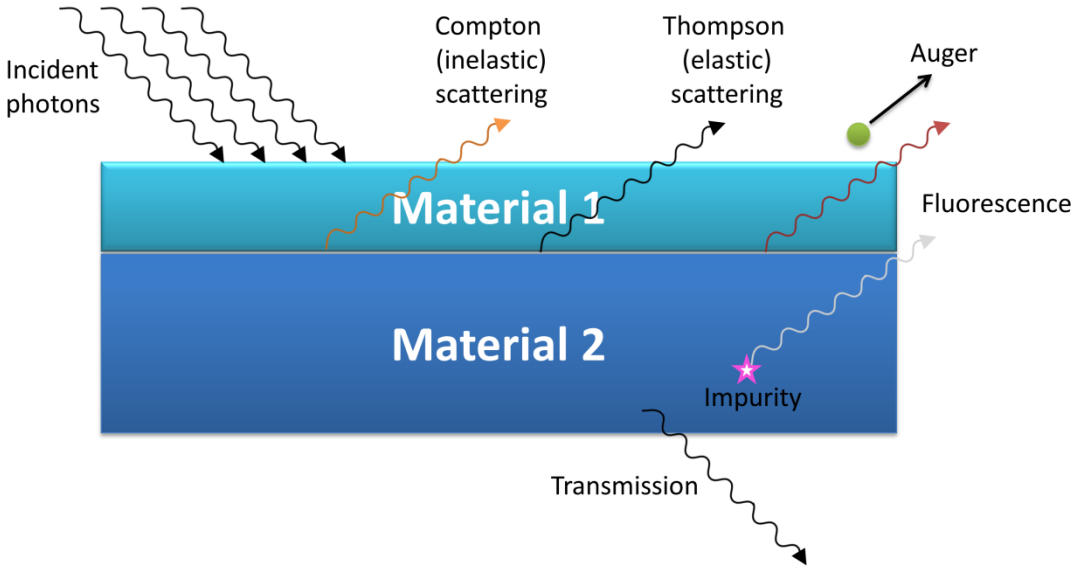

Figure 2.16 Interaction of X-rays with matter. X-rays are either elastically or ineastically scattered at material boundaries, absorbed or transmitted through the sample. If absorbed by the material, lower energy photons or electrons (Auger) are emitted. Refraction occurs when radiation enters a material and, due to a change in velocity, the resulting wave is phase-shifted.

The attenuation of X-rays is therefore dependent on sample thickness and can be described as an exponential decay by the Beer-Lambert equation:

$$\frac{I}{I_0} = e^{-\mu z} \qquad (2\text{-}1)$$

Where I is the intensity of the attenuated X-rays, I_0 is the intensity of the incident beam, z the distance travelled through the material and, μ [cm^{-1}] the absorption coefficient. Absorption is also dependent on density of the material and so a mass attenuation coefficient should be used (μ/ρ, where ρ is density).

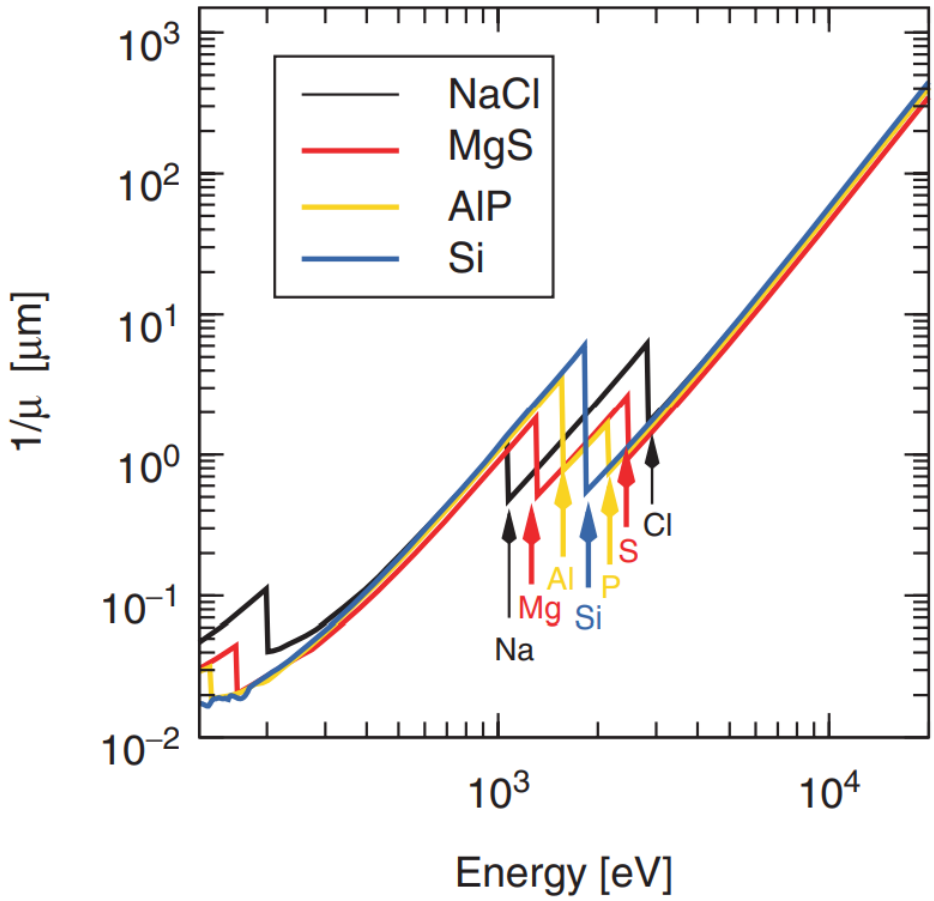

Figure 2.17 Attenuation is proportional to the incident X-ray energy and depends on atomic number. Absorption edges (k-edges) specific to the element and are related to the minimum energy required to ionise the atom. (Willmott, 2011)

Example absorption spectra for different elements are given in Figure 2.17. Absorption is proportional to the incident X-ray energy (E) and atomic number (Z) ($\propto \left(\frac{Z}{E}\right)^3$). Sudden increases, called absorption edges, in the absorption spectra are specific to each element. Absorption edges occur when the incident X-ray energy equals the minimum energy required to knock out an electron.

Besides attenuation, X-rays also change velocity (refraction) when they pass through different mediums. This phenomenon can be described by the complex refractive index;

$$n = 1 - \delta - i\beta \qquad (2\text{-}2)$$

Where, δ is the refractive index decrement and β the absorption index.

Using the complex index of refraction (Equation 2.2), neglecting absorption as the X-ray passes from a vacuum (v_1=c) through an object (v_2=c/n), phase velocity increases and the wavefront therefore stretches by $(1-\delta)^{-1}$. This means that there will be a phase shift (φ) of

$$\varphi = \frac{2\pi L\delta}{\lambda} \qquad (2\text{-}3)$$

Where L is the length of the beam path through the object and λ is wavelength.

2.3.3 X-ray transmission contrast acquisition

As the most basic description of microCT, the transmission of X-rays through a sample are recorded as a series of projections - taken regular intervals whilst the sample is rotated – and are reconstructed into a three-dimensional volume.

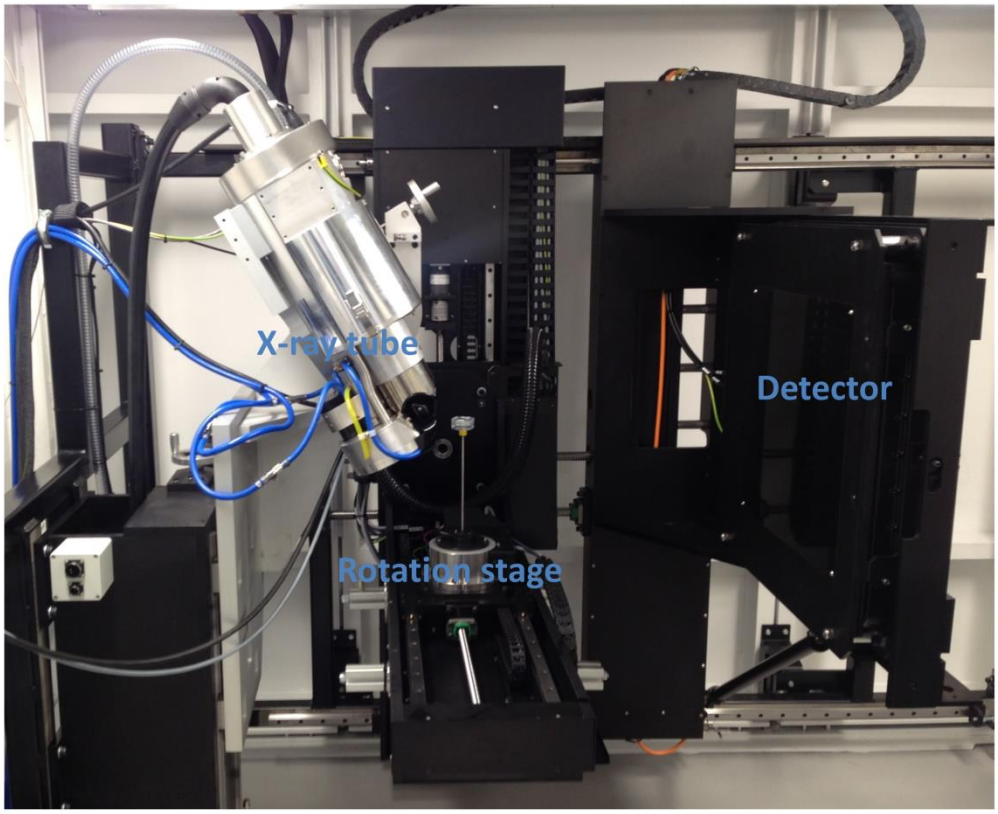

Figure 2.18 Laboratory microCT system. An X-ray beam, originating from an X-ray tube, passes through a sample placed on the rotation stage. The transmitted signal is detected using a scintillator and CCD array.

Figure 2.18 shows the set-up for a laboratory microCT system. A microfocus X-ray tube produces X-rays whose energy spectra depend on input voltage (section 2.3.1.1). These systems generally have cone beams which allows for geometric magnification with sample

position. A sample stage rotates the sample about the perpendicular axis to the incident X-ray beam. The detector comprises of a scintillator to detect X-ray photons as visible light, optics which may be required for magnification and a CCD camera to digitally record the projection. Geometric resolution therefore depends on sample positioning in the cone beam and the detector properties (point-spread function of the scintillator and CCD, optical magnification objectives, pixel size of CCD).

Theoretically the optimal number of projections is given by the 'sampling theorem';

$$N = N_p \times \frac{\pi}{2} \quad (2\text{-}4)$$

where N is the number of projections and N_p the number of pixels per row. However, over-sampling may be advantageous for samples whose scans have low signal to noise or prone to imaging artefacts. Under-sampling produces view aliasing artefacts where fine lines appear in the reconstructed image.

The brightness of each CCD pixel is recorded as a function of the sample rotation angle to produce a sinogram (Figure 2.19).

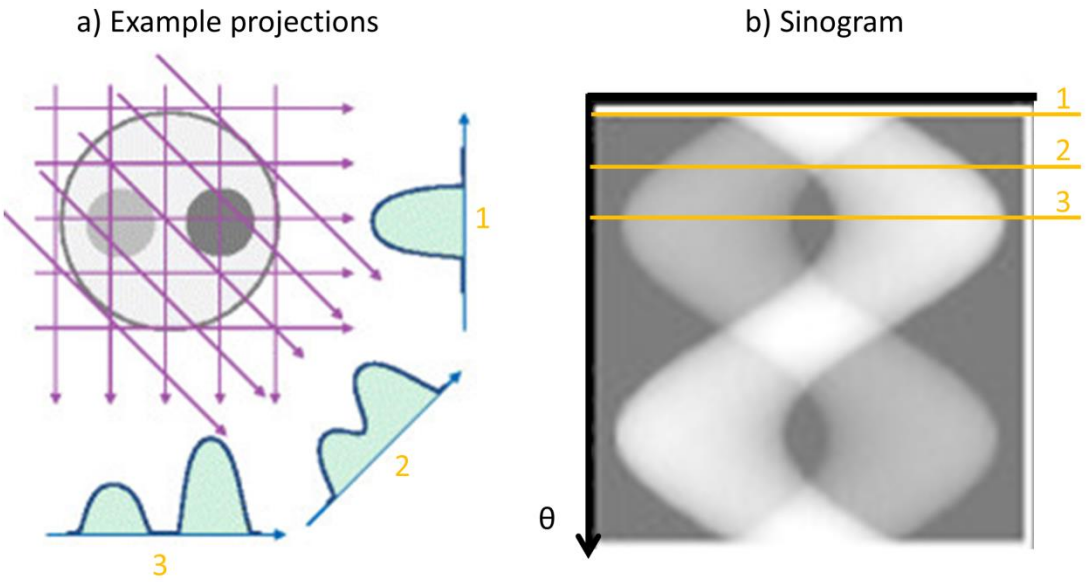

Figure 2.19 Tomography acquisition example. Transmission profiles are taken at multiple different angles through the sample (a) which can represented with respect to the sample rotation angle as a sinogram (b). Adapted from (Iwaguchi et al., 2016)

Using the Beer-Lambert equation (Equation 2.1), the transmitted intensity through a sample with thickness z is by;

$$I = I_0 exp(\sum \mu_k \Delta z) \quad (2\text{-}5)$$

And projection attenuation can be described by;

$$p = -ln\left(\frac{I}{I_0}\right) = \sum \mu_k \Delta z \approx \int \mu(z) dz \qquad (2\text{-}6)$$

This means that the attenuation distribution in a sample can be given by line integrals.

2.3.4 Phase contrast acquisition

Phase contrast imaging is particularly useful for samples which weakly absorb X-rays and therefore have low transmission contrast. There are four main methods which can be used to resolve phase variations in samples. Differential phase contrast imaging uses diffraction gratings to detect upstream refraction and therefore quantify phase gradients in the sample (McDonald *et al.*, 2009, David *et al.*, 2002). Refraction enhanced imaging in principle is similar but uses a crystal for differential measurement (Davis *et al.*, 1995). Alternatively, phase can be measured directly using an X-ray crystal interferometer (Momose, 1995, Bonse and Hart, 1965). In-line (or propagation) phase contrast proposed in the 90s (Wilkins *et al.*, 1996, Snigirev *et al.*, 1995), requires a partially coherent source and sufficient propagation of the beam for Fresnel diffraction. At a certain propagation distance, wave front distortion (refraction and diffraction) gives rise to interference Fresnel fringes which increases structure edge resolution. The propagation distance at which edge enhancement occurs can be given by the following relationship

$$Z_0 \sim \frac{a^2}{\lambda} \qquad (2\text{-}7)$$

Where Z_0 is the propagation distance from the sample and a is the dimension of the scattering object. Beyond this distance the object edges become blurred and at very large distances the detector records far-field diffraction (small angle scattering experiment conditions). This sensitivity to structure size can be problematic when choosing a suitable propagation distance for a sample with wide-ranging structure size. Crucially, a main disadvantage relevant to this thesis, if the sample contains highly scattering material, such as bone, large streaking artefacts and bight edges will interfere with the imaging of surrounding lower scattering material. A major advantage of in-line phase contrast is its simplicity as it does not require any additional optics.

2.3.5 Reconstruction

A commonly used reconstruction algorithm, based on Radon transform (Radon, 1986), is filtered back projection (FBP) (Herman, 2009). This reconstruction simply traces the projection profiles back through the imaging space (Feldkamp *et al.*, 1984). The more

profiles included in the back projection, the more overlapping and summation of information, and the closer the reconstruction is to the real object. However, star-like artefacts and edge blurring can be present when back projecting and so filtering of the projections in Fourier space before reconstruction is usually applied. Low frequency filtering is responsible for blurring and high frequency to smooth noise.

2.3.6 Image artefacts

Overall, insufficient photon count increases the amount of noise which appears as random fluctuations in intensity. Image noise is inversely proportional to the number of photons per unit area and so flux (increase tube current or use synchrotron source) or exposure time should be increased. The reconstructed images may also contain artefacts such as streaking, shading, rings and distortion. These may either occur due to the physics of the acquisition process, be sample-based artefacts or arise from the scanner equipment.

Beam hardening is when the mean energy of the beam increases. As the X-ray beam passes through an object, the lower energy photons are more rapidly absorbed and so the beam becomes 'harder'. This results in two types of artefacts. In homogeneous samples, attenuation appears to be lower in the centre of the object due to beam hardening at the edge producing a cupping artefact. Beam hardening appears as streaks and dark bands in heterogeneous samples (regions with high absorption) (Boas and Fleischmann, 2011). To minimise beam hardening artefacts, the beam can be filtered so that it is 'pre-hardened' and a correction during reconstruction can be used. Monochromatic (synchrotron) sources are less susceptible to beam hardening. For heterogeneous samples it is advised to carefully position the sample to minimise variation in absorption through the beam path to avoid streaking and dark bands (Barrett and Keat, 2004).

Photon starvation also creates similar dark band artefacts across the reconstructed image. This is when insufficient photons reach the detector due to highly attenuating areas, leaving a shadow in the beam path. To avoid photon starvation a higher flux source should be used (such as increasing tube current or using a synchrotron source) or the exposure time should be increased.

Ring artefacts are related to defective pixels in the detector. They appear as partial (common in synchrotron microCT) or full (common in lab microCT) circles centred and superimposed over the reconstructed image data. Flat field projections (without the sample in the beam path) can be taken to account for the defective pixels and subtracted from the image data and ring artefact removal is available during reconstruction (Raven, 1998).

If the sample moves during the acquisition process motion artefacts, such as streaks and image distortion, will be present in the reconstructed image. This is problematic for biological samples, particularly soft tissues, which could be at risk of shrinkage through dehydration and are likely to creep or relax during the scan. Ensuring the sample remains hydrated and is securely attached to sample holders minimises the risk of sample movement during acquisition. A high flux (synchrotron) source is capable of fast scan times (minutes) when compared to laboratory (hours-days). Decreasing scan time by reducing the number of projections and exposure time also decreases the likelihood of motion artefacts but with a compromise with decreased image quality (signal to noise ratio) (Atwood *et al.*, 2015).

2.4 MicroCT of soft tissues

MicroCT is commonly described as a non-destructive imaging technique as intact samples are used and physical sectioning or dissection is not required to resolve internal structure. However, it is important to consider the impact of ionising radiation on tissue structure. Radiation damage is evident as cracks in bone tissue, particularly when using high flux sources (synchrotron) combined with extended exposures leading to high radiation doses (230 kGy) (Fernández *et al.*, 2018a). Even with cracks visible, gross elastic properties remain the same with increasing dose. Due to microCT being an emerging technique to study soft tissue, there has been very little work on the effect of radiation doses to soft tissue microstructure. A recent publication studied the effect of microCT on chemically fixed and paraffin embedded samples and found that structural morphology was persevered even at the highest dose tested (Bedolla *et al.*, 2018). It is logical that radiation damage depends on beam properties (energy, dose), any sample preparation and the composition of the sample. Chemical fixation of tissue cross-links proteins to preserve tissue ultrastructure. Therefore, fixed tissue is less likely to experience radiation damage through chemical breaking of bonds. Native collagen fibril structure in breast tissue has been shown to be sensitive to X-ray dose measured by a drop in signal intensity in a small x-ray scattering pattern (Fernández *et al.*, 2002). Further research is required to quantify the effect of radiation dose to native collagenous tissue micro- and ultra- structure and local mechanical properties. Nevertheless, the localised effect of radiation dose on any biological structures can be considered and dose minimised but with a compromise in image quality.

Soft tissues are composed of low atomic number elements (carbon, hydrogen, oxygen) and thus have low X-ray absorption. Note, absorption is proportional to the atomic number

cubed (Section 2.3.2). Comparable levels of hydration in soft tissues also results in low contrast between constituents. Therefore, transmission contrast in soft tissue samples is low but can be enhanced using heavy metal stains or by drying the sample. Drying the sample is to be avoided as it leads to shrinkage and is not suitable for mechanical testing. In-line phase contrast imaging uses wave information to enhance contrast (Section 2.3.4). This section reviews microCT studies of soft tissue using staining and in-line phase contrast.

2.4.1 Heavy metal stains for collagenous tissues

One advantage of using staining agents is that they do not require any special conditions such as controlled temperature and pressure. The only requirement is the stain must penetrate through the layers of tissue (bulk staining) and have a binding affinity so that it remains in the tissue.

Descamps *et al.* (2014) reviews staining agents for soft tissue microCT and concluded that the best contrast (determined by tissue discrimination in mouse embryos) is obtained by aqueous solutions of osmium tetroxide (OsO4), phosphomolybdenic acid (PMA), or phosphotungstic acid (PTA). However, osmium tetroxide is highly toxic and so should be avoided where possible. PTA and PMA stains gave best results in terms of contrast enhancement and had a binding preference to collagenous connective tissue. PMA was found to stain cartilaginous structures which suggests it may be a suitable stain for the IVD.

The binding affinity of a stain varies according to tissue type which makes it possible to identify different tissues. Binding affinity is also dependent on multiple variables; solvent, concentration, pH, tissue fixation or pre-treatment (Descamps *et al.*, 2014, Pauwels *et al.*, 2013). Iodine solutions have not shown specific adherence to a particular tissue type (Mizutani and Suzuki, 2012) but it is known that iodine trimers have a binding affinity to glycogen and lipids (Metscher, 2009a). Nevertheless, iodine is ideal for bulk staining large specimens as it has been shown to have a higher penetration rate when compared to other stains (PMA and PTA) (Descamps *et al.*, 2014, Gignac and Kley, 2014, Metscher, 2009b). As a result it has been used in multiple soft tissue studies with larger samples such as mouse heads (Cox and Jeffery, 2011, Jeffery *et al.*, 2011), tendons (Balint *et al.*, 2016, Shearer *et al.*, 2014b) and hearts (Butters *et al.*, 2014, Stephenson *et al.*, 2012).

PTA and PMA require longer incubation times, in comparison to iodine stains, for their relatively large molecules to diffuse through the tissue. It can be expected that larger

molecules are less likely to penetrate throughout the sample. However, Pauwels *et al.* (2013) found a positive correlation between atomic number and penetration depth of 12 stains in mice paws after 24 hours and 1 week of staining. The authors noted that penetration depth and rate also depended on the concentration of the solution, the solvent, the tissue composition and any pre-treatment of the samples. The concentration of each stain was not constant and so penetration may have been affected by this.

Although iodine has been found to have a high penetration rate, caution should be taken when choosing concentration and staining duration to minimise tissue shrinkage. Vickerton *et al.* (2013) quantified tissue shrinkage for fixed tissues when using different concentrations of iodine potassium iodide (I_2KI) for various staining times. They concluded that shrinkage is most dependent on stain concentration with the most severe case of 70% shrinkage for 20% I_2KI concentration. As a result, it is important to optimise staining conditions to find the lowest concentration required to visualise structure and minimise artefacts due to shrinkage (Balint *et al.*, 2016). Isotonic staining solutions have been investigated to reduce tissue shrinkage which did reduce the effect but tissue distortion was still present (Degenhardt *et al.*, 2010).

The majority of studies to date have focused on whole model organisms where stains are used for tissue discrimination or for gross tissue anatomy (Helfenstein-Didier *et al.*, 2017, Descamps *et al.*, 2014, Pauwels *et al.*, 2013, Mizutani and Suzuki, 2012, Metscher, 2009a, Metscher, 2009b). Only a few staining studies have aimed to resolve collagenous tissue structure (Sartori *et al.*, 2018, Balint *et al.*, 2016, Shearer *et al.*, 2014b, Nieminen *et al.*, 2015, Nierenberger *et al.*, 2015). These studies used I_2KI, PTA and PMA, all of which have shown promise as potential contrast agents for the IVD.

2.4.2 In-line phase contrast imaging

Soft tissue microstructure can be resolved without the use of stains using in-line phase contrast enhancement (Walton *et al.*, 2015, Naveh *et al.*, 2014, Jiang *et al.*, 2012, Kalson *et al.*, 2012). The phase shift cross section for soft tissue is roughly a thousand times larger than absorption cross section (Figure 2.20) (Willmott, 2011, Momose *et al.*, 1996). Furthermore, phase contrast decreases less rapidly for higher energies: refractive index decrement, $\delta \propto E^{-2}$ compared with absorption index $\beta \propto E^{-3}$. This sensitivity and stability at higher energies means phase contrast imaging is ideal for soft tissue imaging.

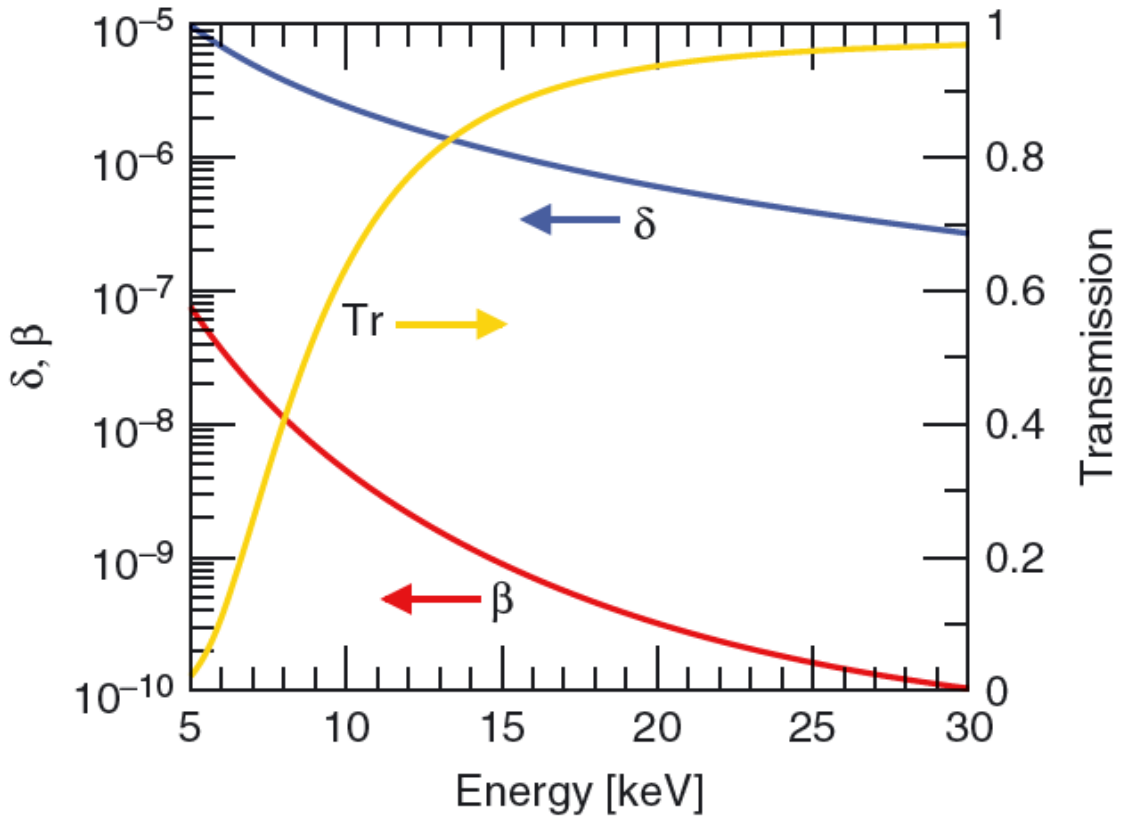

Figure 2.20 Phase shift (refractive index decrement) index (δ) can be a thousand times larger than the absorption index (β). Based on calculations for flesh transmission through 1 mm ($C_{12}H_{60}O_{25}N_5$, density as 1.071 gcm^{-3}) (Willmott, 2011).

Notably, Naveh *et al.* (2014) visualised the main microstructural components of the IVD – distinguishing between the NP and lamellae of AF – using laboratory phase contrast imaging. They concluded that they achieved these imaging results by mechanically stabilising the tissue in a loading device to reduce likelihood of movement artefacts and they used a humidified environment (instead of submerging the sample) to minimise unnecessarily absorbed photons.

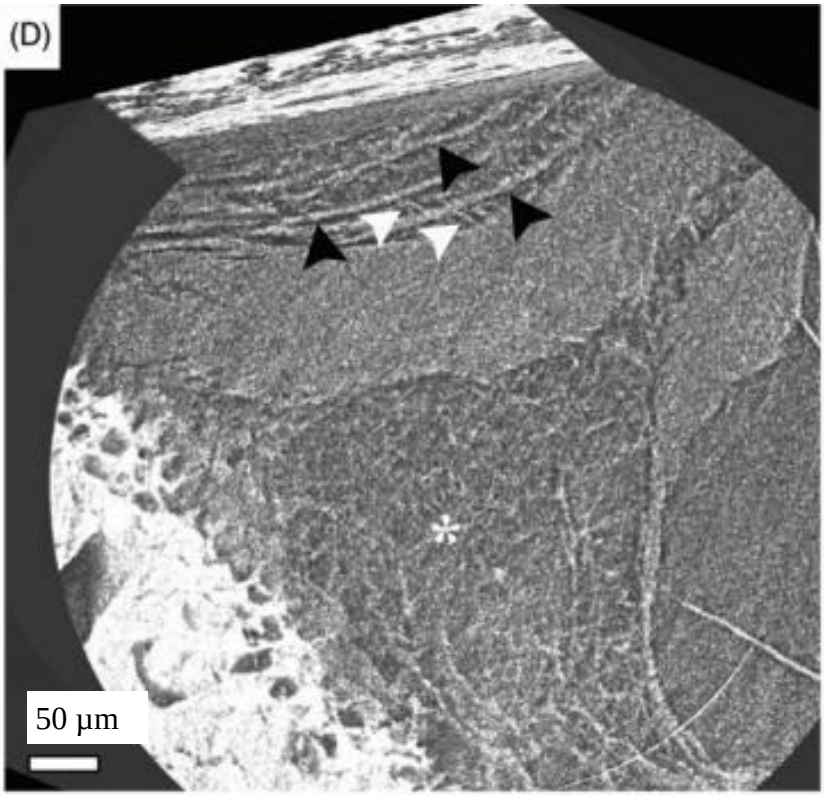

Figure 2.21 In-line phase contrast microCT of rat IVD. Lamellae are indicated by black arrows and bridging by white arrows. Non-lamellar fibrillar NP structure is marked by an asterisk. (Naveh et al., 2014).

Tissue may also be stabilised by embedding in paraffin (Scott *et al.*, 2015, Walton *et al.*, 2015). Walton *et al.* (2015) compared the microstructure of chemically fixed and embedded unpressurised and pressurised arteries using in-line phase contrast microCT. High resolution scans were able to resolve structural remodelling such as an increase in lumen cross-sectional area, straightening of the medial elastic lamellae and remodelling in the adventitial layer. However, this methodology is limited to an observational study as a direct comparison cannot be made before and after pressurisation of the same artery. Furthermore, it is difficult to conduct *in situ* experiments with laboratory phase contrast methods, as creating coherence reduces X-ray flux considerably and scan times become very long (hours-days). The success and challenges of *in situ* imaging for soft tissue mechanics measurement are described in the next two sections and summarised in Figure 2.24.

2.5 Image correlation for strain measurement in soft tissue[2]

Tissue strain has been measured by tracking discrete markers (Fang and Lake, 2015, Karakolis and Callaghan, 2015), beads (Lake *et al.*, 2009), wires or tissue stained with regularly ordered patterns (Fang and Lake, 2015, Szczesny and Elliott, 2014). Tracking discrete markers or patterns provides information on the tissue global biomechanical response. However, these methods are invasive, causing disruption to native structure, and the strain field is inferred from isolated points. The local biomechanical response can be tracked by digital image correlation (DIC) to calculate full-field strain.

2.5.1 Digital image correlation (2D-DIC & 3D-DIC)

Applied speckle patterns or the sample's native structure can be tracked using 2D-DIC to provide displacement fields (Bay, 1995, Sutton *et al.*, 1986, Sutton *et al.*, 1983). Table 2.1 gives examples of soft tissue studies which have used DIC to map strain. Distinct surface features are required for DIC and so frequently a highly-contrasted speckle pattern is created on the sample using stains and ink (Lionello *et al.*, 2014). Briefly, the sample is imaged in its undeformed (reference image) and deformed state and surface patterns correlated for many (often thousands) of subsets distributed over a region of interest. Each subset is tracked from the reference image into the deformed state by optimization of a normalised cross-correlation or sum of squared difference function. Where both, cross-correlation and sum of squared difference, criteria are related (Pan *et al.*, 2007). Normalisation of the function means that it is less sensitive to changes in brightness and contrast. For a detailed review on DIC methods and for derivations of correlations functions please refer to Pan *et al.*, 2009. Relevant to this thesis, the normalised sum of squared differences is calculated as;

$$C_{NCC} = \sum_{i=-M}^{M} \sum_{j=-M}^{M} \left\{ \frac{f(x_i, y_j)}{\bar{f}} - \frac{g(x_i', y_j')}{\bar{g}} \right\} \quad (2\text{-}8)$$

Where M are the sub-sets, f subset of reference image (x, y), g subset of deformed image with applied displacement (x', y') (Figure 2.22), divided by their normalised components. An interpolation function is used to describe f and g, with tricubic a reliable choice for sub-pixel correlation (Lekien and Marsden, 2005).

[2]Section 2.5 has been taken from Disney, C., Lee, P., Hoyland, J., Sherratt, M. & Bay, B. 2018. A review of techniques for visualising soft tissue microstructure deformation and quantifying strain Ex vivo. Journal of microscopy. and adapted for this literature review

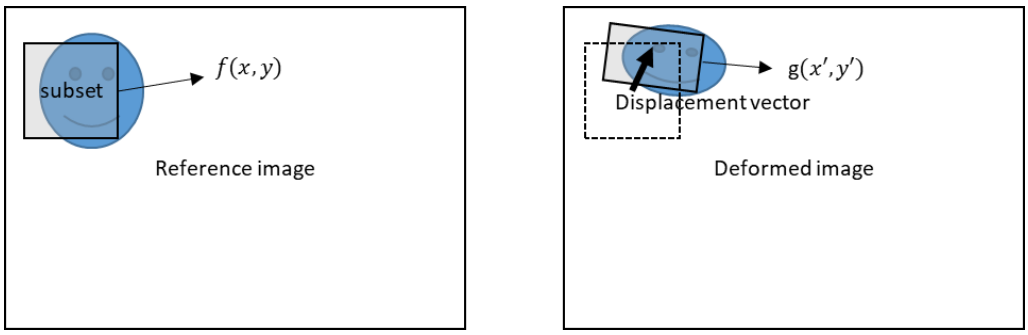

Figure 2.22 Example of a subset before and after deformation. Adapted from Pan et al., 2009.

Change in location of subsets yields displacements, from which gradients are calculated and organised into a full-field surface strain tensor representation. A variety of cameras and microscopes are used as sources of digital images for correlation studies, with the proper imaging method depending on sample size, loading rates, and other considerations. DIC is a well-developed methodology in many areas of experimental mechanics, but soft tissue studies present unique difficulties. Applying speckle patterns to uneven and wet surfaces can be troublesome and cause imaging artefacts such as shadows or reflections. Polarized light can be used to reduce reflections and scattering from wet tissue (LePage *et al.*, 2016). In most cases it is not possible to correlate image areas close to object edges. Locke *et al.* (2017) used DIC to map surface strain of a damaged rotator cuff tendon. But, they were not able to correlate the images close to the defect site (edge) and their study used 2D imaging which is limited to planar samples. If the sample deforms out-of-plane, then in-plane displacement and strain measurements become unreliable with 2D single camera DIC. It is possible to resolve and track non-planar surfaces using stereo imaging and 3D DIC (Mallett and Arruda, 2017, Baldit *et al.*, 2014, Lionello *et al.*, 2014, Badel *et al.*, 2012, Kim *et al.*, 2012, Ning *et al.*, 2010, Sutton *et al.*, 2008). Additionally, panoramic digital image correlation p-DIC has more recently been developed for full surface strain field of arteries (Bersi *et al.*, 2016, Genovese *et al.*, 2013, Genovese, 2009).

CCD cameras have been used to study the surface deformation of tendon (Locke *et al.*, 2017), ligament (Mallett and Arruda, 2017, Lionello *et al.*, 2014), blood vessels (Kim *et al.*, 2012), spine and IVD tissue (Ruspi *et al.*, 2017, Baldit *et al.*, 2014). In these studies, cameras were capable of tracking speckle patterns to map tissue-scale strain distributions but failed to resolve sufficient native tissue structure for tracking. Higher resolution microscopy techniques are able to use tissue structure to track deformation. For example, the displacement of stained cell nuclei was tracked in a murine carotid artery using a

stereomicroscope and 3D DIC (Badel *et al.*, 2012, Ning *et al.*, 2010, Sutton *et al.*, 2008). Similarly, chondrocytes in cartilage were imaged using confocal microscopy which provided sufficient texture to map strain (Kaviani *et al.*, 2016, Amini *et al.*, 2013). Second harmonic generation (SHG) confocal microscopy can resolve collagenous structures without the use of stains. The natural texture of the collagen bundles imaged using SHG has been used to map strain in IVD annulus fibrosus tissue (Vergari *et al.*, 2017, Vergari *et al.*, 2016). Vergari *et al.* (2016) were able to relate the local strain measurements to the microstructure of the tissue, showing low strain at the lamellae boundaries and higher strain or shear depending on the orientation of collagen bundles and loading direction. The main weakness of this method is that the tissue had to be dissected and loaded which impacts on the physiological relevance and strain analysis. Firstly, physiological and consistent loading is difficult to achieve on a dissected section of tissue which has anisotropic mechanical properties. Many biological tissues have a residual strain which is released once dissected (Michalek *et al.*, 2012). Secondly, it was only possible to analyse strain in 2D and so their data must be approached with caution as out-of-plane deformation cannot be accounted for. Finally, there should be careful definition and interpretation of strain from 2D imaging. Local strain mapping using DIC may lead to different conclusions than strain measurement from discrete points. For example, low strain at the lamella boundary measured using DIC but high inter-lamella strain from discrete measurement. The author's conclusion that these strain measurements may be related to lamellae skewing would be more convincing if 3D imaging and analysis were used.

Table 2.1 Soft tissue DIC studies for mapping surface strain. Studies are organised by sample into tissue groups (indicated by shading). Imaging and DIC method are given as well as further information about the features used for correlation (applied speckle or natural image texture).

Study	**Tissue**	**Origin**	**Imaging method**	**DIC method**
(Locke *et al.*, 2017)	Rotator cuff tendon-bone attachment	Murine	Optical high speed camera	Vic-2D, Correlated solutions Speckle pattern
(Mallett and Arruda, 2017)	Anterior cruciate ligament	Ovine	Optical high speed cameras – 2 FastCam, 1 CCD	Vic-3D, Correlated solutions Speckle ink pattern
(Lionello *et al.*, 2014)	Collatoral ligament	Porcine	Stereo cameras, Aramis 5M	Aramis 3D DIC Speckle pattern
(Bersi *et al.*, 2016, Genovese *et al.*, 2013)	Aorta	Murine	Optical camera 45° concave conical mirror	p-DIC, MATLAB (Genovese, 2009) Speckle Pattern
(Wang *et al.*, 2013)	Carotid artery	Non-human primate	Two-photon confocal microscopy	Modified OpenPIV (Taylor *et al.*, 2010) Collagen fibre texture
(Kim *et al.*, 2012)	Aorta	Human	Stereo CCD camera	Aramis 3D DIC Speckle pattern
(Badel *et al.*, 2012, Ning *et al.*, 2010, Sutton *et al.*, 2008)	Carotid artery	Murine	Stereomicroscope	Vic-3D, Correlated solutions Nuclear staining
(Vergari *et al.*, 2017, Vergari *et al.*, 2016)	Outer annulus fibrosus of intervertebral disc	Bovine	Second harmonic generation confocal microscopy	2D DIC custom MATLAB algorithm Collagen bundle texture
(Baldit *et al.*, 2014)	Sections of annulus fibrosus of intervertebral disc	Porcine	Stereo cameras	KelKins (Wattrisse *et al.*, 2001) Tissue texture
(Kaviani *et al.*, 2016, Amini *et al.*, 2013)	Cartilage growth plates	Porcine	Confocal microscopy	Custom MATLAB algorithm Tissue texture

2.5.2 Digital volume correlation (DVC)

Digital volume correlation (DVC) aims to overcome some of the limitations of both 2D- and 3D-DIC methods. DVC utilises volumetric imaging modalities, most commonly but not exclusively X-ray tomography, as the basis of tracking. A volumetric region of interest is populated with small sub-volumes, which are then tracked between the reference and deformed image data sets gathered during *in situ* experimentation. Tracking methodology and data analysis are similar in principle to DIC, but the result is not limited to a sample surface, extending instead throughout the interior.

The first application of DVC was continuum-level strain mapping in trabecular bone from laboratory microCT data (Bay *et al.*, 1999). It was successful due to the readily resolved open cellular structure, creating distinct local texture similar to the applied speckle patterns used in DIC. Global approaches have recently emerged as an adjunct to the more common local approaches, with constraints on displacements introduced to help control tracking uncertainty (Roux *et al.*, 2008) (Figure 2.23).

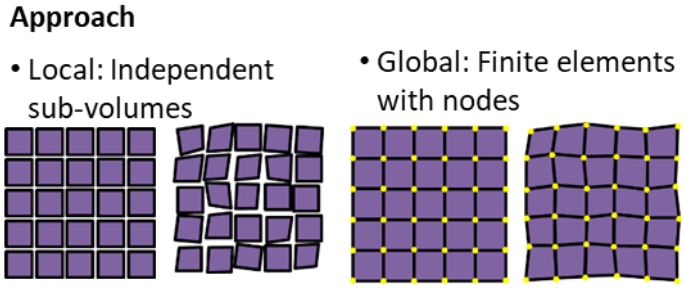

Figure 2.23 The two different approaches taken for DVC. Local correlates independent sub-volumes whereas global uses a mesh and a model of system mechanics to constrain displacements. Global methods have a smoothing effect on displacement results, whilst local approaches retain measurement variability. This variability could be important to learn something new about a systems mechanics. Adapted from Disney et al., 2018.

Since the first application of DVC, strain has been mapped in different bone types and scaffold implants. To approach tissue-level strains, high resolution scans using synchrotron radiation should be taken to resolve textural details within the bone (Dall'Ara *et al.*, 2017). These studies have demonstrated the importance of ensuring that appropriate local texture is available for reliable sub-volume tracking, and tuning DVC parameters to image texture. Authors have placed emphasis on sub-volume or subset size as a key parameter for tracking displacement uncertainties. Displacement precision improved for larger sub-

volume sizes but with a trade-off in tracking resolution (Dall'Ara *et al.*, 2017, Palanca *et al.*, 2017, Madi *et al.*, 2013).

OCT elastography is able to resolve soft tissue structures as small as a few micrometres and map strain in intact samples as a variant of DIC speckle (naturally occurring coherent speckle from OCT) tracking (Schmitt, 1998). The main limitation is the shallow imaging depth of around 1 mm which competes with resolution. Optical clearing can be used to reduce scattering and increase imaging depth. However, A recent OCT DVC study has shown that optical clearing induces mechanical changes at a local level with a differing effect across tissue layers in the aorta (Acosta Santamaría *et al.*, 2018). The applied strain is also limited to 1-2% with higher resolution imaging (Larin and Sampson, 2017). This is an emerging field with few studies in biological tissues such as breast tumours (Allen *et al.*, 2016, Kennedy *et al.*, 2015, Kennedy *et al.*, 2014) and cornea (Lamouche *et al.*, 2012) and two publications using DVC for 3D OCT strain measurement (Fu *et al.*, 2013, Nahas *et al.*, 2013).

Commercial and open source codes are available for DIC and DVC, some examples are given in Table 2.1. Whilst commercial software is designed to be user friendly, it can be expensive, restricted to certain analyses and offer limited flexibility to adapt to complex research questions. Furthermore, commercial software tends to be a 'black box' and so troubleshooting is more difficult in comparison to open source code. In the case of the IVD an open source local approach DVC code (Bay, 2008) will be used. As this will be the first attempt of IVD microCT DVC and a model of the materials mechanics is required for the global approach, the local approach tracking individual sub-volumes will be used.

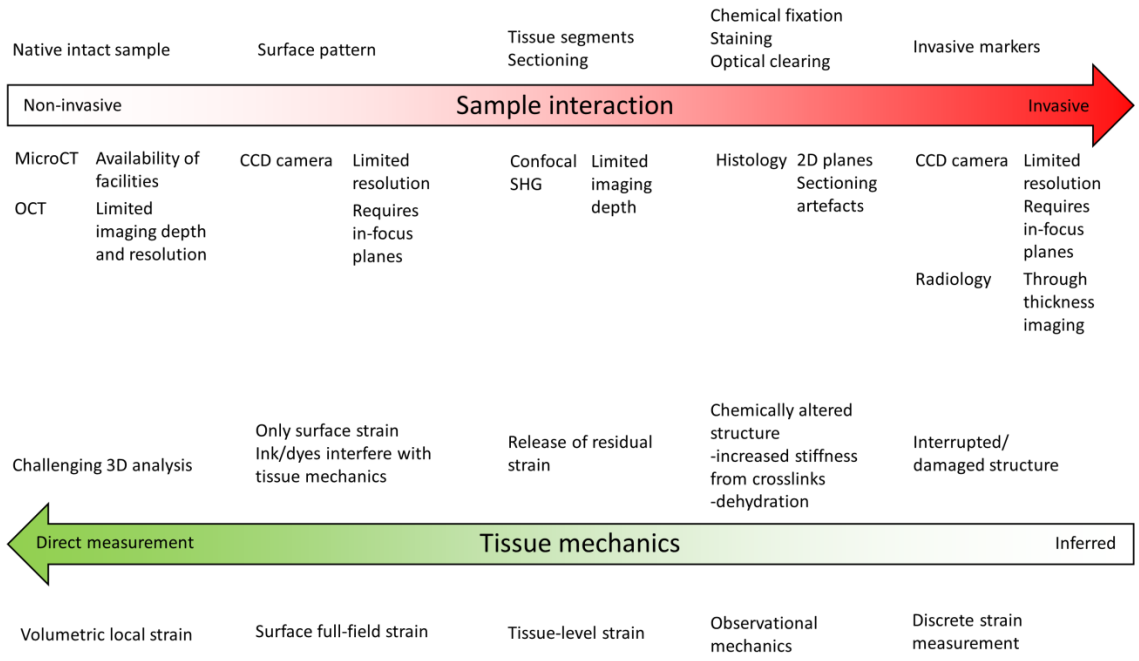

Figure 2.24 In situ imaging to quantify tissue mechanics. The top arrow (sample interaction) describes the sample preparation required for each different imaging technique and their limitations. Tissue mechanics ranging from volumetric strain to discrete strain and observational mechanics can be related to the above imaging techniques (Disney et al., 2018).

2.6 Summary and hypotheses

IVD structures resolved in previous studies are summarised in Table 2.2. It is useful to compare across different imaging methods. Optical techniques are limited to 2D sections or near-surface imaging. The complex structure of the IVD cannot be simplified to 2D; 3D imaging is required to fully characterise structure. OCT is capable of imaging volumetric sections up to 1 mm depth but optical clearing causes changes in tissue morphology. MRI is capable of imaging intact native samples however it is not capable of resolving microstructure and has limited temporal resolution. MicroCT is capable of resolving the microstructure of intact samples however, low X-ray absorption in soft tissues makes gaining contrast challenging. Three-dimensional imaging will enable quantification of; i) endplate curvature, porosity and boundary structure, ii) lamellae organisation and its regional variation, iii) orientation of AF bundles, iv) cell abundance and location in intact IVD.

Table 2.2 Summary of imaging techniques and IVD structures resolved

	Optical microscopy	**Differential interference contrast (DIC)**	**Scanning electron microscopy (SEM)**	**Optical coherence tomography (OCT)**	**Magnetic resonance imaging (MRI)**	**X-ray micro tomography (microCT)**
Specimen	Physical sections, Serial sections for 3D reconstruction			Mesoscale volumetric section	Intact	Intact
Spatial resolution	1,1, >10 µm	10 µm	1, 1, >100 nm	10-20 µm	>300 µm	Depends on FoV 150 nm - > 10µm
Field of view (FoV)	mm, Confocal thickness few hundred microns	mm-cm	mm	mm	cm	mm-cm
Temporal resolution	Seconds	Seconds	Seconds	Seconds	Hours	Hours (lab) Seconds/minutes (synchrotron)
Specimen interaction	Dehydration, fixation and staining Mechanical deformation Fluorescent labelling		Dehydration, fixation and heavy metal staining Digestion of surrounding tissue Mechanical deformation Radiation damage	Fixation, hydrated during imaging Optical clearing causes changes in tissue morphology	None	None for native tissues Heavy metal staining

Table 2.2 Summary of imaging techniques and IVD structures resolved

	Optical microscopy	**Differential interference contrast (DIC)**	**Scanning electron microscopy (SEM)**	**Optical coherence tomography (OCT)**	**Magnetic resonance imaging (MRI)**	**X-ray micro tomography (microCT)**
Compositional information	Chemical from histological staining. Biological from immunohistochemistry staining	Assumed from structure and confirmed with histology				
Potential artefacts	Shrinkage from specimen preparation Tears, holes and debris from sectioning Problematic sections discarded for serial section reconstructions			Motion and flow artefacts		Thermal or oxidative radiation damage Motion artefacts Tissue damage from heavy metal stains
IVD structures visualised	AF, endplate and NP cells NP radial arranged elastic fibres AF collagen I bundles; crimp and organisation AF elastic network; inter-lamella, translamellar cross bridges, compartments Local strain and collagen fibre bundles remodelling under dynamic loading	Translamellar cross bridges AF collagen bundles and compartment arrangement AF-endplate anchorage	NP amorphous fibrillar collagen II framework Inter- and intra- lamellae elastic fibres AF bundle/fibril insertion into endplate	Translamellar cross bridges	Clinical gold standard Macrostructure Strain maps from static loads	Non-lamellar fibrillar NP Lamellar AF Translamellar cross bridges Endplate canal network and porosity

Table 2.2 Summary of imaging techniques and IVD structures resolved

	Optical microscopy	**Differential interference contrast (DIC)**	**Scanning electron microscopy (SEM)**	**Optical coherence tomography (OCT)**	**Magnetic resonance imaging (MRI)**	**X-ray micro tomography (microCT)**
Limitations	Only captures in-plane or near-surface features Sub-sampling when taking sections of heterogeneous tissues. Cannot directly compare structural remodelling of loaded and unloaded tissue. Loading rate cannot be visualised in fixed tissue. DTAF stain used for dynamic studies alters mechanical properties			Imaging depth limited to 1 mm Optical clearing causes	Limited spatial and temporal resolution	Low contrast for soft tissue Radiation damage to tissue Expensive and limited access
Studies	Histology (Figure 2.5) (Walsh and Lotz, 2004) Histology (Figure 2.7) (Melrose *et al.*, 2008) Fluorescence confocal (Michalek *et al.*, 2009) Fluorescence immunohistochemistry (Figure 2.10)(Yu *et al.*, 2015, Yu *et al.*, 2002) Fluorescence confocal (Bruehlmann *et al.*, 2004)	Serial sectioning and 3D reconstruction (Figure 2.8) (Schollum *et al.*, 2009b) (Yu *et al.*, 2015)	(Figure 2.6) (Inoue, 1981) (Rodrigues *et al.*, 2015) Digestion of surrounding tissue to visualise elastic fibres (Figure 2.11) (Tavakoli *et al.*, 2017, Tavakoli and Costi, 2018b)	(Han *et al.*, 2015) (Rodrigues *et al.*, 2015)	(O'Connell *et al.*, 2011b) (Yoder *et al.*, 2014) (Han *et al.*, 2013)	(Naveh *et al.*, 2014) (Gruber *et al.*, 2005) (Rodriguez *et al.*, 2012) (Zehra *et al.*, 2015)

It is important to keep the disc intact when imaging and quantifying microstructural mechanics so that residual stress state is not released. As sample interaction is increased for tissue deformation imaging, such as the use of stains and markers, native tissue mechanics is increasingly affected and strain measurement inferred (Figure 2.24). Image correlation at micro-spatial scale for soft tissue strain measurement has, to date, only been applied in 2D or in limited volumes using OCT. Volumetric strain measurement has been possible in mineralised samples which were readily resolved by microCT.

Three hypotheses have been identified which aims to exploit microCT and DVC for strain measurement in the IVD.

1) **Three-dimensional intervertebral disc microstructure will be resolvable using X-ray micro tomography**

The initial study (Chapter 3) aimed to i) determine if X-ray contrast agents are required to resolve the NP and AF regions of bovine tail IVDs using laboratory microCT, ii) compare three X-ray contrast stains for IVD tissue and iii) assess structural changes caused by staining protocols. I_2KI, PTA and PMA are suitable staining agents based on the literature reviewed. A different approach using phase contrast enhancement aimed to resolve structure in unstained samples building on the scans by Naveh *et al.* (2014) at a similar or higher resolution (4 μm) using laboratory and synchrotron source microCT with the eventual aim of imaging native tissue. Large (bovine) and smaller (murine) animal models were used. Bovine discs were easy to handle but rat IVDs, which are considerably smaller (O'Connell *et al.*, 2007), were more suitable for the field of view of microCT beams.

2) **A series of scans will resolve the microstructure of sequentially compressed, intact native rat intervertebral disc using in-line phase contrast synchrotron microCT**

A proposal submitted to Diamond Light Source (Diamond-Manchester beamline, B) aimed to resolve the microstructure of intact rat intervertebral disc under compression using in-line phase contrast microCT (Chapter 4 & 5). Since it is important to keep the disc intact, spine segments (vertebra-IVD-vertebra) were tested. A simple loading regime was initially used with the consideration of stress relaxation during the experiment. Specialised sample holders for alignment in the beam and a rig with high precision displacement control and force readout were required. Since multiple scans were performed on a single sample, a compromise between image quality and radiation does were made. Volumes of interest were taken for quantitative 3D structural analysis.

3) **Intervertebral disc microstructure deformation can be tracked in microCT image data using digital volume correlation and mapped as strain**

Sufficient image texture was required to track displacements using DVC and parameters were tuned to the image data for reliable tracking. Pre-processing of the image data was necessary to select volumes of interest and for filtering of image noise. Appropriate finite strain calculation was considered as the IVD exhibits large, nonlinear strains. Careful interpretation of the strain tensor using principle strain was chosen as a practical choice. The measured strain was mapped alongside the image data to link IVD microstructure and deformation behaviour. Results are presented in Chapter 4.

3 Visualising the 3D microstructure of stained and native intervertebral discs using X-ray micro tomography

A version of this chapter has been published in Scientific Reports;

Disney *et al.* 2017. Visualising the 3D microstructure of strain and native intervertebral discs using X-ray microtomography. *Scientific Reports*, 7.

Chapter 3

3.1 Author contribution statement:

Catherine M. Disney wrote the paper.

Catherine M. Disney, Michael J. Sherratt, Peter D. Lee and Judith A. Hoyland conceived and designed the study.

Catherine M. Disney, Andrew J. Bodey, Kamel Madi, and Michael J.Sherratt collected the data.

All authors contributed to the analysis and interpretation of the data and to the drafting and final approval of the article.

3.2 Abstract

Intervertebral disc degeneration (IVDD) is linked to low back pain. Microstructural changes during degeneration have previously been imaged using 2D sectioning techniques and 3D methods which are limited to small specimens and prone to inducing artefacts from sample preparation. This study explores X-ray micro-computed tomography (microCT) methods with the aim of resolving IVD 3D microstructure whilst minimising sample preparation artefacts. Low X-ray absorption contrast in non-mineralised tissue can be enhanced using staining and phase contrast techniques. A step-wise approach, including comparing three stains, was used to develop microCT for bovine tail IVD using laboratory and synchrotron sources. Staining successfully contrasted collagenous structures; however not all regions were stained and the procedure induced macroscopic structural changes. Phase contrast microCT of chemically fixed yet unstained samples resolved the nucleus pulposus, annulus fibrosus and constituent lamellae, and finer structures including collagen bundles and cross-bridges. Using the same imaging methods, native tissue scans were of slightly lower contrast but free from sample processing artefacts. In the future these methods may be used to characterise structural remodelling in soft (non-calcified) tissues and to conduct *in situ* studies of native loaded tissues and constructs to characterise their 3D mechanical properties.

3.3 Introduction

Low back pain (LBP) affects up to 84% of the population at some point during their lives (Walker, 2000). Although the aetiology of LBP is complicated, in 40% of cases irreversible structural degeneration of the intervertebral disc (IVD) is thought to be responsible (Cheung *et al.*, 2009). At the centre of each disc is the proteoglycan-rich nucleus pulposus (NP) which is hydrophilic due to a high negative charge density and hence osmotic pressure (Chan *et al.*, 2011). The NP is surrounded by the annulus fibrosus (AF), an outer circumferential ring of fibrocartilage whose anisotropic mechanical behaviour is determined by concentric lamellae composed of alternately angled collagen I fibril bundles (Holzapfel *et al.*, 2005, Marchand and Ahmed, 1990, Humzah and Soames, 1988) (Figure 3.1a). There are many factors linked to IVD degeneration such as ageing (Cheung *et al.*, 2009, Teraguchi *et al.*, 2014), genetics (Battié and Videman, 2006, Battié *et al.*, 2009), reduced nutrient supply and abnormal loading which, as a result of altered cellular and molecular events, causes morphological changes including loss of NP height (Dabbs and Dabbs, 1990, Frobin *et al.*, 2001) and increasingly disorganised AF structure (Urban and Roberts, 2003, Yu *et al.*, 2005). The initiation of the degeneration process has been found to have distinct phenotypes which relate to different risk factors (Adams and Dolan, 2012, Määttä *et al.*, 2014). In order therefore, to characterise the complex nature of IVD structural degeneration and the *in situ* mechanical competency of tissue-engineered IVD replacements, it will be necessary to develop new analysis methods which are capable of visualising and quantifying the effects of applied load on the 3D microstructure of native tissues and organs.

Previously, IVD micro-structure has been characterised by 2D imaging of either tissue sections or the surface of sequentially peeled AF lamellae (Horton, 1958, Inoue, 1973, Marchand and Ahmed, 1990, Cassidy *et al.*, 1989, Eberlein *et al.*, 2001, Holzapfel *et al.*, 2005). However these approaches are: (i) destructive and prone to inducing artefacts, (ii) disruptive of the large residual strains which characterise the unloaded IVD state (Michalek *et al.*, 2012), (iii) reliant on chemical fixation or partial dehydration of the tissues which alters their structure and mechanical properties (Tilley *et al.*, 2011, Hickey and Hukins, 1979) and (iv) confined to imaging relatively small regions of the disc. X-ray micro-computed tomography (microCT) has the potential to circumvent these issues by imaging native (non-chemically fixed) tissues in 3D at microscopic resolutions.

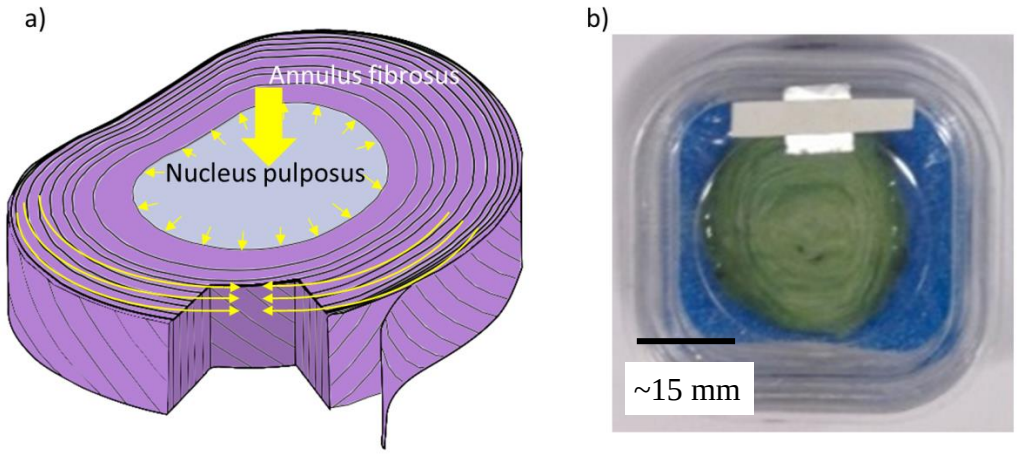

Figure 3.1 Anatomy of the intervertebral disc. Schematic of the IVD (a). IVDs are situated between the vertebral bodies in the spine. They provide flexibility and bear load caused by body weight and physical activity. A portion is cut out to show the central gelatinous NP and the alternating orientation of collagen bundles between adjacent AF lamellae. Yellow arrows indicate the load path. Bovine tail intervertebral disc stained with PMA and stored in membrane box for scanning (b).

Soft tissues and their constituent components weakly attenuate X-rays and as a consequence many microCT imaging studies rely on the use of heavy metal stains to non-specifically enhance X-ray contrast in whole organisms or multiple organs (Mizutani *et al.*, 2008, Gignac and Kley, 2014, Descamps *et al.*, 2014, Metscher, 2009b, Metscher, 2009a, Pauwels *et al.*, 2013). Phosphomolybdic acid has shown to have high affinity for collagens, for example characterising collagen 3D distribution in single organs or tissues at histological resolutions (Shearer *et al.*, 2014a, Nierenberger *et al.*, 2015, Nieminen *et al.*, 2015). However, in most cases these staining procedures are poorly characterised with regards to their biochemical specificity, commonly require the use of chemical fixatives and struggle to penetrate large tissue volumes. An alternative phase-contrast approach is needed to image relatively large native tissues and organs at microscopic resolutions. In-line propagation-based phase contrast imaging makes use of varied refraction of the X-ray wave-front as it passes through an object of varied refractive index. This gives rise to interference fringes and contrast enhancement at the edges of structures and has been shown to be applicable to biomedical applications in which absorption contrast between structures is weak (Walton *et al.*, 2015, Zhang *et al.*, 2014, Kalson *et al.*, 2012).

This study uses a step-wise approach encompassing stained, chemically fixed and native tissues imaged by microCT on 'laboratory' (microfocus tube) and synchrotron X-ray sources with the aim of minimising sample interaction or the effect of preparation on native structure. In the longer term, these methods may be used to characterise age-related structural remodelling in cartilaginous tissues and to map the 3D mechanical properties of tissues and tissue-engineered constructs.

3.4 Methods

3.4.1 Tissues and materials

Three bovine tails (age range 18-36 months) were obtained from the local abattoir (Kurpas Meats PLC). IVDs were dissected as whole structures without endplates. Whole disc samples were ~3 cm in diameter and 1 cm in height. Sample processing and imaging are detailed below with a summary in Figure 3.2. Three stains were chosen for comparison: iodine potassium iodide (I_2KI), phosphomolybdic acid (PMA) and phosphotungstic acid (PTA). All stains were purchased from Sigma Aldrich and solutions prepared following a protocol based on Metscher *et al.* (2009a). A stock of I_2KI was prepared by adding (1g per l) iodine metal (I_2) and (2g per l) potassium iodide (KI) in water and diluting to 10% (v/v) in water just before use. PMA and PTA were made to the same concentration of (2g per l) in water and diluted to 30% (v/v) in absolute ethanol. Due to PMA photosensitivity, the solution was stored and used in opaque containers.

3.4.2 MicroCT of chemically-fixed and stained disc segments and whole discs

Whole IVDs were immediately chemically fixed in 10% formal saline for 24 hours at room temperature and divided into quarter segments to compare the three stains for contrast and penetration. The segments were rinsed with phosphate buffered saline (PBS) before being placed in the staining solutions. After 14 days incubation the segments were then rinsed in 70% ethanol, wrapped in parafilm to minimise drying and scanned in a plastic tube. The segments were scanned using the Phoenix XMT system at the Manchester X-ray Imaging Facility (MXIF: Diamond-Manchester Collaboration, Research Complex at Harwell). The scanner settings were set to a source voltage between 60-90 kV. 2001 projections of 1 s exposure time were recorded. Reconstruction software (Phoenix dato s|x2 reconstruction) was used to generate 3D dataset from the projections. The effective voxel size for the segments varied between 19-21 μm.

Given the low diffusion rate for quarter segments, whole IVDs were incubated in PMA solution for 2 months with regular solution changes. Samples were left at room

temperature with gentle agitation to aid stain penetration. The discs were rinsed in 70% ethanol and placed in a membrane box with a biopsy pad (Figure 3.1b). The membrane clamped the sample to provide stability during the scan. The High Flux Nikon XTEK bay at MXIF was used to image whole discs at source voltage 100 kV (15.8 W). 6433 projections of 1 s exposure time were recorded. Reconstruction software (Nikon 3D pro) was used to give a theoretical reconstructed voxel size of 8.2 μm. Reconstruction of all the stained samples included a beam hardening correction (Nikon 3D pro). Avizo 8.0 was used to visualise and process the reconstructed data. A median filter was applied to denoise the images and a watershed segmentation algorithm was used to separate the sample from the holder. A volume fraction of unstained:stained tissue was calculated for PTA and PMA samples using number of voxels in the segmented volume.

3.4.3 Laboratory and synchrotron phase contrast microCT of unstained IVD tissue

Unstained samples were initially imaged using a laboratory-based microCT system Carl Zeiss Xradia 520 Versa at MXIF with in-line phase contrast enhancement. The sample preparation and imaging were based on methods published by Walton *et al.* (2015). For mounting the samples in paraffin, the fixed IVDs were dehydrated through an alcohol gradient and set in paraffin using Thermo Shandon Citadel 2000 and Thermo Shandon Histocentre 3. A ~3 mm tissue segment of AF was taken to match the system's field of view and excess paraffin was trimmed before scanning. The source voltage was set to 90kV (8W) to provide contrast in the sample and 2501 projections were recorded over 360° using a 4x objective with 3 s exposure time. Source-to-sample and sample-to-detector distances were 33 and 14 mm respectively. This propagation distance (sample-to-detector) allowed for a small amount of phase contrast sufficient to resolve the AF microstructure. The projections were reconstructed using Xradia Versa Reconstructor to achieve an effective voxel size of 2.8 μm.

Paraffin embedded, fixed and native samples were also scanned on the Diamond-Manchester Imaging Branchline I13-2 at Diamond Light Source (DLS) using a filtered (1.3 mm pyrolytic graphite, 3.2 mm aluminium and 70 μm steel) pink beam (5 – 35 keV) with an undulator gap of 5 mm. The higher flux, higher coherence and scope for large propagation distances at I13-2 allows for quicker imaging with greater phase contrast when compared to a laboratory system. In all cases, ~8 mm tissue segments (including NP and AF) were chosen for this study to fit the field of view. The fixed and hydrated native samples were wrapped in film and contained in a sealed plastic tube to minimise drying during the scan. Sample alignment in the beam was under low dose conditions (large

undulator gap and use of shutters). Projections were recorded using the pco.edge 5.5 scintillator-coupled detector (2560 x 2160 pixels and a physical pixel size of 6.5 µm). A 2x objective lens was used to achieve a total magnification of 4x, an effective pixel size of 1.6 µm and a field of view of 4.2 x 3.5 mm. A 4x objective lens was used to achieve a total magnification of 8x, an effective pixel size of 0.81 µm and a field of view of 2.1 x 1.8 mm. Exposure times of 0.045 s and 0.06 s for 4x and 8x total magnification were chosen to give counts representing ~50% of saturation in flat-field images (without sample in beam path). A total of 4001 projection images was found to provide a good compromise between signal:noise and tissue-relaxation artefacts; these were recorded over 180° of continuous rotation ('fly scan') and reconstructed using the proprietary DLS software DAWN (Basham *et al.*, 2015, Titarenko *et al.*, 2010). The propagation distance was increased in ~200 mm increments until sufficient in-line phase contrast was gained to visualise the microstructures. For the sample embedded in paraffin, the propagation distance was 240 mm, whereas 800 mm was required for the fixed and native samples. Avizo XFiber Extension (Rigort *et al.*, 2012, Weber *et al.*, 2012) was used to extract and analyse the collagen bundle structure in the AF. Cylinder Correlation was used to enhance the collagen bundle (fibre-like) structures (Figure 3.7 b). The correlation lines were then traced and displayed as fibres (Figure 3.7 c). Orientation is given by phi (φ, x-y plane relative to the x axis) and theta (θ, with respect to the z axis). Fibre 3D orientation can either be displayed using a coloured fibre render (Figure 3.7 c) or orientation sphere (Figure 3.7 d).

3.5 Results

The experimental design and biological sample details are summarised in Figure.3.2. This figure also conveys the key advantages and disadvantages of different experimental approaches.

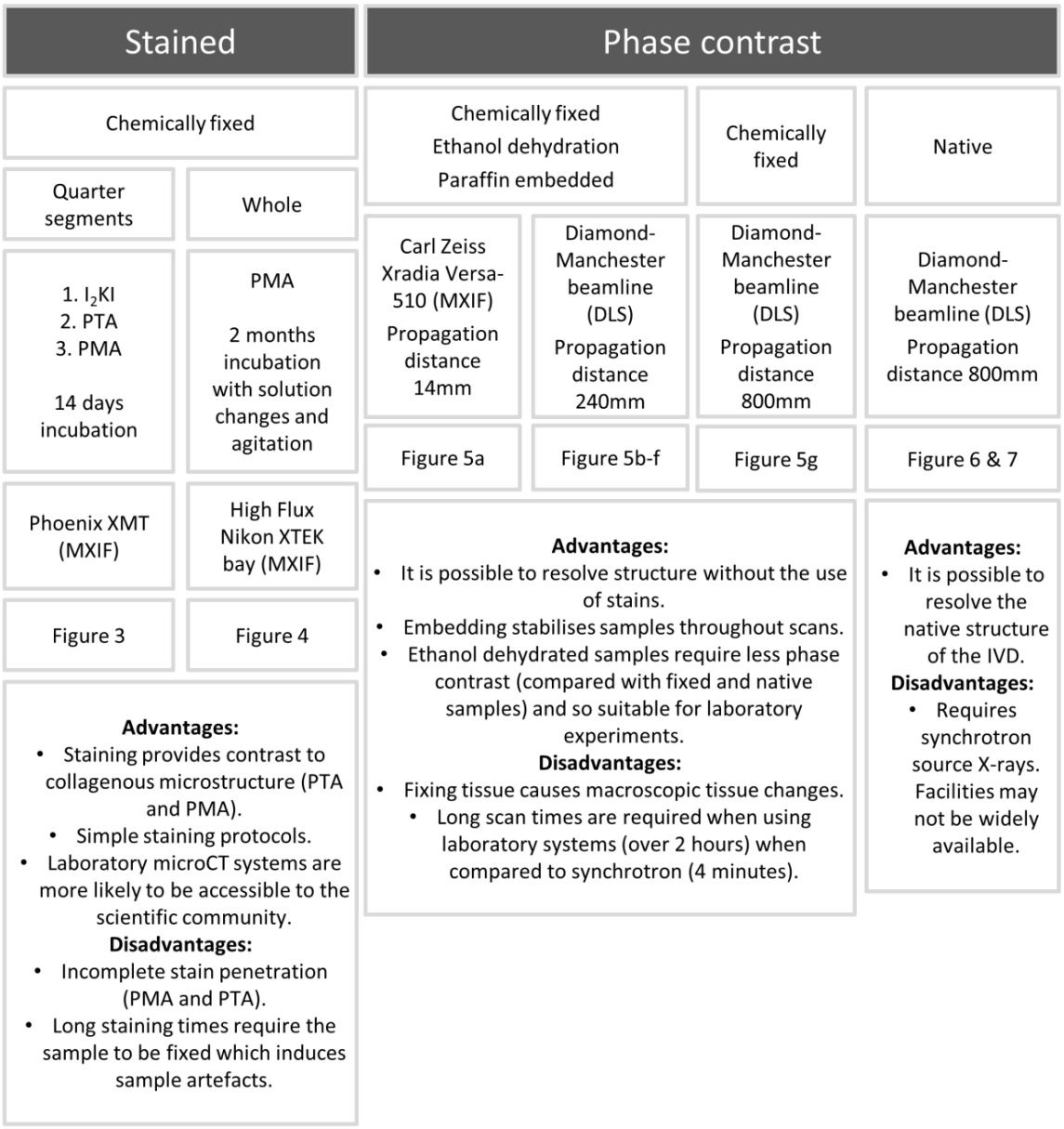

Figure 3.2 Summary of methods. Note: Figure 3 refers to Figure 3.3, Figure 4 refers to Figure 3.4 etc. in this figure.

3.5.1 Laboratory microCT of stained IVD segments

Before attempting to stain a whole disc, quarter segments of bovine tail IVD were stained with either iodine potassium iodide (I_2KI), phosphomolybdic acid (PMA) or phosphotungstic acid (PTA) and scanned on Phoenix XMT laboratory system. Relative stain penetration and contrast enhancement differed markedly between the three stains after 14 days incubation (Figure 3.3). I_2KI fully penetrated the segment whilst PMA failed to penetrate the whole AF and PTA staining was largely confined to the segment edges (unstained regions shown by red volumes in Figure 3.3b & c). The unstained volume fraction for PMA and PTA segments were 15% and 49% respectively. Radial slices clearly

demonstrate that all three stains differentially contrasted AF lamellae (Figure 3.3d-f) but only PMA and PTA were able to resolve the alternating arrangement of collagen fibril bundles in the adjacent lamellae (Figure 3.3h &i). As a consequence, and given its ability to penetrate the tissues more rapidly than PTA, PMA was chosen to stain intact discs.

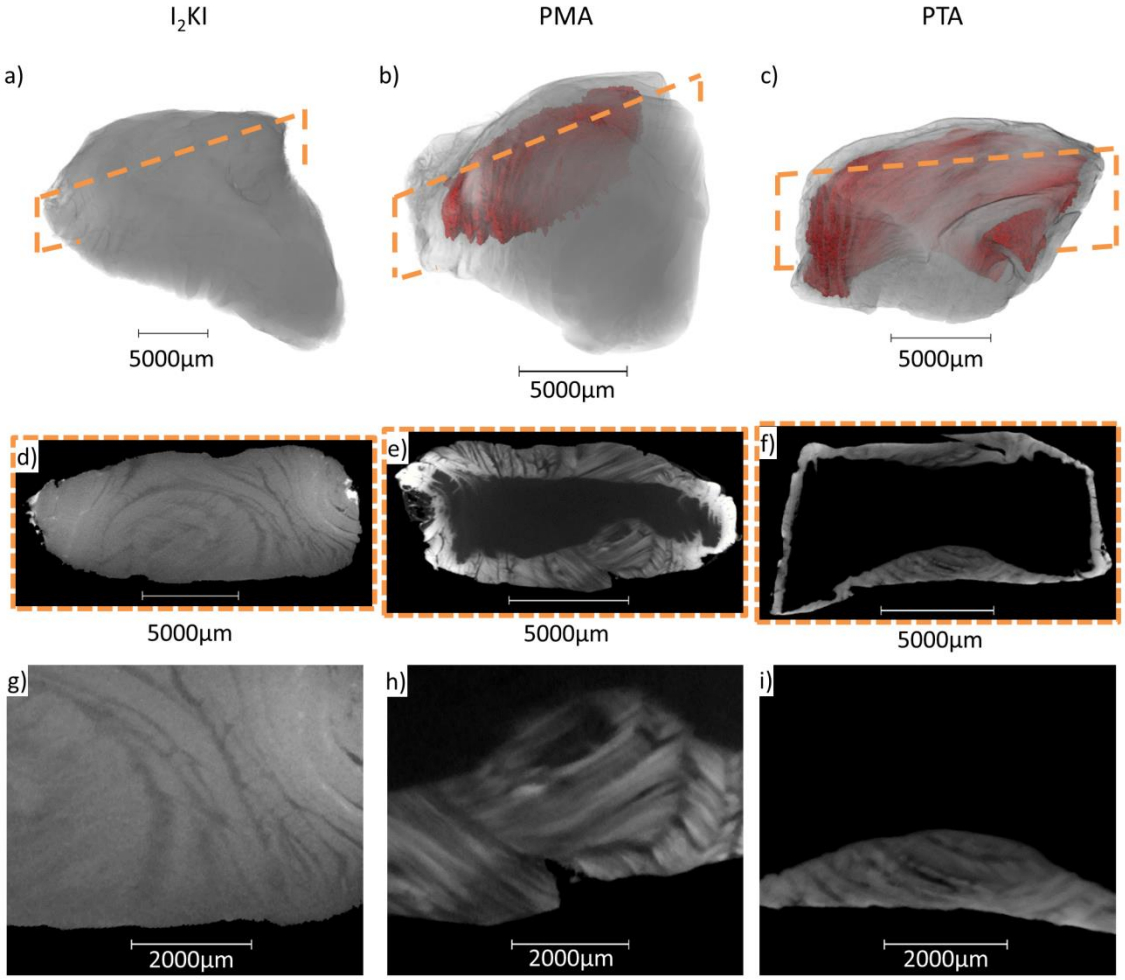

Figure 3.3. Quarter fixed and stained bovine IVD segments. Three heavy metal stains, I_2KI (a, d, g), PMA (b, e, h) and PTA (c, f, i), have been evaluated for enhancing contrast after 2 weeks incubation. Tomogram renders show unstained regions in red (a-c). Radial slices (d-f) showing large unstained regions using PMA and PTA (e, f). Magnified radial slices (g-i) show oblique collagen arrangement in the AF. I_2KI only provides enough contrast to resolve lamella structures in the outer AF region whereas PMA and PTA allow some internal structure of collagen bundles to be resolved.

3.5.2 Laboratory microCT of whole IVD stained with PMA

Whole discs were stained with PMA and scanned on High Flux Nikon XTEK bay laboratory system. When compared with an unstained IVD, PMA staining substantially improved radiographic contrast across the whole disc (Figure 3.4a &b). As with the quarter disc segments, AF lamellae are clearly visible in transverse slices from tomography volumes of PMA stained disc. These structures are not discernible in the tomogram of the unstained disc (Figure 3.4c &d). Although PMA differentially enhanced contrast of the outer collagenous AF compared with the aggrecan-rich NP (Figure 3.4e &f) the stain was unable to penetrate the central region of the AF (Figure 3.4g-i), leaving 4% of the disc's volume unstained. Macroscopically, a comparison of native, chemically fixed and chemically fixed and stained discs showed that fixation and staining caused major structural changes (Figure 3.4j). Chemically fixing the disc caused the NP to swell whilst subsequent staining for long incubation times caused AF lamellae to separate. Given the issues with stain penetration and the effects on tissue structure we next imaged unstained but chemically-fixed tissue using phase contrast on both laboratory and synchrotron X-ray sources.

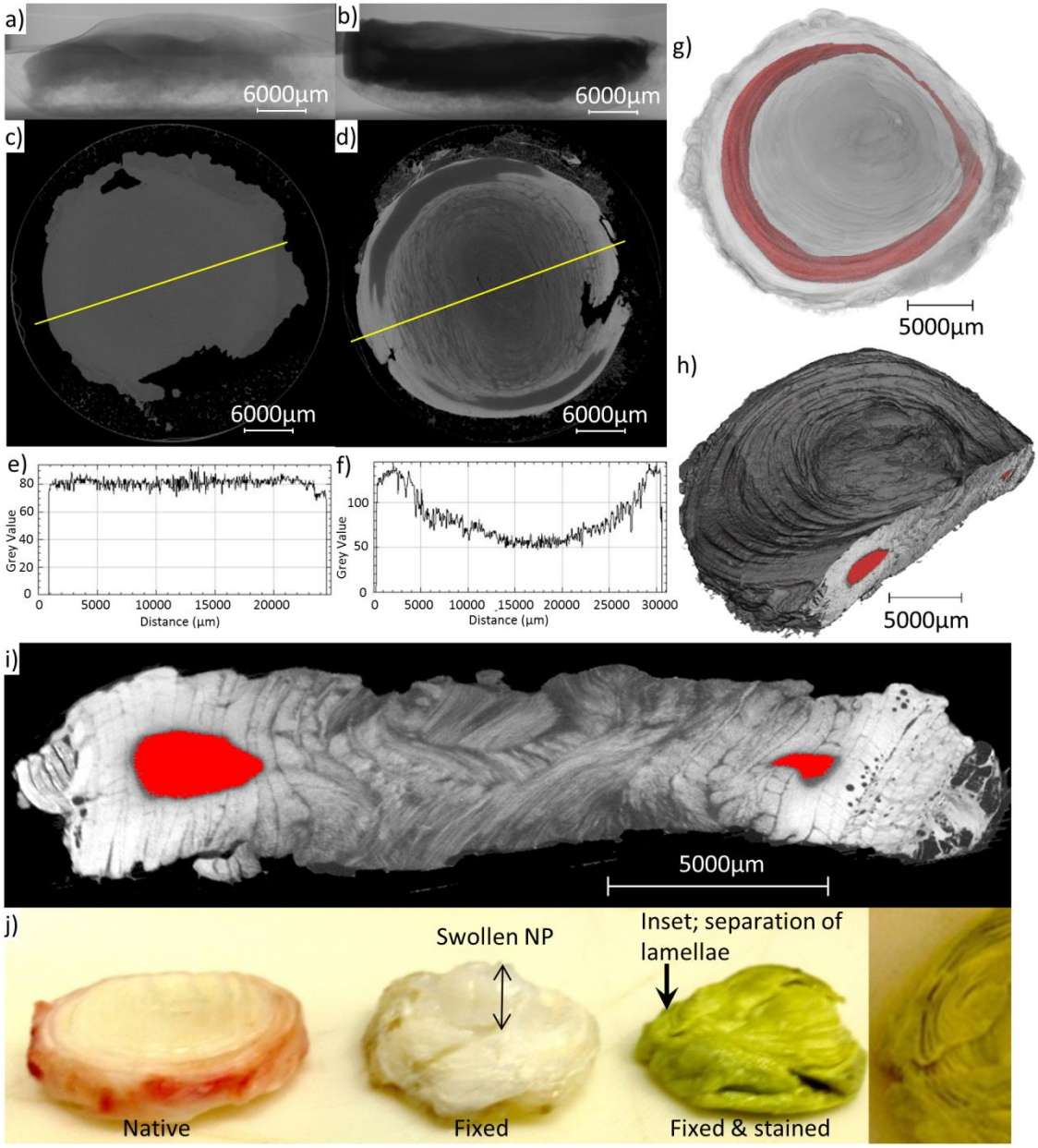

Figure 3.4 Fixing and staining with PMA increases X-ray contrast but fails to fully penetrate a whole bovine disc and causes major structural changes. Whole intervertebral disc unstained (a, c, e) and stained with PMA for 2 months (b, d, f). Radiograph (a), tomography slice (c) and associated line profile (e) show that X-ray attenuation is low and no structural features resolved in unstained IVDs. Attenuation and contrast are improved with PMA staining (b, d, f) although there are still some unstained regions shown in red (g-i). Rendered tomogram (g) clipped to show radial slice (i). Fixing and staining caused visible structural changes (j).

3.5.3 Laboratory and synchrotron source in-line phase contrast microCT of chemically fixed tissue segments

Previous literature has used phase contrast imaging to resolve key structural features in unstained arteries and skin (Walton *et al.*, 2015). Using the same laboratory X-ray source (Carl Zeiss Xradia Versa-510, MXIF) it was possible to resolve alternately oriented collagen fibril rich lamella in the AF (Figure 3.5a) however the signal to noise ratio was relatively low and cracks in the paraffin resulted in conspicuous artefacts. In order to improve both phase contrast and the signal to noise ratio we next imaged the same samples using higher-flux, higher-coherence synchrotron radiation at I13-2 Diamond Light Source (DLS). IVD structures resolved in a single slice from the synchrotron tomogram are shown in Figure 3.5b-e. The NP has an amorphous structure with extremely fine fibres observed in Figure 3.5c. The inner AF has more transitional and less dense lamella structure whereas the outer AF has marked boundaries for each lamella with bridging fibres in the inter-lamella space (indicated by arrows). Taking a radial slice reveals that individual collagen fibres (~5 μm width) have been resolved (Figure 3.5f).

Conventional histological tissue processing utilises three stages: ethanol dehydration, chemical fixation and paraffin embedding. We next demonstrated that it was possible to resolve structures, using synchrotron source X-rays, in chemically fixed tissue without ethanol dehydration or embedding by increasing the amount of phase contrast. The propagation distance was increased from 240 mm for embedded samples to 800 mm for chemically-fixed tissue. The resolved lamellar AF structure is shown in Figure 3.5g.

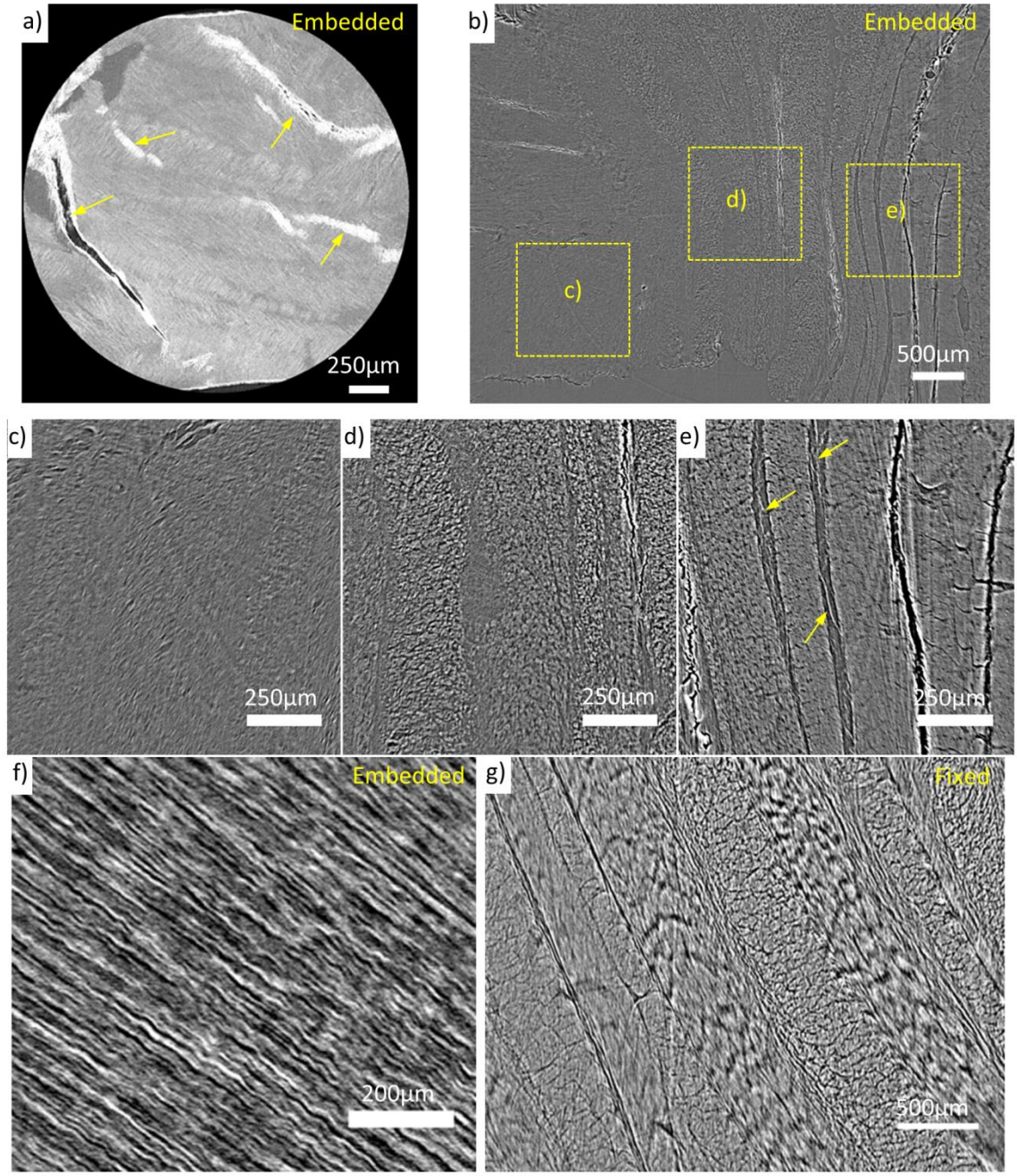

Figure 3.5 In-line phase contrast microCT of unstained bovine IVD segments. Samples scanned using Carl Zeiss Xradia Versa (MXIF) (a) and synchrotron (b-g). Samples have been fixed, through an ethanol dehydration series and embedded in paraffin wax (a-f), or fixed only (g). Overview of IVD structure (c-e) using images taken from one slice (b). Collagen fibres (f) and AF lamella structure (g) were resolved.

3.5.4 Synchrotron source in-line phase contrast microCT of native tissue segments

Although it is possible to image the microstructure of unstained IVD, chemical fixation of the disc causes structural changes, as seen in Figure 3.4j. We therefore next aimed to image native (i.e. non-fixed) tissue. Fine structural details such as collagen bundles, lamella compartments and bridging structures are resolved from the synchrotron source native tissue scans. The images in Figure 3.6 were cropped from the original volume due artefacts around the periphery of the data. A slice and 3D render of the resolved collagen bundles is shown in Figure 3.6a &b. The AF elastic network of compartments and bridges is displayed as a volume and slice in Figure 3.6c &d. These results show that it is possible to image microstructure in native tissues and visualise slices at any location or angle in the volume. The resolution is slightly reduced due to deformation artefacts (slow tissue relaxation during the scan) but this is offset by the absence of sample preparation (fixation and staining) artefacts.

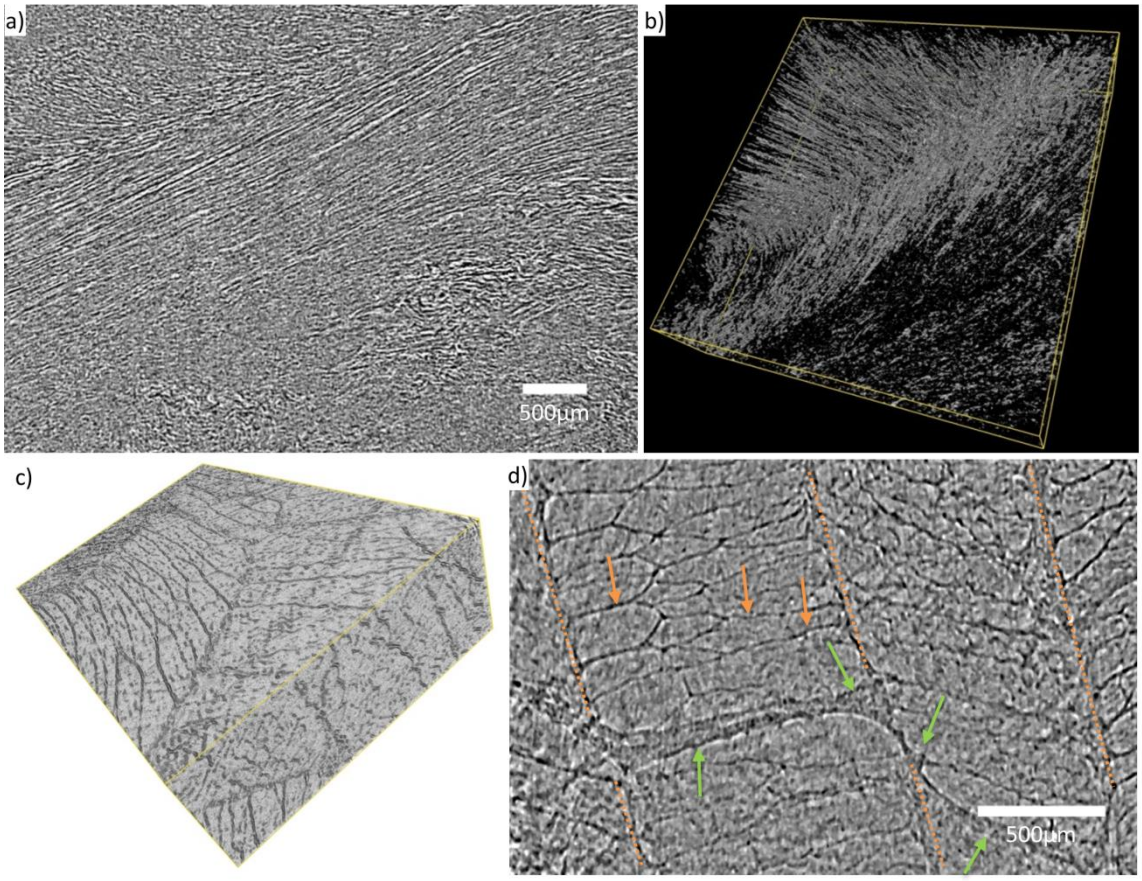

Figure 3.6 Synchrotron source in-line phase contrast microCT resolves bovine IVD microstructure. Scans taken at I13-2 are capable of resolving native tissue structure at histological resolution. A single slice shows AF collagen bundle alignment (a) with 3D render of same region (b) (volume size panel b: 4500 × 1500 × 160 µm). Elastic network of AF (c, d) where orange arrows indicate compartments and green arrows show inter-lamella bridging (volume size panel c: 2540 × 1400 × 500 µm).

3.6 Discussion

The quarter segments scanned on the Phoenix XMT laboratory system after two weeks of incubation showed I_2KI fully stained the IVD tissue but PMA and PTA stains had not completely penetrated the samples. The red rendering in Figure 3.2b and c shows 15% and 49% of the disc's volume unstained for PMA and PTA-stained segments. Slow or incomplete PMA and PTA penetration is in agreement with other staining studies (Metscher, 2009b, Pauwels *et al.*, 2013, Balint *et al.*, 2016). PMA and PTA both have larger molecules ($H_3PMo_{12}O_{40}$ and $H_3PW_{12}O_{40}$) than potassium iodide (KI) and so have lower diffusivity through the dense AF collagen structure. Unstained regions in the PTA and PMA samples were located in the outer AF shown by tomograms (Figure 3.3b, c).

I_2KI staining increased overall X-ray absorption but was limited in revealing tissue sub-structure. This suggests it is more suitable for larger samples such as mammalian organs or smaller organisms where overall anatomical structure is being studied (Vickerton *et al.*, 2013, Gignac and Kley, 2014). Only the outer AF lamella structure was resolved using I_2KI whereas both PTA and PMA clearly stained internal lamellae within the AF (Figure 3.3g-i). An oblique collagen arrangement is visible in samples stained with PTA and PMA. There is a higher take-up of PMA and PTA in the collagen rich AF when compared to the NP. These results indicate that PTA and PMA specifically stains collagenous structures, which is consistent with previous observations (Descamps *et al.*, 2014, Nierenberger *et al.*, 2015, Nieminen *et al.*, 2015, Balint *et al.*, 2016). Both PMA and PTA are present in Masson's Trichrome, used for detection of collagen fibres, although their role in this three stage staining protocol is unclear.

Bovine IVDs are relatively large samples (~30 mm) when compared to those used in previous PMA staining studies (<1 mm) such as iliac veins (Nierenberger *et al.*, 2015), articular cartilage (Nieminen *et al.*, 2015). Considering the discs' volume it was expected that a longer incubation time was required. Agitation and solution changing for whole IVDs was included to aid stain penetration. Solution changing ensured that there was not compound depletion during the two months incubation period. A similar staining pattern was seen in both the quarter segment and whole disc when using PMA; the edges stained with unstained regions inside the AF. This shows that there is not a particular area of the AF that has low affinity but rather the extent of stain penetration through the dense AF structure. Long incubation times, two months for a whole disc, are required for PMA penetration which leads to shrinkage and changes to native tissue structure. Concentration-dependent shrinkage has been reported whilst using I_2KI stains with 70% shrinkage of cardiac muscle after 14 days incubation (Vickerton *et al.*, 2013). Visible structural changes during fixation include NP swelling and consequently an increase in transverse surface area and tissue volume. Long incubation times during PMA staining caused dehydration of the disc and subsequent separation of lamellae (Figure 3.4j). These structural changes are similar to those described in PMA and PTA staining of tendon where shrinkage of up to 25% was inhomogeneous and caused deformation (Balint *et al.*, 2016).

The alternating orientation of collagen bundles in a segment of AF tissue has been visualised in 3D using optical coherence tomography (Han *et al.*, 2015, Han *et al.*, 2016a). Figure 3.4i shows the bundle organisation in an intact disc (IVD dissected as a whole structure and stained) which has not been visualised previously. However higher resolution

is required to fully resolve individual collagen bundles (~5 μm width), but this is limited by the geometric magnification given by a laboratory source cone beam. Multiple structures can be resolved in a whole disc using stains, but the protocol must be improved to stain the entire disc and minimise sample artefacts due to long incubation times. The staining methods used here are simple and are capable of providing contrast to visualise collagenous microstructure (PTA and PMA); however long staining times require the sample to be fixed and staining induces sample artefacts.

Previous work has shown that samples prepared using standard histological preparation (embedded in paraffin wax) and imaged using laboratory source propagation based phase contrast provides sufficient contrast to resolve microstructures in unstained non-calcified tissue (Walton *et al.*, 2015). Figure 3.5a shows the results gained for IVDs using this approach on a Carl Zeiss Xradia Versa laboratory system. Only a small region of interest from a segment of an IVD can be imaged using a laboratory source due to the magnification required to detect interference fringes. A larger field of view and enhanced contrast was possible using synchrotron X-rays at I13-2 (Figure 3.5b, Supplementary video 3.1). However, cracks formed in the supporting paraffin wax and possible effects of dehydration can be seen where cracks aligned with lamella have formed. Further evidence of this is the increase of inter-lamella space, particularly where the lamellae separate and buckle inwards in the outer AF (Figure 3.5e). Imaging fixed tissue resulted in fewer of these artefacts but has been shown to cause morphological changes in IVDs (Figure 3.4j) and structural changes in collagenous tissue such as smaller fibril diameters (Tilley *et al.*, 2011, Hickey and Hukins, 1979). Yet imaging fixed tissue was necessary to be a step closer to imaging native tissue.

To give good phase contrast a larger propagation distance was required for the fixed and fresh samples than for the paraffin samples. This could be related to the hydration of the samples. The paraffin samples had been through an alcohol gradient to dehydrate them before paraffin embedding (standard histological preparation). This leads to larger density gradients across boundaries and thus greater phase contrast. These results agree with Dudak *et al.* (2016) whose work showed that ethanol preservation alone greatly improved contrast.

Importantly, we have demonstrated that it is possible to image IVD tissue without the use of stains, although the samples were fixed which caused macroscopic tissue changes. Imaging native tissue reduces the possibility of sample preparation induced artefacts.

Figure 3.6 demonstrates that it is possible to image native IVD tissue. To our knowledge, only one study has previously imaged the microstructure of native IVD tissue with a laboratory system (Naveh *et al.*, 2014). Laboratory systems have long scans, for example up to 17 hours (2500 projections at 25s exposure) reported in Naveh *et al.* (2014). The mouse IVD AF structure is seen to buckle inwards which is suggestive of sample drying during the long scan time, but the authors comment that this may be related to asymmetric loading. Two different types of IVD structure can be visualised in Figure 3.6. Firstly (Figure 3.6 a, b and 3.7a, Supplementary video 3.2), AF collagen bundles can be seen with a similar resolution to those imaged using confocal techniques (Michalek *et al.*, 2009, Bruehlmann *et al.*, 2004). Secondly (Figure 3.6 c, d), lamella structure and compartments can be determined from reconstructed slices, which is comparable to results from digital interference contrast imaging (Yu *et al.*, 2015) and confocal microscopy (Michalek *et al.*, 2009).

Reports of the elastic network (AF compartments and bridges) in the literature vary depending on the imaging technique used. Elastic fibres (composed of elastin and fibrillin microfibrils) have been found throughout the IVD with the highest concentration in the interlamelar space and in bridging elements between adjacent lamellae (Yu *et al.*, 2007, Yu *et al.*, 2015). AF tissue sections stained with toluidine blue/fast green reveals the translamellar cross bridges (TLCBs) as seen by Melrose *et al.* (2008). However, when using digital interference contrast of serial sectioned AF (Schollum *et al.*, 2009b, Schollum *et al.*, 2009a) or optical coherence tomography of mesoscale volumetric section of AF (Han *et al.*, 2015), the structural complexity was far greater than previously thought from 2D histological studies. Therefore, it is critical to image these structures in 3D in their native form. Using microCT, elastic fibres similar to those seen by Naveh *et al.* (2014), crossing the inter-lamella space in the paraffin embedded samples have been identified (Figure 3.5e). These structures cannot be seen in the fixed and fresh tissue scans; instead the lamellae are closely packed with less organised material between. It may be suggested that dehydration (by paraffin embedding or by the long scan time utilised by Naveh *et al.* (2014)) causes buckling and separation of the lamellae which in turn causes the fibres in the elastic network to be stretched and made visible. Large and small trans-lamella bridges and the finer elastic network within the lamella compartments have been resolved (Figure 3.6 c, d). This shows that the elastic network is a multiscale and a fully integrated structure as demonstrated by Yu *et al.* (2015) using immunostaining.

Fresh tissue is ideal as it possesses near native structure and mechanics, but there may be some imaging artefacts due to sample movement. Artefacts due to sample movement can be minimised by fast scan times, stabilising using a load (Naveh *et al.*, 2014) and by allowing the tissue to relax before scanning (Atwood *et al.*, 2015). Region of interest scanning of a relatively large sample also produces artefacts. The displayed images have been cropped to displayed useable data. A further limitation of taking a region of interest scan is that there is some uncertainty of the exact anatomical location the scan relates to. Future studies may consider a smaller animal model which is more suited to the field of view available with 1.6 µm effective pixel size.

Not only is there a need to visualise the 3D native tissue structure but also to use the acquired image data to quantify structures. Figure 3.7 gives an example of how microCT data can be used to quantify the collagen bundle structure of the AF. Individual bundles can be extracted from the image data and analysed in 3D (Figure 3.7 b, c). Bundle orientation is plotted (Figure 3.7 d) and shows the directional grouping from alternate lamellae.

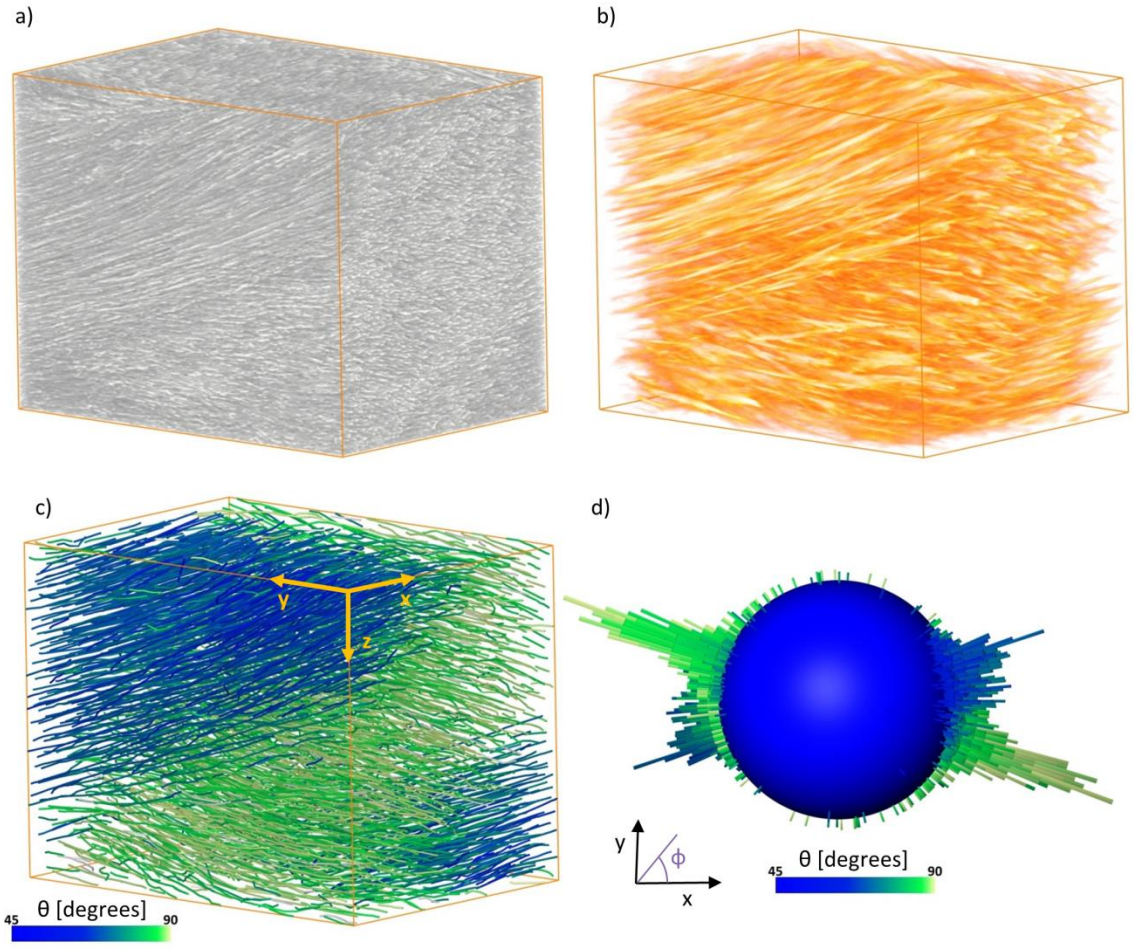

Figure 3.7 Fibre analysis of native bovine annulus fibrosus. Collagen bundles in a cropped volume (1460 x 1030 x 1140 µm) of AF (a) can be correlated to cylinder template (b) and individual fibres traced (c). The 3D orientation of each fibre is calculated and plotted (d). The angle relative to the z axis (θ) is displayed using a colour map and the angle in the x-y plane (φ, 0-360) is shown on the orientation sphere (d) where bar height is frequency.

MicroCT is capable of providing 3D images of intact samples which can be used for structural characterisation of the IVD. Figure 3.2 lists advantages and disadvantages of each approach used in this study. Simple staining protocols using PMA were found to stain the collagenous structure of the AF although it is challenging to fully stain whole bovine discs and staining led to visual changes in structure. Nevertheless, laboratory CT approaches used in this study have potential to quantify changes in tissue structure and mechanisms of AF degeneration which are still unidentified. Importantly, it was possible to resolve a high level of detail in fresh tissue using synchrotron radiation and propagation-based phase contrast. It should be noted that access to synchrotron microCT is limited and

not likely to be as available as a laboratory microCT system. Imaging whole fresh IVDs means that native structure and mechanics are preserved which is significant for potential 3D structural mechanical studies at resolutions in the micron range. These methods have potential to characterise age-related structural remodelling in cartilaginous tissues. This has particular significance for the IVD as both an understanding of structural disc mechanics during progressive degeneration and efficacy assessment of tissue replacements are required for successful LBP treatments.

3.7 Supplementary

Supplementary videos are provided and can be accessed from the online published version of this manuscript (http://dx.doi.org/10.1038/s41598-017-16354-w)

Supplementary video 3.1: Cropped tomogram of paraffin embedded bovine IVD scanned at I13-2. The rendered volume clips radially through the AF to show alternating collagen bundles in each lamellae.

Supplementary video 3.2: Native IVD scanned at I13-2. The volume shows a segment of AF. Individual collagen bundles are visible in all slices through the volume. The dense aligned collagen structure is displayed which is made clearer by taking a smaller volume.

4 Synchrotron tomographic measurement of strain in soft tissue: native intervertebral disc deformation at histological resolution

This chapter is in the style of an original manuscript intended to be submitted to Acta Biomaterialia.

4.1 Author contribution statement:

Catherine M. Disney wrote the paper.

Catherine M. Disney, Brian K. Bay, Michael J. Sherratt, Peter D. Lee and Judith A. Hoyland conceived and designed the study.

Catherine M. Disney, Alexander Eckersley, James C. McConnell, Hua Geng, Andrew J. Bodey and Michael J. Sherratt collected the data.

Catherine M. Disney and Brian K. Bay performed the analysis and interpretation of the data.

All authors contributed editing and final approval of the article.

4.2 Abstract

The intervertebral disc (IVD) has a complex and multiscale extracellular matrix structure which provides unique mechanical properties to withstand physiological loading. Low back pain has been linked to degeneration of the disc but reparative treatments are not currently available. Characterising the discs 3D microstructure and its response in a physiologically relevant loading environment is required to improve understanding of degeneration and to develop new reparative treatments. In this study, techniques for imaging the native IVD, measuring internal deformation and mapping volumetric strain were applied to a compressed spine segment. Synchrotron X-ray micro-tomography (microCT) resolved IVD structures at histological resolution. The image data enabled 3D quantification of collagen bundle orientation and measurement of local displacement in the annulus fibrosus between sequential scans using digital volume correlation. Using correlative imaging methods to map volumetric strain from microCT provided a detailed insight into micromechanics of native IVD tissue. The digital volume correlation findings showed that there was no slipping at lamella boundaries, local strain patterns were at a similar scale and distribution to the elastic network distribution with some heterogeneous areas and maximum strain direction aligned with bundle orientation suggesting bundle stretching and sliding. This method has the potential to bridge the gap between measures of macro-mechanical properties and the local 3D micro-mechanical environment experienced by cells. This is the first evaluation of strain at the micro scale level in the intact IVD and provides a quantitative framework for future IVD degeneration mechanics studies and testing of tissue engineered IVD replacements.

4.3 Introduction

The IVD provides flexibility in the spine whilst transmitting and attenuating loads from body weight and physical activity. Overall, it is the non-linear viscoelastic behaviour of the disc which allows flexibility at low loads and maintains structural integrity with increasing rate and magnitude of loading (Tavakoli and Costi, 2018a, Costi *et al.*, 2008, Race *et al.*, 2000, Iatridis *et al.*, 1997). Regional anisotropic mechanical properties transmit and distribute forces (O'Connell *et al.*, 2007, Holzapfel *et al.*, 2005, Elliott and Setton, 2001, Skaggs *et al.*, 1994). These unique mechanical properties are defined by the IVD's complex and multiscale extracellular matrix (ECM) structure (Cassidy *et al.*, 1989). Yet, direct observation of IVD structural deformation under load has been limited by 2D imaging and strain analysis methods.

Located in the centre of the IVD, the nucleus pulposus (NP) is amorphous and rich in proteoglycans, primarily aggrecan, whose hydrophilicity causes high osmotic pressure to the surrounding tissue. The NP is surrounded by the annulus fibrosus (AF); a ring of fibrocartilage with lamellar architecture. Collagen I fibres form aligned bundles which have alternating oblique orientation between adjacent lamellae (Figure 4.1) (Marchand and Ahmed, 1990, Cassidy *et al.*, 1989). Between the lamellar structures there are fibrous interconnecting bridges mainly consisting of elastin (Han *et al.*, 2015, Yu *et al.*, 2015). As the spine is loaded, cartilage endplates at the vertebrae distribute the load and the hydrostatic pressure generated in the NP is transmitted to a circumferential stress in the AF (O'Connell *et al.*, 2011b, McNally and Adams, 1992, Nachemson, 1963, Keyes and Compere, 1932). Residual stress in the AF helps to safely distribute the high pressures from the NP (Michalek *et al.*, 2012). Recently, detailed studies of the distribution and organisation of elastic fibres in the IVD have been used to infer their role for structural integrity and tissue mechanics (Tavakoli and Costi, 2018b, Tavakoli *et al.*, 2017).

Several microstructural deformation mechanisms of the AF under tension have been observed using optical microscopy (Vergari *et al.*, 2016, Michalek *et al.*, 2009, Bruehlmann *et al.*, 2004). A balance must be made between sample interaction and compromising native mechanics when studying microstructural deformation of a tissue (Disney *et al.*, 2018). These studies were 2D and required segments of tissue to be dissected, which means that it is not possible to characterise 3D tissue structure and observe deformations outside of the imaging plane. Furthermore, the tissue should be intact for physiological loading conditions to preserve residual strain (Michalek *et al.*, 2012) and forces from surrounding tissue such as ligaments (Adams *et al.*, 1996). Magnetic resonance

imaging (MRI) has been used to map strain in an intact disc but resolution is limited and unable to resolve the disc's multiscale hierarchical structure and map strain at histological resolution (Chan and Neu, 2014, O'Connell *et al.*, 2007).

Recent advances in X-ray micro-tomography (microCT) imaging have meant it is possible to image the 3D microstructure of native soft tissues (Disney *et al.*, 2017, Naveh *et al.*, 2014). Soft tissues are challenging to image using microCT as they weakly absorb X-rays and they exhibit stress relaxation during long scans (hours for laboratory sources) where microstructure may move, resulting in image artefacts (Atwood *et al.*, 2015). In-line phase contrast imaging can resolve structures in soft tissue due to variations in X-ray refractive index which alter the wave front and, with sufficient propagation past the sample, Fresnel fringes occur giving contrast enhancement at the edges of structures (Wilkins *et al.*, 1996, Snigirev *et al.*, 1995). A high flux source, such as synchrotron, reduces overall scan time due to shorter exposures and less projections required for a high signal:noise reconstruction meaning that motion artefacts from tissue stress relaxation are lessened.

The objective of this study was to use synchrotron microCT with in-line phase contrast to resolve the native structure of an intact IVD inside a spine segment and quantify microstructural deformation under applied sequential compression. This provides the first direct observation of AF microstructural deformation in an intact IVD which includes the mechanical influence of surrounding spinal tissues. Three-dimensional quantification of AF deformation using digital volume correlation (Bay, 2008, Bay *et al.*, 1999) offers analysis of how strain is transferred through native tissue and the cellular environment. The novel imaging and strain analysis presented here builds on 2D techniques and inferences made by structural characterisation studies to understand IVD mechanical function. It is hoped that future application of these methods and detailed observations will help predict the likely mechanical causes of IVD degeneration and positively impact on the design and testing of tissue engineered IVD replacements (Nerurkar *et al.*, 2010) with a wider impact on soft tissue biomechanics studies.

4.4 Materials and methods

4.4.1 Tissue and materials

Retired Sprague-Dawley rats (8 week-old, male) from the University of Manchester Biological Services Facility were culled by carbon dioxide inhalation. The lumbar spine was dissected *en bloc*, snap frozen and stored at -80°C. Spines were thawed before using a high precision diamond cutting blade (Accumtom-50; Struers, UK) to dissect lumbar

segments (L4/L3, L3/L2) by cutting through the vertebral bodies. A slow feed speed (0.01 mm/s) and rotation blade speed (1500 rpm) with water cooling was used to minimise potential damage to the sample. Excess muscle tissue was removed from the spine segments, leaving a thin layer of muscle and ligaments intact. Samples were then set in a customised sample holder using non-exothermic epoxy resin (Ultra Repair; Loctite, UK).

4.4.2 Equipment and testing

An *in situ* compression stage Deben CT5000 (Deben, UK) with a 500 N load cell provided precise displacement control (300 nm resolution) with force readout (accuracy 1% of full scale range). Custom made sample holders aided sample alignment. Samples were held under cumulative compression using the bottom plate. A 1 N preload was applied to ensure the sample was securely in place. The compression was held for 20 minutes to account for tissue stress relaxation. A slow strain rate of 0.00167 strain/s (0.1 mm/min) was used during compression to minimise peak force response and stress relaxation time. Two scans were taken at this reference load (L0). The sample was then compressed by 0.02 mm (2% strain) displacement and 12 minutes allowed for stress relaxation before scanning (L1). The 2% strain compression, stress relaxation period and scanning were repeated a further 3 times (L2-L4). The compression stage recorded the force throughout the experiment which showed the stress relaxation of the tissue during compression before scanning (Figure 4.2a).

4.4.3 In-line phase contrast synchrotron microCT

Synchrotron microCT of the samples was acquired on the Diamond-Manchester branchline I13-2, Diamond Light Source. Compared with micro-focus tube sources, synchrotron radiation has high flux, high coherence and allows large propagation distances and so is able to resolve native soft tissue microstructures using in-line phase contrast techniques. Pink beam (8-30 keV) with an undulator gap of 5 mm was filtered (0.95 mm pyrolytic graphite, 2 mm aluminium, 0.1 mm iron) to reduce beam damage. Dose during alignment was minimised by firstly using a laser and manual adjustments of the sample holder on the beamline and then using projections with the beam set to a large undulator gap (reduced flux) and use of shutters.

A PCO.edge 5.5 scintillator-couple detector with a 2x objective to give a total magnification of 4x, effective pixel size 1.6 µm and field of view 4.2 x 3.5 mm was used to record the projections. Exposure time for each projection was set to 0.15 s according to ~50% saturation in flat-field projections. A total of 8001 projections were taken over 180° continuous rotation to provide a high signal:noise reconstruction. Propagation distance of

sample to detector was set to 500 mm which was decided by increasing in 100 mm increments until there was sufficient in-line phase contrast to resolve the IVD microstructure. Scans were taken after sample compression and stress relaxation (Figure 4.2). The projections were reconstructed with ring artefact suppression using Diamond Light Source software DAWN (Atwood *et al.*, 2015, Basham *et al.*, 2015).

4.4.4 Image processing and DVC analysis

Contrast was adjusted to visualise IVD structures. Light median 3D filtering (1 pixel) was used to remove noise. Two cube volumes were selected from the AF for analysis (Figure 4.3a-c). Avizo 8.0 (FEI Visualization Sciences Group, Mérignac Cedex, France) was used to visualise and render the image data.

Bundle orientation in both cubes was analysed using XFiber Extension in Avizo 8.0 (Rigort *et al.*, 2012, Weber *et al.*, 2012). Cylinder Correlation (length 40 pixels, angular sampling 5°, mask of 10 pixels and 8 pixels outer radius) was used to enhance fibre-like structures. Fibres were traced from initial seed points above correlation coefficient of 40 (>30 to continue tracing). A low (0.2) direction coefficient and 30° search angle was chosen to trace straighter structures and results filtered to have a minimum fibre length of 20 pixels. Orientation of each traced structure is given by theta (θ), angle with the *z* axis, and phi (φ), angle in the *x-y* plane. Orientation angle was transformed to the lamella-local coordinate system (Figure 4.3d) and plotted as a histogram.

Displacement of structures between images was tracked using digital volume correlation (DVC) (Bay, 2008, Bay *et al.*, 1999). Point locations were set up for the centres of sub-volumes which were independently tracked between consecutive image volumes in 6 degrees of freedom (3 translation and 3 rotation) by optimisation of normalised sum of squared difference function. Tricubic interpolation of the grey-level values with 2,500 points in each sub-volume was found to be sufficient. Preliminary analysis with a smaller number of sub-volumes (1000s) and different sub-volume sizes showed that 20 pixels (Figure 4.5a) had reliable tracking whilst maintaining high tracking resolution for the AF. Points (~133,000) were evenly distributed throughout the cube volumes with average spacing of 4 pixels (Figure 4.5b). The displacements were then added onto the original positions of each sub-volume and the process repeated for the next compression steps. DVC between the two scans at L0 serves to test the validity of the analysis. The second scan at load L0 was used for as the reference for the compression sequence.

4.4.5 Transformation to local coordinates and strain calculation

Displacement data was transformed using an angle-axis rotation in Avizo to a local coordinate system so that lamellae were in the *x-y* plane (Figure 4.3d). Strain was calculated using MATLAB R2018a (Mathworks Inc., Natick, Massachusetts, USA) (Supplementary information 4.1). The displacement vectors were interpolated (natural) to a regular-spaced grid of 3 pixels, a median filter was applied to remove outliers followed by Gaussian as a low-pass filter (both with 3,3,3 neighbourhood). The displacement gradient across the image volume was calculated to find the Lagrangian finite strain tensor for each location.

$$\mathbf{D}=\begin{bmatrix} \frac{\partial u}{\partial x} & \frac{\partial u}{\partial y} & \frac{\partial u}{\partial z} \\ \frac{\partial v}{\partial x} & \frac{\partial v}{\partial y} & \frac{\partial v}{\partial z} \\ \frac{\partial w}{\partial x} & \frac{\partial w}{\partial y} & \frac{\partial w}{\partial z} \end{bmatrix} \qquad (4\text{-}1)$$

$$\mathbf{L}=\frac{1}{2}[\mathbf{D}+\mathbf{D}^{T}+\mathbf{D}^{T}\mathbf{D}] \qquad (4\text{-}2)$$

Eigenvectors and values gave the maximum principle vectors and strain which were saved as 32-bit unsigned images for visualisation.

4.5 Results

4.5.1 Synchrotron micro-tomography of native IVD within the spine segment

Using in-line phase contrast synchrotron microCT, the structure of native IVD within a spine segment was resolved, with overall structure presented in Figure 4.1b. The porous endplates are mineralised and so absorb X-rays meaning that they were readily resolved. The non-mineralised AF and NP are weakly X-ray attenuating and so were resolved by increasing structure edge contrast using in-line phase contrast techniques. The amorphous structure of the NP found in the centre of the disc is surrounded by the lamella AF structure. Virtual slices can be taken from any location in the volume to show the 3D structural organisation (Figure 4.1c). A sagittal slice shows the thickness of the disc with lamellae running from the upper endplate to the lower endplate (Figure 4.1d). Transverse slices show concentric layers of the AF around the NP (Figure 4.1e). A radial slice reveals the structure within lamellae where there is an alternating orientation of collagen bundles (Figure 4.1f).

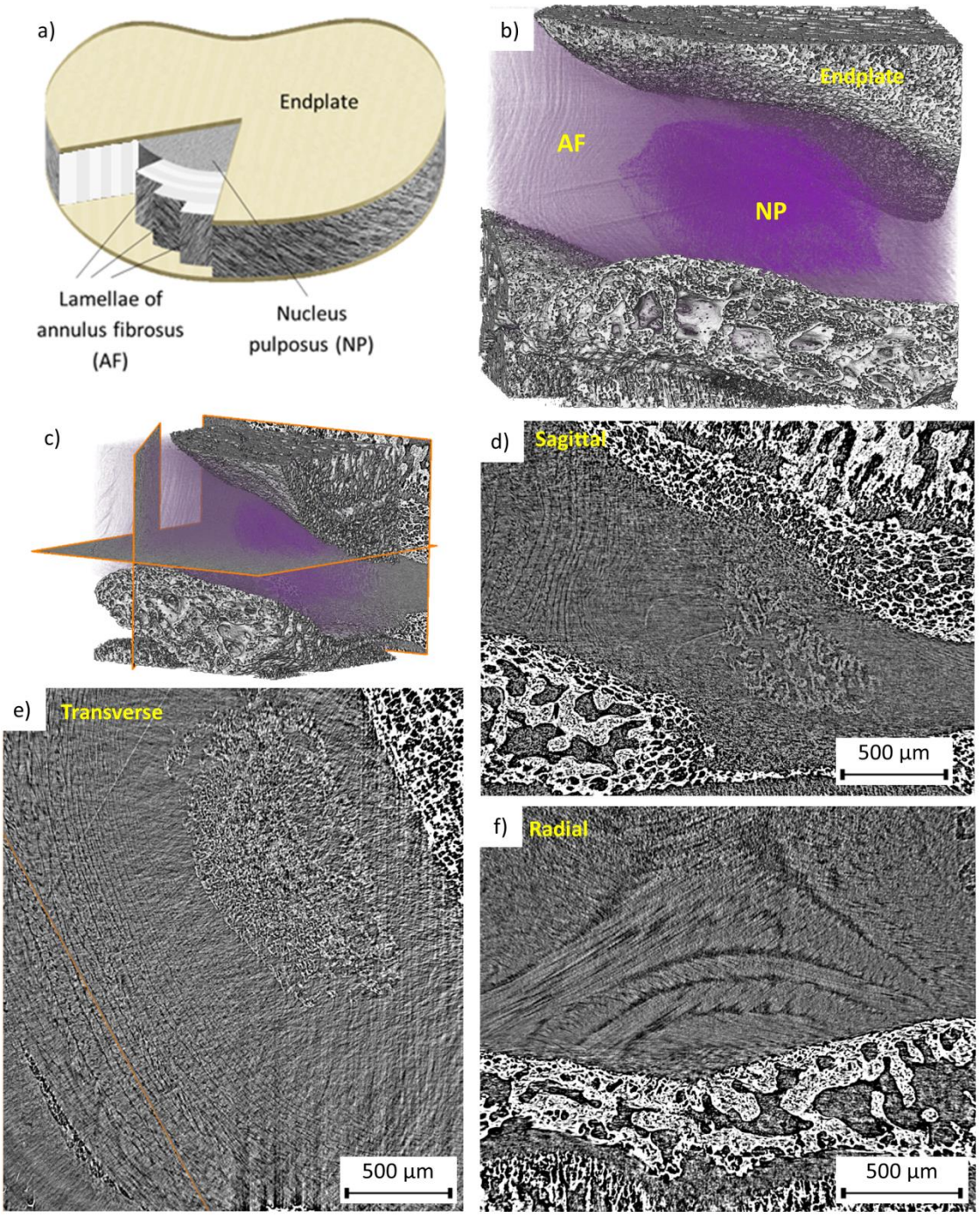

Figure 4.1 Structure of native intervertebral disc; a) schematic of the IVD, b) rendered tomogram, c) virtual slices taken from three anatomical positions, d) sagittal, e) transverse and f) radial.

4.5.2 *In situ* loading; tomography after stress relaxation

IVD structures were resolved in a series of time lapse scans during the spine segment compression. As expected, samples had a viscoelastic stress relaxation response to each cumulative compression step with an initial force peak which decreased over time (Figure 4.2a). The scans were taken after stress relaxation and showed no movement or slipping of the sample in the holder. The IVD was compressed from the bottom endplate with minimal bending (Figure 4.2b, Supplementary video 4.1). Contrast in the NP decreased after each compression step which is due to obscuring streaking artefacts from the highly absorbing endplate.

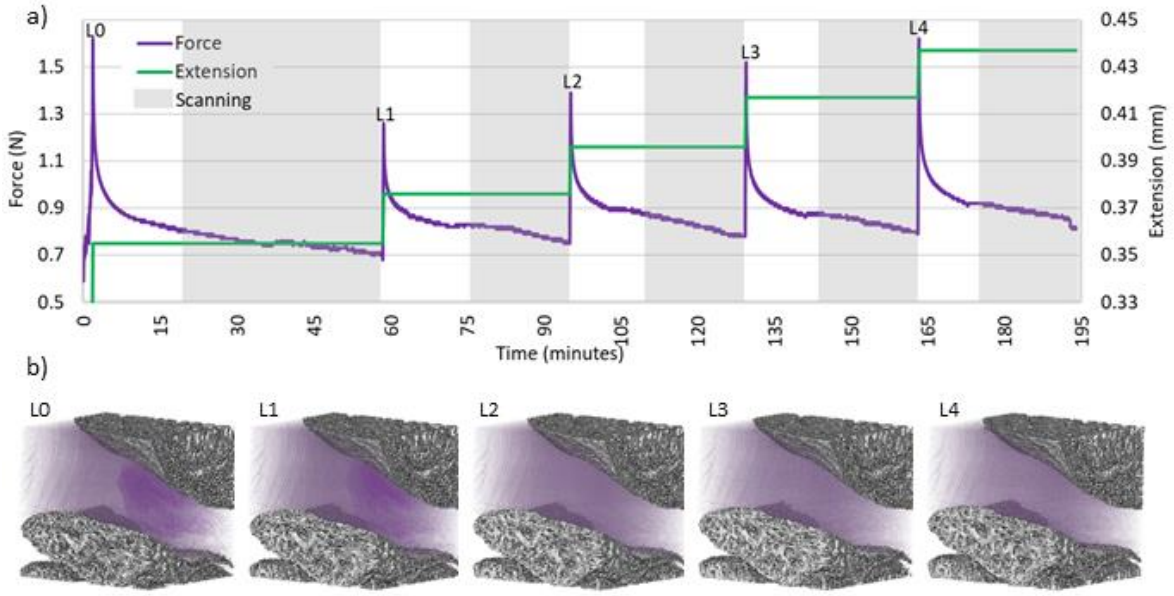

Figure 4.2 In situ loading; a) force reading from sequential compression, b) sequence of 3D renders of the disc being compressed from the lower endplate.

4.5.3 Lamellae bundle angle

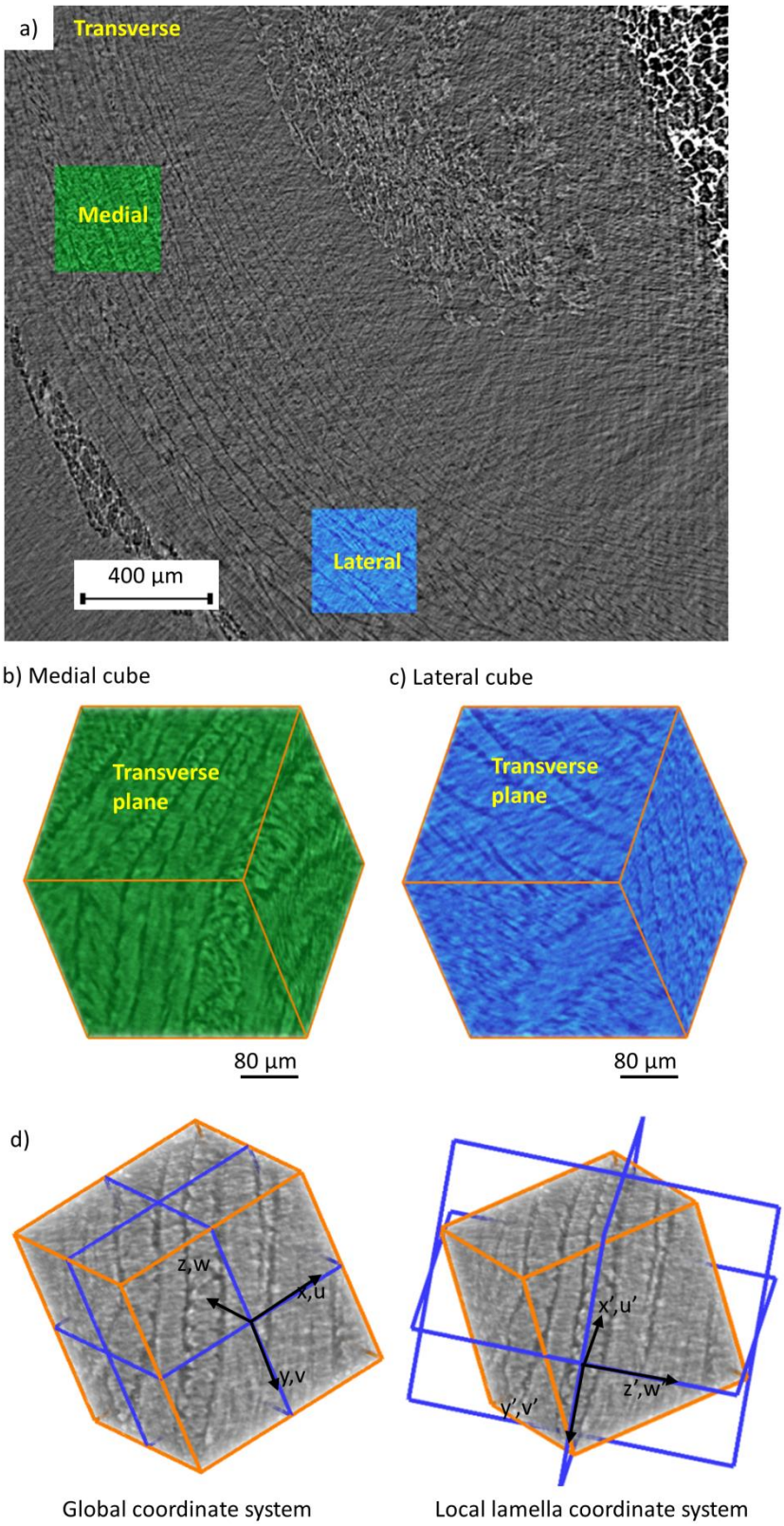

Figure 4.3 Volumes of interest selected for analysis and defining a local coordinate system; a) transverse slice showing position of medial and lateral cube volumes b) rendered medial cube c) rendered lateral cube d) global and local lamella coordinate system.

Two cube volumes from different anatomical areas (Figure 4.3a-c) were chosen for bundle analysis at ‘zero’ compression (L0) and the final compression step (L4). The alternating orientation of lamellae bundles could be observed and extracted using fibre tracing analysis (Figure 4.4, Supplementary video 4.2 & 4.3). Bundle orientation can be compared between the two volumes after transformation to a local coordinate system where φ is the angle in the lamella plane measured from the horizontal axis. A bi-modal distribution centred roughly at 0° was shown for both volumes (Figure 4.4c & f). The two peaks for the medial cube indicated a steeper inclination (55° and -65°) when compared to the lateral cube (20° and -30°). Figure 4.4c & f do not show a notable change in bundle angle after sample compression. However, when average orientation of separate lamella were taken, bundles reoriented by 0.9°±0.4°.

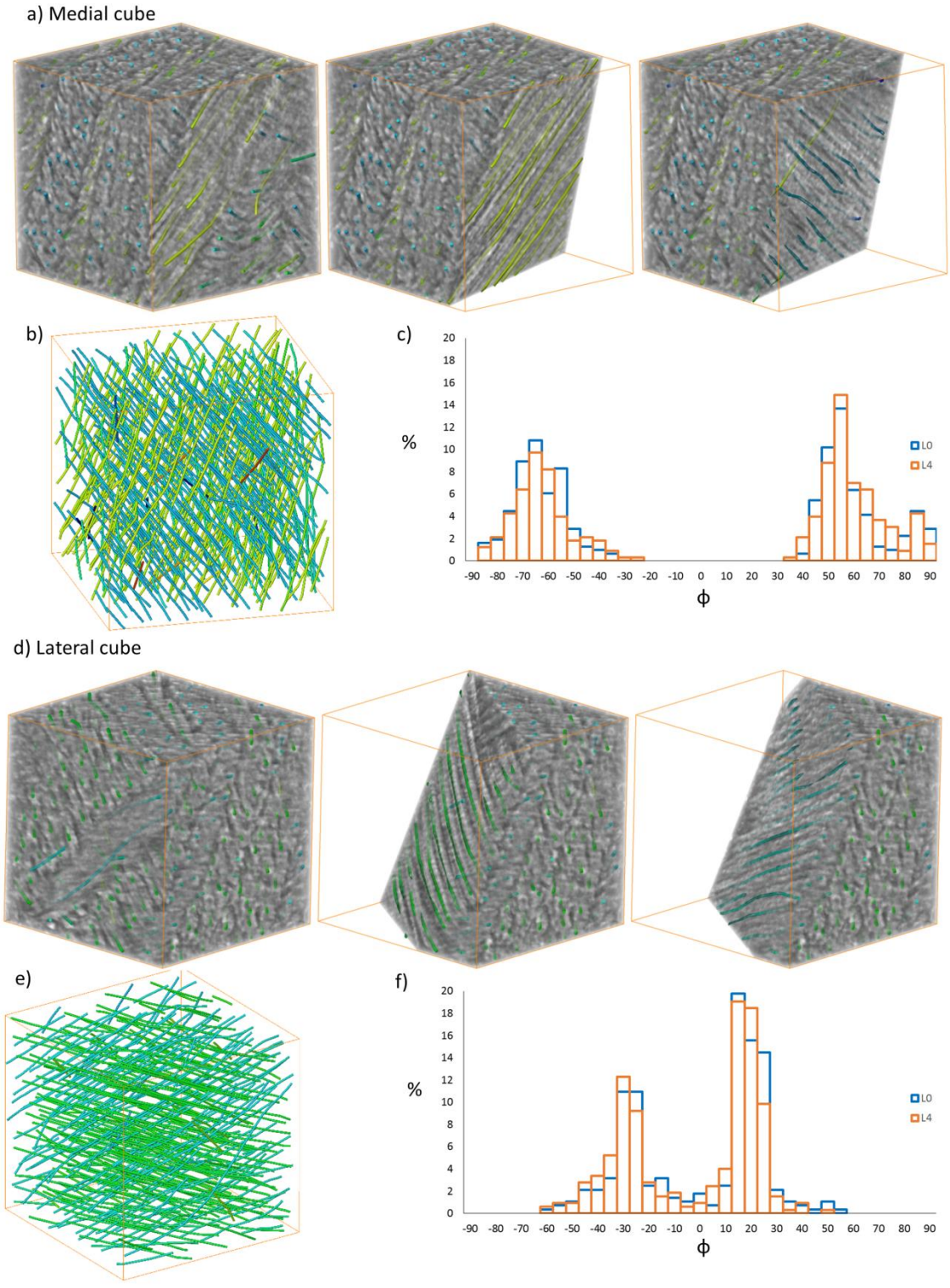

Figure 4.4 Bundle orientation varies with anatomical location; a) d) two alternating orientations of collagen bundles shown by clipping in the lamella plane b) e) all traced bundles are shown with view in lamella plane c) f) bundle orientation for L0 and L4 after rotation transformation to lamella local coordinate system where phi φ is in-plane angle. a-c) medial volume of interest d-f) lateral volume of interest. Cube volumes have 320 µm dimensions.

4.5.4 Digital volume correlation; displacement of structures can be tracked and mapped as strain

An overview of the image processing and DVC-based strain results is shown in Supplementary video 4.4. Evenly distributed points within the two cube volumes were tracked using DVC (Figure 4.5b) with an overall mean tracking residual of 0.0042 for the medial cube and 0.0038 for the lateral cube. Mean tracking residual and standard deviation is shown in (Figure 4.5c). Residual values do not increase or change distribution in comparison with the repeat scan (L0). Median displacement relative to the local coordinate system of each cube is plotted in Figure 4.5d and interquartile range marked with error bars. There is a relatively low magnitude displacement for lower loads which gradually increases for higher loads, moving out of the range of the repeat scan. The difference between displacement directions shows the anisotropic mechanical behaviour of the AF. The radial displacement (w') shows that the AF bulges outwards with increasing load. Highest displacement is in the loading direction (v') whilst the greatest variation is in the horizontal direction of lamellae plane (u'). However, these displacement values are relative to the original image data and not the local displacement within the cube volumes. Nevertheless, variation in displacement values indicates that there is relative movement within tracking points. Strain measurement removes this problem by providing an accurate description of local changes in displacement.

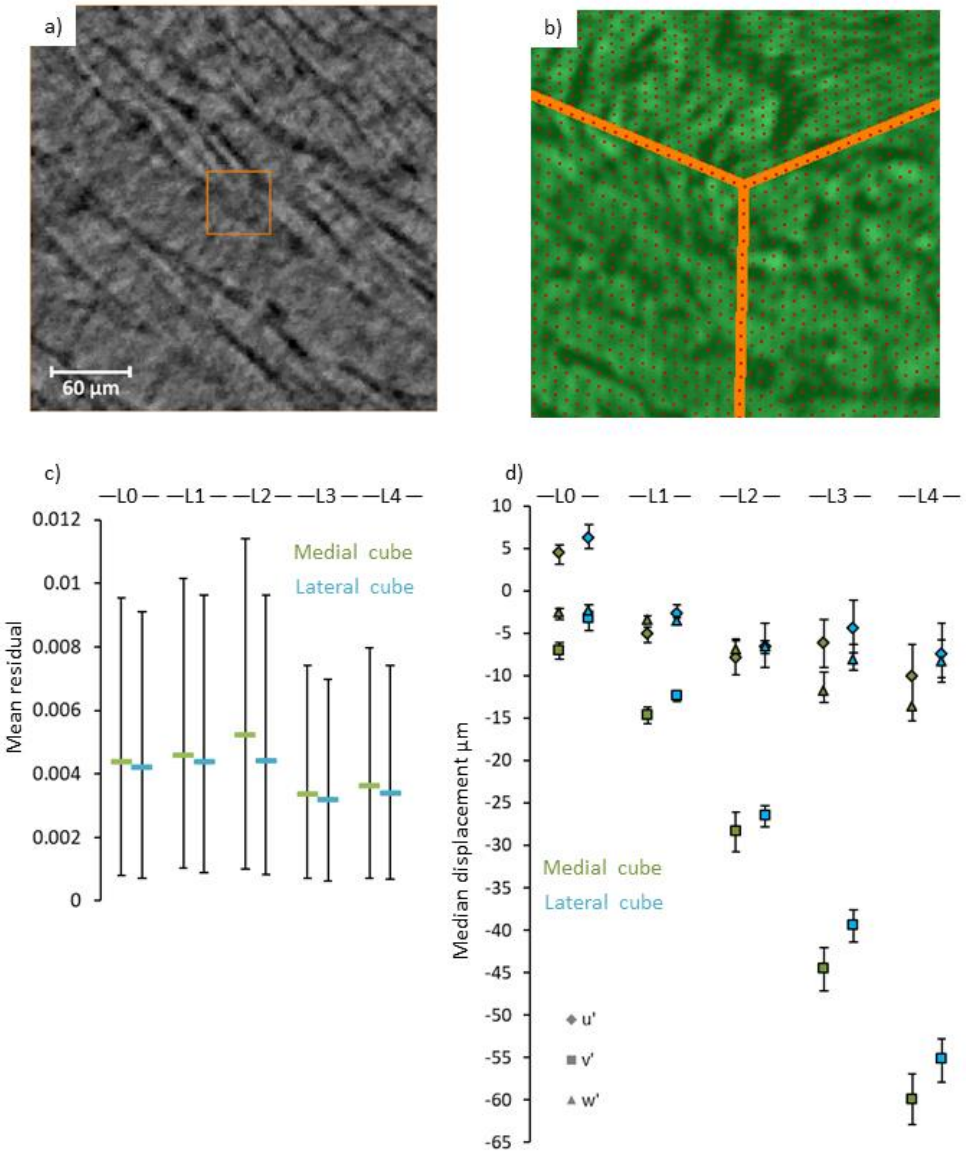

Figure 4.5 Tracking displacement using DVC; a) sub-volume used for tracking was a 20 pixel (32 µm) cube shown by the orange box on the image data b) tracking points had a 4 pixel (6.4 µm) spacing c) mean tracking residual for all compression steps d) median and interquartile range for displacement values in the local lamella coordinate system.

Maximum principle strain and vectors, transformed to the local lamellae coordinate system, were calculated and mapped alongside the image data (Figure 4.6 & Figure 4.7). Overall the strain patterns are heterogeneous and not localised to lamellae boundaries. Vector components are displayed in a histogram to show overall strain values, where the medial cube (Figure 4.6a) has areas of greater radial strain ($\varepsilon_{z'}$) than the lateral cube (Figure 4.7a). Maximum principle strain appears to localise and span radially across several lamellae in a network at roughly 60 µm spacing. Maximum principle strain vectors for the lateral cube align with the collagen bundle structure (Figure 4.7d & f).

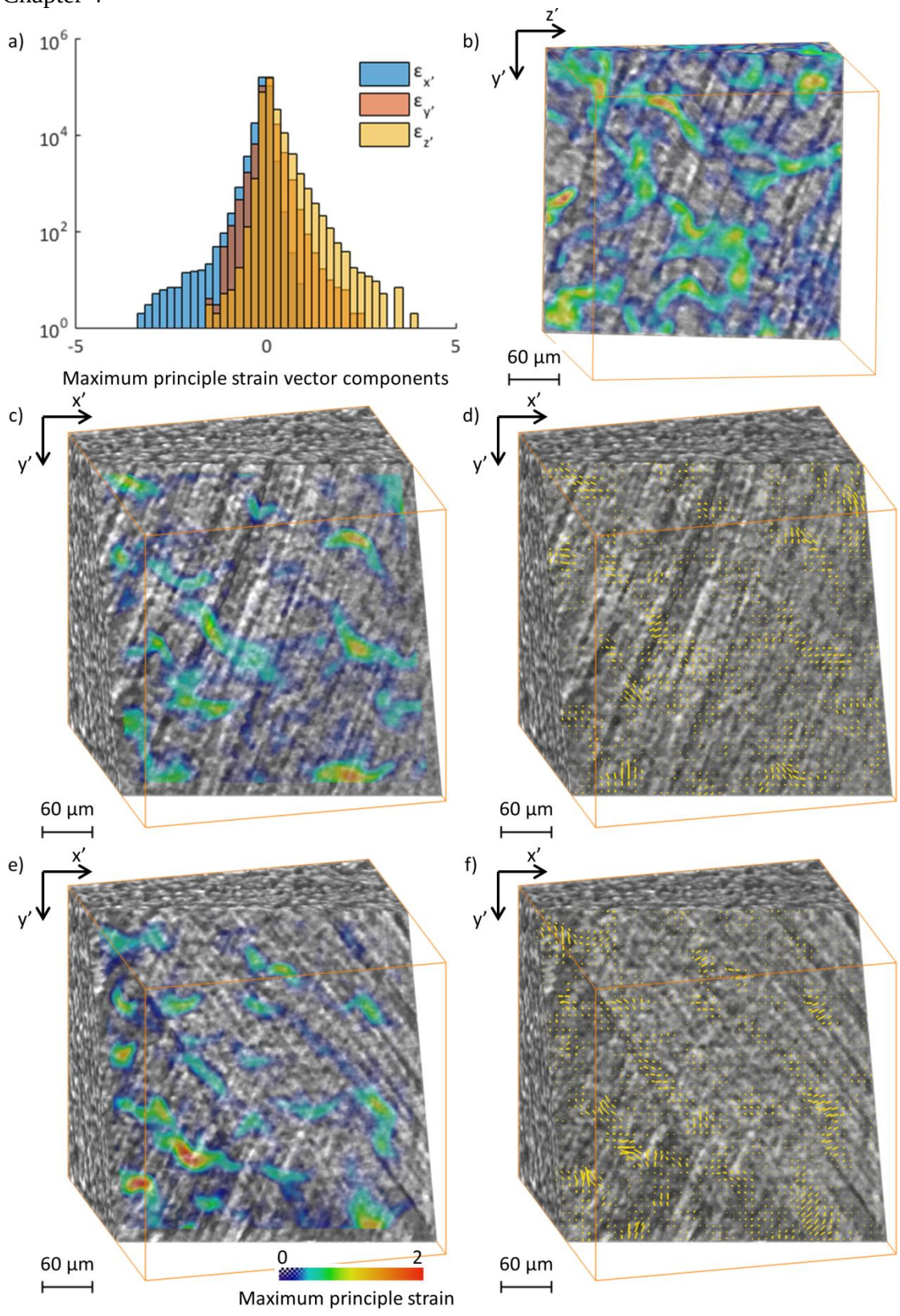

Figure 4.6 Medial cube maximum principle strain; a) maximum principle strain vector components defined in local lamella coordinate system b,c,e) maximum principle strain plotted with image data, clipped across lamella (b) and clipped in the lamella plane (c & e) d & f) shows principle strain vectors in the lamella plane plotted with image data.

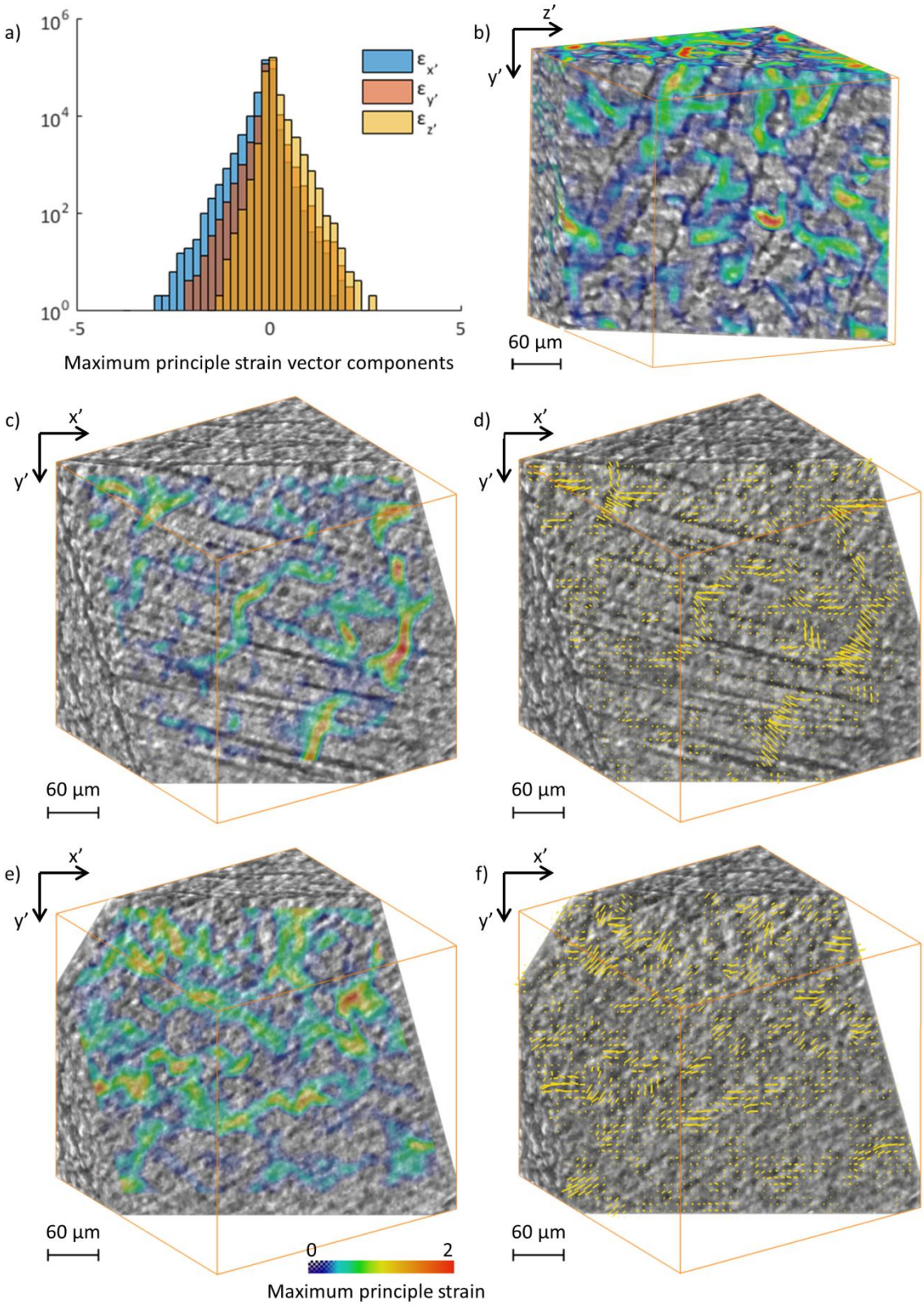

Figure 4.7 Lateral cube maximum principle strain; a) maximum principle strain vector components defined in local lamella coordinate system b,c,e) maximum principle strain plotted with image data, clipped across lamella (b) and clipped in the lamella plane (c & e) d & f) shows principle strain vectors in the lamella plane plotted with image data.

4.6 Discussion

4.6.1 Novel 3D imaging of intact native IVD microstructure

MicroCT is a non-destructive technique allowing imaging of the disc in a spine segment. Different tissues of the disc – endplate, NP and AF - have been identified (Figure 4.1b). Navel *et al.* (2014) were also able to resolve these structures in native mouse IVD using laboratory microCT. In comparison, the synchrotron microCT presented here clearly resolved the detailed AF hierarchical microstructure, including AF collagen bundles, which has not been imaged in 3D from an intact disc. Yet, there are two observations to note. The calcified endplates are highly X-ray absorbing which reduced flux through the IVD and caused streaking artefacts. Additionally, NP contrast decreased after each compression step (Figure 4.2b, Supplementary video 4.1). This may be due to obscuration by streaking artefacts directed towards the centre of the sample as the endplates come closer together. These artefacts are common in samples where sudden changes in X-ray absorption, such as metal implants (Boas and Fleischmann, 2011), are observed. Image quality could be improved in future studies by removing the posterior elements which protrude from the vertebra into the beam path and by carefully aligning the sample in the beam so that endplates run parallel with the beam.

Previous imaging studies which observed microstructure deformation were performed in 2D and required tissue dissection. Testing whole spine segments meant that the disc was maintained in its native physiological environment and loaded with the curved endplates and ligaments are left intact. Previously, removing these has shown to effect internal IVD mechanics (Adams *et al.*, 1996). Furthermore, dissection of IVD tissue releases AF residual strain (Michalek *et al.*, 2012). Also, although MRI is capable of imaging intact samples, resolution is limited to ~200 µm which only allows for macro-scale analysis (Chan *et al.*, 2014, O'Connell *et al.*, 2007). MicroCT has a higher resolution (1.6 µm pixel size, ~4.8 µm resolution) which enabled resolution of IVD microstructure (Figure 4.1d-f).

4.6.2 Lamellae bundle angle depends on anatomical position

Lamellae bundle angle has previously been shown to vary with circumferential position (Stadelmann *et al.*, 2018a, Zhu *et al.*, 2008, Holzapfel *et al.*, 2005, Eberlein *et al.*, 2001, Marchand and Ahmed, 1990) but not radially towards the nucleus with the exception of a single dated study (Cassidy *et al.*, 1989) (Table 4.1). Fibre tracing image analysis showed that lamellae bundle angle varied from ±55-65° in the medial cube to ±25-30° in the lateral cube (Figure 4.4c & f), which closely matches MRI diffusion characterisation from intact IVD (Stadelmann *et al.*, 2018a).

Table 4.1 Lamella bundle angle from transverse plane has been shown to vary circumferentially. Most studies used dissection or lamella peeling and observation to measure bundle angle.

Reference	**Bundle angle**	**Sample handling**	**Method of measuring angle**
Cassidy *et al.*, 1989	28°- 45° inward to nucleus	Dissection	Optical microscopy
Marchand and Ahmed, 1990	Average 30°, posterior 70°	Lamella peeling and dehydration	Microscopic examination
Eberlein *et al.*, 2001	23° ventral to 57° dorsal	Dissection	Photography
Holzapfel *et al.*, 2005	23° ventral-47° dorsal	Lamella peeling	CCD camera analysis
Zhu *et al.*, 2008	25-30° front to 70-90° towards posterior ligament	Delamination	Photography
Stadelmann *et al.*, 2018	Ranged between 25° to 50°	Intact joint	MR diffusion

The histograms in Figure 4.4 do not show notable reorientation of collagen bundles after the spine segment is compressed. However, when average values from separate lamella are taken, the bundles reoriented by 0.9°±0.4°. Previous studies reported a similar value of bundles re-orientated during loading of around 1°/% strain and towards the orientation of the adjacent lamella (Vergari *et al.*, 2016, Guerin and Elliott, 2006).

4.6.3 Maximum principle strain

Importantly, the resolved microstructure provided sufficient image texture to track internal deformation using DVC (an overview of the process is presented in Supplementary video 4.4). This is advantageous, as some previous methods required stains, dyed patterns or invasive markers to track displacements which can cause changes in mechanical behaviour. In this study, full-field strain measurement is possible, which means that the local tissue strain can be observed when compared to the more global response from tracking markers.

Figure 4.6 and Figure 4.7 show the maximum principle strain plotted alongside the image data for both cube volumes. Overall, the maximum principle strain pattern is heterogeneous throughout the local ECM without strain concentration at lamellae

boundaries. These results support the conclusions of Michalek *et al.* (2009) and Vergari *et al.* (2016) who found that there was no slipping of the lamella boundary from direct confocal observations of AF tissue under load. It also provides further evidence against a disputed interpretation in an earlier study by Bruehlmann *et al.* (2004) who suggested slipping at lamella boundary due to cells undergoing large motions in the interlamellar space. This is an example where tracking discrete markers can be misleading when compared to full-field strain measurement.

Maximum principle strain appears to be localised and traverse across lamellae in a network with spacing of ~60 µm. These localised strain results appear to be high but this can be related to the type of strain measurement which is at a more refined spatial scale compared to values that are usually measured such as nominal applied or homogenised strain. There is growing recognition that strains in biological strains are heterogeneous with higher strain in some regions than the applied strain when measured at a local scale. For example, Vergari *et al*. (2016) showed high localised strain magnitudes over 23% for a 5% applied strain. Furthermore, the observed strain pattern has a similar description to the AF shear strain inhomogeneities described by Han *et al.* (2016a). In their study, there was strong strain localisation which is comparable to the results in Figure 4.6 and Figure 4.7. But, idfferent spatial patterns may be present due to different loading modes (circumferrential shear was applied by Han *et al.,* (2016a)) and testing dissected tissue. The spatial pattern observed in Figure 4.6 and Figure 4.7 has some similarities to the elastic network distribution depicted by Tavakoli *et al.* (2018b, 2017) who suggests that this network is important for disc structural integrity. The inter lamellae dependency, shown by higher strain regions across multiple lamellae and no slipping at the lamellae boundary, relates well with the converging elastic network. Still, an improvement in imaging is required to confirm this. Therefore, we propose that the AF should be described as a multiscale fibre reinforced composite which includes both fibrous collagen and elastic fibre networks. The fibrous collagen bundles are acting as a composite fibre reinforcement phase, whereas the dense and interconnected elastic network is functioning as a matrix phase with low shear stiffness for flexibility and high strength to support loads. These are unique properties as it is unlikely that a non-fibrous biopolymer material would have this combination of properties.

A comparison between the two cubes shows that there is regional variation in overall deformation mechanics. The medial cube has higher radial strain values when compared to the lateral cube (Figure 4.6a and Figure 4.7a). The maximum principle strain vectors are

plotted alongside the image data in the lamella plane showing that their direction is aligned with bundle structure (Figure 4.6d,f, and Figure 4.7d,f). Supplementary figure 4.8 quantifies strain direction in the lamella plane which shows overall good alignment with the different bundle orientations for both cubes. It is encouraging to compare the results of these figures to several reports which showed that collagen fibrils un-crimped or stretched when load was applied to AF tissue segments (Vergari *et al.*, 2016, Michalek *et al.*, 2009, Bruehlmann *et al.*, 2004). Whilst fibrous collagen structures clearly have a mechanical role in the AF, proteoglycan domains have been suggested to be responsible for heterogeneous strain patterns through the local ECM (Han *et al.*, 2013).

The results displayed in Figure 4.6 and Figure 4.7 show the cumulative strain from L0 to L4. To help demonstrate the validity of the analysis, strain data from the repeat scan at L0 and the intermediate results can be found in Supplementary figure 4.9 (tracking information in Figure 4.5). It is reassuring that these intermediate results show a progression of increasing strain in both cubes. Supplementary figure 4.10 and 4.11 show maximum principle strain for the repeat scan at L0 plotted with the image data for both cubes (equivalent locations are taken as in Figure 4.6 and 4.7). In comparison, the strain patterns displayed for the cubes at L0 appear to be similar to L4 but with a lower magnitude, this may be related to microstructural creep during the repeat scan time. Importantly, residual tracking error does not increase or change distribution through the compression sequence which indicates reliable tracking (Figure 4.5c).

Note the advantages of taking measurements within the interior of intact samples when compared to surface observations of dissected tissue under load. The dissected samples from previous studies were not restrained by endplates or influenced by NP hydrostatic pressure which may have caused the AF to behave non-physiologically. Vergari *et al.* (2016) described considerable transverse shrinkage of AF tissue without endplates during tensile loading. Furthermore, the applied uniaxial strain used in these studies could be greater than the strain present in the AF when an intact disc is compressed; for example, strain applied until failure (Guerin and Elliott, 2006).

4.6.4 Study limitations and future directions

It is important to bear in mind limitations of synchrotron microCT. Firstly, synchrotron facilities can be accessed based on peer review application but are not as widely available as other imaging techniques. Secondly, the experiment is restricted to the beamline's capabilities. For example, rat spine samples were chosen to suit the beamline field of view and loading regime depended on the scan time. Shorter scan times limit the amount of slow

tissue relaxation movement during the scan and so would enable a higher loading frequency. Image quality was considerably reduced by obscuring streaking artefacts which may be improved in future by carefully positioning the sample in the beam. Finally, imaging parameters must be carefully considered to compromise between image quality and minimising radiation dose.

A key strength of this study is that a native intact sample was tested. However, physiological loading of the disc, besides compression from weight bearing, includes many different load types including torsion and bending for flexibility. More complex loading regimes will be important for future studies.

4.7 Conclusions

The purpose of this study was to quantify IVD deformation within an intact spine segment. Synchrotron microCT resolved the 3D structure of the disc at histological resolution which allowed measurement of bundle angle and supported digital volume correlation to track displacement of AF microstructure. This is the first study to directly image and measure AF bundle orientation within an intact spine segment which will be of use to IVD mechanics research (Malandrino *et al.*, 2014, Noailly *et al.*, 2011). The strain analysis undertaken here builds on previous research in IVD experimental mechanics and 2D imaging observations where; no slipping is observed at the lamella boundary (Vergari *et al.*, 2016, Michalek *et al.*, 2009), heterogeneous strain patterns can be found throughout the local ECM (Han *et al.*, 2013) and strain localises to form a network similar to the distribution of the elastic network (Tavakoli and Costi, 2018b, Tavakoli *et al.*, 2017) and is aligned with bundle structure (Vergari *et al.*, 2016, Michalek *et al.*, 2009, Bruehlmann *et al.*, 2004).

These methods provide a detailed insight into native IVD micromechanics and have the potential to bridge the gap between measures of macro-mechanical properties with the local 3D micro-mechanical environment experienced by cells. This study lays the groundwork for future research into: i) mechanical models which will be closer to IVD structure, ii) informing the design of potential tissue engineered IVD replacements and iii) evaluating the effects of surgical intervention on IVD mechanics. Beyond the IVD, it is likely that similar approaches could be employed to map 3D structure and strain within other non-calcified tissues.

4.8 Supplementary

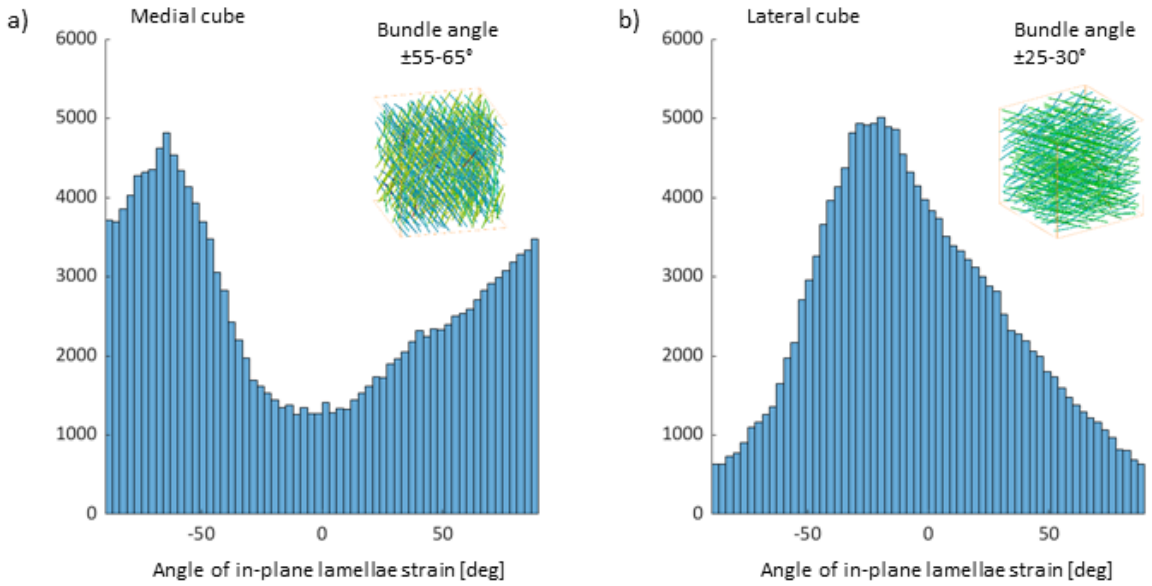

Supplementary figure 4.8 Angle of maximum principle strain in the lamellae plane. Strain magnitude is thresholded to only include values above the 0.25 quantile. a) Strains in the medial cube are directed more vertically (>50° and <-50°), matching the steeper inclination of the bundle angle, whereas b) strains in the lateral cube are closer to horizontal, tending towards the shallow bundle angle.

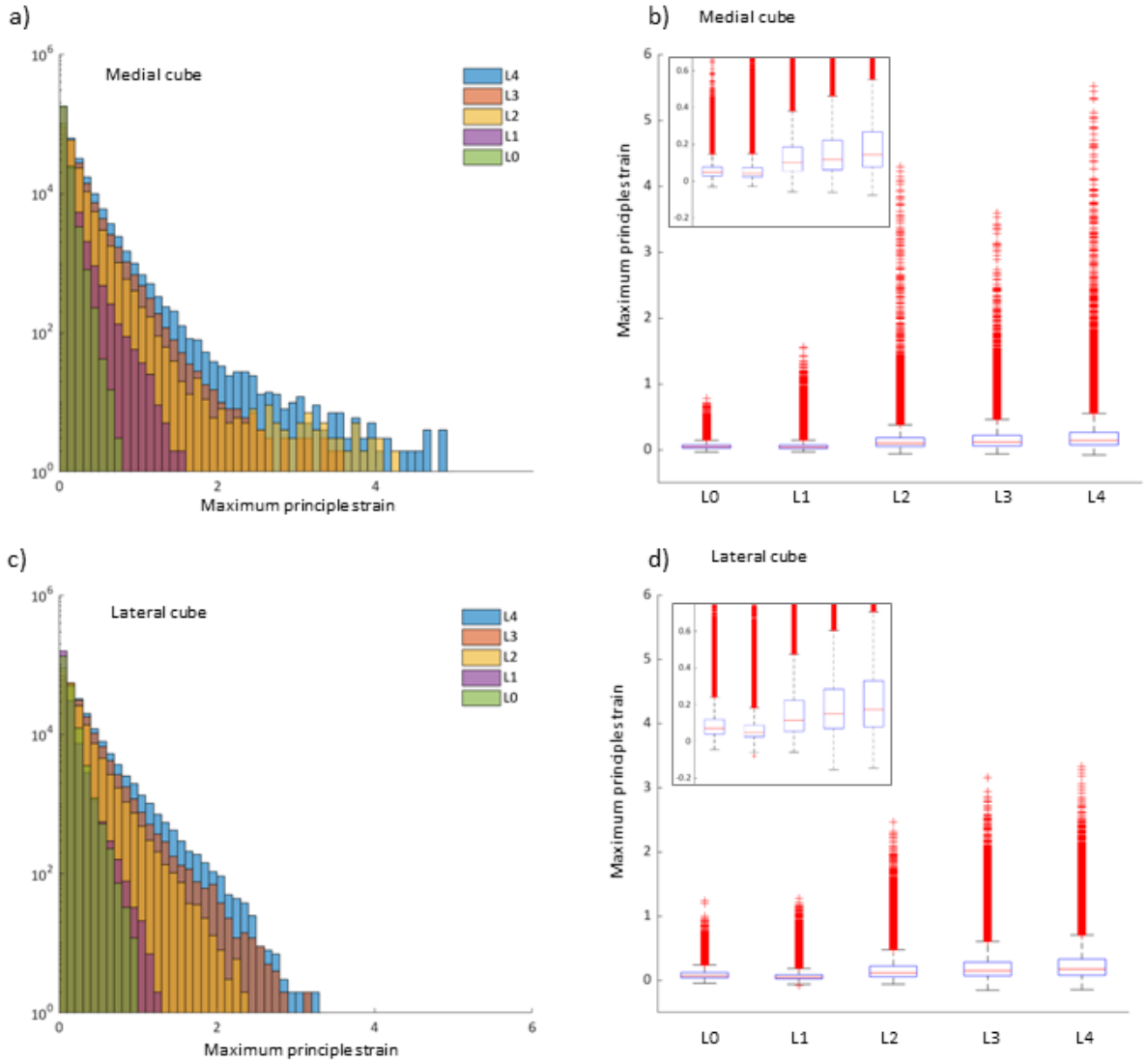

Supplementary figure 4.9 Maximum principle strain magnitudes for all load steps. Histograms and boxplots of interquartile range show the distribution of strain magnitudes for a) & b) the medial cube and c) & d) the lateral cube. A progression of increasing strain with increasing load is shown for both cubes. It is expected that the maximum principle strain distribution is skewed toward higher values and becomes more skewed with higher applied loads.

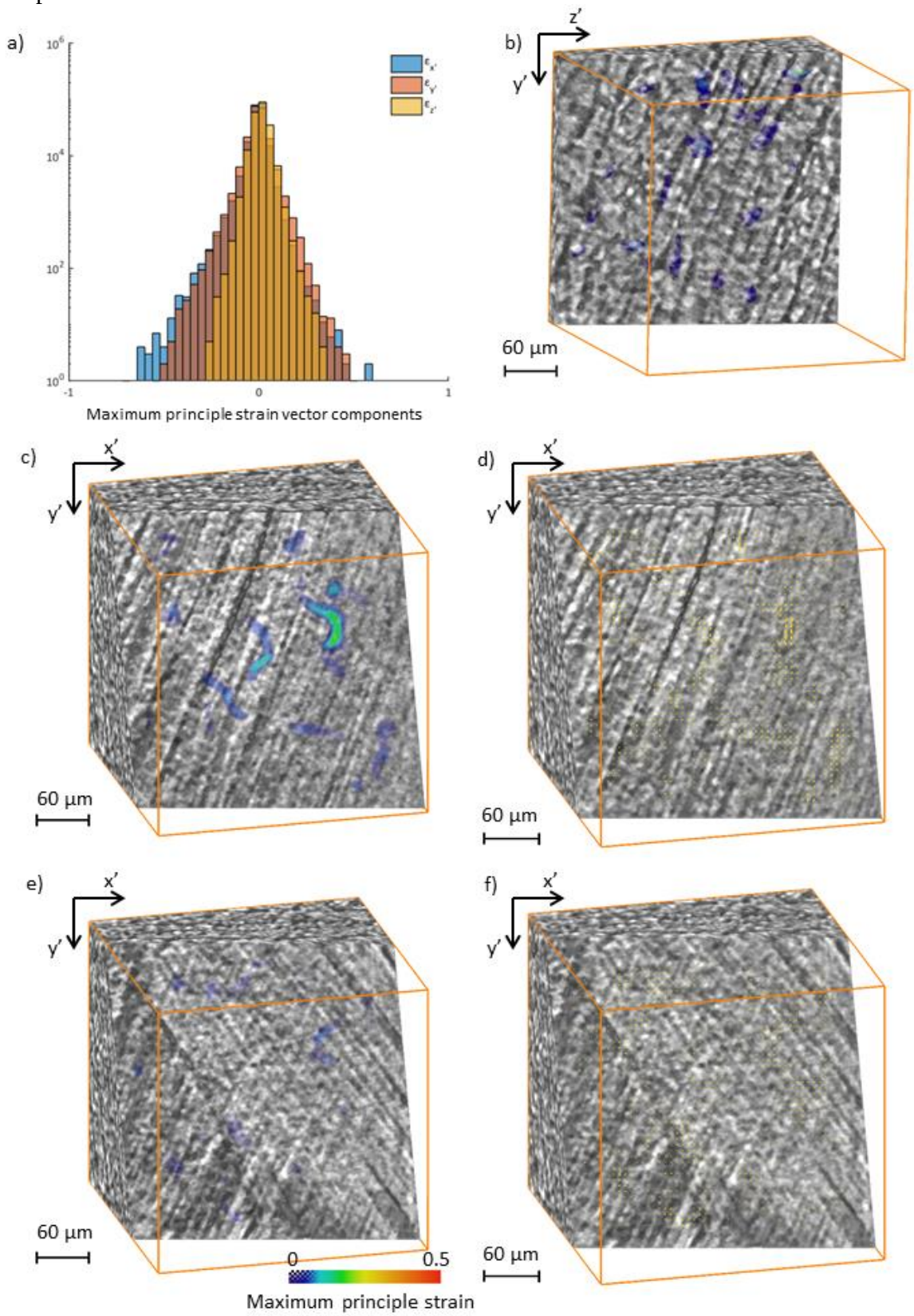

Supplementary figure 4.10 Medial cube maximum principle strain for the repeat scan at L0; a) maximum principle strain vector components defined in local lamella coordinate system b,c,e) maximum principle strain plotted with image data, clipped across lamella (b) and clipped in the lamella plane (c & e) d & f) shows principle strain vectors in the lamella plane plotted with image data.

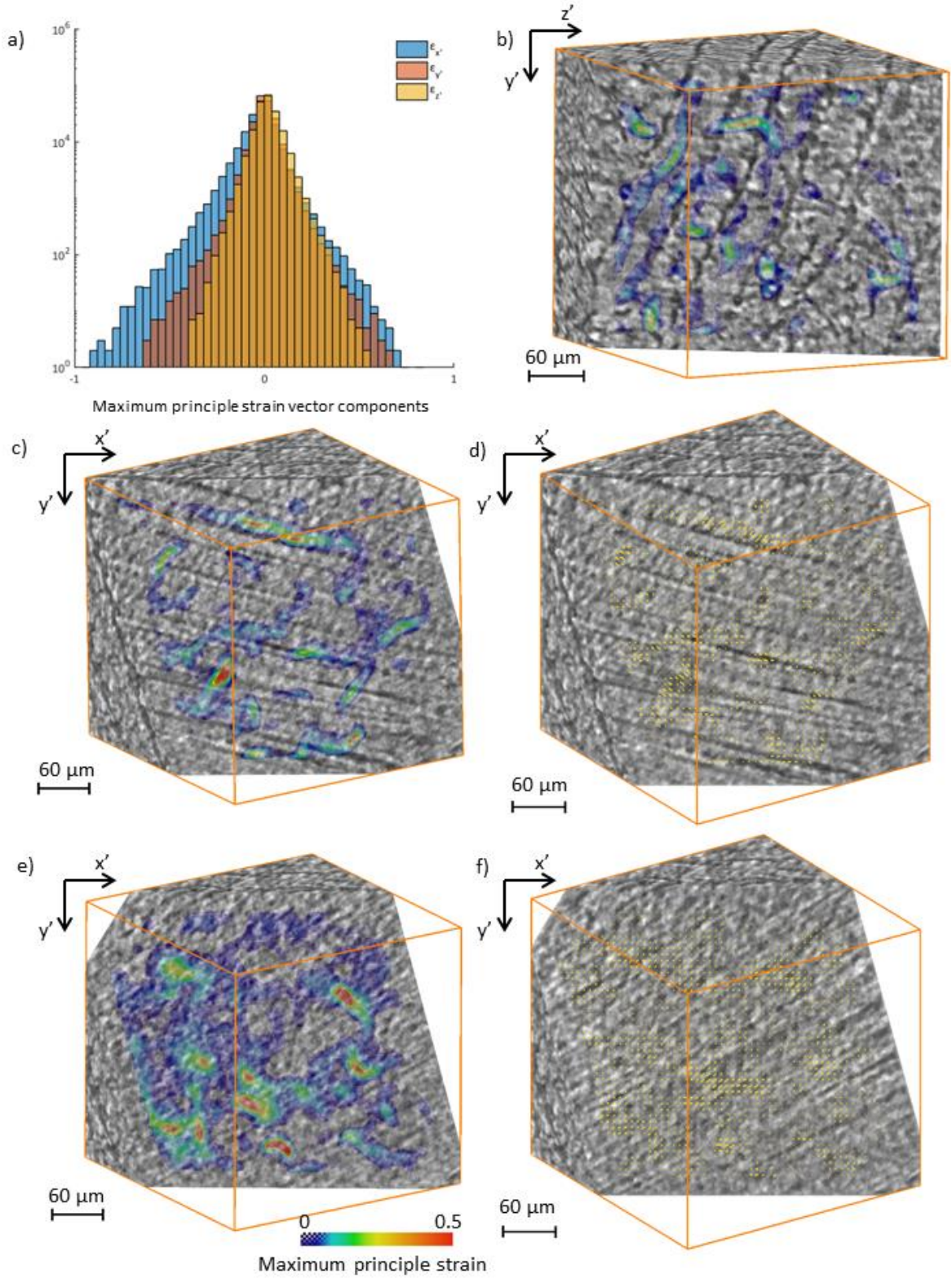

Supplementary figure 4.11 Lateral cube maximum principle strain for the repeat scan at L0; a) maximum principle strain vector components defined in local lamella coordinate system b,c,e) maximum principle strain plotted with image data, clipped across lamella (b) and clipped in the lamella plane (c & e) d & f) shows principle strain vectors in the lamella plane plotted with image data.

Supplementary videos are provided and can be accessed online using the following web-link:

https://data.mendeley.com/datasets/37nfzfcsjk/draft?a=dee23d33-be6d-43f4-a9f3-c7df6fd555af

Supplementary video 4.1: Sequence of 3D renders of a rat spine segment being compressed from the lower endplate.

Supplementary video 4.2: AF collagen bundles traced in the medial volume of interest (cube with 320 μm dimensions).

Supplementary video 4.3: AF collagen bundles traced in the lateral volume of interest (cube with 320 μm dimensions).

Supplementary video 4.4: Overview of the work in this chapter is presented; i) A transverse slice shows the IVD structures resolved using microCT, ii) a medial cube volume of interest is selected and bundle analysis shown, iii) points are setup in the cube and sub-volume size is defined for displacement tracking using digital volume correlation, iv) after displacement of each point was found over all compression steps (4 x 2% strain), maximum principle strain and associated vectors were calculated and plotted with the image data.

Supplementary information 4.1: MATLAB code for strain calculations

General script for 3D strain calculation from unstructured data

```
% basic steps:
 % create n,x,y,z,u,v,w,objmin column vectors from data set
 % rotate column vectors of x,y,z,u,v,w into new coord syst. (optional)
 % remap onto a regular space with meshgrid-griddata
 % filter displacements
 % Lagrangian strain calculation
 % Save strain
```

Import sub-volume positions

```
% assume n (vector of point labels) is available
x = x13;
y = y13;
z = z13;
% objmin = fmin14;
% creating displacements from 14 - 13 positions
```

```
u = x14 - x13;
v = y14 - y13;
w = z14 - z13;
```

Rotate using axis-angle

```
% % axis = [0.5646625  -0.8066085     -0.1718505];
% % angle = [0.722059292]; % cube1 axis-angle rotation
% axis = [ -0.40601275 -0.5234825 -0.74886625];
% angle = [2.088997672]; % cube3 axis-angle rotation
%
% ex = axis(1); ey = axis(2); ez = axis(3);
%
% % Rotation matrix
%
%   R   =   [cos(angle)+ex^2*(1-cos(angle))   ex*ey*(1-cos(angle))-ez*sin(angle)   ex*ez*(1-
cos(angle))+ey*sin(angle); ...
%             ey*ex*(1-cos(angle))+ez*sin(angle)   cos(angle)+ey^2*(1-cos(angle))   ey*ez*(1-
cos(angle))-ex*sin(angle); ...
%                   ez*ex*(1-cos(angle))-ey*sin(angle)    ez*ey*(1-cos(angle))+ex*sin(angle)
cos(angle)+ez^2*(1-cos(angle))];
%
% % define positions and displacements in new coordinate system
%
% N = numel(pos)/3; %number of vectors
% pos_rot = pos;
% dis_rot = dis; % initialize rotated vector array
%
% for i = 1:N
%   pos_rot(i,:) = (R*pos(i,:)')';
%   dis_rot(i,:) = (R*dis(i,:)')';
%   end
%
% %update
% clear x y z u v w
%
% x=pos_rot(:,1);
% y=pos_rot(:,2);
% z=pos_rot(:,3);
%
% u=dis_rot(:,1);
% v=dis_rot(:,2);
% w=dis_rot(:,3);
%
% clear pos dis pos_rot dis_rot
% pos=[x y z];
% disp=[u v w];
```

Remap to regular space

```
% x y coordinates swapped for avizo visualisation
inc = 3;
[mx,my,mz] = meshgrid(min(y):inc:max(y),min(x):inc:max(x),min(z):inc:max(z));

mu = griddata(y,x,z,u,mx,my,mz,'natural');
mv = griddata(y,x,z,v,mx,my,mz,'natural');
mw = griddata(y,x,z,w,mx,my,mz,'natural');
```

Displacement filtering

```
med_span = 3;   % odd itegers, zero for don't apply
gau_span = 3;   % odd itegers, zero for don't apply

% apply median filter to displacements first
if med_span > 0
    muf1 = medfilt3(mu,[med_span,med_span,med_span]);
    mvf1 = medfilt3(mv,[med_span,med_span,med_span]);
    mwf1 = medfilt3(mw,[med_span,med_span,med_span]);
else
    muf1 = mu;
    mvf1 = mv;
    mwf1 = mw;
end

% apply gaussian filter to displacements second
if gau_span > 0
    muf2 = smooth3(muf1,'gaussian',[gau_span,gau_span,gau_span]);
    mvf2 = smooth3(mvf1,'gaussian',[gau_span,gau_span,gau_span]);
    mwf2 = smooth3(mwf1,'gaussian',[gau_span,gau_span,gau_span]);
else
    muf2 = muf1;
    mvf2 = mvf1;
    mwf2 = mwf1;
end

% load total filter result and clear intermediates
muf = muf2;
mvf = mvf2;
mwf = mwf2;
clear muf1 mvf1 mwf1 muf2 mvf2 mwf2
```

Lagrangian strain calculation

```
[nx,ny,nz] = size(mx);

mtD = zeros(nx,ny,nz,3,3);      % displacement gradient
mte = zeros(nx,ny,nz,3,3);      % infinitesimal strain tensor
mtL = zeros(nx,ny,nz,3,3);      % Lagrangian strain tensor

mePval = zeros(nx,ny,nz,3);        % Principals of e in mech order
mLPval = zeros(nx,ny,nz,3);        % Principals of L in mech order

mePvec = zeros(nx,ny,nz,3,3);       % Prin vects, columns, ordered
mLPvec = zeros(nx,ny,nz,3,3);       % Prin vects, columns, ordered


% single term storage used for calcs ahead of storage back into matrices
tD = zeros(3,3);
te = zeros(3,3);
tL = zeros(3,3);

ePval = zeros(3,1);
LPval = zeros(3,1);

ePvec = zeros(3,3);
LPval = zeros(3,3);

[mtD(:,:,:,1,1),mtD(:,:,:,1,2),mtD(:,:,:,1,3)] = gradient(muf,inc,inc,inc);
[mtD(:,:,:,2,1),mtD(:,:,:,2,2),mtD(:,:,:,2,3)] = gradient(mvf,inc,inc,inc);
[mtD(:,:,:,3,1),mtD(:,:,:,3,2),mtD(:,:,:,3,3)] = gradient(mwf,inc,inc,inc);
```

```
for i=1:nx
    for j=1:ny
        for k=1:nz
           tD(:,:) = mtD(i,j,k,:,:);    % load D at location i,j,k
           te = (1/2)*(tD + tD');       % calc infinitesimal
           tL = te + (1/2)*(tD'*tD);      % add higher order terms
           %tL = (1/2)*(tD + tD' + tD'*tD);
           mte(i,j,k,:,:) = te(:,:);    % load back into matrix storage
           mtL(i,j,k,:,:) = tL(:,:);    % load back into matrix storage

           if sum(isnan(te(:))) > 0         % trap tes containing NaNs
              ePval = NaN(3,1);
              ePvec = NaN(3,3);
           else
              [vec,val] = eig(te);
              ePval = [val(1,1) val(2,2) val(3,3)];
              [ePval,indx] = sort(ePval,'descend');
              ePvec(:,1) = vec(:,indx(1));
              ePvec(:,2) = vec(:,indx(2));
              ePvec(:,3) = vec(:,indx(3));
              % ePval = sort(eig(te),'descend');
           end
           mePval(i,j,k,:) = ePval(:);
           mePvec(i,j,k,:,:) = ePvec(:,:);
% e.g. quiver3(mx,my,mz,mePvec(:,:,:,1,1),mePvec(:,:,:,2,1),mePvec(:,:,:,3,1));
       if sum(isnan(tL(:))) > 0      % trap tL's containing NaNs
              LPval = NaN(3,1);
              LPvec = NaN(3,3);
           else
              [vec,val] = eig(tL);
              LPval = [val(1,1) val(2,2) val(3,3)];
              [LPval,indx] = sort(LPval,'descend');
              LPvec(:,1) = vec(:,indx(1));
              LPvec(:,2) = vec(:,indx(2));
              LPvec(:,3) = vec(:,indx(3));
              % LPval = sort(eig(tL),'descend');
           end
           mLPval(i,j,k,:) = LPval(:);
           mLPvec(i,j,k,:,:) = LPvec(:,:);

        end
    end
end
```

Save Lagrangian strain components (mtL)

```
E11 = mtL(:,:,:,1,1);
E12 = mtL(:,:,:,1,2);
E13 = mtL(:,:,:,1,3);
E21 = mtL(:,:,:,2,1);
E22 = mtL(:,:,:,2,2);
E23 = mtL(:,:,:,2,3);
E31 = mtL(:,:,:,3,1);
E32 = mtL(:,:,:,3,2);
E33 = mtL(:,:,:,3,3);
```

Save principle strain (mLPval descending order)

```
e1 = mLPval(:,:,:,1);
```

```
e2 = mLPval(:,:,:,2);
e3 = mLPval(:,:,:,3);

maxshear = 0.5*(e1-e3);

write_rawfloat32b('cube1-84013-84017-67-67-67-3-e1-float32.raw',e1);
write_rawfloat32b('cube1-84013-84017-67-67-67-3-maxshear-float32.raw',maxshear);
```

Save principle vectors (mePvec)

```
uP = mePvec(:,:,:,1,1);
vP = mePvec(:,:,:,2,1);
wP = mePvec(:,:,:,3,1);


% principle strain*vectors

uPv = e1.*uP;
vPv = e1.*vP;
wPv = e1.*wP;


write_rawfloat32b('cube1-84013-84017-uPv-67-67-67-3-float32.raw',uPv);
write_rawfloat32b('cube1-84013-84017-vPv-67-67-67-3-float32.raw',vPv);
write_rawfloat32b('cube1-84013-84017-wPv-67-67-67-3-float32.raw',wPv);
```

5 An update on high resolution synchrotron micro-computed tomography of the native intact intervertebral disc

This chapter is in the style of a short report intended to be submitted to Acta Biomaterialia

5.1 Author contribution statement:

Catherine M. Disney wrote the paper.

Catherine M. Disney, Brian K. Bay, Amie Kilkenny, Alexander Eckersley, Jingyi Mo and Michael J. Sherratt collected the data.

Amie Kilkenny is accredited for the histology in Figure 5.2.

5.2 Abstract

This short report describes improvements made to the imaging of native rat intervertebral disc using in-line phase contrast synchrotron microCT. Improved signal:noise and reduced streaking artefacts now mean that; resolved structures are extended to the full disc with all lamellae visible, cells throughout the disc were identified and imaging remained consistent in a series of scans where the disc was sequentially compressed.

5.3 Introduction

Studying the micro- mechanical environment is possible using a non-destructive imaging such as X-ray micro-computed tomography (microCT), applying an *in situ* load and correlating the image volumes to track microstructural displacements (Disney *et al.*, 2018)(Chapter 4).

To date, microCT for soft tissue has either used heavy metal stains (Metscher, 2009b) or in-line phase contrast to enhance contrast and resolve tissue microstructure (Disney *et al.*, 2017, Walton *et al.*, 2015, Naveh *et al.*, 2014). Staining commonly induces morphological and mechanical changes to the tissue and is therefore ill-suited for microstructural deformation studies. It is possible to resolve the microstructure of unstained samples using in-line phase contrast techniques. High resolution imaging using laboratory and synchrotron in-line phase contrast microCT has been achieved by embedding samples in paraffin (Walton *et al.*, 2015) which ensured the sample did not move however, *in situ* loading is not possible for embedded samples. The structure of native IVD has recently been resolved in a static laboratory study (Naveh *et al.*, 2014) and an *in situ* compression synchrotron study (Chapter 4). However, these studies did not achieve the high resolution reported by Walton *et al.* (2015) obtained in other soft tissues. When comparing between laboratory and synchrotron source microCT; synchrotron source considerably improved the image quality with hierarchical structure of the IVD resolved (collagen bundles within outer lamellae) and shorter scan times which allowed *in situ* imaging. Nevertheless, there were obscuring streaking artefacts from the calcified endplates which meant that it was impossible to resolve all lamellae and the NP was not visible throughout the compression sequence (Chapter 4). This short report aims to improve image quality by building on previous phase contrast synchrotron microCT imaging of native rat IVD and employing careful sample preparation and alignment of the sample in the beam.

5.4 Materials and methods

5.4.1 Tissue and materials

Male 8-week-old Sprague Dawley rats (University of Manchester Biological Services Facility) were sacrificed by carbon dioxide inhalation. Spines were dissected *en bloc* and snap frozen in liquid nitrogen. Samples were stored at -80°C and thawed at room temperature before use. Figure 5.1a shows the sample preparation steps. Angled cuts were made through L4/L3 and L3/L2 vertebra at ~70° using a high precision diamond cutting blade (Accumtom-50, Struers). Slow feed speed and blade rotation minimised any

potential damage to the sample. Posterior elements of both vertebrae were removed from the spine segment using a scalpel. Samples were then set in the holders using epoxy resin and an alignment tool.

5.4.2 Equipment and testing

Samples were compressed on the beamline using Deben CT5000 (Deben, UK) rig which was controlled remotely. A 1 N preload was applied and displacement held for a stress relaxation period of ~15 minutes or until the force readout had settled. The first scan was then acquired and a compression of 0.02 mm (~2% strain) applied and held during the second stress relaxation period and scan. This process was repeated a further three times to have a total of 8% applied strain for the last scan. A slow strain rate of 0.00167 strain/s (0.1 mm/min) was used to minimise the peak stress response and reduce stress relaxation time.

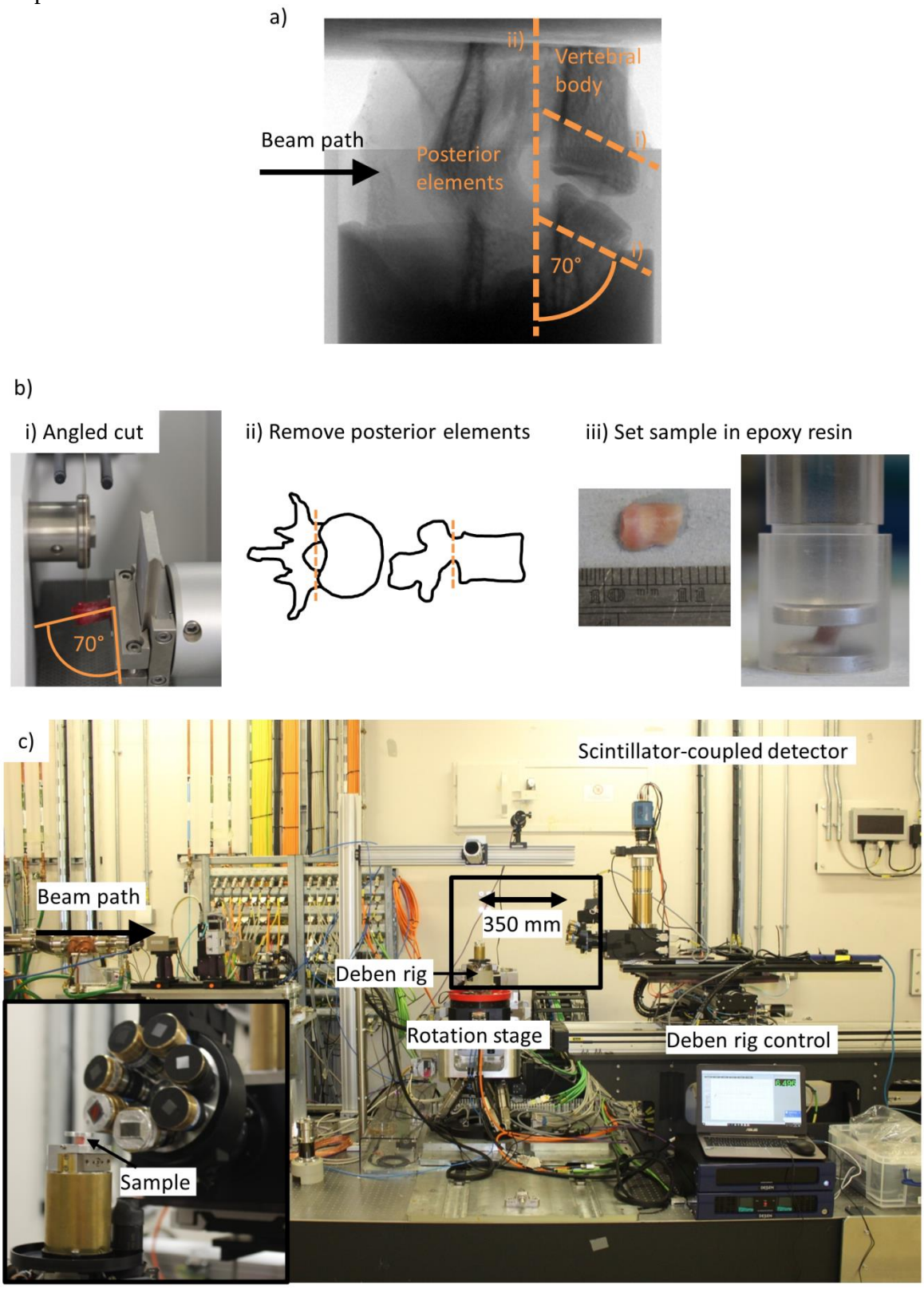

Figure 5.1 Sample preparation and Diamond-Manchester beamline (I13-2); a) Radiograph of spine segment. Orange lines shows position of cuts made for sample preparation. b) Sample preparation steps. c) Diamond-Manchester beamline set-up with Deben rig (open) and sample in place.

5.4.3 In-line phase contrast synchrotron microCT

Imaging was acquired on the Diamond-Manchester beamline (I13-2) at Diamond Light Source (Figure 5.1). Pink beam (8-30 keV) and undulator gap of 5 mm provided high flux to minimise scan time. The beam was filtered (1.34 mm pyrolytic graphite, 3.2 mm aluminium, 0.14 mm iron) to reduce beam damage. PCO.edge 5.5 scintillator-couple detector with a 2x objective for whole IVD imaging and 4x objective for region of interest scans was used to record the projections. The 2x objective gave a total magnification of 4x, effective pixel size 1.6 µm and field of view 4.2 x 3.5 mm and 4x objective gave a total magnification of 8x, effective pixel size 0.81 µm and field of view 2.1 x 1.8 mm. Exposure time for each projection was set to 0.15 s for the 2x objective and 0.2 s for the 4x objective according to ~50% saturation in flat-field projections. A total of 5001 projections were taken for all scans over 180° continuous rotation. Propagation distance of sample to detector was set to 350 mm which provided sufficient in-line phase contrast to resolve IVD microstructure. Scans were taken after sample compression and stress relaxation (~15 minutes) to minimise sample movement during acquisition. The projections were reconstructed using Diamond Light Source software DAWN (Atwood *et al.*, 2015, Basham *et al.*, 2015). A light median filter (1-2 pixels) was applied to the reconstructed images and results were visualised with figures prepared using ImageJ (Schneider *et al.*, 2012).

5.5 Results and discussion

The overall image quality is shown in Figure 5.2a. When compared to previous results of Naveh *et al.* (2014) and in Chapter 4, there was less noise with an increase in signal to noise ratio and fewer streaking and dark band artefacts from the endplate obscuring the IVD structure. This means that all lamellae of varying thickness were resolved from inner to outer AF. A high level of detail, equivalent to histology, can be seen in a single slice (Figure 5.2b & c) with individual cells resolved between lamellae. The increase in signal to noise ratio was likely due to removing the spine segment posterior elements. Firstly, this increased the number of photons reaching the structures being scanned and secondly it decreased the variation in absorption in the beam path (which causes streaking). Figure 5.1a is a projection through a spine segment where the dark areas indicate high X-ray absorption by the posterior elements and vertebral bodies demonstrating the variation in absorption in the beam path and that had the posterior elements not been removed there would have been reduced photon flux to the IVD. Increased photon flux to the structures being scanned also meant that the number of projections was reduced (from 8001 to 5001) which is beneficial for soft tissue imaging, reducing scan time and radiation dose.

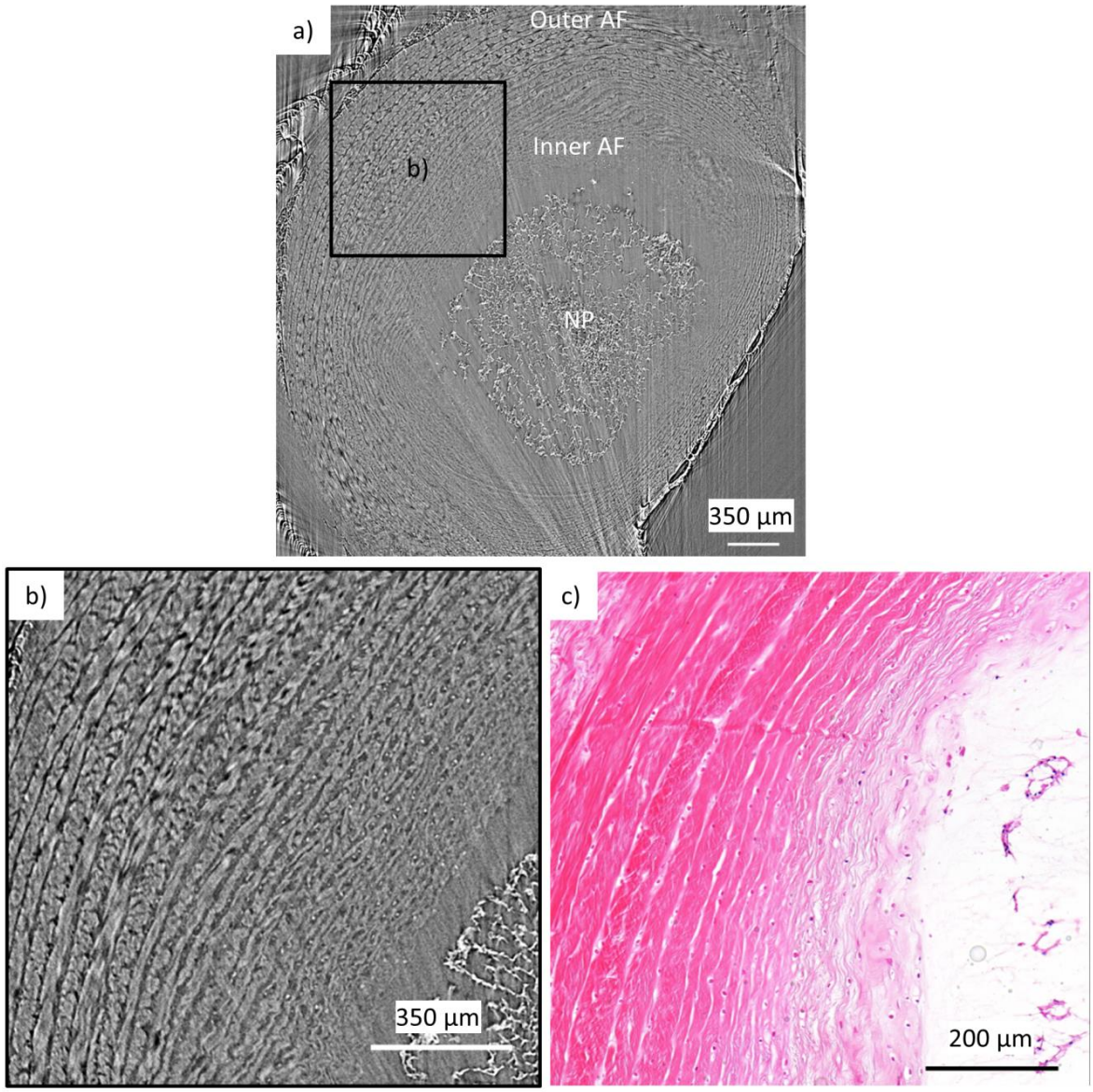

Figure 5.2 MicroCT of native intact rat IVD a) all lamellae from inner to outer AF can be resolved, b) & c) a virtual transverse slice shows that results have histological resolution. Histology courtesy of Amie Kilkenny: rat IVD section stained with haematoxylin and eosin.

Details of NP microstructure which have not previously been imaged in an intact disc before can be seen in Figure 5.3. Clustered NP cells are found in the centre surrounded by radially arranged fibres (orange arrows). Elastic radial fibres in the NP with similar length (150 µm) have been previously observed in bovine tail IVD using immunostaining by Yu *et al.* (2002). Individual NP cells are not entirely apparent however, when viewed using higher magnification (4x compared with 2x objectives), individual spheroid cells can be identified with 8-10 µm diameter. Clustered round cells are consistent with the cobblestone description and scale of *in vitro* (differentiated) NP cells given by Van der Akker *et al.* (2014).

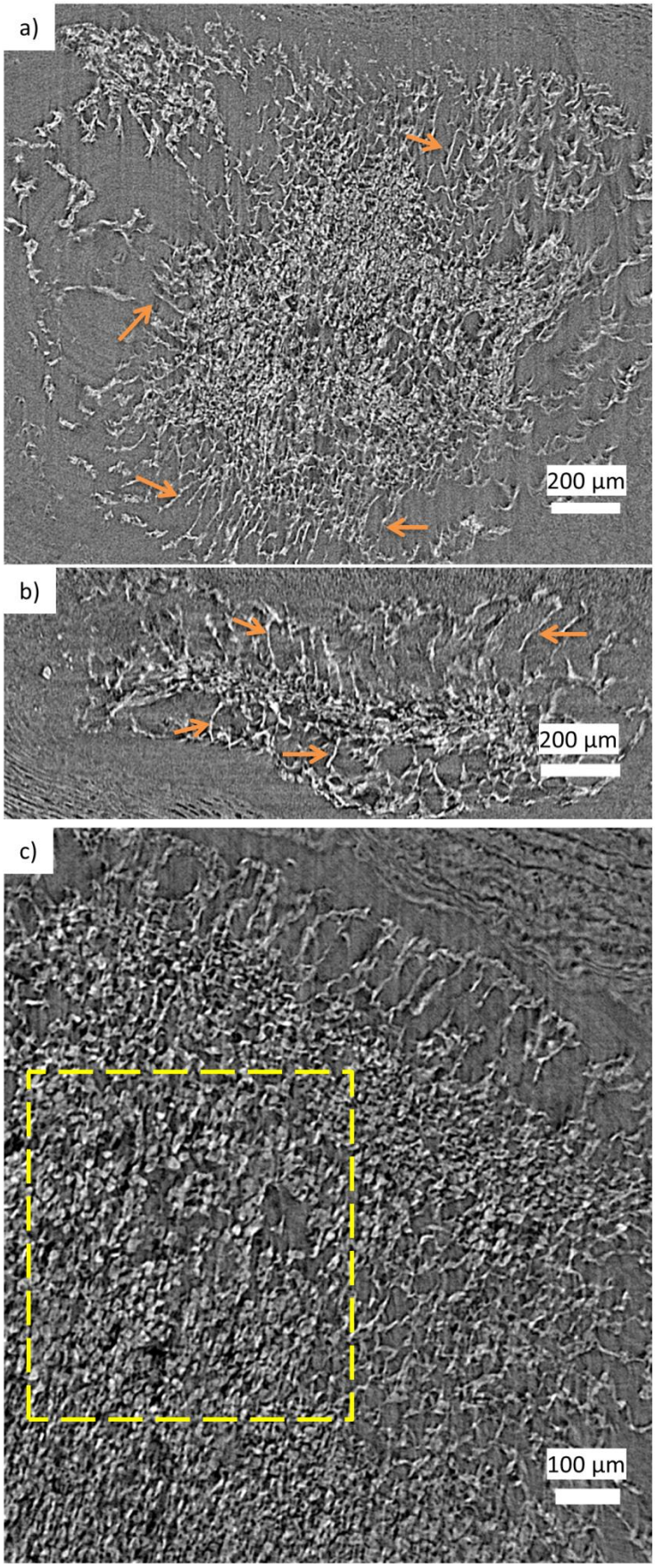

Figure 5.3 Virtual slices of NP. a) Transverse and b) longitudinal slices show NP cells in the centre of the IVD surrounded by radially arranged fibres (orange arrows), c) higher magnification (4x objective) resolved individual cells of 8-10 µm diameter (yellow box).

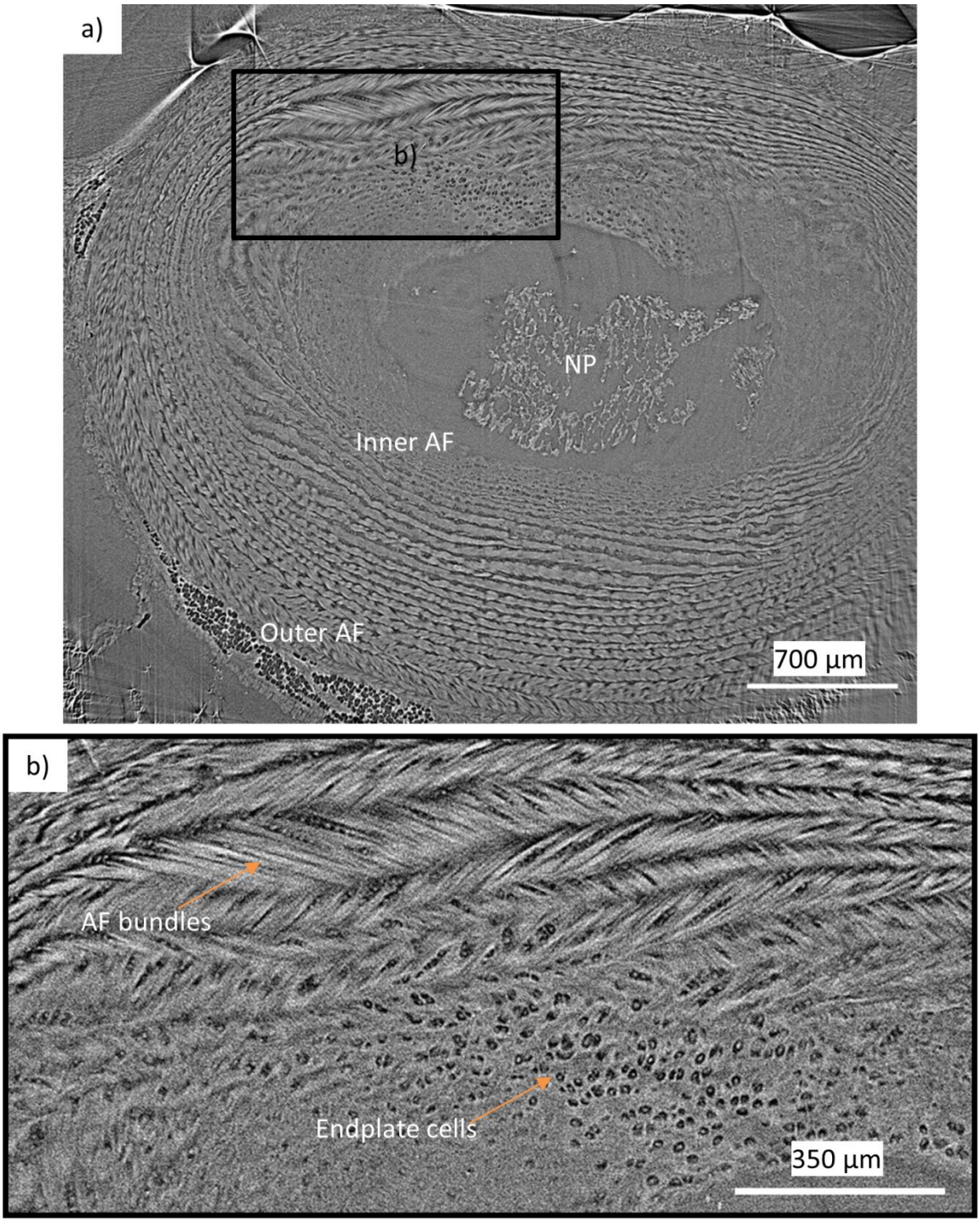

Figure 5.4 a) Transverse slice showing lamellae and individual AF bundles in the anterior portion of the disc, b) the bundles change orientation as they approach the endplate where cells have been resolved.

Figure 5.4 shows individual AF bundles changing orientation to meet the endplate where cells have been resolved. Previous imaging (Chapter 4) was not able to image this level of detail presented in Figure 5.3 and Figure 5.4 which may be explained by a decrease in the

propagation distance (500 mm compared with 350 mm) for phase contrast imaging and hence, an increase in sensitivity to smaller features (Snigirev *et al.*, 1995). Note that propagation distance is proportional to the dimension squared of the scattering structure for the Fresnel-diffraction regime.

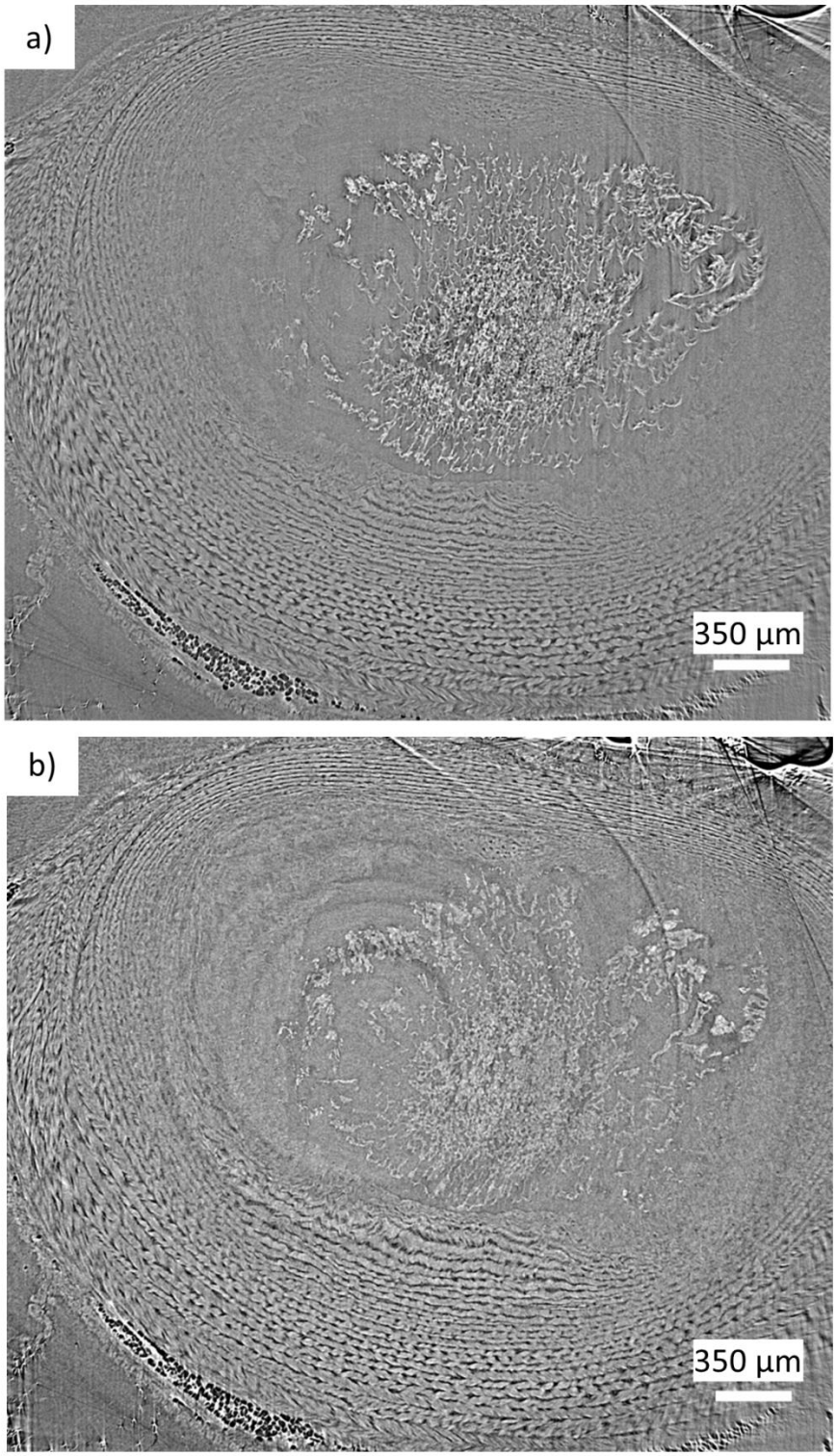

Figure 5.5 NP is resolved throughout the in situ compression sequence. Transverse slices taken from a) first scan and b) last (fifth) scan in the compression sequence.

Finally, the imaging remained relatively stable for all scans during the compression sequence. This is an improvement on previous work where the NP structures appeared to vanish due to the increasing presence of obscuring streaking artefacts crossing into the NP when the endplates moved closer together. This improvement could be attributed to the careful alignment of the sample in the beam to ensure endplates were parallel with the beam path. The angle of the disc relative to the spine axis was measure using a radiograph (70°) and used to make angled cuts through the vertebra using a high precision diamond saw.

5.6 Conclusions

The imaging presented here has resolved the 3D microstructure of native IVD at unprecedented and previously unachieved levels of detail using microCT. Other reconstruction software such as Savu (Wadeson and Basham, 2016) combined with ring artefact removal (Raven, 1998) and Paganin phase retrieval (Paganin *et al.*, 2002) could provide further improvements. This data-set has great potential for micro- scale strain measurement across the whole IVD whereas the previously attempted strain measurement was only possible in outer AF regions, where sufficient structure was resolved to support digital volume correlation. Future work involving quantification of 3D microstructural characterisation of the native intervertebral disc will be valuable for computational models and in the design of tissue replacements.

6 Summary and conclusion

The work detailed in this thesis set out to evaluate the use of microCT and digital volume correlation (DVC) for strain measurement in the intervertebral disc (IVD) to gain an improved characterisation of the native disc's micro- structural and mechanical environment under load. IVD micro- structural and mechanical characterisation is a fundamental element required to understand the IVD vicious circle disease model described by Vergroesen *et al.* (2015) where cells, extracellular matrix (microstructure) and biomechanics form a positive feedback loop.

The initial challenge was to gain sufficient X-ray contrast to resolve the structure of the IVD. A comparison of heavy metal stains demonstrated the potential of microCT as a non-destructive 3D imaging technique; however, there were deleterious morphological changes to the tissue. It was possible to resolve unstained IVD microstructure in small tissue segments using laboratory in-line phase contrast microCT. When compared to laboratory source, the in-line phase contrast tomography resolved from synchrotron source X-rays had a larger field of view, higher signal to noise ratio and shorter scan times (minutes compared to hours/days) which, importantly, enabled imaging of native tissue. Rat spine segments, chosen for their suitability to the beam size, were used to image intact native intervertebral disc. After successfully acquiring image data of an intact disc under sequential compression, AF bundle orientation could be quantified, and displacement of features tracked using DVC and mapped as strain in two outer AF regions. The characterisation of local strains in the AF significantly adds to previous research in IVD experimental mechanics as this study is in 3D and taken from an intact sample. Still, only outer AF microstructure was fully resolved throughout the compression sequence and able to support DVC. Improved image quality has been accomplished by refining sample preparation and positioning in the beam. Importantly, the latest results in high resolution synchrotron microCT of the intact IVD show unprecedented levels of detail, resolving all lamellae and cells consistently through the compression sequence. The two remaining sections describe the workflow and considerations which must be made for microCT-DVC studies of soft tissue and finally the impact of future work in applying these methods to study IVD degeneration and mechanical efficacy of tissue engineered replacements.

6.1 Workflow for imaging microstructure deformation and strain measurement in intact soft tissues[3]

This section summarises the methodology and workflow developed throughout this thesis for imaging 3D microstructural deformation and strain measurement within intact soft tissue samples. Figure 6.1 and the sections below are taken and adapted, with some text changes, from Disney *et al.* (2018) so that it is directly relevant to this thesis.

6.1.1 Sample preparation and loading conditions

6.1.1.1 Precise and consistent sample dissection

Biological tissues have complex, viscoelastic, anisotropic mechanical behaviour and therefore precise and consistent sample preparation is required. Additionally, prior knowledge of anatomy and reproducible sample preparation is important for imaging as shown in Chapter 5 where angled cuts were made so that the disc endplates were parallel with the X-ray beam. If the sample preparation and positioning is optimal for imaging, there is also an added benefit of reducing scan time; fewer projections are required resulting in a decreased radiation dose to the sample.

6.1.1.2 Effect of sample preparation on tissue mechanics

Consistent dissection and mechanical testing of tissues under different controlled conditions, such as uniaxial loading of the sample in multiple orientations, gives valuable material characterisation. However, dissected samples do not retain their residual strain (Michalek *et al.*, 2012) and so intact samples should ideally be used for testing organs or tissue under physiological loads. Applying loads to dissected tissue is also challenging and may alter tissue mechanics. Additionally, tissues have a natural composition gradient and irregular shape at loading interfaces which is challenging to replicate when loading dissected segments of tissue. For instance, the concave morphology of intervertebral disc endplates which varies between adjacent endplates and depends on lumbar region (Wang *et al.*, 2012).

6.1.1.3 Physiologically relevant loading regimes are limited by imaging capabilities

Soft tissues function in a dynamic environment where loading frequency can be seconds. Observing structural deformation at this loading frequency is only possible when using

[3]Section 6.1 is an adapted version from Disney, C., Lee, P., Hoyland, J., Sherratt, M. & Bay, B. 2018. A review of techniques for visualising soft tissue microstructure deformation and quantifying strain *Ex vivo*. *Journal of microscopy*.

imaging techniques with a short acquisition time (<ms). Deciding on a loading protocol becomes more challenging when there are long acquisition times for 3D imaging techniques such as microCT (minutes to hours) and a long relaxation period for tissue creep. Loading must be interrupted to allow for long imaging acquisition. It is recommended that all regimes follow the same general protocol below. The applied deformation step must be small enough to track using image correlation and many steps may be required depending on stiffness or physiological range. Importantly, there must be a relaxation period after each load step is applied which allows for tissue creep before image acquisition and avoids imaging artefacts. Future studies could explore using different beamlines such as TOMCAT beamline at Swiss Light Source (Walker *et al.*, 2014, Mokso *et al.*, 2011) or a complementary non-destructive techniques such as small angle X-ray scattering to capture the more dynamic changes at a fibril scale but at a single sample point (without spatial measurement) (Inamdar *et al.*, 2017).

6.1.2 Imaging microstructure; towards 3D imaging of native samples using microCT

6.1.2.1 Balancing contrast, resolution and field of view

To this date, soft tissue *in situ* imaging studies are 2D or have been limited to small volumes. MicroCT has the potential to provide 3D microstructural imaging of intact native samples. Nevertheless, soft tissues are weakly X-ray absorbing and so contrast enhancement is required. Contrast agents can alter tissue structure and mechanics due to long staining times and tissue preservation or fixation (Disney *et al.*, 2017, Balint *et al.*, 2016, Vickerton *et al.*, 2013, Tilley *et al.*, 2011, Hickey and Hukins, 1979). Alternatively, contrast enhancement can be achieved in native tissue using in-line phase contrast imaging techniques (Disney *et al.*, 2017). However, laboratory microCT phase contrast approaches do not provide a large enough field of view to image the whole small animal organs at the required resolution. Synchrotron imaging has a larger field of view and has been shown to give lower tracking uncertainties for image correlation when compared to laboratory microCT (Dall'Ara *et al.*, 2017). The considerably bright synchrotron X-rays are able to obtain higher signal:noise reconstructions and shorter scans times. A short scan time is required to mitigate against slow tissue relaxation. The high coherence and tomography beamline configurations (such as Diamond-Manchester I13-2) allow for large propagation distances which is ideal for in-line phase contrast imaging of soft tissue.

6.1.2.2 Compromise between image quality and radiation dose

Although synchrotron microCT is capable of high signal:noise reconstructions, a balance must be made between radiation dose and scanning parameters (beam filters, number of projections and exposure time). It is recommended that the sample should be aligned in the beam under low dose conditions by using large undulator gap and shutters. The use of low temperatures has shown some promise in reducing radiation induced damage in trabecular bone (Fernández *et al.*, 2018b). Whilst reducing damage, it is important to consider the effect low temperatures may have on tissue mechanics.

6.1.2.3 Data handling and image processing

After reconstruction it may be advantageous to process the tomography data such as using filters to reduce random noise or image artefacts. Synchrotron microCT produces large data-sets which can be challenging to handle and computationally expensive to analyse. A volume of interest or some segmentation of the data to only include certain features may be required before image correlation analysis.

6.1.3 Tracking displacement of features using image correlation

6.1.3.1 Sufficient features to track

Image correlation is only possible if there are small features to track. Applied speckle patterns and image correlation have been used for mapping strain on surfaces of biological tissues. DIC measurements are sensitive to the quality of the pattern and creating a speckle pattern can be problematic for hydrated soft tissues without changes in mechanical properties. However, these methods do not provide information on internal strains and how they relate to the 3D microstructure of the tissue. DVC can be used for non-invasive sub-voxel displacement tracking using natural image texture.

6.1.3.2 Tracking reliability depends on correlation parameters

Using the DVC results it is possible to obtain a local strain map and relate it to the microstructure of the tissue. The DVC parameters must be carefully tuned to the image texture and aligned with the research question. It has already been shown that the sub-volume size is important for tracking uncertainty. The density and location of the tracking points may improve reliability or follow microstructures that are of interest e.g. fascicles in tendon, lamellae in IVD or collagen fibres in arterial tissue. Tuning DVC parameters will particularly be important for future *in situ* studies where the structures are heterogeneous and hierarchical. The influence of texture characteristics on the precision and spatial resolution of image correlation, and optimal tracking procedures for challenging

conditions, are topics of continuing research. In the absence of definitive guidelines, the best strategies for ensuring reliable results are correlation of multiple image volumes under static conditions (repeat unloads), and careful analysis of residuals associated with normalised correlation functions.

6.1.3.3 Correlation is inclusive of image noise and artefacts

Image correlation is sensitive to all features in the data including noise and artefacts which can cause complications. Firstly, the level of noise may change between and within images which leads to varied reliability. Image filtering to reduce noise can help but also be detrimental if small scale features are lost. In the case of the study in this thesis (Chapter 4), noise varied considerably across the image volume and so volumes of interest (cubes) had to be selected from the outer AF where the structure was consistently resolved. Secondly, results may appear to be reliable with excellent correlation, but displacement values are associated with motion artefacts and not to tissue deformation. Rigid body motion artefacts, once identified, can be removed by adjusting reference points for displacement values without altering relative deformations. As proper strain measures are insensitive to rigid body motion, the calculation of strain from displacements will reveal sample deformation more definitively.

6.1.4 Strain calculation and interpretation

Strain calculation and interpretation must be appropriate for the specific tissue. For example, published work has shown collagen fibre sliding to be the main deformation mechanism in tendon and IVD and so a shear strain map may be the most appropriate measurement. Furthermore, choosing how to measure strain may depend on the loading mode e.g. measuring circumferential/ hoop strain for inflated arteries or in the AF of compressed IVD. A new or local coordinate system which is relevant to the tissue structure may be necessary to analyse the results, for example, the local lamella coordinate system defined in this thesis. Soft tissues also exhibit large, nonlinear strains, and an appropriate finite strain measure should be used, with Green-Lagrange a common choice. When interpreting results and comparing between studies it is important to take note of sample preparation, loading conditions and their strain definition for the reasons mentioned above.

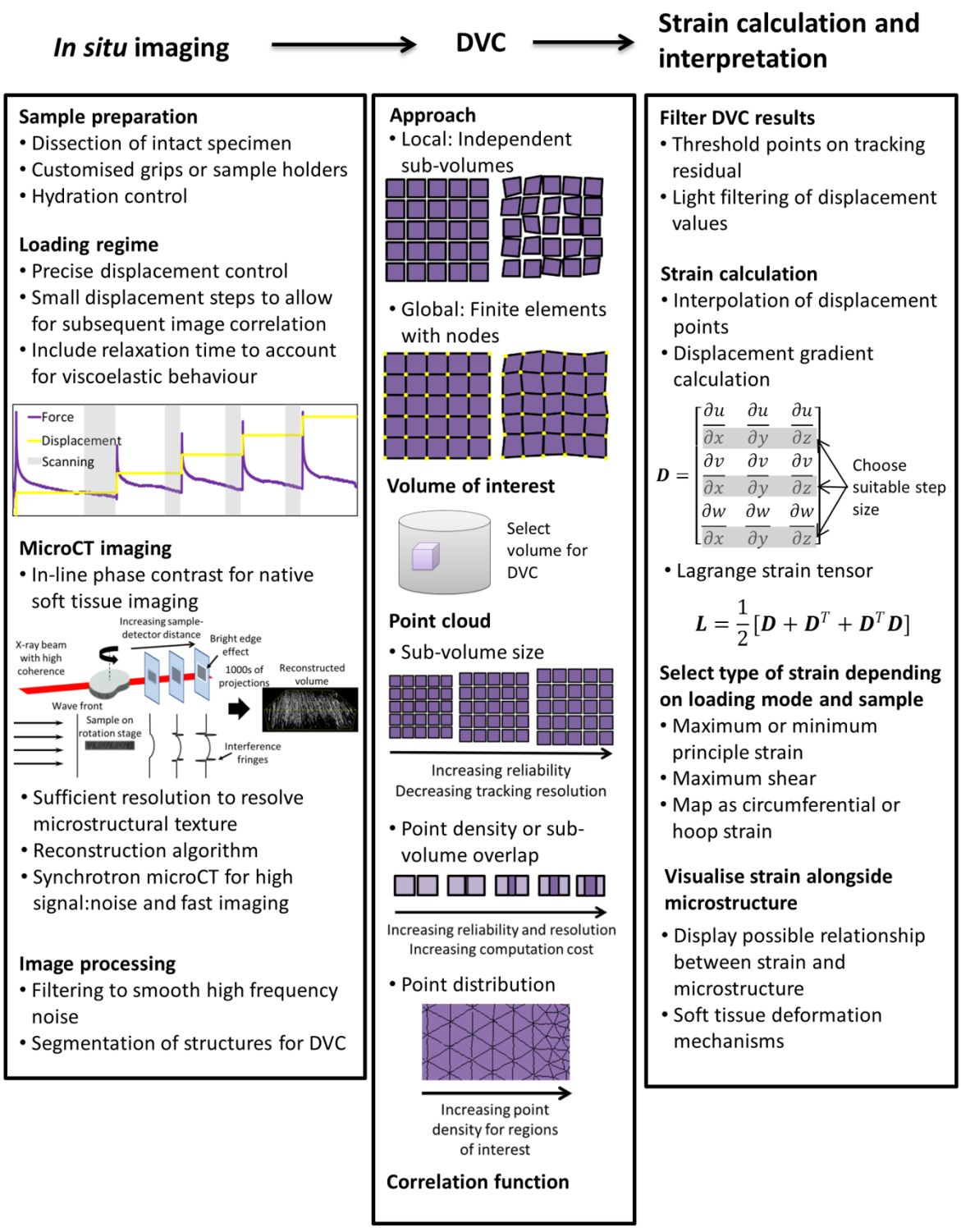

Figure 6.1 Proposed workflow for soft tissue microCT-DVC studies (Disney et al., 2018).

6.2 Advances in IVD structure and mechanical characterisation and future studies

The improved imaging presented in Chapter 5 showcases unprecedented levels of detail of IVD microstructure for volumetric imaging. The following structural information is currently not available for intact IVD but can be obtained from this tomography data: i) Endplate curvature, porosity and boundary structure, ii) lamellae organisation including curvature, varying thickness from inner to outer AF, distribution and frequency of partial lamellae, iii) anatomical map of AF bundle orientation, iv) cell abundance and location in intact IVD. This structural characterisation will be valuable for IVD computational models which will be closer to anatomy than previously attempted and have potential to predict the mechanical causes of degeneration. For example, one of the most recent image-based finite element modelling studies used MRI for disc geometry and diffusion tensor imaging at 30 sample points for fibre organisation (Stadelmann *et al.*, 2018b). Although Stadelmann *et al.* (2018b) included regional variation in bundle orientation, their model did not incorporate lamellae organisation where structural heterogeneity such as partial lamellae may play a vital role in regional tissue mechanics.

6.2.1 Studying the effects of IVD degeneration and needle injury on microstructure deformation

Please note that synchrotron microCT has already been collected for these studies under Diamond Light Source proposal 19322 (Appendix C) and is presented below. Analysis on this data will be performed during my successfully awarded EPSRC Doctoral Prize Fellowship (proposal in Appendix D).

An *ex vivo* model of IVD degeneration has been established using bovine discs (Roberts *et al.*, 2008). Based on the protocol published by Roberts *et al.* (2008), trypsin was injected into rat IVDs to enzymatically digest NP tissue. In-line phase contrast synchrotron microCT of these samples, sequentially compressed using the methods developed in this thesis, has been acquired. Figure 6.2 shows two virtual slices taken from the tomography where a) is a control sample (untreated) and b) a sample with trypsin injected. It demonstrates a clear loss of NP structure without notable changes to AF structure. These are similar changes as reported by Roberts *et al.* (2008) using histology. Future work on this data will include volumetric strain measurement (as performed in Chapter 4) which will be a fundamental study into the micro mechanical environment of disc degeneration and underpin structural and mechanical design criteria of replacement tissues. This will be

the first study comparing microstructural deformation between healthy and degenerated (*ex vivo* model) discs, where samples are kept intact enabling regional examination.

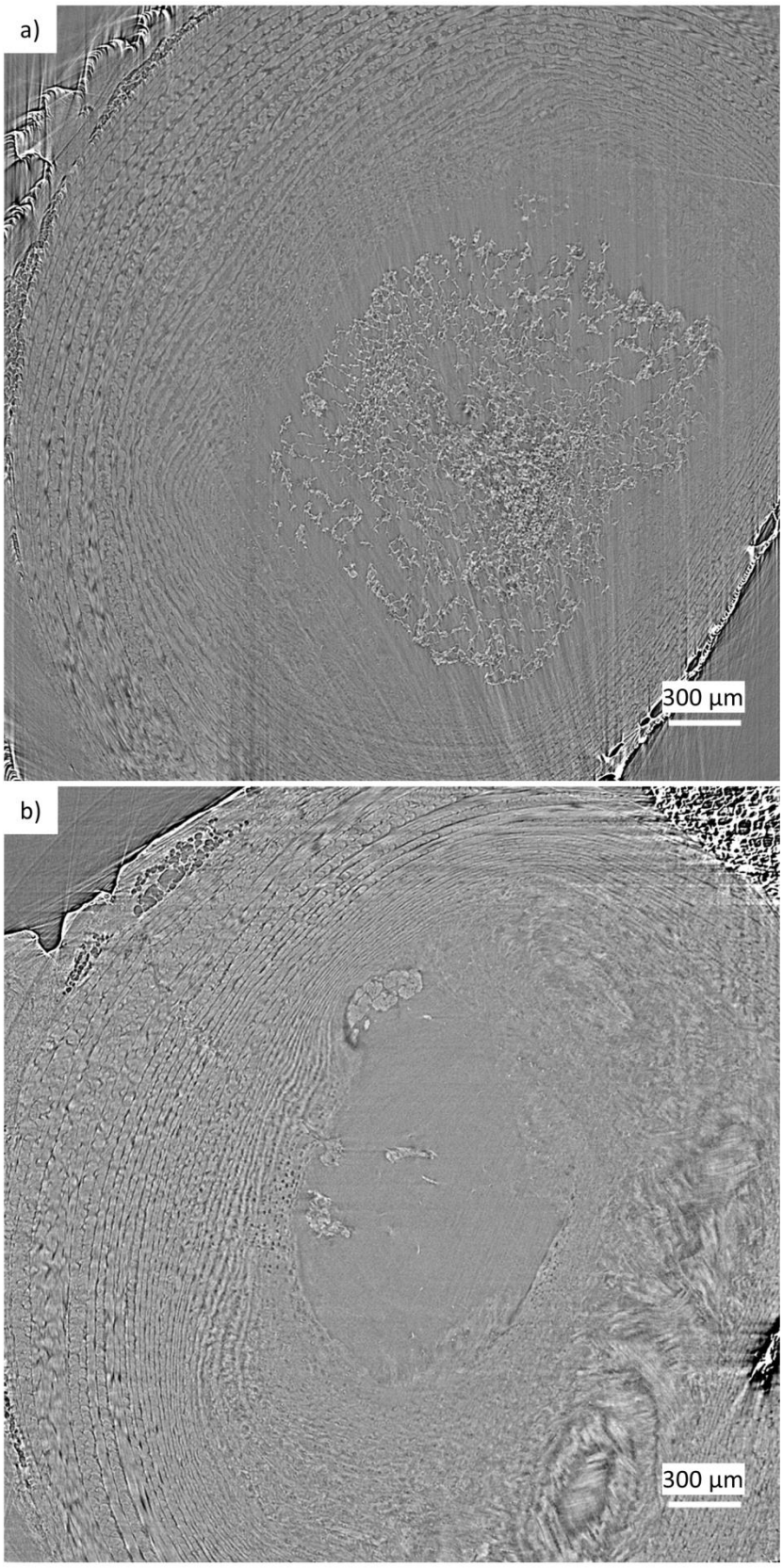

Figure 6.2 Ex vivo IVD degeneration study a) control sample b) sample with trypsin digested NP.

Needle injuries, alone, and created when injecting chemicals, such as enzymes, are used to model disc degeneration. Furthermore, tissue replacements and therapies for disc degeneration are being developed with a requirement for delivery by injection. It has been shown that larger needle injuries cause NP depressurisation which, in turn, changes IVD mechanics however, smaller needle injuries do not cause significant changes in gross mechanical testing (Elliott *et al.*, 2008). Despite no significant changes in disc mechanics, the local effect of needle injuries and how this affects mechanics at the tissue scale remains unknown. Therefore, future work using the imaging and analysis methods developed in this thesis will measure full-field volumetric strain of compressed samples to study local mechanical changes caused by injury of two different needle gauges (based on the work of Elliott *et al.* (2008)). Figure 6.3 gives example slices of the needle injuries and some microstructural changes induced after needle puncture. Although the smaller needle (33G) appears to self-seal, there is notable buckling and separation of lamella suggesting release of residual strain which may cause stress concentrations and eventual failure of the disc. Interlamellar fibres are visible (Figure 6.3f yellow arrows) which have previously been hypothesised to be critical to disc structural integrity (Tavakoli *et al.*, 2017). Analysis of this image data will provide information on the extent of needle damage at tissue level, predict whether needle injury will cause further complications and guide potential requirements for repair of needle injury if used in IVDD treatments.

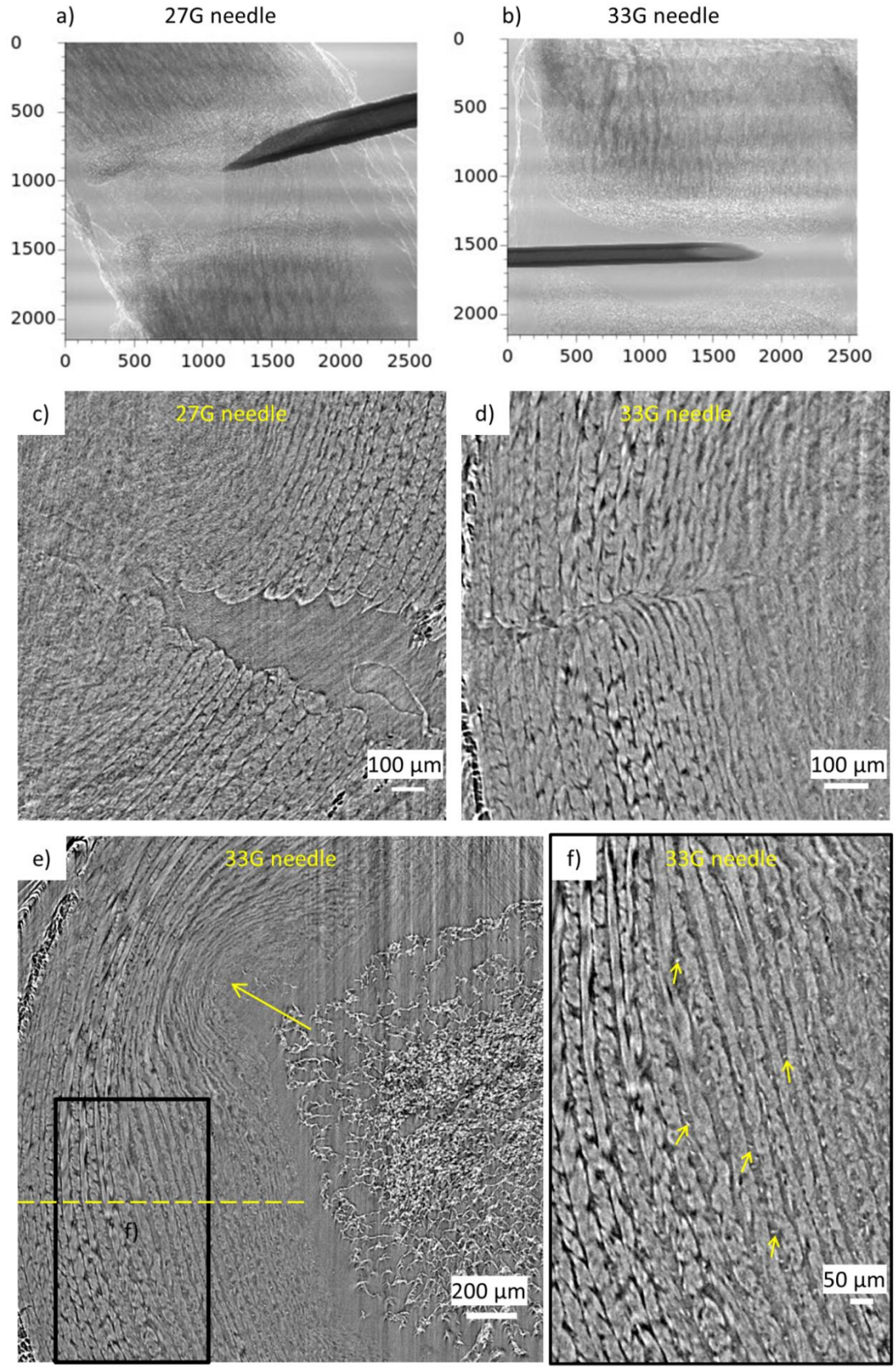

Figure 6.3 Needle injury study a) radiograph of 27 gauge needle inserted into posterior of the IVD b) radiograph of smaller 33 gauge needle inserted into posterior of the IVD c) & d) comparison of needle injuries e) buckling of lamellae (yellow arrow) positioned laterally to the need injury (yellow dashed line) f) Inter-lamella fibres (yellow arrows).

6.3 Conclusion

The experimental studies undertaken in this PhD successfully imaged the native intervertebral disc using microCT and measured volumetric strain at the micro scale providing an important framework for future studies of disc degeneration and needle injury. The long-term impact of the methodology developed in this thesis is to ultimately test tissue engineered replacements. Following the IVD degeneration and needle injury study, the next stage is to restore mechanical function based on knowledge of the degenerated micro mechanical environment and guidance on delivery.

7 References

ACKERMAN, J. E., BAH, I., JONASON, J. H., BUCKLEY, M. R. & LOISELLE, A. E. 2017. Aging does not alter tendon mechanical properties during homeostasis, but does impair flexor tendon healing. *Journal of Orthopaedic Research*.

ACOSTA SANTAMARÍA, V.A., FLECHAS GARCÍA, M., MOLIMARD, J. AND AVRIL, S. 2018. Three-Dimensional Full-Field Strain Measurements across a Whole Porcine Aorta Subjected to Tensile Loading Using Optical Coherence Tomography–Digital Volume Correlation. *Frontiers in Mechanical Engineering*, 4, p.3.

ADAMS, M., MCNALLY, D. & DOLAN, P. 1996. 'STRESS'DISTRIBUTIONS INSIDE INTERVERTEBRAL DISCS. *J Bone Joint Surg Br,* 78**,** 965-972.

ADAMS, M. A. 2015. Intervertebral Disc Tissues. *Mechanical Properties of Aging Soft Tissues.* Springer.

ADAMS, M. A. & DOLAN, P. 2012. Intervertebral disc degeneration: evidence for two distinct phenotypes. *Journal of anatomy,* 221**,** 497-506.

ADAMS, M. A. & ROUGHLEY, P. J. 2006. What is intervertebral disc degeneration, and what causes it? *Spine,* 31**,** 2151-2161.

ADNAN, K., ROBINSON, C., BIGGS, M., MORGAN, B., RUTTY, G., BORSEN, A., DIJKSTRA, J., KITSLAAR, P. & ADLAM, D. 2017. P2357Measurement of coronary artery compliance and stiffness index with novel application of optical coherence tomography in re-pressurised cadaveric coronary arteries. *European Heart Journal,* 38.

AGUIAR, D. J., JOHNSON, S. L. & OEGEMA JR, T. R. 1999. Notochordal cells interact with nucleus pulposus cells: regulation of proteoglycan synthesis. *Experimental cell research,* 246**,** 129-137.

ALLEN, W. M., CHIN, L., WIJESINGHE, P., KIRK, R. W., LATHAM, B., SAMPSON, D. D., SAUNDERS, C. M. & KENNEDY, B. F. 2016. Wide-field optical coherence micro-elastography for intraoperative assessment of human breast cancer margins. *Biomedical optics express,* 7**,** 4139-4153.

AMINI, S., MORTAZAVI, F., SUN, J., LEVESQUE, M., HOEMANN, C. D. & VILLEMURE, I. 2013. Stress relaxation of swine growth plate in semi-confined compression: depth dependent tissue deformational behavior versus extracellular matrix composition and collagen fiber organization. *Biomechanics and modeling in mechanobiology***,** 1-12.

APPEL, A. A., ANASTASIO, M. A., LARSON, J. C. & BREY, E. M. 2013. Imaging challenges in biomaterials and tissue engineering. *Biomaterials,* 34**,** 6615-6630.

ARGOUBI, M. & SHIRAZIADL, A. 1996. Poroelastic creep response analysis of a lumbar motion segment in compression. *Journal of Biomechanics,* 29**,** 1331-1339.

ATWOOD, R. C., BODEY, A. J., PRICE, S. W., BASHAM, M. & DRAKOPOULOS, M. 2015. A high-throughput system for high-quality tomographic reconstruction of large datasets at Diamond Light Source. *Philosophical Transactions of the Royal Society of London A: Mathematical, Physical and Engineering Sciences,* 373**,** 20140398.

BADEL, P., AVRIL, S., LESSNER, S. & SUTTON, M. 2012. Mechanical identification of layer-specific properties of mouse carotid arteries using 3D-DIC and a hyperelastic anisotropic constitutive model. *Computer methods in biomechanics and biomedical engineering,* 15**,** 37-48.

BALDIT, A., AMBARD, D., CHERBLANC, F. & ROYER, P. 2014. Experimental analysis of the transverse mechanical behaviour of annulus fibrosus tissue. *Biomechanics and Modeling in Mechanobiology,* 13**,** 643-652.

References

BALINT, R., LOWE, T. & SHEARER, T. 2016. Optimal contrast agent staining of ligaments and tendons for X-ray computed tomography. *PloS one,* 11**,** e0153552.

BARBIR, A., MICHALEK, A.J., ABBOTT, R.D. AND IATRIDIS, J.C. 2010. Effects of enzymatic digestion on compressive properties of rat intervertebral discs. *Journal of biomechanics*, 43(6), pp.1067-1073.

BARRETT, J. F. & KEAT, N. 2004. Artifacts in CT: recognition and avoidance. *Radiographics,* 24**,** 1679-1691.

BASHAM, M., FILIK, J., WHARMBY, M. T., CHANG, P. C., EL KASSABY, B., GERRING, M., AISHIMA, J., LEVIK, K., PULFORD, B. C. & SIKHARULIDZE, I. 2015. Data Analysis WorkbeNch (DAWN). *Journal of synchrotron radiation,* 22**,** 853-858.

BATTIÉ, M. C. & VIDEMAN, T. 2006. Lumbar disc degeneration: epidemiology and genetics. *JBJS,* 88**,** 3-9.

BATTIÉ, M. C., VIDEMAN, T., KAPRIO, J., GIBBONS, L. E., GILL, K., MANNINEN, H., SAARELA, J. & PELTONEN, L. 2009. The Twin Spine Study: contributions to a changing view of disc degeneration. *The Spine Journal,* 9**,** 47-59.

BAY, B. 2008. Methods and applications of digital volume correlation. *The Journal of Strain Analysis for Engineering Design,* 43**,** 745-760.

BAY, B. K. 1995. Texture correlation: a method for the measurement of detailed strain distributions within trabecular bone. *Journal of Orthopaedic Research,* 13**,** 258-267.

BAY, B. K., SMITH, T. S., FYHRIE, D. P. & SAAD, M. 1999. Digital volume correlation: three-dimensional strain mapping using X-ray tomography. *Experimental mechanics,* 39**,** 217-226.

BECKSTEIN, J. C., SEN, S., SCHAER, T. P., VRESILOVIC, E. J. & ELLIOTT, D. M. 2008. Comparison of animal discs used in disc research to human lumbar disc: axial compression mechanics and glycosaminoglycan content. *Spine,* 33**,** E166-E173.

BEDOLLA, D.E., MANTUANO, A., PICKLER, A., MOTA, C.L., BRAZ, D., SALATA, C., ALMEIDA, C.E., BIRARDA, G., VACCARI, L., BARROSO, R.C. AND GIANONCELLI, A. 2018. Effects of soft X-ray radiation damage on paraffin-embedded rat tissues supported on ultralene: a chemical perspective. *Journal of synchrotron radiation*, 25(3), pp.848-856.

BERSI, M. R., BELLINI, C., DI ACHILLE, P., HUMPHREY, J. D., GENOVESE, K. & AVRIL, S. 2016. Novel methodology for characterizing regional variations in the material properties of murine aortas. *Journal of biomechanical engineering,* 138**,** 071005.

BOAS, F. E. & FLEISCHMANN, D. 2011. Evaluation of Two Iterative Techniques for Reducing Metal Artifacts in Computed Tomography. *Radiology,* 259**,** 894-902.

BONSE, U. AND HART, M. 1965. An X-ray interferometer. *Applied Physics Letters*, 6(8), pp.155-156.

BOTSFORD, D., ESSES, S. & OGILVIE-HARRIS, D. 1994. *In vivo* diurnal variation in intervertebral disc volume and morphology. *Spine,* 19**,** 935-940.

BOXBERGER, J.I., ORLANSKY, A.S., SEN, S. AND ELLIOTT, D.M. 2009. Reduced nucleus pulposus glycosaminoglycan content alters intervertebral disc dynamic viscoelastic mechanics. *Journal of biomechanics*, 42(12), pp.1941-1946.

BRAY, J. P. & BURBIDGE, H. M. 1998. The canine intervertebral disk. Part Two: Degenerative changes--nonchondrodystrophoid versus chondrodystrophoid disks. *Journal of the American Animal Hospital Association,* 34**,** 135-144.

BROBERG, K.B. 1993. Slow deformation of intervertebral discs. *Journal of Biomechanics,* 26(4), pp.501-512.

References

BRUEHLMANN, S. B., MATYAS, J. R. & DUNCAN, N. A. 2004. ISSLS prize winner: collagen fibril sliding governs cell mechanics in the anulus fibrosus: an *in situ* confocal microscopy study of bovine discs. *Spine,* 29**,** 2612-2620.

BUCKWALTER, J.A., COOPER, R.R. AND MAYNARD, J.A. 1976. Elastic fibers in human intervertebral discs. *The Journal of bone and joint surgery. American volume*, 58(1), pp.73-76.

BUCKWALTER JA, PEDRINI-MILLE AN, PEDRINI VI, TUDISCO C. 1985. Proteoglycans of human infant intervertebral disc. Electron microscopic and biochemical studies. *The Journal of bone and joint surgery. American volume*, 67(2), pp.284-294.

BUTTERS, T.D., CASTRO, S.J., LOWE, T., ZHANG, Y., LEI, M., WITHERS, P.J. AND ZHANG, H. 2014. Optimal iodine staining of cardiac tissue for X-ray computed tomography. *PloS one*, 9(8), p.e105552.

CAO, Y., LIAO, S., ZENG, H., NI, S., TINTANI, F., HAO, Y., WANG, L., WU, T., LU, H. & DUAN, C. 2017. 3D characterization of morphological changes in the intervertebral disc and endplate during aging: A propagation phase contrast synchrotron micro-tomography study. *Scientific Reports,* 7**,** 43094.

CASSIDY, J., HILTNER, A. & BAER, E. 1989. Hierarchical structure of the intervertebral disc. *Connective tissue research,* 23**,** 75-88.

CAVINATO, C., HELFENSTEIN-DIDIER, C., OLIVIER, T., DU ROSCOAT, S. R., LAROCHE, N. & BADEL, P. 2017. Biaxial loading of arterial tissues with 3D *in situ* observations of adventitia fibrous microstructure: A method coupling multi-photon confocal microscopy and bulge inflation test. *Journal of the Mechanical Behavior of Biomedical Materials,* 74**,** 488-498.

CHAN, D. D., GOSSETT, P. C., BUTZ, K. D., NAUMAN, E. A. & NEU, C. P. 2014. Comparison of intervertebral disc displacements measured under applied loading with MRI at 3.0 T and 9.4 T. *Journal of Biomechanics,* 47**,** 2801-2806.

CHAN, D. D. & NEU, C. P. 2014. Intervertebral Disc Internal Deformation Measured by Displacements Under Applied Loading with MRI at 3T. *Magnetic Resonance in Medicine,* 71**,** 1231-1237.

CHAN, S. C. W., FERGUSON, S. J. & GANTENBEIN-RITTER, B. 2011. The effects of dynamic loading on the intervertebral disc. *European Spine Journal,* 20**,** 1796-1812.

CHANDRAN, P.L. AND HORKAY, F. 2012. Aggrecan, an unusual polyelectrolyte: review of solution behavior and physiological implications. *Acta biomaterialia*, 8(1), pp.3-12.

CHEUNG, K. M. C., KARPPINEN, J., CHAN, D., HO, D. W. H., SONG, Y.-Q., SHAM, P., CHEAH, K. S. E., LEONG, J. C. Y. & LUK, K. D. K. 2009. Prevalence and Pattern of Lumbar Magnetic Resonance Imaging Changes in a Population Study of One Thousand Forty-Three Individuals. *Spine,* 34**,** 934-940.

CHOI, H., TESSIER, S., SILAGI, E.S., KYADA, R., YOUSEFI, F., PLESHKO, N., SHAPIRO, I.M. AND RISBUD, M.V. 2018. A novel mouse model of intervertebral disc degeneration shows altered cell fate and matrix homeostasis. *Matrix Biology*.

COMPER, W.D. AND LAURENT, T.C. 1978. Physiological function of connective tissue polysaccharides. *Physiological reviews*, 58(1), pp.255-315.

COSTI, J. J., STOKES, I. A., GARDNER-MORSE, M. G. & IATRIDIS, J. C. 2008. Frequency-dependent behavior of the intervertebral disc in response to each of six degree of freedom dynamic loading: solid phase and fluid phase contributions. *Spine,* 33**,** 1731.

COUPPE, C., HANSEN, P., KONGSGAARD, M., KOVANEN, V., SUETTA, C., AAGAARD, P., KJAER, M. & MAGNUSSON, S. P. 2009. Mechanical properties

and collagen cross-linking of the patellar tendon in old and young men. *Journal of Applied Physiology,* 107**,** 880-886.

COX, P. G. & JEFFERY, N. 2011. Reviewing the Morphology of the Jaw-Closing Musculature in Squirrels, Rats, and Guinea Pigs with Contrast-Enhanced MicroCt. *The Anatomical Record,* 294**,** 915-928.

CRAIG, A.S., BIRTLES, M.J., CONWAY, J.F. AND PARRY, D.A. 1989. An estimate of the mean length of collagen fibrils in rat tail-tendon as a function of age. *Connective tissue research*, 19(1), pp.51-62.

DABBS, V. M. & DABBS, L. G. 1990. Correlation between disc height narrowing and low-back pain. *Spine,* 15**,** 1366-1368.

DAI, J., WANG, H., LIU, G., XU, Z., LI, F. & FANG, H. 2014. Dynamic compression and co-culture with nucleus pulposus cells promotes proliferation and differentiation of adipose-derived mesenchymal stem cells. *Journal of Biomechanics,* 47**,** 966-972.

DALL'ARA, E., PEÑA-FERNÁNDEZ, M., PALANCA, M., GIORGI, M., CRISTOFOLINI, L. & TOZZI, G. 2017. Precision of Digital Volume Correlation Approaches for Strain Analysis in Bone Imaged with Micro-Computed Tomography at Different Dimensional Levels. *Frontiers in Materials,* 4.

DAVID, C., NÖHAMMER, B., SOLAK, H. AND ZIEGLER, E. 2002. Differential x-ray phase contrast imaging using a shearing interferometer. *Applied physics letters*, 81(17), pp.3287-3289.

DAVIS, T.J., GAO, D., GUREYEV, T.E., STEVENSON, A.W. AND WILKINS, S.W., 1995. Phase-contrast imaging of weakly absorbing materials using hard X-rays. *Nature*, 373(6515), p.595.

DEGENHARDT, K., WRIGHT, A.C., HORNG, D., PADMANABHAN, A. AND EPSTEIN, J.A. 2010. Rapid three-dimensional phenotyping of cardiovascular development in mouse embryos by micro-CT with iodine staining. *Circulation: Cardiovascular Imaging*, pp.CIRCIMAGING-109.

DESCAMPS, E., SOCHACKA, A., DE KEGEL, B., VAN LOO, D., VAN HOOREBEKE, L. & ADRIAENS, D. 2014. Soft tissue discrimination with contrast agents using micro-CT scanning. *Belgian Journal of Zoology,* 144**,** 20-40.

DISNEY, C., LEE, P., HOYLAND, J., SHERRATT, M. & BAY, B. 2018. A review of techniques for visualising soft tissue microstructure deformation and quantifying strain *Ex vivo*. *Journal of microscopy*.

DISNEY, C., MADI, K., BODEY, A., LEE, P., HOYLAND, J. & SHERRATT, M. 2017. Visualising the 3D microstructure of stained and native intervertebral discs using X-ray microtomography. *Scientific Reports,* 7.

DOBRYNIN, A. V. & CARRILLO, J.-M. Y. 2010. Universality in nonlinear elasticity of biological and polymeric networks and gels. *Macromolecules,* 44**,** 140-146.

DUDAK, J., ZEMLICKA, J., KARCH, J., PATZELT, M., MRZILKOVA, J., ZACH, P., HERMANOVA, Z., KVACEK, J. & KREJCI, F. 2016. High-contrast X-ray micro-radiography and micro-CT of ex-vivo soft tissue murine organs utilizing ethanol fixation and large area photon-counting detector. *Scientific Reports,* 6.

EBERLEIN, R., HOLZAPFEL, G. A. & SCHULZE-BAUER, C. A. 2001. An anisotropic model for annulus tissue and enhanced finite element analyses of intact lumbar disc bodies. *Computer methods in biomechanics and biomedical engineering,* 4**,** 209-229.

ELLIOTT, D. M. & SETTON, L. A. 2001. Anisotropic and inhomogeneous tensile behavior of the human anulus fibrosus: Experimental measurement and material model predictions. *Journal of Biomechanical Engineering-Transactions of the Asme,* 123**,** 256-263.

ELLIOTT, D.M., YERRAMALLI, C.S., BECKSTEIN, J.C., BOXBERGER, J.I., JOHANNESSEN, W. AND VRESILOVIC, E.J. 2008. The effect of relative needle

diameter in puncture and sham injection animal models of degeneration. *Spine*, 33(6), pp.588-596.

EMANUEL, K.S., VERGROESEN, P.P., PEETERS, M., HOLEWIJN, R.M., KINGMA, I. AND SMIT, T.H. 2015. Poroelastic behaviour of the degenerating human intervertebral disc: a ten-day study in a loaded disc culture system. *Eur Cell Mater*, 29(29), pp.330-340.

EYRE, D. R. & MUIR, H. 1977. Quantitative analysis of types I and II collagens in human intervertebral discs at various ages. *Biochimica et Biophysica Acta (BBA)-Protein Structure,* 492**,** 29-42.

FANG, F. & LAKE, S. P. 2015. Multiscale strain analysis of tendon subjected to shear and compression demonstrates strain attenuation, fiber sliding, and reorganization. *Journal of Orthopaedic Research,* 33**,** 1704-1712.

FANG, F. & LAKE, S. P. 2017. Experimental evaluation of multiscale tendon mechanics. *Journal of Orthopaedic Research,* 35**,** 1353-1365.

FELDKAMP, L., DAVIS, L. & KRESS, J. 1984. Practical cone-beam algorithm. *JOSA A*, 1**,** 612-619.

FELDKAMP, L. A., GOLDSTEIN, S. A., PARFITT, M. A., JESION, G. & KLEEREKOPER, M. 1989. The direct examination of three-dimensional bone architecture *in vitro* by computed tomography. *Journal of bone and mineral research,* 4**,** 3-11.

FERGUSON, S. J., ITO, K. & NOLTE, L. P. 2004. Fluid flow and convective transport of solutes within the intervertebral disc. *Journal of Biomechanics,* 37**,** 213-221.

FERNÁNDEZ, M.P., CIPICCIA, S., DALL'ARA, E., BODEY, A.J., PARWANI, R., PANI, M., BLUNN, G.W., BARBER, A.H. AND TOZZI, G. 2018a. Effect of SR-microCT radiation on the mechanical integrity of trabecular bone using in situ mechanical testing and digital volume correlation. *Journal of the mechanical behavior of biomedical materials*, 88, pp.109-119.

FERNÁNDEZ, M.P., DALL'ARA, E., KAO, A., BODEY, A., KARALI, A., BLUNN, G., BARBER, A. AND TOZZI, G. 2018. Preservation of bone tissue integrity with temperature control for in situ SR-MicroCT experiments. *Materials*, 11(11), p.2155.

FERNÁNDEZ, M., KEYRILÄINEN, J., SERIMAA, R., TORKKELI, M., KARJALAINEN-LINDSBERG, M.L., TENHUNEN, M., THOMLINSON, W., URBAN, V. AND SUORTTI, P. 2002. Small-angle x-ray scattering studies of human breast tissue samples. *Physics in Medicine & Biology*, 47(4), p.577.

FESSEL, G., LI, Y., DIEDERICH, V., GUIZAR-SICAIROS, M., SCHNEIDER, P., SELL, D. R., MONNIER, V. M. & SNEDEKER, J. G. 2014. Advanced glycation end-products reduce collagen molecular sliding to affect collagen fibril damage mechanisms but not stiffness. *PloS one,* 9**,** e110948.

FRANZ, J. R., SLANE, L. C., RASSKE, K. & THELEN, D. G. 2015. Non-uniform *in vivo* deformations of the human Achilles tendon during walking. *Gait & posture,* 41**,** 192-197.

FROBIN, W., BRINCKMANN, P., KRAMER, M. & HARTWIG, E. 2001. Height of lumbar discs measured from radiographs compared with degeneration and height classified from MR images. *European radiology,* 11**,** 263-269.

FU, J., PIERRON, F. & RUIZ, P. D. 2013. Elastic stiffness characterization using three-dimensional full-field deformation obtained with optical coherence tomography and digital volume correlation. *Journal of biomedical optics,* 18**,** 121512-121512.

GARDNER-MORSE, M.G. AND STOKES, I.A. 2003. Physiological axial compressive preloads increase motion segment stiffness, linearity and hysteresis in all six degrees of freedom for small displacements about the neutral posture. Journal of Orthopaedic Research, 21(3), pp.547-552.

References

GASSER, T. C., OGDEN, R. W. & HOLZAPFEL, G. A. 2006. Hyperelastic modelling of arterial layers with distributed collagen fibre orientations. *Journal of the royal society interface,* 3**,** 15-35.

GENOVESE, K. 2009. A video-optical system for time-resolved whole-body measurement on vascular segments. *Optics and Lasers in Engineering,* 47**,** 995-1008.

GENOVESE, K., LEE, Y., LEE, A. & HUMPHREY, J. 2013. An improved panoramic digital image correlation method for vascular strain analysis and material characterization. *Journal of the mechanical behavior of biomedical materials,* 27**,** 132-142.

GIGNAC, P. M. & KLEY, N. J. 2014. Iodine-enhanced micro-CT imaging: Methodological refinements for the study of the soft-tissue anatomy of post-embryonic vertebrates. *Journal of Experimental Zoology Part B: Molecular and Developmental Evolution,* 322**,** 166-176.

GOH, K., HOLMES, D., LU, H.-Y., RICHARDSON, S., KADLER, K., PURSLOW, P. & WESS, T. 2008. Ageing changes in the tensile properties of tendons: influence of collagen fibril volume fraction. *Journal of biomechanical engineering,* 130**,** 021011.

GRAHAM, H. K., AKHTAR, R., KRIDIOTIS, C., DERBY, B., KUNDU, T., TRAFFORD, A. W. & SHERRATT, M. J. 2011. Localised micro-mechanical stiffening in the ageing aorta. *Mechanisms of ageing and development,* 132**,** 459-467.

GREGORY, D. E. & CALLAGHAN, J. P. 2012. An examination of the mechanical properties of the annulus fibrosus: The effect of vibration on the intra-lamellar matrix strength. *Medical Engineering & Physics,* 34**,** 472-477.

GRUBER, H.E., ASHRAF, N., KILBURN, J., WILLIAMS, C., NORTON, H.J., GORDON, B.E. AND HANLEY JR, E.N. 2005. Vertebral endplate architecture and vascularization: application of micro-computerized tomography, a vascular tracer, and immunocytochemistry in analyses of disc degeneration in the aging sand rat. *Spine,* 30(23), pp.2593-2600.

GRUBER, H.E., JOHNSON, T., NORTON, H.J. AND HANLEY JR, E.N. 2002. The sand rat model for disc degeneration: radiologic characterization of age-related changes: cross-sectional and prospective analyses. *Spine,* 27(3), pp.230-234.

GUERIN, H. A. L. & ELLIOTT, D. M. 2006. Degeneration affects the fiber reorientation of human annulus fibrosus under tensile load. *Journal of biomechanics,* 39**,** 1410-1418.

GUERIN, H. L. & ELLIOTT, D. M. 2007. Ouantifying the contributions of structure to annulus fibrosus mechanical function using a nonlinear, anisotropic, hyperelastic model. *Journal of Orthopaedic Research,* 25**,** 508-516.

GULLBRAND, S. E., ASHINSKY, B. G., MARTIN, J. T., PICKUP, S., SMITH, L. J., MAUCK, R. L. & SMITH, H. E. 2016. Correlations between quantitative T2 and T1ρ MRI, mechanical properties and biochemical composition in a rabbit lumbar intervertebral disc degeneration model. *Journal of Orthopaedic Research,* 34**,** 1382-1388.

GUPTA, H., SETO, J., KRAUSS, S., BOESECKE, P. & SCREEN, H. 2010. *In situ* multi-level analysis of viscoelastic deformation mechanisms in tendon collagen. *Journal of structural biology,* 169**,** 183-191.

HAN, S. K., CHEN, C.-W., LABUS, K. M., PUTTLITZ, C. M., CHEN, Y. & HSIEH, A. H. 2016a. Optical coherence tomographic elastography reveals mesoscale shear strain inhomogeneities in the annulus fibrosus. *Spine,* 41**,** E770.

HAN, S. K., CHEN, C. W., WIERWILLE, J., CHEN, Y. & HSIEH, A. H. 2015. Three dimensional mesoscale analysis of translamellar cross-bridge morphologies in the

annulus fibrosus using optical coherence tomography. *Journal of Orthopaedic Research*.

HAN, W. M., HEO, S.-J., DRISCOLL, T. P., DELUCCA, J. F., MCLEOD, C. M., SMITH, L. J., DUNCAN, R. L., MAUCK, R. L. & ELLIOTT, D. M. 2016b. Microstructural Heterogeneity in Native and Engineered Fibrocartilage Directs Micromechanics and Mechanobiology. *Nature materials,* 15**,** 477.

HAN, W. M., HEO, S.-J., DRISCOLL, T. P., SMITH, L. J., MAUCK, R. L. & ELLIOTT, D. M. 2013. Macro- to Microscale Strain Transfer in Fibrous Tissues is Heterogeneous and Tissue-Specific. *Biophysical Journal,* 105**,** 807-817.

HAPPEL, C. M., KLOSE, C., WITTON, G., ANGRISANI, G. L., WIENECKE, S., GROOS, S., BACH, F.-W., BORMANN, D., MÄNNER, J. & YELBUZ, T. M. 2010. Non-Destructive, High-Resolution 3-Dimensional Visualization of a Cardiac Defect in the Chick Embryo Resembling Complex Heart Defect in Humans Using Micro-Computed Tomography Double Outlet Right Ventricle With Left Juxtaposition of Atrial Appendages. *Circulation,* 122**,** e561-e564.

HAYASHI, K. & HIRAYAMA, E. 2017. Age-related changes of wall composition and collagen cross-linking in the rat carotid artery–In relation with arterial mechanics. *Journal of the mechanical behavior of biomedical materials,* 65**,** 881-889.

HEINDEL, P., TUCHMAN, A., HSIEH, P. C., PHAM, M. H., D'ORO, A., PATEL, N. N., JAKOI, A. M., HAH, R., LIU, J. C., BUSER, Z. & WANG, J. C. 2017. Reoperation Rates After Single-level Lumbar Discectomy. *Spine,* 42**,** E496-E501.

HELFENSTEIN-DIDIER, C., TAÏNOFF, D., VIVILLE, J., ADRIEN, J., MAIRE, É. & BADEL, P. 2017. Tensile rupture of medial arterial tissue studied by X-ray micro-tomography on stained samples. *Journal of the Mechanical Behavior of Biomedical Materials*.

HERMAN, G. T. 2009. *Fundamentals of computerized tomography: image reconstruction from projections*, Springer Science & Business Media.

HICKEY, D. S. & HUKINS, D. W. 1979. Effect of methods of preservation on the arrangement of collagen fibrils in connective tissue matrices: an x-ray diffraction study of annulus fibrosus. *Connective tissue research,* 6**,** 223-228.

HOLMES, D.F., LU, Y., STARBORG, T. AND KADLER, K.E., 2018. Collagen Fibril Assembly and Function. *In Current topics in developmental biology (Vol. 130, pp. 107-142). Academic Press*.

HOLZAPFEL, G. A., SCHULZE-BAUER, C., FEIGL, G. & REGITNIG, P. 2005. Single lamellar mechanics of the human lumbar anulus fibrosus. *Biomechanics and modeling in mechanobiology,* 3**,** 125-140.

HORTON, W. 1958. Further observations on the elastic mechanism of the intervertebral disc. *Journal of Bone & Joint Surgery, British Volume,* 40**,** 552-557.

HOY, D., MARCH, L., BROOKS, P., BLYTH, F., WOOLF, A., BAIN, C., WILLIAMS, G., SMITH, E., VOS, T. & BARENDREGT, J. 2014. The global burden of low back pain: estimates from the Global Burden of Disease 2010 study. *Annals of the rheumatic diseases,* 73**,** 968-974.

HUANG, C.-Y. & GU, W. Y. 2008. Effects of mechanical compression on metabolism and distribution of oxygen and lactate in intervertebral disc. *Journal of biomechanics,* 41**,** 1184-1196.

HUMZAH, M. & SOAMES, R. 1988. Human intervertebral disc: structure and function. *The Anatomical Record,* 220**,** 337-356.

IATRIDIS, J.C., SETTON, L.A., FOSTER, R.J., RAWLINS, B.A., WEIDENBAUM, M. AND MOW, V.C. 1998. Degeneration affects the anisotropic and nonlinear behaviors of human anulus fibrosus in compression. *Journal of biomechanics*, 31(6), pp.535-544.

References

IATRIDIS, J. C., SETTON, L. A., WEIDENBAUM, M. & MOW, V. C. 1997. The viscoelastic behavior of the non-degenerate human lumbar nucleus pulposus in shear. *Journal of Biomechanics,* 30**,** 1005-1013.

IATRIDIS, J.C., WEIDENBAUM, M., SETTON, L.A. AND MOW, V.C. 1996. Is the nucleus pulposus a solid or a fluid? Mechanical behaviors of the nucleus pulposus of the human intervertebral disc. *Spine*, 21(10), pp.1174-1184.

INAMDAR, S. R., KNIGHT, D. P., TERRILL, N. J., KARUNARATNE, A., CACHO-NERIN, F., KNIGHT, M. M. & GUPTA, H. S. 2017. The secret life of collagen: temporal changes in nanoscale fibrillar pre-strain and molecular organization during physiological loading of cartilage. *ACS nano,* 11**,** 9728-9737.

INOUE, H. 1973. Three-dimensional observation of collagen framework of intervertebral discs in rats, dogs and humans. *Archivum histologicum japonicum,* 36**,** 39-56.

INOUE, H. 1981. Three-dimensional architecture of lumbar intervertebral discs. Spine, 6(2), pp.139-146.

IWAGUCHI, T., FUNATOMI, T., KUBO, H. & MUKAIGAWA, Y. 2016. Light path alignment for computed tomography of scattering material. *IPSJ Transactions on Computer Vision and Applications,* 8**,** 2.

JAUMARD, N. V., LEUNG, J., GOKHALE, A. J., GUARINO, B. B., WELCH, W. C. & WINKELSTEIN, B. A. 2015. Relevant Anatomic and Morphological Measurements of the Rat Spine. *Spine,* 40**,** E1084-E1092.

JEFFERY, N. S., STEPHENSON, R. S., GALLAGHER, J. A., JARVIS, J. C. & COX, P. G. 2011. Micro-computed tomography with iodine staining resolves the arrangement of muscle fibres. *Journal of biomechanics,* 44**,** 189-192.

JIANG, Y., TONG, Y., XIAO, T. & LU, S. 2012. Phase-contrast microtomography with synchrotron radiation technology: A new noninvasive technique to analyze the three-dimensional structure of dermal tissues. *Dermatology,* 225**,** 75-80.

JOHNSON, E.F., CHETTY, K., MOORE, I.M., STEWART, A. AND JONES, W. 1982. The distribution and arrangement of elastic fibres in the intervertebral disc of the adult human. *Journal of anatomy*, 135(Pt 2), p.301.

JOHNSTONE, B. AND BAYLISS, M.T. 1995. The large proteoglycans of the human intervertebral disc. Changes in their biosynthesis and structure with age, topography, and pathology. *Spine,* 20(6), pp.674-684.

KALAF, E. A. G., SELL, S. A. & BLEDSOE, J. G. 2014. Developing a Mechanical and Chemical Model of Degeneration in Young Bovine Lumbar Intervertebral Disks and Reversing Loss in Mechanical Function. *Journal of Spinal Disorders & Techniques,* 27**,** E168-E175.

KALSON, N., MALONE, P., BRADLEY, R., WITHERS, P. & LEES, V. 2012. Fibre bundles in the human extensor carpi ulnaris tendon are arranged in a spiral. *Journal of Hand Surgery (European Volume),* 37**,** 550-554.

KARAKOLIS, T. & CALLAGHAN, J. P. 2015. Localized strain measurements of the intervertebral disc annulus during biaxial tensile testing. *Computer methods in biomechanics and biomedical engineering,* 18**,** 1737-1743.

KAVIANI, R., LONDONO, I., PARENT, S., MOLDOVAN, F. & VILLEMURE, I. 2016. Growth plate cartilage shows different strain patterns in response to static versus dynamic mechanical modulation. *Biomechanics and modeling in mechanobiology,* 15**,** 933-946.

KENNEDY, B. F., MCLAUGHLIN, R. A., KENNEDY, K. M., CHIN, L., CURATOLO, A., TIEN, A., LATHAM, B., SAUNDERS, C. M. & SAMPSON, D. D. 2014. Optical coherence micro-elastography: mechanical-contrast imaging of tissue microstructure. *Biomedical optics express,* 5**,** 2113-2124.

KENNEDY, B. F., MCLAUGHLIN, R. A., KENNEDY, K. M., CHIN, L., WIJESINGHE, P., CURATOLO, A., TIEN, A., RONALD, M., LATHAM, B. & SAUNDERS, C.

References

M. 2015. Investigation of optical coherence microelastography as a method to visualize cancers in human breast tissue. *Cancer Research,* 75**,** 3236-3245.

KEYES, D. C. & COMPERE, E. L. 1932. The normal and pathological physiology of the nucleus pulposus of the intervertebral disc: an anatomical, clinical, and experimental study. *JBJS,* 14**,** 897-938.

KIM, J.-H., AVRIL, S., DUPREY, A. & FAVRE, J.-P. 2012. Experimental characterization of rupture in human aortic aneurysms using a full-field measurement technique. *Biomechanics and modeling in mechanobiology,* 11**,** 841-853.

KLEIN, J. A. & WL, H. D. 1982. Collagen fibre orientation in the annulus fibrosus of intervertebral disc during bending and torsion measured by X-ray diffraction. *Biochimica et Biophysica Acta (BBA)-General Subjects,* 719**,** 98-101.

KOBIELARZ, M., SZOTEK, S., GŁOWACKI, M., DAWIDOWICZ, J. AND PEZOWICZ, C. 2016. Qualitative and quantitative assessment of collagen and elastin in annulus fibrosus of the physiologic and scoliotic intervertebral discs. *Journal of the mechanical behavior of biomedical materials*, 62, pp.45-56.

KRAEMER, J. 1985. Dynamic characteristics of the vertebral column, effects of prolonged loading. *Ergonomics,* 28**,** 95-97.

KRASNY, W., MORIN, C., MAGOARIEC, H. & AVRIL, S. 2017. A comprehensive study of layer-specific morphological changes in the microstructure of carotid arteries under uniaxial load. *Acta Biomaterialia*.

KROEBER, M. W., UNGLAUB, F., WANG, H., SCHMID, C., THOMSEN, M., NERLICH, A. & RICHTER, W. 2002. New *in vivo* animal model to create intervertebral disc degeneration and to investigate the effects of therapeutic strategies to stimulate disc regeneration. *Spine,* 27**,** 2684-2690.

LAKE, S. P., MILLER, K. S., ELLIOTT, D. M. & SOSLOWSKY, L. J. 2009. Effect of fiber distribution and realignment on the nonlinear and inhomogeneous mechanical properties of human supraspinatus tendon under longitudinal tensile loading. *Journal of Orthopaedic Research,* 27**,** 1596-1602.

LAMOUCHE, G., KENNEDY, B. F., KENNEDY, K. M., BISAILLON, C.-E., CURATOLO, A., CAMPBELL, G., PAZOS, V. & SAMPSON, D. D. 2012. Review of tissue simulating phantoms with controllable optical, mechanical and structural properties for use in optical coherence tomography. *Biomedical optics express,* 3**,** 1381-1398.

LARIN, K. V. & SAMPSON, D. D. 2017. Optical coherence elastography–OCT at work in tissue biomechanics. *Biomedical optics express,* 8**,** 1172-1202.

LEKIEN, F. AND MARSDEN, J. 2005. Tricubic interpolation in three dimensions. *International Journal for Numerical Methods in Engineering*, 63(3), pp.455-471.

LEPAGE, W. S., DALY, S. H. & SHAW, J. A. 2016. Cross polarization for improved digital image correlation. *Experimental Mechanics,* 56**,** 969-985.

LIONELLO, G., SIRIEIX, C. & BALEANI, M. 2014. An effective procedure to create a speckle pattern on biological soft tissue for digital image correlation measurements. *Journal of the mechanical behavior of biomedical materials,* 39**,** 1-8.

LOCKE, R. C., PELOQUIN, J. M., LEMMON, E. A., SZOSTEK, A., ELLIOTT, D. M. & KILLIAN, M. L. 2017. Strain Distribution of Intact Rat Rotator Cuff Tendon-to-Bone Attachments and Attachments With Defects. *Journal of Biomechanical Engineering,* 139**,** 111007.

LUDWINSKI, F. E., GNANALINGHAM, K., RICHARDSON, S. M. & HOYLAND, J. A. 2013. Understanding the native nucleus pulposus cell phenotype has important implications for intervertebral disc regeneration strategies. *Regenerative medicine,* 8**,** 75-87.

References

MADI, K., TOZZI, G., ZHANG, Q., TONG, J., COSSEY, A., AU, A., HOLLIS, D. & HILD, F. 2013. Computation of full-field displacements in a scaffold implant using digital volume correlation and finite element analysis. *Medical engineering & physics,* 35**,** 1298-1312.

MALANDRINO, A., NOAILLY, J. & LACROIX, D. 2014. Numerical exploration of the combined effect of nutrient supply, tissue condition and deformation in the intervertebral disc. *Journal of Biomechanics,* 47**,** 1520-1525.

MALLETT, K. F. & ARRUDA, E. M. 2017. Digital image correlation-aided mechanical characterization of the anteromedial and posterolateral bundles of the anterior cruciate ligament. *Acta Biomaterialia*.

MANIADAKIS, N. & GRAY, A. 2000. The economic burden of back pain in the UK. *Pain,* 84**,** 95-103.

MARCHAND, F. & AHMED, A. M. 1990. Investigation of the laminate structure of lumbar disc anulus fibrosus. *Spine,* 15**,** 402-410.

MARINI, G., HUBER, G., PUESCHEL, K. & FERGUSON, S. J. 2015. Nonlinear dynamics of the human lumbar intervertebral disc. *Journal of Biomechanics,* 48**,** 479-488.

MARTIN, C., SUN, W., PRIMIANO, C., MCKAY, R. & ELEFTERIADES, J. 2013. Age-dependent ascending aorta mechanics assessed through multiphase CT. *Annals of biomedical engineering,* 41**,** 2565-2574.

MCDONALD, S.A., MARONE, F., HINTERMÜLLER, C., MIKULJAN, G., DAVID, C., PFEIFFER, F. AND STAMPANONI, M. 2009. Advanced phase-contrast imaging using a grating interferometer. *Journal of synchrotron radiation*, 16(4), pp.562-572.

MCNALLY, D. & ADAMS, M. 1992. Internal intervertebral disc mechanics as revealed by stress profilometry. *Spine,* 17**,** 66-73.

MELROSE, J., GHOSH, P. AND TAYLOR, T.K. 2001. A comparative analysis of the differential spatial and temporal distributions of the large (aggrecan, versican) and small (decorin, biglycan, fibromodulin) proteoglycans of the intervertebral disc. *The Journal of Anatomy*, 198(1), pp.3-15.

MELROSE, J., SMITH, S. M., APPLEYARD, R. C. & LITTLE, C. B. 2008. Aggrecan, versican and type VI collagen are components of annular translamellar crossbridges in the intervertebral disc. *European Spine Journal,* 17**,** 314-324.

MENGONI, M., LUXMOORE, B. J., WIJAYATHUNGA, V. N., JONES, A. C., BROOM, N. D. & WILCOX, R. K. 2015. Derivation of inter-lamellar behaviour of the intervertebral disc annulus. *Journal of the mechanical behavior of biomedical materials,* 48**,** 164-172.

METSCHER, B. D. 2009a. MicroCT for comparative morphology: simple staining methods allow high-contrast 3D imaging of diverse non-mineralized animal tissues. *BMC physiology,* 9**,** 11.

METSCHER, B. D. 2009b. MicroCT for developmental biology: A versatile tool for high-contrast 3D imaging at histological resolutions. *Developmental Dynamics,* 238**,** 632-640.

MICHALEK, A. J., BUCKLEY, M. R., BONASSAR, L. J., COHEN, I. & IATRIDIS, J. C. 2009. Measurement of local strains in intervertebral disc anulus fibrosus tissue under dynamic shear: Contributions of matrix fiber orientation and elastin content. *Journal of Biomechanics,* 42**,** 2279-2285.

MICHALEK, A. J., BUCKLEY, M. R., BONASSAR, L. J., COHEN, I. & IATRIDIS, J. C. 2010. The effects of needle puncture injury on microscale shear strain in the intervertebral disc annulus fibrosus. *The Spine Journal,* 10**,** 1098-1105.

MICHALEK, A. J., GARDNER-MORSE, M. G. & IATRIDIS, J. C. 2012. Large residual strains are present in the intervertebral disc annulus fibrosus in the unloaded state. *Journal of Biomechanics,* 45**,** 1227-1231.

References

MILLER, J.A., SCHMATZ, C. AND SCHULTZ, A.B. 1988. Lumbar disc degeneration: correlation with age, sex, and spine level in 600 autopsy specimens. *Spine,* 13(2), pp.173-178.

MIZUTANI, R. & SUZUKI, Y. 2012. X-ray microtomography in biology. *Micron,* 43**,** 104-115.

MIZUTANI, R., TAKEUCHI, A., UESUGI, K., TAKEKOSHI, S., OSAMURA, R. Y. & SUZUKI, Y. 2008. X-ray microtomographic imaging of three-dimensional structure of soft tissues. *Tissue Engineering Part C: Methods,* 14**,** 359-363.

MOKSO, R., MARONE, F., HABERTHÜR, D., SCHITTNY, J., MIKULJAN, G., ISENEGGER, A. & STAMPANONI, M. Following dynamic processes by X-ray tomographic microscopy with sub-second temporal resolution. AIP conference proceedings, 2011. AIP, 38-41.

MOMOSE, A., TAKEDA, T., ITAI, Y. & HIRANO, K. 1996. Phase-contrast X-ray computed tomography for observing biological soft tissues. *Nature medicine***,** 473-5.

MOMOSE, A. 1995. Demonstration of phase-contrast X-ray computed tomography using an X-ray interferometer. *Nuclear Instruments and Methods in Physics Research Section A: Accelerators, Spectrometers, Detectors and Associated Equipment*, 352(3), pp.622-628.

MOSKOWITZ, R. W., ZIV, I., DENKO, C. W., BOJA, B., JONES, P. K. & ADLER, J. H. 1990. Spondylosis in sand rats: a model of intervertebral disc degeneration and hyperostosis. *Journal of Orthopaedic Research,* 8**,** 401-411.

MURIUKI, M.G., HAVEY, R.M., VORONOV, L.I., CARANDANG, G., ZINDRICK, M.R., LORENZ, M.A., LOMASNEY, L. AND PATWARDHAN, A.G. 2016. Effects of motion segment level, Pfirrmann intervertebral disc degeneration grade and gender on lumbar spine kinematics. *Journal of Orthopaedic Research,* 34(8), pp.1389-1398.

MÄÄTTÄ, J. H., KRAATARI, M., WOLBER, L., NIINIMÄKI, J., WADGE, S., KARPPINEN, J. & WILLIAMS, F. M. 2014. Vertebral endplate change as a feature of intervertebral disc degeneration: a heritability study. *European Spine Journal,* 23**,** 1856-1862.

NACHEMSON, A. 1963. The influence of spinal movements on the lumbar intradiscal pressure and on the tensile stresses in the annulus fibrosus. *Acta Orthopaedica Scandinavica,* 33**,** 183-207.

NACHEMSON, A., LEWIN, T., MAROUDAS, A. AND FREEMAN, M.A.R. 1970. In vitro diffusion of dye through the end-plates and the annulus fibrosus of human lumbar inter-vertebral discs. *Acta Orthopaedica Scandinavica,* 41(6), pp.589-607.

NAHAS, A., BAUER, M., ROUX, S. & BOCCARA, A. C. 2013. 3D static elastography at the micrometer scale using Full Field OCT. *Biomedical optics express,* 4**,** 2138-2149.

NAISH, J. & COURT, D. S. 2014. *Medical Sciences*, Elsevier Health Sciences UK.

NAP, R.J. AND SZLEIFER, I. 2008. Structure and interactions of aggrecans: statistical thermodynamic approach. *Biophysical journal*, 95(10), pp.4570-4583.

NAVEH, G. R., BRUMFELD, V., DEAN, M., SHAHAR, R. & WEINER, S. 2014. Direct MicroCT imaging of non-mineralized connective tissues at high resolution. *Connective tissue research,* 55**,** 52-60.

NEIDLINGER-WILKE, C., GALBUSERA, F., PRATSINIS, H., MAVROGONATOU, E., MIETSCH, A., KLETSAS, D. & WILKE, H.-J. 2014. Mechanical loading of the intervertebral disc: from the macroscopic to the cellular level. *European Spine Journal,* 23**,** 333-343.

NERURKAR, N. L., ELLIOTT, D. M. & MAUCK, R. L. 2010. Mechanical design criteria for intervertebral disc tissue engineering. *Journal of Biomechanics,* 43**,** 1017-1030.

References

NEWELL, N., LITTLE, J., CHRISTOU, A., ADAMS, M., ADAM, C. & MASOUROS, S. 2017. Biomechanics of the human intervertebral disc: a review of testing techniques and results. *Journal of the mechanical behavior of biomedical materials*.

NIEMINEN, H. J., YLITALO, T., KARHULA, S., SUURONEN, J.-P., KAUPPINEN, S., SERIMAA, R., HÆGGSTRÖM, E., PRITZKER, K. P., VALKEALAHTI, M. & LEHENKARI, P. 2015. Determining Collagen Distribution in Articular Cartilage Using Contrast-Enhanced Micro-Computed Tomography. *Osteoarthritis and Cartilage*.

NIERENBERGER, M., RÉMOND, Y., AHZI, S. & CHOQUET, P. 2015. Assessing the three-dimensional collagen network in soft tissues using contrast agents and high resolution micro-CT: application to porcine iliac veins. *Comptes Rendus Biologies*.

NING, J., XU, S., WANG, Y., LESSNER, S. M., SUTTON, M. A., ANDERSON, K. & BISCHOFF, J. E. 2010. Deformation measurements and material property estimation of mouse carotid artery using a microstructure-based constitutive model. *Journal of biomechanical engineering,* 132**,** 121010.

NOAILLY, J., PLANELL, J. A. & LACROIX, D. 2011. On the collagen criss-cross angles in the annuli fibrosi of lumbar spine finite element models. *Biomechanics and modeling in mechanobiology,* 10**,** 203-219.

O'CONNELL, G. D., JACOBS, N. T., SEN, S., VRESILOVIC, E. J. & ELLIOTT, D. M. 2011a. Axial creep loading and unloaded recovery of the human intervertebral disc and the effect of degeneration. *Journal of the Mechanical Behavior of Biomedical Materials,* 4**,** 933-942.

O'CONNELL, G. D., JOHANNESSEN, W., VRESILOVIC, E. J. & ELLIOTT, D. M. 2007. Human internal disc strains in axial compression measured noninvasively using magnetic resonance imaging. *Spine,* 32**,** 2860-2868.

O'CONNELL, G. D., VRESILOVIC, E. J. & ELLIOTT, D. M. 2011b. Human Intervertebral Disc Internal Strain in Compression: The Effect of Disc Region, Loading Position, and Degeneration. *Journal of Orthopaedic Research,* 29**,** 547-555.

O'CONNELL, M. K., MURTHY, S., PHAN, S., XU, C., BUCHANAN, J., SPILKER, R., DALMAN, R. L., ZARINS, C. K., DENK, W. & TAYLOR, C. A. 2008. The three-dimensional micro-and nanostructure of the aortic medial lamellar unit measured using 3D confocal and electron microscopy imaging. *Matrix Biology,* 27**,** 171-181.

O'CONNELL, G. D., VRESILOVIC, E. J. & ELLIOTT, D. M. 2007. Comparison of animals used in disc research to human lumbar disc geometry. *Spine,* 32**,** 328-333.

PAGANIN, D., MAYO, S., GUREYEV, T. E., MILLER, P. R. & WILKINS, S. W. 2002. Simultaneous phase and amplitude extraction from a single defocused image of a homogeneous object. *Journal of microscopy,* 206**,** 33-40.

PALANCA, M., BODEY, A. J., GIORGI, M., VICECONTI, M., LACROIX, D., CRISTOFOLINI, L. & DALL'ARA, E. 2017. Local displacement and strain uncertainties in different bone types by digital volume correlation of synchrotron microtomograms. *Journal of Biomechanics*.

PAN, B., QIAN, K., XIE, H. AND ASUNDI, A. 2009. Two-dimensional digital image correlation for in-plane displacement and strain measurement: a review. *Measurement science and technology*, 20(6), p.062001.

PAN, B., XIE, H., GUO, Z. AND HUA, T. 2007. Full-field strain measurement using a two-dimensional Savitzky-Golay digital differentiator in digital image correlation. *Optical Engineering*, 46(3), p.033601.

PANJABI, M. M., OXLAND, T., YAMAMOTO, I. & CRISCO, J. 1994. Mechanical behavior of the human lumbar and lumbosacral spine as shown by three-dimensional load-displacement curves. *JBJS,* 76**,** 413-424.

References

PARRY, D.A.D., BARNES, G.R.G. AND CRAIG, A.S. 1978. A comparison of the size distribution of collagen fibrils in connective tissues as a function of age and a possible relation between fibril size distribution and mechanical properties. *Proc. R. Soc. Lond. B*, 203(1152), pp.305-321.

PAUL, C. P. L., SCHOORL, T., ZUIDERBAAN, H. A., DOULABI, B. Z., VAN DER VEEN, A. J., VAN DE VEN, P. M., SMIT, T. H., VAN ROYEN, B. J., HELDER, M. N. & MULLENDER, M. G. 2013. Dynamic and Static Overloading Induce Early Degenerative Processes in Caprine Lumbar Intervertebral Discs. *Plos One,* 8.

PAUWELS, E., VAN LOO, D., CORNILLIE, P., BRABANT, L. & VAN HOOREBEKE, L. 2013. An exploratory study of contrast agents for soft tissue visualization by means of high resolution X-ray computed tomography imaging. *Journal of microscopy,* 250**,** 21-31.

PEDERSEN, J. A. & SWARTZ, M. A. 2005. Mechanobiology in the third dimension. *Annals of biomedical engineering,* 33**,** 1469-1490.

PEZOWICZ, C.A., ROBERTSON, P.A. AND BROOM, N.D. 2006. The structural basis of interlamellar cohesion in the intervertebral disc wall. *Journal of anatomy,* 208(3), pp.317-330.

PHAM, D.T., SHAPTER, J.G. AND COSTI, J.J. 2018. Tensile behaviour of individual fibre bundles in the human lumbar anulus fibrosus. *Journal of biomechanics,* 67, pp.24-31.

PUXKANDL, R., ZIZAK, I., PARIS, O., KECKES, J., TESCH, W., BERNSTORFF, S., PURSLOW, P. & FRATZL, P. 2002. Viscoelastic properties of collagen: synchrotron radiation investigations and structural model. *Philosophical Transactions of the Royal Society of London B: Biological Sciences,* 357**,** 191-197.

PÉRIÉ, D., KORDA, D. AND IATRIDIS, J.C. 2005. Confined compression experiments on bovine nucleus pulposus and annulus fibrosus: sensitivity of the experiment in the determination of compressive modulus and hydraulic permeability. *Journal of biomechanics*, 38(11), pp.2164-2171.

RACE, A., BROOM, N. D. & ROBERTSON, P. 2000. Effect of loading rate and hydration on the mechanical properties of the disc. *Spine,* 25**,** 662-669.

RADON, J. 1986. On the determination of functions from their integral values along certain manifolds. *IEEE transactions on medical imaging,* 5(4), pp.170-176.

RAJ, P. P. 2008. Intervertebral Disc: Anatomy-Physiology-Pathophysiology-Treatment. *Pain Practice,* 8**,** 18-44.

RASTOGI, V., PURI, N., ARORA, S., KAUR, G., YADAV, L. & SHARMA, R. 2013. Artefacts: a diagnostic dilemma–a review. *Journal of clinical and diagnostic research: JCDR,* 7**,** 2408.

RAU, C., WAGNER, U., PEŠIĆ, Z. & DE FANIS, A. 2011. Coherent imaging at the Diamond beamline I13. *physica status solidi (a),* 208**,** 2522-2525.

RAVEN, C. 1998. Numerical removal of ring artifacts in microtomography. *Review of scientific instruments,* 69**,** 2978-2980.

RICHARDSON, D. S. & LICHTMAN, J. W. 2015. Clarifying tissue clearing. *Cell,* 162**,** 246-257.

RICHARDSON, S. M., FREEMONT, A. J. & HOYLAND, J. A. 2014. Pathogenesis of Intervertebral Disc Degeneration. *The Intervertebral Disc.* Springer.

RIGORT, A., GÜNTHER, D., HEGERL, R., BAUM, D., WEBER, B., PROHASKA, S., MEDALIA, O., BAUMEISTER, W. & HEGE, H.-C. 2012. Automated segmentation of electron tomograms for a quantitative description of actin filament networks. *Journal of structural biology,* 177**,** 135-144.

ROBERTS, S., EVANS, H., TRIVEDI, J. & MENAGE, J. 2006. Histology and pathology of the human intervertebral disc. *The Journal of Bone & Joint Surgery,* 88**,** 10-14.

References

ROBERTS, S., MENAGE, J., SIVAN, S. AND URBAN, J.P. 2008. Bovine explant model of degeneration of the intervertebral disc. *BMC musculoskeletal disorders*, 9(1), p.24.

ROBERTS, S., MENAGE, J. AND URBAN, J.P. 1989. Biochemical and structural properties of the cartilage end-plate and its relation to the intervertebral disc. *Spine*, 14(2), pp.166-174.

ROBERTS, S., URBAN, J.P., EVANS, H. AND EISENSTEIN, S.M. 1996. Transport properties of the human cartilage endplate in relation to its composition and calcification. *Spine*, 21(4), pp.415-420.

ROCK, M. J., CAIN, S. A., FREEMAN, L. J., MORGAN, A., MELLODY, K. T., MARSON, A., SHUTTLEWORTH, C. A., WEISS, A. S. & KIELTY, C. M. 2004. Molecular basis of elastic fiber formation: critical interactions and a tropoelastin-fibrillin-1 crosslink. *Journal of Biological Chemistry*.

RODRIGUES, S. A., THAMBYAH, A. & BROOM, N. D. 2015. A multiscale structural investigation of the annulus-endplate anchorage system and its mechanisms of failure. *Spine Journal,* 15**,** 405-416.

RODRIGUES, S.A., THAMBYAH, A. AND BROOM, N.D. 2017. How maturity influences annulus-endplate integration in the ovine intervertebral disc: a micro-and ultra-structural study. *Journal of anatomy*, 230(1), pp.152-164.

RODRIGUES, S. A., WADE, K. R., THAMBYAH, A. & BROOM, N. D. 2012. Micromechanics of annulus-end plate integration in the intervertebral disc. *Spine Journal,* 12**,** 143-150.

RODRIGUEZ, A.G., RODRIGUEZ-SOTO, A.E., BURGHARDT, A.J., BERVEN, S., MAJUMDAR, S. AND LOTZ, J.C. 2012. Morphology of the human vertebral endplate. *Journal of orthopaedic research*, 30(2), pp.280-287..

ROLLS, G. O., FARMER, N. J. & HALL, J. B. 2008. Artifacts in histological and cytological preparations. *Melbourne: Leica Microsystems,* 106.

ROUGHLEY, P. J. 2004. Biology of intervertebral disc aging and degeneration: involvement of the extracellular matrix. *Spine,* 29**,** 2691-2699.

ROUGHLEY, P. J., MELCHING, L. I., HEATHFIELD, T. F., PEARCE, R. H. & MORT, J. S. 2006. The structure and degradation of aggrecan in human intervertebral disc. *European Spine Journal,* 15**,** 326-332.

ROUX, S., HILD, F., VIOT, P. & BERNARD, D. 2008. Three-dimensional image correlation from X-ray computed tomography of solid foam. *Composites Part A: Applied science and manufacturing,* 39**,** 1253-1265.

RUSPI, M.L., PALANCA, M., FALDINI, C. AND CRISTOFOLINI, L. 2017. Full-field in vitro investigation of hard and soft tissue strain in the spine by means of Digital Image Correlation. *Muscles, ligaments and tendons journal*, 7(4), p.538.

SAHLMAN, J., INKINEN, R., HIRVONEN, T., LAMMI, M.J., LAMMI, P.E., NIEMINEN, J., LAPVETELÄINEN, T., PROCKOP, D.J., ARITA, M., LI, S.W. AND HYTTINEN, M.M. 2001. Premature vertebral endplate ossification and mild disc degeneration in mice after inactivation of one allele belonging to the Col2a1 gene for Type II collagen. *Spine*, 26(23), pp.2558-2565.

SALOMON, J. A., WANG, H., FREEMAN, M. K., VOS, T., FLAXMAN, A. D., LOPEZ, A. D. & MURRAY, C. J. 2013. Healthy life expectancy for 187 countries, 1990–2010: a systematic analysis for the Global Burden Disease Study 2010. *The Lancet*, 380**,** 2144-2162.

SARTORI, J., KÖHRING, S., WITTE, H., FISCHER, M.S. AND LÖFFLER, M. 2018. Three-dimensional imaging of the fibrous microstructure of Achilles tendon entheses in Mus musculus. *Journal of Anatomy*.

SCHMITT, J. M. 1998. OCT elastography: imaging microscopic deformation and strain of tissue. *Optics express,* 3**,** 199-211.

References

SCHNEIDER, C. A., RASBAND, W. S. & ELICEIRI, K. W. 2012. NIH Image to ImageJ: 25 years of image analysis. *Nature methods,* 9**,** 671.

SCHOLLUM, M., ROBERTSON, P. & BROOM, N. 2009a. Microstructural analysis of the translamellar bridging network of the disc annulus. *Journal of Bone & Joint Surgery, British Volume,* 91**,** 434-434.

SCHOLLUM, M. L., APPLEYARD, R. C., LITTLE, C. B. & MELROSE, J. 2010. A Detailed Microscopic Examination of Alterations in Normal Anular Structure Induced by Mechanical Destabilization in an Ovine Model of Disc Degeneration. *Spine,* 35**,** 1965-1973.

SCHOLLUM, M. L., ROBERTSON, P. A. & BROOM, N. D. 2009b. A microstructural investigation of intervertebral disc lamellar connectivity: detailed analysis of the translamellar bridges. *Journal of anatomy,* 214**,** 805-816.

SCHRAUWEN, J., VILANOVA, A., REZAKHANIHA, R., STERGIOPULOS, N., VAN DE VOSSE, F. & BOVENDEERD, P. 2012. A method for the quantification of the pressure dependent 3D collagen configuration in the arterial adventitia. *Journal of structural biology,* 180**,** 335-342.

SCOTT, A.E., VASILESCU, D.M., SEAL, K.A., KEYES, S.D., MAVROGORDATO, M.N., HOGG, J.C., SINCLAIR, I., WARNER, J.A., HACKETT, T.L. AND LACKIE, P.M. 2015. Three dimensional imaging of paraffin embedded human lung tissue samples by micro-computed tomography. PLoS One, 10(6), p.e0126230.

SCREEN, H., LEE, D., BADER, D. & SHELTON, J. 2004. An investigation into the effects of the hierarchical structure of tendon fascicles on micromechanical properties. *Proceedings of the Institution of Mechanical Engineers, Part H: Journal of Engineering in Medicine,* 218**,** 109-119.

SCREEN, H. R., BERK, D. E., KADLER, K. E., RAMIREZ, F. & YOUNG, M. F. 2015. Tendon functional extracellular matrix. *Journal of Orthopaedic Research,* 33**,** 793-799.

SEIBERT, J. A. 2004. X-ray imaging physics for nuclear medicine technologists. Part 1: Basic principles of x-ray production. *Journal of nuclear medicine technology,* 32**,** 139-147.

SETTON, L. A. & CHEN, J. 2004. Cell mechanics and mechanobiology in the intervertebral disc. *Spine,* 29**,** 2710-2723.

SETTON, L. A. & CHEN, J. 2006. Mechanobiology of the intervertebral disc and relevance to disc degeneration. *JBJS,* 88**,** 52-57.

SHAN, Z., LI, S., LIU, J., MAMUTI, M., WANG, C. AND ZHAO, F. 2015. Correlation between biomechanical properties of the annulus fibrosus and magnetic resonance imaging (MRI) findings. *European Spine Journal*, 24(9), pp.1909-1916.

SHAPIRO, I. M. & RISBUD, M. V. 2014. Introduction to the Structure, Function, and Comparative Anatomy of the Vertebrae and the Intervertebral Disc. *The Intervertebral Disc.* Springer.

SHARMA, A., LANCASTER, S., BAGADE, S. & HILDEBOLT, C. 2014. Early Pattern of Degenerative Changes in Individual Components of Intervertebral Discs in Stressed and Nonstressed Segments of Lumbar Spine An *In vivo* Magnetic Resonance Imaging Study. *Spine,* 39**,** 1084-1090.

SHEARER, T., BRADLEY, R. S., HIDALGO-BASTIDA, L. A., SHERRATT, M. J. & CARTMELL, S. H. 2016. Three-dimensional visualisation of soft biological structures by X-ray computed micro-tomography. *J Cell Sci,* 129**,** 2483-2492.

SHEARER, T., RAWSON, S., CASTRO, S. J., BALINT, R., BRADLEY, R. S., LOWE, T., VILA-COMAMALA, J., LEE, P. D. & CARTMELL, S. H. 2014a. X-ray computed tomography of the anterior cruciate ligament and patellar tendon. *Muscles, ligaments and tendons journal,* 4**,** 238-44.

References

SHERRATT, M. J. 2013. Structural proteins and arterial ageing. *Artery Research,* 7**,** 15-21.

BECKSTEIN, J.C., SEN, S., SCHAER, T.P., VRESILOVIC, E.J. AND ELLIOTT, D.M. 2008. Comparison of animal discs used in disc research to human lumbar disc: axial compression mechanics and glycosaminoglycan content. *Spine,* 33(6), pp.E166-E173.

SKAGGS, D. L., WEIDENBAUM, M., IATRIDIS, J. C., RATCLIFFE, A. & MOW, V. C. 1994. Regional Variation In Tensile Properties And Biochemical-Composition Of The Human Lumbar Anulus Fibrosus. *Spine,* 19**,** 1310-1319.

SMITH, L.J. AND FAZZALARI, N.L. 2006. Regional variations in the density and arrangement of elastic fibres in the anulus fibrosus of the human lumbar disc. *Journal of anatomy,* 209(3), pp.359-367.

SMITH, L.J., BYERS, S., COSTI, J.J. AND FAZZALARI, N.L. 2008. Elastic fibers enhance the mechanical integrity of the human lumbar anulus fibrosus in the radial direction. *Annals of biomedical engineering,* 36(2), pp.214-223.

SMITH, L. J., NERURKAR, N. L., CHOI, K.-S., HARFE, B. D. & ELLIOTT, D. M. 2011. Degeneration and regeneration of the intervertebral disc: lessons from development. *Disease models & mechanisms,* 4**,** 31-41.

SNIGIREV, A., SNIGIREVA, I., KOHN, V., KUZNETSOV, S. & SCHELOKOV, I. 1995. On the possibilities of x-ray phase contrast microimaging by coherent high-energy synchrotron radiation. *Review of scientific instruments,* 66**,** 5486-5492.

STADELMANN, M. A., MAQUER, G., VOUMARD, B., GRANT, A., HACKNEY, D. B., VERMATHEN, P., ALKALAY, R. N. & ZYSSET, P. K. 2018a. Integrating MRI-based geometry, composition and fiber architecture in a finite element model of the human intervertebral disc. *Journal of the mechanical behavior of biomedical materials*.

STADELMANN, M. A., MAQUER, G., VOUMARD, B., GRANT, A., HACKNEY, D. B., VERMATHEN, P., ALKALAY, R. N. & ZYSSET, P. K. 2018b. Integrating MRI-based geometry, composition and fiber architecture in a finite element model of the human intervertebral disc. *Journal of the Mechanical Behavior of Biomedical Materials,* 85**,** 37-42.

STEPHENSON, R. S., BOYETT, M. R., HART, G., NIKOLAIDOU, T., CAI, X., CORNO, A. F., ALPHONSO, N., JEFFERY, N. & JARVIS, J. C. 2012. Contrast enhanced micro-computed tomography resolves the 3-dimensional morphology of the cardiac conduction system in mammalian hearts. *PloS one,* 7**,** e35299-e35299.

STORM, C., PASTORE, J. J., MACKINTOSH, F. C., LUBENSKY, T. C. & JANMEY, P. A. 2005. Nonlinear elasticity in biological gels. *Nature,* 435**,** 191.

SUTTON, M., KE, X., LESSNER, S., GOLDBACH, M., YOST, M., ZHAO, F. & SCHREIER, H. 2008. Strain field measurements on mouse carotid arteries using microscopic three-dimensional digital image correlation. *Journal of Biomedical Materials Research Part A,* 84**,** 178-190.

SUTTON, M., MINGQI, C., PETERS, W., CHAO, Y. & MCNEILL, S. 1986. Application of an optimized digital correlation method to planar deformation analysis. *Image and Vision Computing,* 4**,** 143-150.

SUTTON, M., WOLTERS, W., PETERS, W., RANSON, W. & MCNEILL, S. 1983. Determination of displacements using an improved digital correlation method. *Image and vision computing,* 1**,** 133-139.

SZCZESNY, S.E., EDELSTEIN, R.S. AND ELLIOTT, D.M. 2014. DTAF dye concentrations commonly used to measure microscale deformations in biological tissues alter tissue mechanics. *PloS one,* 9(6), p.e99588.

SZCZESNY, S. E. & ELLIOTT, D. M. 2014. Interfibrillar shear stress is the loading mechanism of collagen fibrils in tendon. *Acta biomaterialia,* 10**,** 2582-2590.

References

SZTROLOVICS, R., ALINI, M., ROUGHLY, P. & MORT, J. 1997. Aggrecan degradation in human intervertebral disc and articular cartilage. *Biochem. J,* 326**,** 235-241.

TAKAHASHI, K., AOKI, Y. & OHTORI, S. 2008. Resolving discogenic pain. *European Spine Journal,* 17**,** 428-431.

TAVAKOLI, J. & COSTI, J. J. 2018a. New findings confirm the viscoelastic behaviour of the inter-lamellar matrix of the disc annulus fibrosus in radial and circumferential directions of loading. *Acta Biomaterialia,* 71**,** 411-419.

TAVAKOLI, J. AND COSTI, J.J. 2018. Ultrastructural organization of elastic fibres in the partition boundaries of the annulus fibrosus within the intervertebral disc. *Acta biomaterialia*, 68, pp.67-77.

TAVAKOLI, J., ELLIOTT, D.M. AND COSTI, J.J. 2017. The ultra-structural organization of the elastic network in the intra-and inter-lamellar matrix of the intervertebral disc. *Acta biomaterialia*, 58, pp.269-277.

TAYLOR, J., SCOTT, J., CRIBB, A. & BOSWORTH, T. 1992. Human intervertebral disc acid glycosaminoglycans. *Journal of anatomy,* 180**,** 137.

TAYLOR, Z. J., GURKA, R., KOPP, G. A. & LIBERZON, A. 2010. Long-duration time-resolved PIV to study unsteady aerodynamics. *IEEE Transactions on Instrumentation and Measurement,* 59**,** 3262-3269.

TERAGUCHI, M., YOSHIMURA, N., HASHIZUME, H., MURAKI, S., YAMADA, H., MINAMIDE, A., OKA, H., ISHIMOTO, Y., NAGATA, K. & KAGOTANI, R. 2014. Prevalence and distribution of intervertebral disc degeneration over the entire spine in a population-based cohort: the Wakayama Spine Study. *Osteoarthritis and cartilage,* 22**,** 104-110.

THOMOPOULOS, S., WILLIAMS, G. R., GIMBEL, J. A., FAVATA, M. & SOSLOWSKY, L. J. 2003. Variation of biomechanical, structural, and compositional properties along the tendon to bone insertion site. *Journal of orthopaedic research,* 21**,** 413-419.

THORPE, C. T., GODINHO, M. S., RILEY, G. P., BIRCH, H. L., CLEGG, P. D. & SCREEN, H. R. 2015. The interfascicular matrix enables fascicle sliding and recovery in tendon, and behaves more elastically in energy storing tendons. *Journal of the mechanical behavior of biomedical materials,* 52**,** 85-94.

TILLEY, J., CARR, A. & CZERNUSZKA, J. 2011. Atomic Force Microscopy of bulk tendon samples: affect of location and fixation on tissue ultrastructure. *Micron,* 42**,** 531-535.

TITARENKO, V., BRADLEY, R., MARTIN, C., WITHERS, P. J. & TITARENKO, S. Regularization methods for inverse problems in X-ray tomography. SPIE Optical Engineering+ Applications, 2010. International Society for Optics and Photonics, 78040Z-78040Z-10.

TSAI, T.-L., NELSON, B. C., ANDERSON, P. A., ZDEBLICK, T. A. & LI, W.-J. 2014. Intervertebral disc and stem cells cocultured in biomimetic extracellular matrix stimulated by cyclic compression in perfusion bioreactor. *Spine Journal,* 14**,** 2127-2140.

UNITED NATIONS, R. 2013. World Population Ageing 2013. New York.

URBAN, J. P. & ROBERTS, S. 2003. Degeneration of the intervertebral disc. *Arthritis Res Ther,* 5**,** 120.

URBAN, J. P. G., SMITH, S. & FAIRBANK, J. C. T. 2004. Nutrition of the intervertebral disc. *Spine,* 29**,** 2700-2709.

VAN DEN AKKER, G. G., SURTEL, D. A., CREMERS, A., RODRIGUES-PINTO, R., RICHARDSON, S. M., HOYLAND, J. A., VAN RHIJN, L. W., WELTING, T. J. & VONCKEN, J. W. 2014. Novel immortal human cell lines reveal subpopulations in the nucleus pulposus. *Arthritis research & therapy,* 16**,** R135.

References

VAN DER VEEN, A.J., BISSCHOP, A., MULLENDER, M.G. AND VAN DIEËN, J.H. 2013. Modelling creep behaviour of the human intervertebral disc. *Journal of biomechanics*, 46(12), pp.2101-2103.

VERGARI, C., CHAN, D., CLARKE, A., MANSFIELD, J. C., MEAKIN, J. R. & WINLOVE, P. C. 2017. Bovine and degenerated human annulus fibrosus: a microstructural and micromechanical comparison. *Biomechanics and modeling in mechanobiology***,** 1-10.

VERGARI, C., MANSFIELD, J., MEAKIN, J. R. & WINLOVE, P. C. 2016. Lamellar and fibre bundle mechanics of the annulus fibrosus in bovine intervertebral disc. *Acta biomaterialia,* 37**,** 14-20.

VERGROESEN, P.-P., KINGMA, I., EMANUEL, K. S., HOOGENDOORN, R. J., WELTING, T. J., VAN ROYEN, B. J., VAN DIEËN, J. H. & SMIT, T. H. 2015. Mechanics and biology in intervertebral disc degeneration: a vicious circle. *Osteoarthritis and cartilage,* 23**,** 1057-1070.

VERGROESEN, P.-P. A., VAN DER VEEN, A. J., VAN ROYEN, B. J., KINGMA, I. & SMIT, T. H. 2014. Intradiscal pressure depends on recent loading and correlates with disc height and compressive stiffness. *European Spine Journal,* 23**,** 2359-2368.

VICKERTON, P., JARVIS, J. & JEFFERY, N. 2013. Concentration-dependent specimen shrinkage in iodine-enhanced microCT. *Journal of anatomy,* 223**,** 185-193.

WADESON, N. & BASHAM, M. 2016. Savu: A Python-based, MPI Framework for Simultaneous Processing of Multiple, N-dimensional, Large Tomography Datasets. *arXiv preprint arXiv:1610.08015*.

WAGENSEIL, J. E. & MECHAM, R. P. 2009. Vascular Extracellular Matrix and Arterial Mechanics. *Physiological Reviews,* 89**,** 957-989.

WALKER, B. F. 2000. The prevalence of low back pain: A systematic review of the literature from 1966 to 1998. *Journal of Spinal Disorders,* 13**,** 205-217.

WALKER, S. M., SCHWYN, D. A., MOKSO, R., WICKLEIN, M., MÜLLER, T., DOUBE, M., STAMPANONI, M., KRAPP, H. G. & TAYLOR, G. K. 2014. *In vivo* time-resolved microtomography reveals the mechanics of the blowfly flight motor. *PLoS biology,* 12**,** e1001823.

WALSH, A. J. & LOTZ, J. C. 2004. Biological response of the intervertebral disc to dynamic loading. *Journal of biomechanics,* 37**,** 329-337.

WALTON, L. A., BRADLEY, R. S., WITHERS, P. J., NEWTON, V. L., WATSON, R. E., AUSTIN, C. & SHERRATT, M. J. 2015. Morphological Characterisation of Unstained and Intact Tissue Micro-architecture by X-ray Computed Micro-and Nano-Tomography. *Scientific reports,* 5.

WAN, W., YANAGISAWA, H. & GLEASON, R. L. 2010. Biomechanical and microstructural properties of common carotid arteries from fibulin-5 null mice. *Annals of biomedical engineering,* 38**,** 3605-3617.

WANG, R., BREWSTER, L. P. & GLEASON, R. L. 2013. *In situ* characterization of the uncrimping process of arterial collagen fibers using two-photon confocal microscopy and digital image correlation. *Journal of biomechanics,* 46**,** 2726-2729.

WANG, S., RUI, Y., LU, J. & WANG, C. 2014. Cell and molecular biology of intervertebral disc degeneration: current understanding and implications for potential therapeutic strategies. *Cell proliferation,* 47**,** 381-390.

WANG, Y., BATTIÉ, M. C. & VIDEMAN, T. 2012. A morphological study of lumbar vertebral endplates: radiographic, visual and digital measurements. *European Spine Journal,* 21**,** 2316-2323.

WATTRISSE, B., CHRYSOCHOOS, A., MURACCIOLE, J.-M. & NÉMOZ-GAILLARD, M. 2001. Analysis of strain localization during tensile tests by digital image correlation. *Experimental Mechanics,* 41**,** 29-39.

References

WEBER, B., GREENAN, G., PROHASKA, S., BAUM, D., HEGE, H.-C., MÜLLER-REICHERT, T., HYMAN, A. A. & VERBAVATZ, J.-M. 2012. Automated tracing of microtubules in electron tomograms of plastic embedded samples of Caenorhabditis elegans embryos. *Journal of structural biology,* 178**,** 129-138.

WEINSTEIN, J. N., LURIE, J. D., TOSTESON, T. D., TOSTESON, A. N. A., BLOOD, E. A., ABDU, W. A., HERKOWITZ, H., HILIBRAND, A., ALBERT, T. & FISCHGRUND, J. 2008. Surgical Versus Nonoperative Treatment for Lumbar Disc Herniation Four-Year Results for the Spine Patient Outcomes Research Trial (SPORT). *Spine,* 33**,** 2789-2800.

WIJESINGHE, P., JOHANSEN, N. J., CURATOLO, A., SAMPSON, D. D., GANSS, R. & KENNEDY, B. F. 2017. Ultrahigh-resolution optical coherence elastography images cellular-scale stiffness of mouse aorta. *Biophysical Journal,* 113**,** 2540-2551.

WILKINS, S., GUREYEV, T. E., GAO, D., POGANY, A. & STEVENSON, A. 1996. Phase-contrast imaging using polychromatic hard X-rays. *Nature,* 384**,** 335.

WILLMOTT, P. 2011. *An introduction to synchrotron radiation: techniques and applications*, John Wiley & Sons.

WOLINSKY, H. & GLAGOV, S. 1964. Structural basis for the static mechanical properties of the aortic media. *Circulation research,* 14**,** 400-413.

YEE, A., LAM, M.P.Y., TAM, V., CHAN, W.C.W., CHU, I.K., CHEAH, K.S.E., CHEUNG, K.M.C. AND CHAN, D. 2016. Fibrotic-like changes in degenerate human intervertebral discs revealed by quantitative proteomic analysis. *Osteoarthritis and cartilage*, 24(3), pp.503-513.

YODER, J. H., PELOQUIN, J. M., SONG, G., TUSTISON, N. J., MOON, S. M., WRIGHT, A. C., VRESILOVIC, E. J., GEE, J. C. & ELLIOTT, D. M. 2014. Internal Three-Dimensional Strains in Human Intervertebral Discs Under Axial Compression Quantified Noninvasively by Magnetic Resonance Imaging and Image Registration. *Journal of Biomechanical Engineering-Transactions of the Asme,* 136.

YU, J., FAIRBANK, J. C., ROBERTS, S. & URBAN, J. P. 2005. The elastic fiber network of the anulus fibrosus of the normal and scoliotic human intervertebral disc. *Spine,* 30**,** 1815-1820.

YU, J., PETER, C., ROBERTS, S. AND URBAN, J.P. 2002. Elastic fibre organization in the intervertebral discs of the bovine tail. *Journal of anatomy,* 201(6), pp.465-475.

YU, J., SCHOLLUM, M. L., WADE, K. R., BROOM, N. D. & URBAN, J. 2015. A Detailed Examination of the Elastic Network Leads to a New Understanding of Annulus Fibrosus Organisation. *Spine*.

YU, J., TIRLAPUR, U., FAIRBANK, J., HANDFORD, P., ROBERTS, S., WINLOVE, C. P., CUI, Z. & URBAN, J. 2007. Microfibrils, elastin fibres and collagen fibres in the human intervertebral disc and bovine tail disc. *Journal of anatomy,* 210**,** 460-471.

ZEHRA, U., ROBSON-BROWN, K., ADAMS, M.A. AND DOLAN, P. 2015. Porosity and thickness of the vertebral endplate depend on local mechanical loading. *Spine*, 40(15), pp.1173-1180.

ZHANG, J., TIAN, D., LIN, R., PENG, G. & SU, M. 2014. Phase-contrast X-ray CT Imaging of Esophagus and Esophageal Carcinoma. *Scientific reports,* 4.

ZHU, D., GU, G., WU, W., GONG, H., ZHU, W., JIANG, T. & CAO, Z. 2008. Micro-structure and mechanical properties of annulus fibrous of the L4-5 and L5-S1 intervertebral discs. *Clinical Biomechanics*, 23**,** S74-S82.

ZIV, I., MOSKOWITZ, R.W., KRAISE, I., ADLER, J.H. AND MAROUDAS, A. 1992. Physicochemical properties of the aging and diabetic sand rat intervertebral disc. *Journal of orthopaedic research*, 10(2), pp.205-210.

References

ZYSK, A. M., GARSON, A. B., XU, Q., BREY, E. M., ZHOU, W., BRANKOV, J. G., WERNICK, M. N., KUSZAK, J. R. & ANASTASIO, M. A. 2012. Nondestructive volumetric imaging of tissue microstructure with benchtop x-ray phase-contrast tomography and critical point drying. *Biomedical optics express,* 3**,** 1924-1932.

Appendix

A. A Review of Techniques for Visualising Soft Tissue Microstructure Deformation and Quantifying Strain *Ex vivo*

A version of this chapter has been published in Journal of Microscopy special issue;

Disney *et al.* 2018. A Review of Techniques for Visualising Soft Tissue Microstructure Deformation and Quantifying Strain *Ex vivo*. *Journal of microscopy*.

Appendix A

A.1 Author contribution statement:

Catherine M. Disney wrote the review. All other authors (Peter D. Lee, Judith A. Hoyland, Michael J. Sherratt and Brain K. Bay) edited and approved the final version of the manuscript.

Appendix A

A.2 Abstract

Many biological tissues have a complex hierarchical structure allowing them to function under demanding physiological loading conditions. Structural changes caused by ageing or disease can lead to loss of mechanical function. Therefore, it is necessary to characterise tissue structure to understand normal tissue function and the progression of disease. Ideally intact native tissues should be imaged in 3D and under physiological loading conditions. The current published *in situ* imaging methodologies demonstrate a compromise between imaging limitations and maintaining the samples native mechanical function. This review gives an overview of *in situ* imaging techniques used to visualise microstructural deformation of soft tissue, including three case studies of different tissues (tendon, intervertebral disc and artery). Some of the imaging techniques restricted analysis to observational mechanics or discrete strain measurement from invasive markers. Full-field local surface strain measurement has been achieved using digital image correlation. Volumetric strain fields have successfully been quantified from *in situ* X-ray micro tomography (microCT) studies of bone using digital volume correlation but not in soft tissue due to low X-ray transmission contrast. With the latest developments in microCT showing in-line phase contrast capability to resolve native soft tissue microstructure, there is potential for future soft tissue mechanics research where 3D local strain can be quantified. These methods will provide information on the local 3D micro-mechanical environment experienced by cells in healthy, aged and diseased tissues. It is hoped that future applications of *in situ* imaging techniques will impact positively on the design and testing of potential tissue replacements or regenerative therapies.

A.3 Introduction

The mechanical function of biological tissues relies on their hierarchical structure. To fully understand normal tissue function and the progression of disease, it is necessary to visualise structure and characterise mechanical behaviour at multiple levels of tissue hierarchy and in three dimensions. Three-dimensional tissue architecture does not conveniently simplify into the two-dimensional representation given by histology. Many tissues have evolved complex structures in order to function under demanding dynamic physiological loading conditions. For example, blood vessels must accommodate to changes in pressure, tendons are required to transmit forces during movement and intervertebral discs (IVD) allow small movements between the vertebrae for the spine to bend and twist whilst supporting body weight (Figure 7.1). The physical and mechanical properties of these tissues are directly related to the complex and sophisticated structures created by their constituent cells and extracellular matrices (ECM). Elastic arteries have a layered structure which provides remarkable resilience and strength (Wagenseil and Mecham, 2009). The lamellar elastin-rich medial layer protects smaller blood vessels by dampening large changes in pressure. Energy is stored during high pressure (systole) and released as the vessel returns to resting diameter (diastole). The outer collagen-rich adventitia layer restricts extreme arterial diameter changes. Fibrous connective tissue such as tendon and IVD must have low stiffness for flexibility but high strength under increasing load to bear or transmit load. This non-linear mechanical behaviour is created by a composite and hierarchical structure of aligned collagen fibrils, fibres, fibre bundles and fascicles or lamellae for tendon and IVD (Dobrynin and Carrillo, 2010, Lake *et al.*, 2009, Guerin and Elliott, 2007, Storm *et al.*, 2005).

The structure and therefore function of tissues does not however remain static. Both ageing and many associated pathologies negatively impact on tissues. The proportion of older people (aged 60 years or older) in Europe and North America is increasing and is expected to reach up to 21% by 2050 (United Nations, 2013). Mortality, morbidity and quality of life during old age are increasingly determined by age-related disease (Salomon *et al.*, 2013). This can be associated with structural and mechanical changes of soft tissues such as arteriosclerosis of blood vessels (Adnan *et al.*, 2017, Hayashi and Hirayama, 2017, Wijesinghe *et al.*, 2017, Sherratt, 2013, Graham *et al.*, 2011), compositional changes in tendon (Ackerman *et al.*, 2017, Fessel *et al.*, 2014, Couppe *et al.*, 2009, Goh *et al.*, 2008) and IVD degeneration (Gullbrand *et al.*, 2016, Richardson *et al.*, 2014, Wang *et al.*, 2014, Adams and Dolan, 2012, Raj, 2008, Urban and Roberts, 2003). Thus, the ageing population presents a major challenge for healthy ageing and medicine.

Appendix A

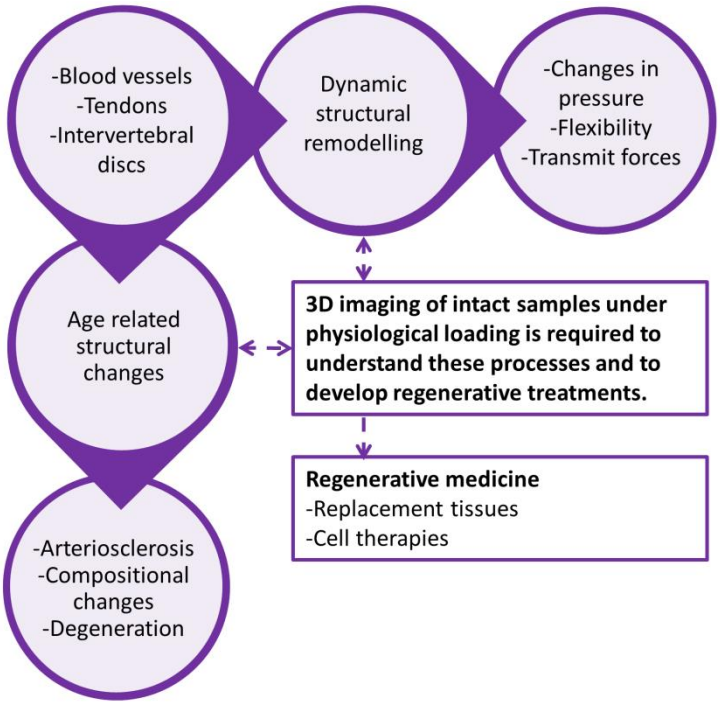

Figure 7.1 In situ imaging studies are essential to characterise biological tissue structure during function, ageing and to develop regenerative treatments.

In order to understand the structure and function of healthy, aged and diseased tissues, it is necessary to characterise soft tissue microstructure under different loading conditions (Figure 7.1) (Fang and Lake, 2017, Locke *et al.*, 2017, Wan *et al.*, 2010). Ultrasound, MRI or CT have been used for *in vivo* mechanics studies allowing accurate physiological loading (Franz *et al.*, 2015, Yoder *et al.*, 2014, Martin *et al.*, 2013). However, these techniques have limited resolution and are unable to resolve microstructure which is central to native tissue mechanical function and cell-matrix interactions (Screen *et al.*, 2015, Neidlinger-Wilke *et al.*, 2014, Setton and Chen, 2006). Therefore, this review only includes microstructural imaging of *ex vivo* samples. Experimental mechanics and imaging studies of *ex vivo* samples have the potential to recapitulate soft tissue microstructure and function required for the development and testing of novel tissue engineering or regenerative therapies (Appel *et al.*, 2013, Pedersen and Swartz, 2005). Here we review *in situ* imaging techniques - a combination of mechanical loading and imaging - used to visualise soft tissue microstructure under load and to quantify or map strain. Focus is on the compromise between optimal imaging characteristics and maintaining native mechanical function.

A.4 Imaging soft tissue microstructure to observe mechanical function

A.4.1 Imaging soft tissue microstructure

Optical microscopy techniques are commonly used to identify constituent cells and ECM in tissue. Histological visualisation requires micro-spatial resolution and sufficient contrast between cells and ECM structural components. Image contrast between different structures and compositional information can be determined by their affinity for various stains. Although serial sectioning and reconstruction can be employed to visualise structures in 3D, the approach is labour intensive and has varied results (Mizutani and Suzuki, 2012). Problematic sections may have to be discarded for a low error reconstruction. Moreover when viewed by these sectioning techniques, their structure may not be representative as in their natural environment. Sectioning often results in structural damage artefacts such as tears, fractures, folds and compressions. Ideally imaging should be 3D and non-destructive, leaving the tissue intact in its physiological environment (Walton *et al.*, 2015).

Optical coherence tomography (OCT) uses a relatively longer wavelength light than standard histology and so is capable of penetrating deeper into the tissue (1-2 mm) allowing imaging of mesoscale volumes. Optical clearing of specimens can help to reduce light scattering and hence improve imaging depth. Richardson and Lichtman (2015) review various clearing techniques showing that protocols can range from hours to months and importantly clearing causes changes in tissue morphology. The 3D structural complexity of tissues can be imaged using OCT, for example the connectivity of translamellar cross bridges in the IVD (Han *et al.*, 2015). Furthermore, OCT uses intact native samples allowing for imaging during functional conditions such as artery stiffness changes in pressurised diseased arteries (Adnan *et al.*, 2017). Confocal microscopy has higher resolution than OCT but imaging thickness is limited to a few hundred microns and is only capable of viewing in-plane or nearly in-plane features. The higher resolution, achieved by a focussed high intensity beam and a pinhole to select in focus regions, allows visualisation of microstructures which are responsible for soft tissue mechanical behaviour (Wang *et al.*, 2013, Michalek *et al.*, 2009, Bruehlmann *et al.*, 2004).

X-ray micro tomography (microCT) is capable of 3D imaging of relatively large intact specimens at micro-spatial resolution. In comparison to the above imaging techniques, X-rays are more transmissive and less refractile. This means that they can penetrate the specimen with the ability for non-destructive 3D imaging. Two observations can be made once X-ray radiation has passed through a sample; i) the wave's amplitude is reduced due to absorption (dependent on the electron density of the sample) ii) the wave front is

distorted (phase distortion) due to the wave travelling at different speeds through different areas of attenuation in the sample. Transmission based X-ray tomography records a cross-section of the sample according to the intensity of the X-rays after passing through the sample. The sample is mounted and rotated by a stage to gather many projections which are reconstructed to form a 3D image. The first cone beam reconstruction algorithm (Feldkamp *et al.*, 1984) enabled 3D histological resolution imaging of cancellous bone (Feldkamp *et al.*, 1989). Contrast in these samples is due to the high-atomic-number of the mineralised constituent (calcium phosphate).

Conversely soft tissue is composed of low-atomic-number elements (carbon, hydrogen, oxygen) and so has low X-ray transmission contrast. The comparable level of hydration within the different components of soft tissue also contributes to low absorption contrast and lack of resolved detail. Contrast enhancement can be achieved using heavy element staining agents or by drying the sample, both of which cause distortion and changes in material properties. Simple drying of soft tissue leads to shrinkage and significant damage to the tissue's native structure. Freeze drying and critical point drying reduce but do not eliminate these artefacts (Zysk *et al.*, 2012, Happel *et al.*, 2010). The use of contrast agents is less complicated than drying procedures as they do not require any special conditions such as controlled temperature and pressure. Staining affinity and protocols are not well defined but this is a growing field with a number of recent publications in whole model organisms and organs to distinguish gross anatomy (Helfenstein-Didier *et al.*, 2017, Descamps *et al.*, 2014, Pauwels *et al.*, 2013, Mizutani and Suzuki, 2012, Metscher, 2009a, Metscher, 2009b) and at tissue level to resolve the microstructure of collagenous tissues and vasculature (Figure 7.2a) (Disney *et al.*, 2017, Balint *et al.*, 2016, Shearer *et al.*, 2016, Nieminen *et al.*, 2015, Nierenberger *et al.*, 2015). A degree of tissue preservation or fixation is required for staining (mostly ethanol based) which alters tissue structure and mechanics (Tilley *et al.*, 2011, Hickey and Hukins, 1979). Long staining times are often required for diffusion of contrast agents into bulk tissue samples, and this has been shown to cause tissue distortion (Disney *et al.*, 2017, Balint *et al.*, 2016, Vickerton *et al.*, 2013).

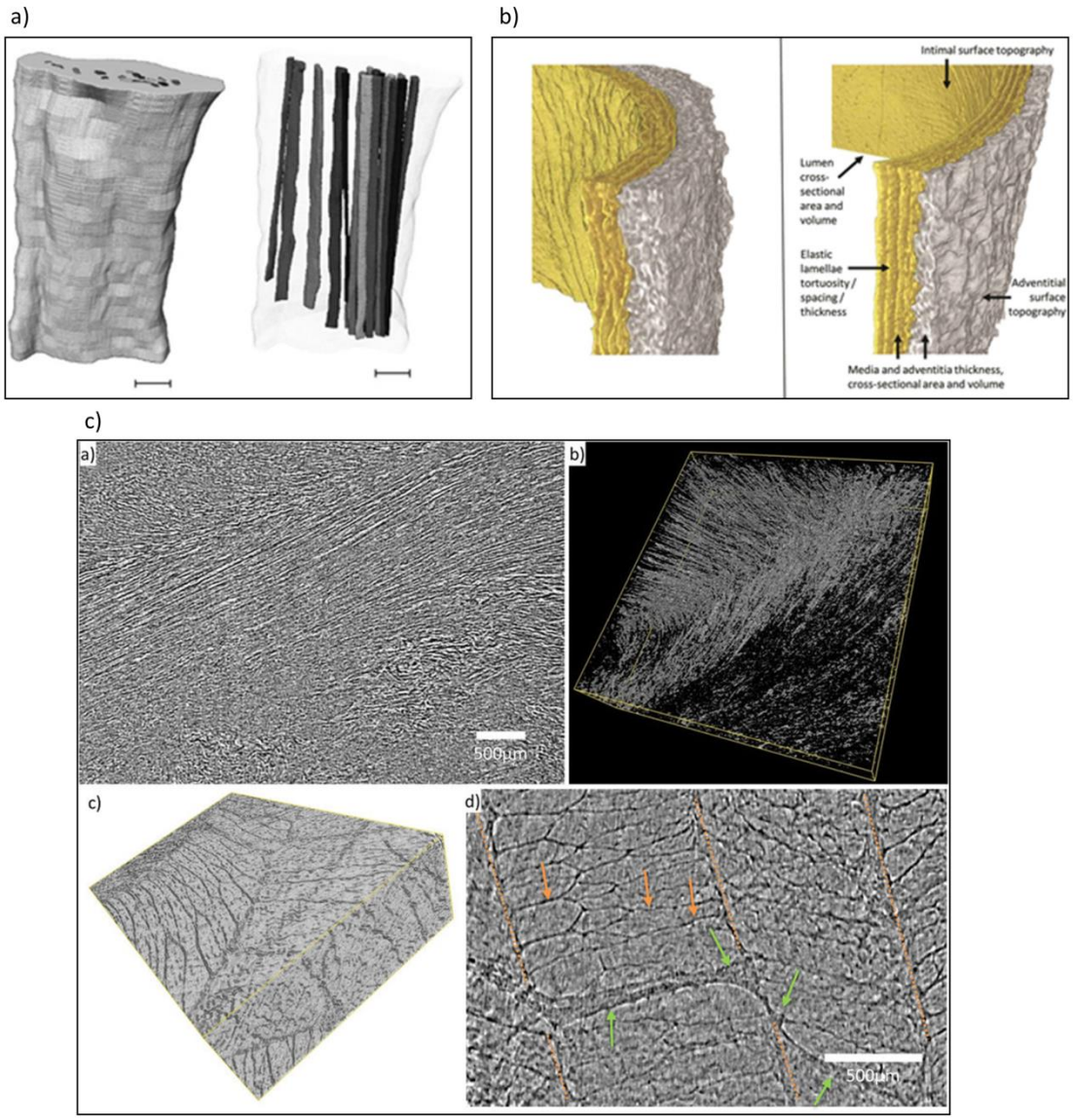

Figure 7.2 MicroCT imaging of soft tissue. Individual fascicles have been resolved in tendon stained with iodine potassium iodide (a) (Shearer et al., 2016). Paraffin embedded unpressurised and pressurised aorta imaged using in-line phase contrast microCT (b) (Walton et al., 2015). Native annulus fibrosus of the intervertebral disc imaged using in-line phase contrast synchrotron microCT (c) (Disney et al., 2017). All panels adapted with permission.

It is possible to resolve soft tissue microstructure without the use of stains using in-line phase contrast enhancement (Disney *et al.*, 2017, Walton *et al.*, 2015, Naveh *et al.*, 2014, Jiang *et al.*, 2012, Kalson *et al.*, 2012). This method proposed in the 90s (Wilkins *et al.*, 1996, Snigirev *et al.*, 1995) requires a partially coherent source but does not require any additional optics. The detector is moved away from the sample to provide sufficient

propagation for Fresnel diffraction to occur from the wave front distortion. The interference Fresnel fringes increase structure edge resolution. In-line phase contrast enhancement has been used with both synchrotron and laboratory microfocus sources. Walton *et al.*(2015) used phase contrast enhanced microCT to visualise microstructural changes in pressurised embedded arteries. Their high resolution scans are able to resolve structural remodelling such as an increase in lumen cross-sectional area, straightening of the medial elastic lamellae and remodelling in the adventitial layer (Figure 7.2b). However, this methodology is limited to an observational study as the tissue was chemically fixed and paraffin embedded and so a direct comparison cannot be made before and after pressurisation of the same artery. It is difficult to conduct *in situ* experiments with laboratory phase contrast methods, as creating coherence reduces X-ray flux considerably and scan time become very long (days). The success and challenges of *in situ* imaging for soft tissue mechanics measurement are described in the next two sections and summarised in Figure 7.3.

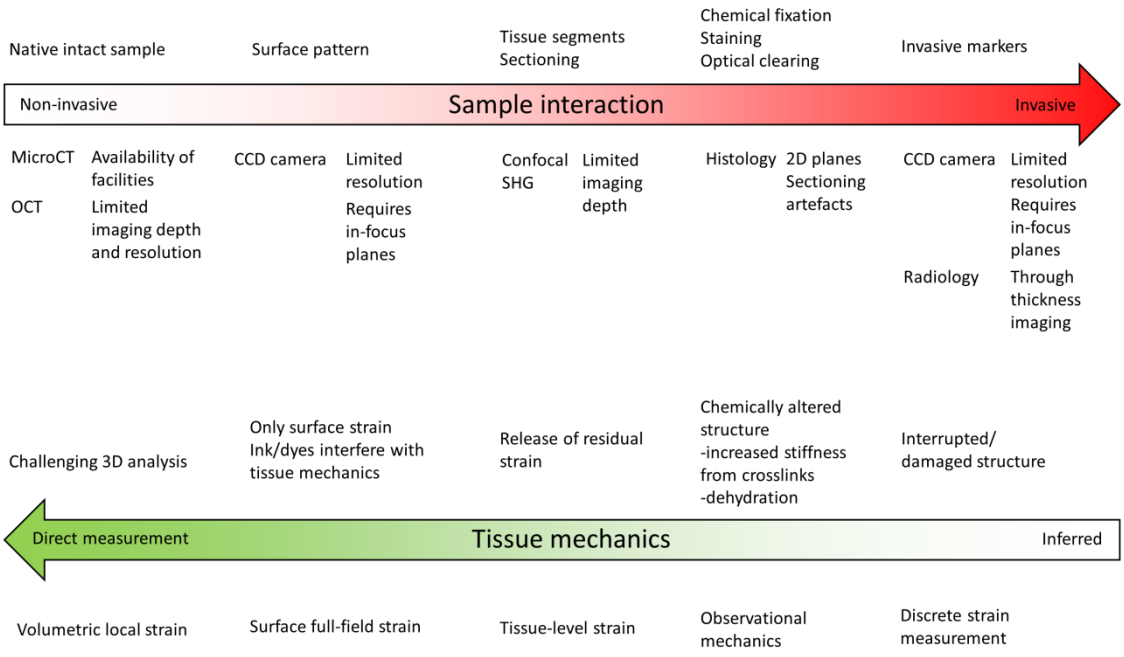

Figure 7.3 In situ imaging to quantify tissue mechanics. The top arrow (sample interaction) describes the sample preparation required for each different imaging technique and their limitations. Tissue mechanics ranging from volumetric strain to discrete strain and observational mechanics can be related to the above imaging techniques.

A.4.2 *In situ* imaging to observe microstructural deformation mechanisms

Microstructural deformation mechanisms and local strain attenuation is important for native tissue mechanical function. Mechanisms such as collagen fibre sliding, fibre uncrimping, fibre realignment and attenuation by structural heterogeneities have been observed in connective tissue imaging studies. Three case studies of soft tissue *in situ* imaging studies are given below.

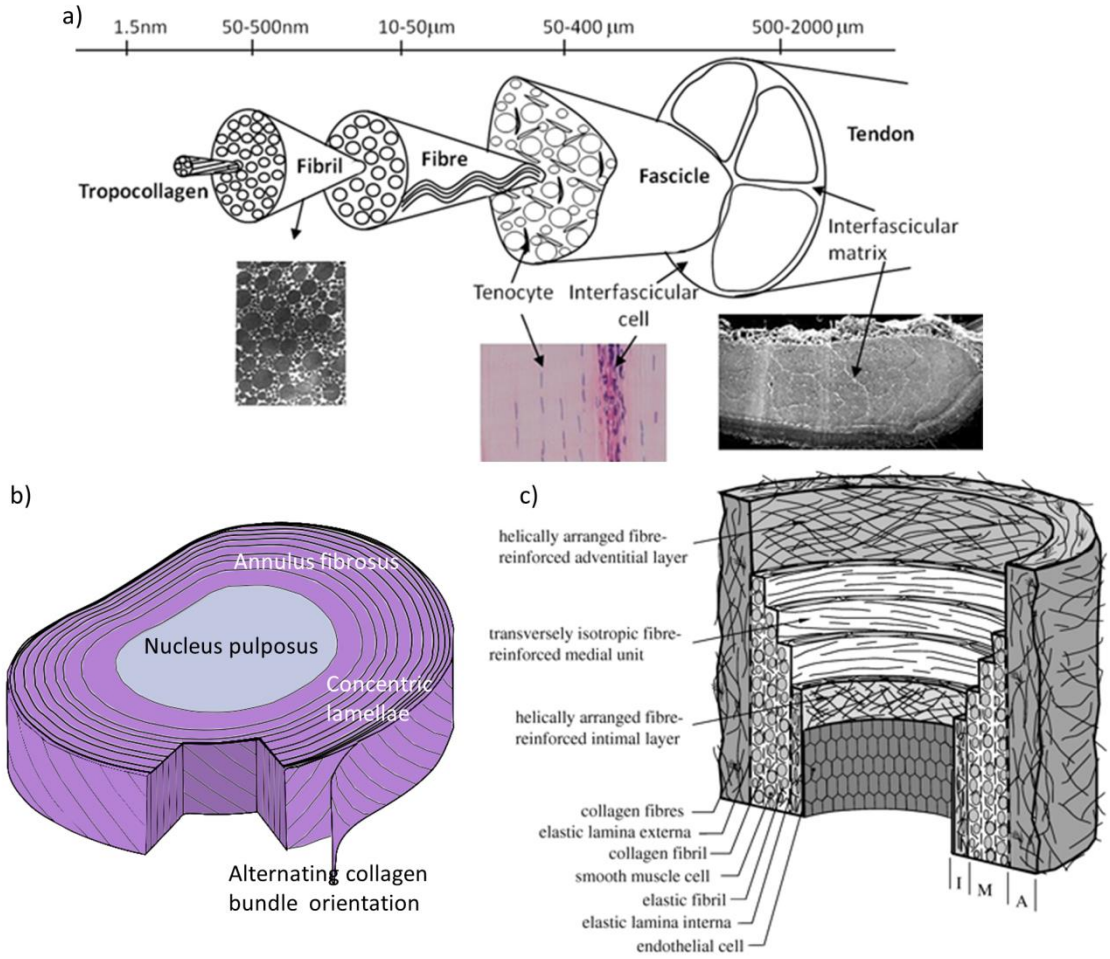

Figure 7.4 Schematics showing the microstructure of different organs. Tendon (a) (Screen et al., 2015), intervertebral disc (b) (Disney et al., 2017) and artery (c) (Gasser et al., 2006) are given as examples. All panels adapted with permission.

A.4.2.1 Tendon

Tendon is a strong fibrous collagen tissue with a hierarchical structure of fibrils, fibres and fascicles (Figure 7.4a), whose mechanical role is to transmit forces between muscle and bone. The reader can find detailed information on tendon mechanics in a recently published review (Fang and Lake, 2017). Initially tendon fibres uncrimp and realign but the major deformation mechanism is fibre or fascicle sliding under load and during

relaxation (Fang and Lake, 2015, Thorpe *et al.*, 2015, Szczesny and Elliott, 2014, Gupta *et al.*, 2010, Screen *et al.*, 2004). This sliding mechanism indicates load is transferred through the tissue by shear as the fibres do not bear load independently (Szczesny and Elliott, 2014). Confocal microscopy has frequently been used where cell nuclei are stained and tissue mechanics inferred by cell movement (Gupta *et al.*, 2010, Screen *et al.*, 2004). Photobleached lines have also been used to visually observe tissue mechanics (Fang and Lake, 2015, Szczesny and Elliott, 2014) but the DTAF stain used has been shown to alter tissue mechanics (Szczesny *et al.*, 2014).

The main challenge in tendon mechanics research is that their shape and loading conditions are extremely varied. The deformation mechanisms depend on loading conditions: for example, shear attenuation is dominated by fibre sliding whereas compression attenuation is dominated by uncrimping and fibre reorganisation in the rotator cuff tendon (Fang and Lake, 2015). To accurately observe and measure microstructure deformation further studies are required using different loading conditions and 3D imaging.

Whilst fascicle sliding is clearly a major microstructural deformation mechanism, the contribution of sliding is dependent on the tendon type (energy storing versus force transmission) and governed by tendon composition, specifically the interfascicular matrix characteristics (Thorpe *et al.*, 2015). Similarly differing composition of fibrocartilage (proteoglycan micro-domains) has been shown to influence overall deformation and the subtle local heterogeneities responsible for the complex deformation mechanisms (Han *et al.*, 2016b). To fully understand this behaviour between tendon types a full-field local strain map is required.

A.4.2.2 Intervertebral disc

Intervertebral discs are located between the vertebrae in the spine where they provide flexibility whilst bearing load from body weight and physical activity (Newell *et al.*, 2017, Adams *et al.*, 1996, Panjabi *et al.*, 1994). At the centre of the disc there is an amorphous gel-like core (nucleus pulposus), composed of the proteoglycan aggrecan and type II collagen (Taylor *et al.*, 1992), surrounded by a ring of fibrocartilage (annulus fibrosus) which has residual strain in the unloaded state (Figure 7.4b)(Michalek *et al.*, 2012). The annulus fibrosus (AF) is composed of concentric lamellae with alternating angled collagen I fibril bundles (Marchand and Ahmed, 1990, Cassidy *et al.*, 1989, Humzah and Soames, 1988, Eyre and Muir, 1977). This highly organised and multi-scale structure is responsible for the tissue's anisotropic mechanical behaviour. Sections of AF from the IVD have been imaged under load using confocal techniques. Collagen fibrils uncrimped or stretched

whilst bundles reoriented and were observed sliding past each other (Vergari *et al.*, 2016, Michalek *et al.*, 2009, Bruehlmann *et al.*, 2004). There's some inconsistency in the observations made at the lamellae boundaries. Bruehlmann *et al.*(2004) reported cells undergo large motions in the interlamellar space suggesting slipping between lamellae. Whereas Michalek *et al.*(2009) and Vergari *et al.*(2016) described no slipping at lamella boundaries. These studies used a 2D imaging technique and different loading conditions of dissected samples for an anisotropic tissue. Cutting samples from the intact structure relieves and disrupts the residual stress state and consequently changing the response to applied loads. The problem is particularly acute with non-linear materials which shift into different stiffness regimes with the release of residual stress. Further research is required to study IVD microstructural deformation mechanisms in intact samples.

A.4.2.3 Vascular

Arteries carry blood away from the heart and so are required to withstand cyclic changes in pressure. Composed of three concentric layers; collagen fibres make up a connective tissue (tunica adventitia) which surrounds the outside of the vessel, smooth muscle cells and elastic tissue form the central layer (tunica media) and endothelia cells line the inside (tunic intima) (Figure 7.4c). A reduction of waviness in the elastic lamellae of arteries has been seen with increased internal pressure using confocal and electron microscopy (Krasny *et al.*, 2017, Schrauwen *et al.*, 2012, O'Connell *et al.*, 2008, Wolinsky and Glagov, 1964) and more recently using microCT (Walton *et al.*, 2015). In pioneering studies, unfixed arterial tissue was loaded *in situ*, imaged using confocal techniques and uncrimping of collagen fibres was consistently observed (Cavinato *et al.*, 2017, Krasny *et al.*, 2017, Schrauwen *et al.*, 2012). However, there are differing observations regarding the realignment of fibres which may be related to the diverse sample dissection and loading conditions. Cavinato *et al.*(2017) used bulge inflation on segments of tissue (not an intact vessel) and aimed to mimic *in vivo* luminal pressures. Schrauwen *et al.*(2012) used whole-body inflation tests over a range of pressures some of which were not physiological. Krasny *et al.*(2017) applied uniaxial loading in three directions to rectangular strips of tissue. Cavinato *et al.*(2017) states that there was not evident reorientation of collagen fibres under pressurisation, whereas Schrauwen *et al.*(2012) describes fibres aligning to form a symmetrical double helix and Krasny *et al.*(2017) observes realignment of fibres in the applied loading direction. Whilst each study is valuable in characterising structure and mechanical function of arterial tissue, these studies highlight the importance of careful sample preparation and choice of loading mode. The experimental design and conclusions therefore must be interpreted with caution.

The above case studies show how sample preparation required for imaging and choice of loading can affect experimental outcome. Dissecting samples can lead to release of residual strain, and since soft tissue are viscoelastic, this changes their mechanical response to applied loads. Therefore, the desired imaging technique should leave the tissue intact. Furthermore, 2D confocal imaging techniques do not fully capture tissue deformation of an intact sample and so 3D imaging is required. Full-field strain measurement could prove important to investigate deformation mechanisms and how variations in tissue composition, such as proteoglycan content, influence overall and local deformation behaviour.

A.5 Tracking microstructure to map local strain

A.5.1 Discrete strain measurement

Tissue strain has been measured by tracking discrete markers (Fang and Lake, 2015, Karakolis and Callaghan, 2015), beads (Lake *et al.*, 2009), wires or tissue stained with regularly ordered patterns (Fang and Lake, 2015, Szczesny and Elliott, 2014). Tracking discrete markers or patterns provides information on the tissue global biomechanical response. However, these methods are invasive, causing disruption to native structure, and the strain field is inferred from isolated points. The local biomechanical response can be tracked by digital image correlation (DIC) to calculate full-field strain.

A.5.2 Full-field strain measurement

A.5.2.1 Digital image correlation

Applied speckle patterns or the sample's native structure can be tracked using 2D digital image correlation (DIC) to provide displacement fields (Bay, 1995, Sutton *et al.*, 1986, Sutton *et al.*, 1983). Table A.1 gives examples of soft tissue studies which have used DIC to map strain. Distinct surface features are required for DIC and so frequently a highly-contrasted speckle pattern is created on the sample using stains and ink (Lionello *et al.*, 2014).

Appendix A

Table A.1 Soft tissue DIC studies for mapping surface strain. Studies are organised by sample into tissue groups. Imaging and DIC method are given as well as further information about the features used for correlation (applied speckle or natural image texture).

Study	**Tissue**	**Origin**	**Imaging method**	**DIC method**
(Locke *et al.*, 2017)	Rotator cuff tendon-bone attachment	Murine	Optical high speed camera	Vic-2D, Correlated solutions Speckle pattern
(Mallett and Arruda, 2017)	Anterior cruciate ligament	Ovine	Optical high speed cameras – 2 FastCam, 1 CCD	Vic-3D, Correlated solutions Speckle ink pattern
(Lionello *et al.*, 2014)	Collatoral ligament	Porcine	Stereo cameras, Aramis 5M	Aramis 3D DIC Speckle pattern
(Bersi *et al.*, 2016, Genovese *et al.*, 2013)	Aorta	Murine	Optical camera 45° concave conical mirror	p-DIC, MATLAB (Genovese, 2009) Speckle Pattern
(Wang *et al.*, 2013)	Carotid artery	Non-human primate	Two-photon confocal microscopy	Modified OpenPIV (Taylor *et al.*, 2010) Collagen fibre texture
(Kim *et al.*, 2012)	Aorta	Human	Stereo CCD camera	Aramis 3D DIC Speckle pattern
(Badel *et al.*, 2012, Ning *et al.*, 2010, Sutton *et al.*, 2008)	Carotid artery	Murine	Stereomicroscope	Vic-3D, Correlated solutions Nuclear staining
(Vergari *et al.*, 2017, Vergari *et al.*, 2016)	Outer annulus fibrosus of intervertebral disc	Bovine	Second harmonic generation confocal microscopy	2D DIC custom MATLAB algorithm Collagen bundle texture
(Baldit *et al.*, 2014)	Sections of annulus fibrosus of intervertebral disc	Porcine	Stereo cameras	KelKins (Wattrisse *et al.*, 2001) Tissue texture
(Kaviani *et al.*, 2016, Amini *et al.*, 2013)	Cartilage growth plates	Porcine	Confocal microscopy	Custom MATLAB algorithm Tissue texture

Briefly, the sample is imaged in its undeformed (reference image) and deformed state and surface patterns correlated for many (often thousands) of subsets distributed over a region

of interest. Each subset is tracked from the reference image into the deformed state by optimization of a normalized cross-correlation or sum of squared difference function. Change in location of subsets yields displacements, from which gradients are calculated and organised into a full-field surface strain tensor representation. A variety of cameras and microscopes are used as sources of digital images for correlation studies, with the proper imaging method depending on sample size, loading rates, and other considerations. DIC is a well-developed methodology in many areas of experimental mechanics, but soft tissue studies present unique difficulties. Applying speckle patterns to uneven and wet surfaces can be troublesome and cause imaging artefacts such as shadows or reflections. Polarized light can be used to reduce reflections and scattering from wet tissue (LePage *et al.*, 2016). In most cases it is not possible to correlate image areas close to object edges. Locke *et al.*(2017) used DIC to map surface strain of a damaged rotator cuff tendon. But, they were not able to correlate the images close to the defect site (edge) and their study used 2D imaging which is limited to planar samples. If the sample deforms out-of-plane, then in-plane displacement and strain measurements become unreliable with 2D single camera DIC. It is possible to resolve and track non-planar surfaces using stereo imaging and 3D DIC (Mallett and Arruda, 2017, Baldit *et al.*, 2014, Lionello *et al.*, 2014, Badel *et al.*, 2012, Kim *et al.*, 2012, Ning *et al.*, 2010, Sutton *et al.*, 2008). Additionally, panoramic digital image correlation p-DIC has more recently been developed for full surface strain field of arteries (Bersi *et al.*, 2016, Genovese *et al.*, 2013, Genovese, 2009).

CCD cameras have been used to study the surface deformation of tendon (Locke *et al.*, 2017), ligament (Mallett and Arruda, 2017, Lionello *et al.*, 2014), blood vessels (Kim *et al.*, 2012) and IVD tissue (Baldit *et al.*, 2014). In these studies, cameras were capable of tracking speckle patterns to map tissue-scale strain distributions but failed to resolve sufficient native tissue structure for tracking. Higher resolution microscopy techniques are able to use tissue structure to track deformation. For example, the displacement of stained cell nuclei was tracked in a murine carotid artery using a stereomicroscope and 3D DIC (Badel *et al.*, 2012, Ning *et al.*, 2010, Sutton *et al.*, 2008). Similarly, chondrocytes in cartilage were imaged using confocal microscopy which provided sufficient texture to map strain (Kaviani *et al.*, 2016, Amini *et al.*, 2013). Second harmonic generation (SHG) confocal microscopy can resolve collagenous structures without the use of stains. The natural texture of the collagen bundles imaged using SHG has been used to map strain in IVD annulus fibrosus tissue (Vergari *et al.*, 2017, Vergari *et al.*, 2016). Vergari *et al.*(2016) were able to relate the local strain measurements to the microstructure of the tissue, showing low strain at the lamellae boundaries and higher strain or shear depending

on the orientation of collagen bundles and loading direction. The main weakness of this method is that the tissue had to be dissected and loaded which impacts on the physiological relevance and strain analysis. Firstly, physiological and consistent loading is difficult to achieve on a dissected section of tissue which has anisotropic mechanical properties. Many biological tissues have a residual strain which is released once dissected (Michalek *et al.*, 2012). Secondly, it was only possible to analyse strain in 2D and so their data must be approached with caution as out-of-plane deformation cannot be accounted for. Finally, there should be careful definition and interpretation of strain from 2D imaging. Local strain mapping using DIC may lead to different conclusions than strain measurement from discrete points. For example, low strain at the lamella boundary measured using DIC but high inter-lamella strain from discrete measurement. The author's conclusion that these strain measurements may be related to lamellae skewing would be more convincing if 3D imaging and analysis were used.

A.5.2.2 Digital volume correlation

Digital volume correlation (DVC) aims to overcome some of the limitations of both 2D and 3D DIC methods. DVC utilises volumetric imaging modalities, most commonly but not exclusively X-ray tomography, as the basis of tracking. A volumetric region of interest is populated with small sub-volumes, which are then tracked between the reference and deformed image data sets gathered during *in situ* experimentation. Tracking methodology and data analysis are similar in principle to DIC, but the result is not limited to a sample surface, extending instead throughout the interior.

The first application of DVC was continuum-level strain mapping in trabecular bone from laboratory microCT data (Bay *et al.*, 1999). It was successful due to the readily resolved open cellular structure, creating distinct local texture similar to the applied speckle patterns used in DIC. Global approaches have recently emerged as an adjunct to the more common local approaches, with constraints on displacements introduced to help control tracking uncertainty (Roux *et al.*, 2008).

Since the first application of DVC, strain has been mapped in different bone types and scaffold implants. To approach tissue-level strains, high resolution scans using synchrotron radiation should be taken to resolve textural details within the bone (Dall'Ara *et al.*, 2017). These studies have demonstrated the importance of ensuring that appropriate local texture is available for reliable sub-volume tracking, and tuning DVC parameters to image texture. Authors have placed emphasis on sub-volume or subset size as a key parameter for tracking displacement uncertainties. Displacement precision improved for larger sub-

volume sizes but with a trade-off in tracking resolution (Dall'Ara *et al.*, 2017, Palanca *et al.*, 2017, Madi *et al.*, 2013).

OCT elastography is able to resolve soft tissue structures as small as a few micrometres and map strain in intact samples as a variant of DIC speckle (naturally occurring coherent speckle from OCT) tracking (Schmitt, 1998). The main limitation is the shallow imaging depth of around 1 mm which competes with resolution. The applied strain is also limited to 1-2% with higher resolution imaging (Larin and Sampson, 2017). This is an emerging field with few studies in biological tissues such as breast tumours (Allen *et al.*, 2016, Kennedy *et al.*, 2015, Kennedy *et al.*, 2014) and cornea (Lamouche *et al.*, 2012) and two publications using DVC for 3D OCT strain measurement (Fu *et al.*, 2013, Nahas *et al.*, 2013).

A.6 Outlook: volumetric strain measurement in soft tissue

This review has given a brief introduction to *in situ* imaging and strain measurement of soft tissue. The challenges from the reviewed literature of strain measurement in soft tissue are summarised below and some suggested approaches given.

A.6.1 Sample preparation and loading conditions

A.6.1.1 Precise and consistent sample dissection

Biological tissues have complex, viscoelastic, anisotropic mechanical behaviour and therefore precise and consistent sample preparation is required. For example, two sample orientations to account for annulus fibrosus anisotropic mechanical behaviour (Michalek *et al.*, 2009) and consistent dissection from the same anatomical region in tendon where variations in interfascicular matrix or proteoglycan content affects tissue mechanics (Han *et al.*, 2016b, Thorpe *et al.*, 2015).

A.6.1.2 Effect of sample preparation on tissue mechanics

Consistent dissection and mechanical testing of tissues under different controlled conditions, such as uniaxial loading of the sample in multiple orientations, gives valuable material characterisation. However, dissected samples do not retain their residual strain and so intact samples should ideally be used for testing organs or tissue under physiological loads. Applying loads to dissected tissue is also challenging and may alter tissue mechanics. The vascular case study is a good illustration of differing microstructural deformation which may be as a result of the glued loading boundary of a segment of tissue compared with whole body inflation. Additionally, tissues have a natural composition gradient and irregular shape at loading interfaces which is challenging to replicate when

loading dissected segments of tissue. For instance, the concave morphology of intervertebral disc endplates which varies between adjacent endplates and depends on lumbar region (Wang *et al.*, 2012). Or a further example of composition gradient at the tendon to bone interface (Thomopoulos *et al.*, 2003).

A.6.1.3 Physiologically relevant loading regimes are limited by imaging capabilities

Soft tissues function in a dynamic environment where loading frequency can be seconds. Observing structural deformation at this loading frequency is only possible when using imaging techniques with a short acquisition time (<ms). Deciding on a loading protocol becomes more challenging when there are long acquisition times for 3D imaging techniques such as microCT (minutes to hours) and a long relaxation period for tissue creep. Loading must be interrupted to allow for long imaging acquisition. It is recommended all regimes follow the same general protocol below. The applied deformation step must be small enough to track using image correlation and many steps may be required depending on stiffness or physiological range. Importantly, there must be a relaxation period after each load step is applied which allows for tissue creep before image acquisition to avoid imaging artefacts.

A.6.2 Imaging microstructure; towards 3D imaging of native samples using microCT

A.6.2.1 Balancing contrast, resolution and field of view

To this date *in situ* imaging studies are 2D or have been limited to small volumes. MicroCT has the potential to provide 3D microstructural imaging of intact native samples. Nevertheless, soft tissues are weak X-ray absorbing and so contrast enhancement is required. Contrast agents can alter tissue structure and mechanics due to long staining times and tissue preservation or fixation (Disney *et al.*, 2017, Balint *et al.*, 2016, Vickerton *et al.*, 2013, Tilley *et al.*, 2011, Hickey and Hukins, 1979). Contrast enhancement can be achieved in native tissue using in-line phase contrast imaging techniques (Figure 7.2c) (Disney *et al.*, 2017). However, laboratory microCT phase contrast approaches do not provide a large enough field of view to image the whole small animal organs at the required resolution. Synchrotron imaging has a larger field of view and has been shown to give lower tracking uncertainties for image correlation when compared to laboratory microCT (Dall'Ara *et al.*, 2017). The considerably bright synchrotron X-rays are able to obtain higher signal:noise reconstructions and shorter scans times. A short scan time is required to mitigate against slow tissue relaxation. The high coherence and tomography

beamline configurations (such as Diamond-Manchester I13-2) allow for large propagation distances which is ideal for in-line phase contrast imaging of soft tissue.

A.6.2.2 Compromise between image quality and radiation dose

Although synchrotron microCT is capable of high signal:noise reconstructions, a balance must be made between radiation dose and scanning parameters (beam filters, number of projections and exposure time). It is recommended that the sample should be aligned in the beam under low dose conditions by using large undulator gap and shutters.

A.6.2.3 Data handling and image processing

After reconstruction it may be advantageous to process the tomography data such as using filters to reduce random noise or image artefacts. Synchrotron microCT produces large data sets which can be challenging to handle and computationally expensive to analyse. A volume of interest or some segmentation of the data to only include certain features may be required before image correlation analysis.

A.6.3 Tracking displacement of features using image correlation

A.6.3.1 Sufficient features to track

Image correlation is only possible if there are small features to track. Applied speckle patterns and image correlation have been used for mapping strain on surfaces of biological tissues. DIC measurements are sensitive to the quality of the pattern and creating a speckle pattern can be problematic for hydrated soft tissues without changes in mechanical properties. However, these methods do not provide information on internal strains and how they relate to the 3D microstructure of the tissue. DVC can be used for non-invasive sub-voxel displacement tracking using natural image texture.

A.6.3.2 Tracking reliability depends on correlation parameters

Using the DVC results it is possible to obtain a local strain map and relate it to the microstructure of the tissue. The DVC parameters must be carefully tuned to the image texture and aligned with the research question. It has already been shown that the sub-volume size is important for tracking uncertainty. The density and location of the tracking points may improve reliability or follow microstructures that are of interest e.g. fascicles in tendon, lamellae in IVD or collagen fibres in arterial tissue. Tuning DVC parameters will particularly be important for future *in situ* studies where the structures are heterogeneous and hierarchical. The influence of texture characteristics on the precision and spatial resolution of image correlation, and optimal tracking procedures for challenging conditions, are topics of continuing research. In the absence of definitive guidelines, the

best strategies for ensuring reliable results are correlation of multiple image volumes under static conditions (repeat unloads), and careful analysis of residuals associated with normalised correlation functions.

A.6.3.3 Correlation is inclusive of image noise and artefacts

Image correlation is sensitive to all features in the data including noise and artefacts which can cause complications. Firstly, the level of noise may change between and within images which leads to varied reliability. Image filtering to reduce noise can help but also be detrimental if small scale features are lost. Secondly, results may appear to be reliable with excellent correlation, but displacement values are associated with motion artefacts and not to tissue deformation. Rigid body motion artefacts, once identified, can be removed by adjusting reference points for displacement values without altering relative deformations. And as proper strain measures are insensitive to rigid body motion, the calculation of strain from displacements will reveal sample deformation more definitively.

A.6.4 Strain calculation and interpretation

Strain calculation and interpretation must be appropriate for the specific tissue. For example, published work has shown collagen fibre sliding to be the main deformation mechanism in tendon and IVD and so a shear strain map may be the most appropriate measurement. Furthermore, choosing how to measure strain may depend on the loading mode e.g. measuring circumferential/ hoop strain for inflated arteries or in the AF of compressed IVD. Soft tissues also exhibit large, nonlinear strains, and an appropriate finite strain measure should be used, with Green-Lagrange a common choice. When interpreting results and comparing between studies it is important to take note of sample preparation, loading conditions and their strain definition for the reasons mentioned above.

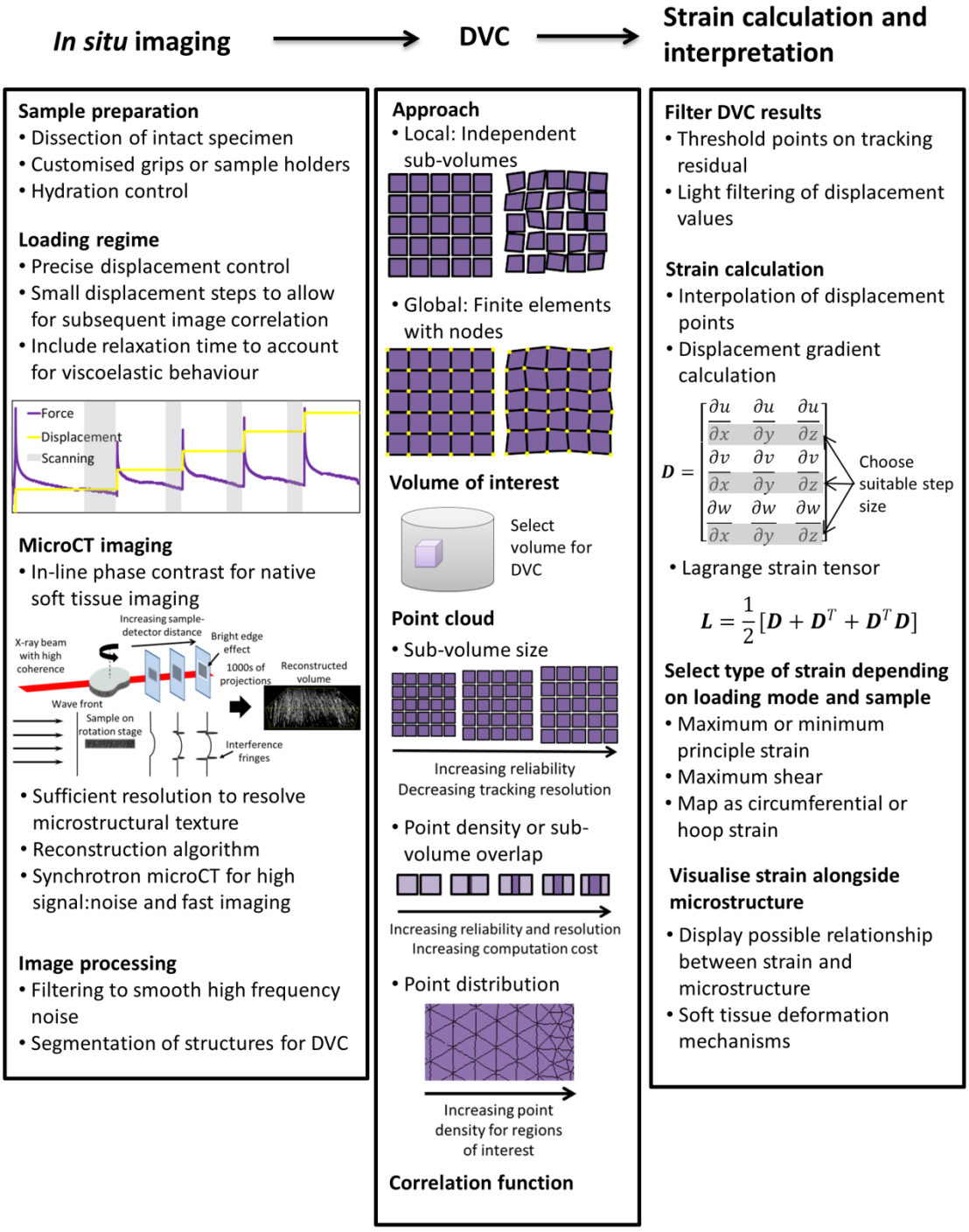

Figure 7.5 Proposed workflow for soft tissue microCT-DVC studies.

A.7 Conclusion

The reviewed *in situ* imaging studies have been 2D or small segments of tissue. Novel application of phase contrast microCT and DVC to measure volumetric strain in native soft tissue has the potential to provide a detailed insight into tissue structural micromechanics. A proposed workflow for soft tissue microCT-DVC studies is given in Figure 7.5. This has the potential to bridge the gap between direct measurement of macro-mechanics and the local 3D micro-mechanical environment experienced by cells. In the long term,

mechanobiology studies of soft tissues could be possible where the local strain field is related to cell mediated responses to mechanical stimuli. These studies would help characterise pathology in ageing or diseased tissues such as mechanical changes due to microstructural damage accumulation in the AF or strain patterns that develop during aortic aneurysm. Importantly these methods could be applied to accelerate development and testing of new tissue engineered replacements.

B. Diamond Light Source proposal 15444 Manchester Collaboration: Structural and mechanical characterisation intervertebral discs loaded *in situ*

This chapter contains the science overview for Diamond-Manchester MT15444 proposal awarded 3 days beam time. Catherine M. Disney is a co-investigator, wrote the proposal and led the experiment. Michael J. Sherratt (principle investigator), Judith A. Hoyland (co-investigator), Peter D. Lee (co-investigator) and Brain K. Bay (co-investigator) contributed to study design.

Appendix B

B.1 Abstract

Intervertebral discs undergo degeneration during ageing which is closely associated with the development of untreatable low back pain. The causative mechanisms remain poorly understood and there are currently no reparative treatments. This proposal aims to develop new imaging methods to map local micro-strains in the loaded disc (a potential risk factor in cell-driven remodelling). These methodologies will have wider application to soft tissues and the specific data on IVD mechanics will be of considerable interest to researchers studying IVD pathology and repair.

B.2 Scientific background and aims

The intervertebral disc (IVD) undergoes profound structural remodelling as a consequence of age or disease. Over 40% of low back pain (LBP) cases are attributable to degeneration of the IVD. This painful and debilitating disorder, which affects at least 80% of adults at some time during their lifespan, is estimated to cost the UK economy in excess of £12 billion pounds per year. Currently, there are no treatments for IVD degeneration other than symptomatic pain relief. The 3D structure of the mechanically loaded IVD has been inferred form 2D histological sections of unloaded tissue. In order to understand the pathological mechanisms and develop new treatments it will be necessary to characterise the 3D microstructure of the IVD under different loading conditions.

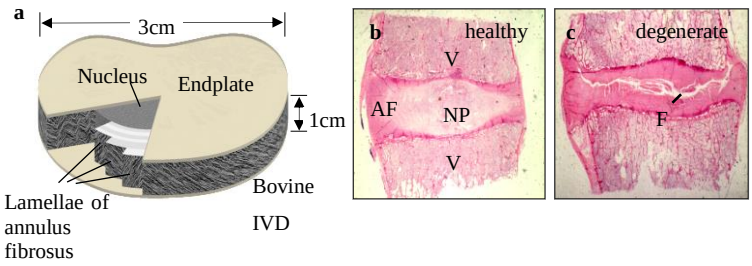

Figure 7.6 ***Intervertebral disc: structure and pathology.*** *a) Schematic of IVD. Cartilaginous endplates transmit compressive force from the vertebrae to the inner collagen II- and aggrecan-rich nucleus pulposus and the outer collagen-I rich annulus fibrosus. b) histological structure of a healthy, decalcified, sectioned and H&E stained vertebral unit comprising vertebrae (V) and annulus fibrosus (AF) and nucleus pulposus (NP) regions of the intervertebral disc. c) the degenerate disc is characterised by fissures (F) within the NP.*

The IVD which is composed of two cartilaginous vertebral end-plates, an outer tendon-like annulus fibrous [AF] and an inner gel-like nucleus pulposus [NP], acts as shock absorbers between vertebrae (Figure 7.6) IVD degeneration (IVDD), which originates in the NP, is thought to be mediated by cells in response to aberrant loading but the local mechanical environment in the IVD is poorly defined.

Using in-line phase contrast imaging technique at the Diamond-Manchester Beamline we have already shown that it is possible to image IVD microstructure of fresh tissue samples, without contrast agents, and track features in 2D slices after sequential compression (Figure 7.7). Preliminary digital volume correlation (DVC) results show that it is possible to map displacement within the tissue. Our goals are to: i) characterise the 3D structure of

the IVD, ii) improve understanding of 3D microstructure remodelling under compressive load, iii) map 3D strain from DVC analysis.

This work will be the first step towards characterising the microstructure and 3D local mechanics (at cellular level) of a degenerated disc and testing the efficacy of tissue engineering strategies.

B.3 Experimental methods

Bovine tail IVD will be dissected at RCaH and transported to the beamline immediately before scanning. Deben CT5000 will be adapted using customised sample holders and compression plates. A humid environment will be used to ensure the tissue remains hydrated without causing swelling (over-hydrated). Four load steps will be applied and real-time force feedback from the rig will give an indication of when the tissue has relaxed (~20 minutes) and scanning can commence.

Previous scan conditions for fresh tissue will be used a guide for this experiment. A pink beam (8-30 keV) will be used to provide maximum flux and filtered (2 mm aluminium, 70 um steel) to minimise dose from low energy radiation. pco.4000 detector with 1.25x objective lens will be used to achieve maximum field of view. Higher magnification will be used for region of interest scans. Sample to camera propagation distance will be chosen for sufficient phase contrast to visualise the microstructure (800 mm).

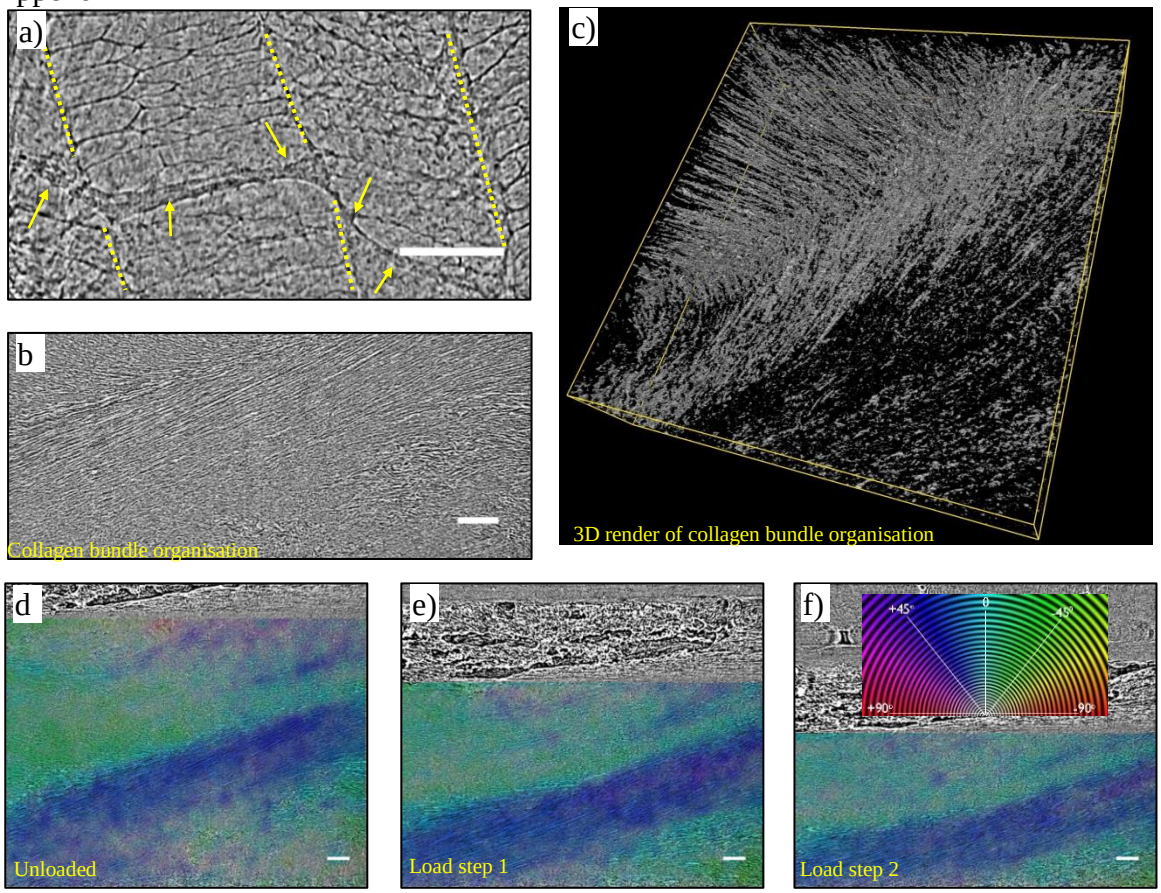

Figure 7.7 ***MicroCT of fresh IVD tissue using phase contrast imaging at the Diamond-Manchester Beamline.*** *a) Longitudinal slice where lines mark lamella boundaries and arrows indicate bridging structures. b) Radial slice showing collagen bundle organisation. c) 3D render of collagen bundles. d-f) radial slices with orientation analysis showing compression of IVD tissue.*

B.4 Beamline and beamtime justification

Previous experiments using lab absorption based imaging required the sample to be stained. This altered the tissue structure and mechanics and so is not suitable for mechanically loaded *in situ* studies. Lab phase contrast approaches do not provide a large enough field of view therefore we propose to use the Diamond-Manchester Beamline (I13-2) using in-line phase contrast imaging which will provide 7.2 um resolution with 14 x 9.6 mm field of view. The high coherence and beamline configuration for large propagation distances, allowing interference fringes to develop, is able to resolve fine structural details as shown in Figure 7.7.

High flux synchrotron source X-rays enable short acquisition times which in turn minimise radiation dose, allow for control of hydration and crucially facilitate imaging at multiple sequential loads whilst reducing creep and motion artefacts during scanning.

A simple compression device was used for the preliminary compression results shown in Figure 7.7. During this beamtime we propose to use Deben CT 5000 which will give force feedback and consistent experimental conditions through precise control of the applied strain.

We request 2 shifts to mount, align and integrate the Deben rig onto the beamline, 6 shifts to perform stepped loading experiments.

B.5 Expected results and impact

We expect this application to result in the first 3D evaluation of microstructural remodelling in a mechanical loaded IVD and maps of micro-strain in intact IVDs. This work will have impact on: i) methodology development towards fast scanning to investigate physiological mechanical function, disease and aging of dynamically loaded IVDs, ii) stress concentrations as a driver of IVD remodelling and iii) assessing the efficacy of repair and tissue replacement strategies using the developed imaging methodologies and applying physiological loading regimes. Manuscripts summarising impacts i and ii will be submitted to leading journals in imaging and skeletal biology.

C. Diamond Light Source proposal 19322: Structural and mechanical characterisation of the intervertebral disc and degeneration

This chapter contains the science overview for Diamond-Manchester MT19322 proposal awarded 4 days beam time. Catherine M. Disney is a co-investigator, wrote the proposal and led the experiment. Michael J. Sherratt (principle investigator), Judith A. Hoyland (co-investigator), Peter D. Lee (co-investigator) and Brain K. Bay (co-investigator) contributed to study design.

Appendix C

C.1 Abstract

Intervertebral discs (IVD) are distributed throughout the spine, providing flexibility while supporting loads from body weight and physical activity. This mechanical function is directly related to their complex microstructure, and degeneration of these structures is associated with low back pain. In order to understand the pathological mechanisms and develop new treatments it is necessary to characterise the 3D microstructure of the IVD under different loading conditions. From previous Diamond beam times we have resolved native IVD microstructure and mapped strain of sequentially loaded discs. Here we propose to i) collect bovine IVD structural data from synchrotron microCT for FEA, ii) establish the effects of different injury models on the 3D strain behaviour of sequentially loaded rat IVDs, and iii) determine the mechanical efficacy of an injected collagenous gel.

C.2 Scientific background and aims

Intervertebral disc biology and pathology: Intervertebral discs (IVDs) which act as shock absorbers in the spine undergo structural changes as a consequence of age or disease. Over 40% of low back pain cases are attributable to IVD degeneration (IVDD). This painful and debilitating disorder costs the UK economy £12 billion pounds per year. Currently, there are no treatments for IVDD other than symptomatic pain relief. In order to understand the pathology of IVDD and develop new treatments it is necessary to characterise the 3D microstructure and strain in healthy and degenerated discs.

The IVD is composed of two cartilaginous vertebral end-plates, an outer tendon-like annulus fibrous (AF) and an inner gel-like nucleus pulposus (NP). IVDD is thought to be mediated by cells in response to aberrant mechanical loading; however, the local micro-mechanical environment in the IVD is poorly defined. Pain caused by IVDD is commonly relieved by surgical intervention (Takahashi *et al.*, 2008). However, the prognosis is poor and revision surgery is often required to correct herniation through the AF defect.

Previous experimental results: Using in-line phase contrast imaging at the Diamond-Manchester Beamline I13-2, we have shown that it is possible to image the microstructure of fresh (native) segments of bovine tail IVD, without contrast agents (Figure 7.8a).

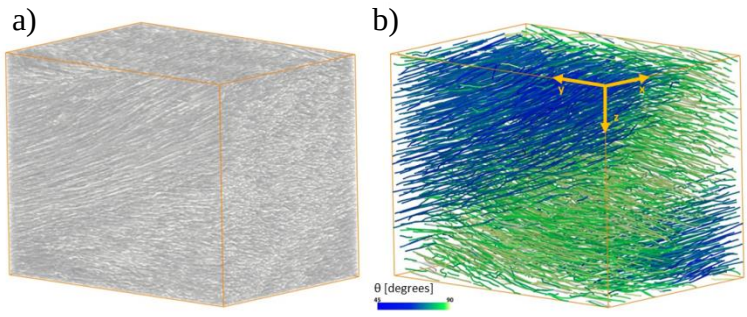

Figure 7.8 a) tomogram of native AF, b) individual collagen bundles have been traced and their orientation displayed.

The high signal:noise tomography provided by synchrotron imaging allows individual collagen bundles to be traced, which gives structural information such as the orientation of each bundle (Figure 7.8b). Quantifiable 3D structural information is extremely valuable for finite element analyses (FEA). However, these experiments used segments of bovine IVD (rather than the whole disc). As a consequence, the naturally occurring AF residual stress

was released. We propose futher imaging of native bovine IVD, dissected as a whole structure, allowing for FEA.

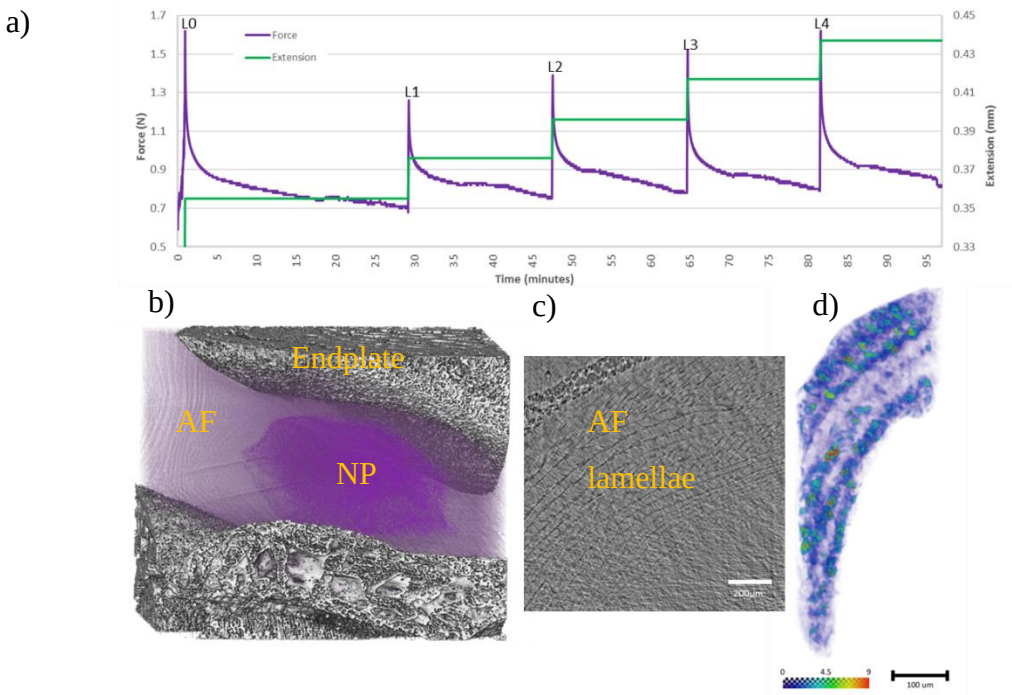

Figure 7.9 a) In situ compression of rat spine segment, b) rendered tomogram of the IVD, c) tranverse slice showing AF, d) principle strain in the AF.

In our recent beam time (MT15444) we imaged whole rat IVDs within a spine segment (IVD, vertebrae and surrounding muscle) under sequential compression using a Deben CT5000 rig (Figure 7.9). Key tissue structures including collagenous lamellae and the nucleus pulposus (Figure 7.9b, c) were readily identifiable in sequential scans. This approach provided *in situ* loading conditions with high precision displacement control and measurement of force curves (Figure 7.9a). Crucially, the image data supported the use of digital volume correlation for displacement and strain mapping in the AF (Figure 7.9d). Using the devleoped methods, these characterisation could now be applied to a model of IVDD.

Beam time proposal: Our goals are to: i) collect structural data from high quality images for finite element analysis and ii) perform *in situ* tomography of discs with AF defect for strain analysis.

C.3 Experimental methods

Rat spine segments and bovine tail discs will be prepared at Research Complex at Harwell and transported to the beamline immediately before scanning. Customised sample holders and Deben rig will be used to compress samples and measure the loading curve throughout the experiment (Figure 7.9a). Four load steps will be applied and real-time force feedback from the rig will give an indication of when the tissue has relaxed (~20 minutes) and scanning can commence.

Previous scan conditions for fresh tissue will be used a guide for this experiment. A pink beam (8-30 keV) will be used to provide maximum flux and filtered (0.95 mm pyr graphite, 2 mm Al, 0.1 mm Fe) to minimise beam damage. pco.edge 5.5 detector with 2x objective lens will be used to achieve appropriate field of view and voxel size. Higher magnification will be used for region-of-interest scans. The propagation distance will be chosen for sufficient phase contrast to visualise the microstructure (500mm).

Samples will include bovine tail IVD (disc dissected as whole structure) and rat spine segments including healthy IVDs and IVDs with AF defect.

C.4 Beamline and beamtime justification

We have shown that it is possible to trace collagen bundles within the native AF. This was enabled by the faster scan times and higher signal:noise tomography at I13-2 when compared to laboratory sources.

Lab-CT phase contrast approaches do not provide a large enough field of view to image the whole IVD at the required resolution and a short scan time is required to mitigate against slow tissue relaxation therefore we propose to use the Diamond-Manchester Beamline (I13-2) using in-line phase contrast imaging. The high coherence and beamline configuration for large propagation distances, allowing interference fringes to develop, is able to resolve fine structural details as shown in Figure 7.9b and c. We request 2 shifts to gather bovine disc tomograms, 2 shifts to mount, align and integrate the rig onto the beamline, 10 shifts to perform stepped loading experiments of healthy (control) and AF defect IVD groups.

C.5 Expected results and impact

We expect this application to result in the first 3D evaluation of microstructural remodelling in mechanically loaded fresh intact IVDs and local strain field surrounding AF herniation.

In relation to the current literature, Cao *et al.*(2017) used propagation phase contrast synchrotron tomography to characterise morphological changes in aged mouse intervertebral discs. They observed changes in disc thickness and volume but failed to resolve microstructure and used chemically fixed tissue.

IVD local mechanics has been evaluated using optical techniques that are 2D or have limited imaging depth (Mengoni *et al.*, 2015, Gregory and Callaghan, 2012, Bruehlmann *et al.*, 2004, Yu *et al.*, 2015, Vergari *et al.*, 2016). These methods require dissection of the disc which depressurises the NP and releases AF pre-stress (Michalek *et al.*, 2012). Stains are used and patterns photobleached to track displacement (Michalek *et al.*, 2009) which have been shown to alter the mechanics of tissue (Szczesny *et al.*, 2014). Our proposed method (DVC) uses the natural texture to track displacement. Furthermore, imaging the microstructure offers in-depth strain analysis that is multiscale and can be linked to IVD anatomy (calculating lamella or inter-lamella strain).

This work will have impact on the following: i) methodology development towards 3D imaging of fresh soft tissue and bone to investigate physiological mechanical function, disease and aging of compression loaded IVDs, ii) application of DVC to heterogeneous structures in one sample, iii) assessing beam damage using mechanical testing data and biochemistry techniques, iv) local strain field around IVD degeneration defects such as annulus herniation and tears. Manuscripts summarising the above impacts will be submitted to a leading journal.

D. EPSRC Doctoral Prize Fellowship proposal

A version of this proposal was submitted to be considered for the EPSRC Doctoral Prize Fellowship at the University of Manchester.

Awarded 12 months funding to commence November 2018.

Appendix D

D.1 Project proposal

Societal impact.

Over 40% of **low back pain** cases are attributed to **intervertebral disc degeneration (IVDD)**, costing the UK £12 billion per year. IVDD is characterised by loss of disc height and structural changes. The **local micro- and macro-mechanical environment** during function and through progressive degeneration remains poorly understood. Currently, there are **no treatments for IVDD** other than pain relief. Replacement nucleus pulposus (NP) hydrogels, injected through the annulus fibrosus (AF) (Figure.1.), are being developed but the local effect of the resulting needle injury to mechanical function is unknown.

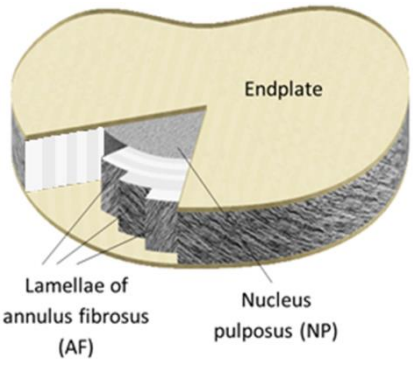

Figure 1. The intervertebral disc is composed of two cartilaginous vertebral end-plates, an outer tendon-like annulus fibrous (AF) organised in lamellae with alternating bundles and an inner gel-like nucleus pulposus (NP).

Research focus.

This proposal exploits **synchrotron in-line phase contrast microCT (PCXMT)**–collected 28th June-2nd July 2018 - for strain measurement and mechanical modelling to investigate and **predict the mechanical causes of IVDD** and to evaluate the **invasiveness of injecting** potential NP replacements.

Objective 1: PCXMT image processing to gather structural information for IVD modelling.

Imaging capabilities at Diamond-Manchester beamline (I13).

The University's investment in I13, which has **world-leading** phase contrast imaging capabilities, makes it the best location to carry out this research. Soft tissue structure has been visualised at **unprecedented levels of detail** for volumetric imaging (Disney *et al.*, 2017). A key strength of PCXMT is that the **3D microstructure of intact, native rat IVD** in an *ex vivo* spine segment has been resolved (Figure.2.).

Appendix D

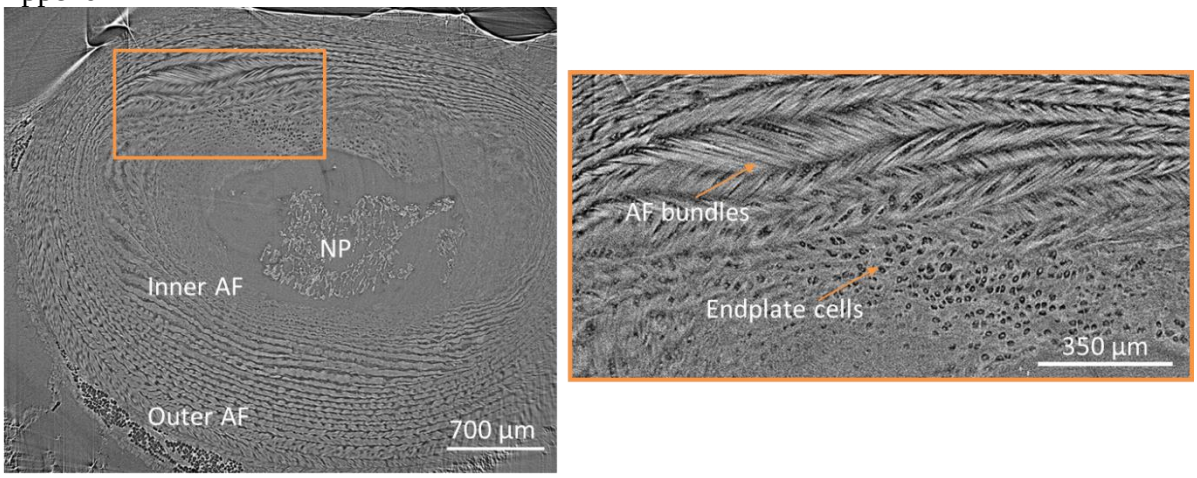

Figure 2. Improved image quality able to resolve NP, inner and outer lamellae, AF bundles and cells throughout *in situ* compression sequence.

Targets.

The following structural information is currently not available for intact IVD but can be obtained from the PCXMT data.

1.1. Endplate curvature, porosity and boundary structure.

1.2. Lamellae organisation including curvature, varying thickness from inner to outer AF, distribution and frequency of partial lamellae.

1.3. Anatomical map of AF **bundle orientation**.

1.4. Cell abundance and location in intact IVD.

<u>Objective 2: PCXMT-based volumetric strain measurement of intact rat IVD, studying different anatomical regions, the mechanical effect of enzymatically digested NP tissue (model of IVDD) and the local strain-field surrounding AF needle injuries.</u>

Advanced image-based metrology is emerging as the method of choice for tissue- and cell-spatial scale experimental investigations.

A **combination of *in situ* mechanical testing and PCXMT** can be used to record volumetric IVD microstructure deformation. Through collaboration with **Brain Bay** (Oregon State University), **tissue strains** were measured using **Digital Volume Correlation (DVC)** at higher spatial resolution than before achieved, producing the **first direct evidence** of intra- and inter-lamellae load transfer among AF bundles (manuscript prepared). Results relate well to the dense elastin fibre network which appears to function as a matrix analogous to those of synthetic composites. This work significantly **advanced**

technical capabilities for IVD mechanics research and gained strong momentum within the functional imaging community through international conference presentations, subsequent manuscript invitation (Disney *et al.*, 2018) and image prize.

Targets.

Recently acquired PCXMT has **improved image quality** (Figure.2.) and, importantly, two animal **models of injury** were tested. This will allow:

2.1. A comprehensive **comparison of strain between different regions of the IVD** (IVDD has regional variation).

2.2. Cell-scale measurement of **strain in samples with enzymatically digested NP** (model of IVDD). This is important as IVDD is thought to be **mediated by cells**.

2.3. Study of the **local strain field around two different gauge needle injuries**.

The above meets the EPSRC Assistive Technology, Rehabilitation and Musculoskeletal Biomechanics remit to "provide **new understanding and insights… of musculoskeletal disease"** and in assessing how to "**restore function with minimum invasiveness**" for NP replacements.

<u>Objective 3: Develop novel mechanical computational models.</u>

Modelling will be closer to anatomy than previously attempted.

Current models capture the overall effect of lamellar structure on response to loading, but do not resolve strain at the **spatial scale** obtained from PCXMT. Modelling will improve knowledge of the **complex and heterogeneous structure-function relationship** of the IVD, **predict** the likely causes of **degeneration** and failure mechanisms and elucidate the cellular microenvironment for therapeutic and tissue engineering research. DVC strain measurements will provide validation of modelling results at high spatial resolution, a unique aspect of this research.

Lee Margetts is experienced in and will advise on modelling. Collaboration between IVD research and **modelling expertise** will provide **new breakthroughs in IVD mechanics** and aligns with the **EPSRC strategic focus**. From a career development standpoint, this proposal **extends my technical skills** to modelling which is important to becoming an **independent researcher**.

Targets.

Structural information from Objective 1 will be used to build models of the IVD.

3.1. Attend Finite Elements course and three workshops (Figure.3.).

3.2. Define anatomical **geometry** from PCXMT, mesh, initial **material properties** from literature and run analysis.

3.3. Compare analysis to DVC results and **refine initial parameters**.

3.4. Post-processing and presentation of results for manuscript.

Timescales.

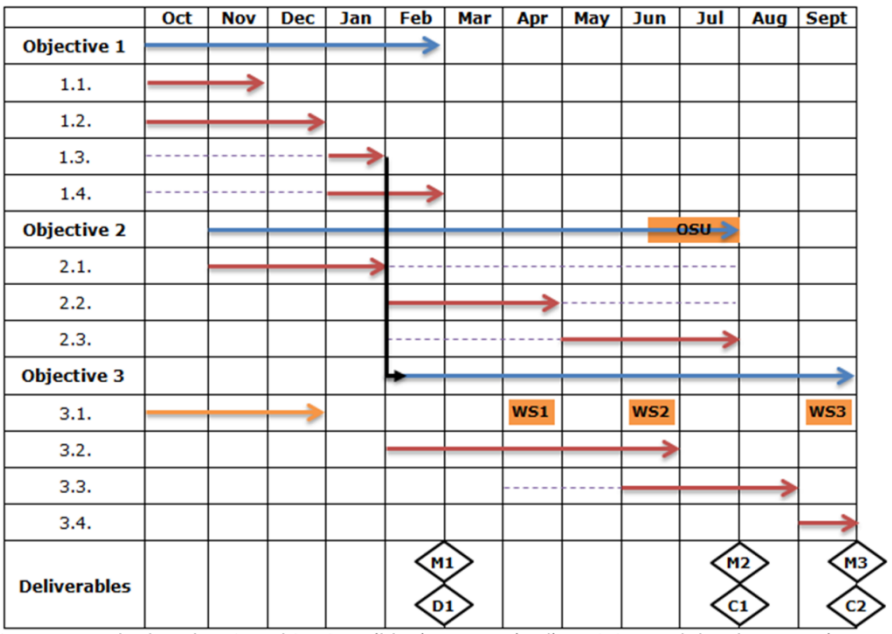

Figure 3. Work-plan showing objectives (blue), targets (red), training and development (orange) and deliverables (section 4B). Purple dashed line shows slack time for the targets.
OSU – placement at Oregon State University – collaboration with Brian Bay.
WS1 - 1 week finite element course run by Lee Margetts, University of Manchester.
WS2 - Soft tissue modelling workshop, SofTMech, 5-6 June 2019, Glasgow.
WS3 - Modelathon workshop, EPSRC funded MultiSim and OATech+Network, 4 days, Sheffield.

D.2 Expected outputs from proposed research programme

Deliverables of this proposal will be **three manuscripts** (3-4 star REF publications), presentations at two **international conferences** and **data made publicly available**. These outputs align with the **bio-engineering** and the **modelling and simulation MACE research themes**. Each deliverable is described below and their expected completion date given in Figure 3.

M1 **Manuscript:** Microstructural characterisation of an intact native intervertebral disc.

Aim to **showcase advances in microCT** IVD imaging and to **disseminate detailed structural information** currently not available to IVD researchers.

D1 **Data and knowledge transfer:** The image and structural data will be made publicly available for other researchers to use.

IVD structural data will be populated in a database and volumetrically mapped. This data will be presented and discussed in M1 in terms of IVD anatomy. However, this deliverable aims to **fulfil FAIR (Findable, Accessible, Interopable and Resuable) principles** required by funding bodies and the University. With that goal in mind, the data will be a **published in Scientific Data** which is an open-access journal for descriptions of scientifically valuable datasets. Both the raw structural data and image data will be made available on Mendeley Data Repository.

M2 **Manuscript:** Volumetric strain measurement in the native intervertebral disc; in untreated, a model of degeneration and the effect of needle injury.

Aims to investigate possible mechanical causes and cellular environment of IVDD and invasiveness of future repair strategies through experimental measures. Will **impact on IVD regenerative medicine researchers** and **clinicians** for guidance on needle size.

C1 **Congress of the International Society of Biomechanics, Calgary.**

As a member of the largest network of biomechanists (ISB) I will present the latest **methodological developments in soft tissue imaging, strain analysis and initial modelling** results. The submitted abstract will be aimed at an imaging or soft tissue modelling session.

M3 **Manuscript:** Modelling the intervertebral disc; accurate structure taken from microCT of intact native disc.

Aims to provide a more physiological model than previously attempted to predict the mechanical causes of IVDD or points of structural failure. These results will **impact on IVD researchers** and the **long-term impact will be for patients** as further understanding on the mechanical causes of IVDD is required to develop replacement tissues.

C2 European Orthopaedic Research Society (EORS), Maastricht, Netherlands

Attended by renowned engineers, scientists, clinicians and industry partners. This conference will be important to **connect will potential collaborators for future fellowship applications**. The abstract will be submitted to the **spine session** and focus on the IVD findings from the proposed project.

Targeted journals include Nature communications (12.5), PNAS (9.6), Acta Biomaterialia (6.3), Scientific Data (4.8), PLOS Computational Biology (4.5), Scientific reports (4.1), The Spine Journal (3.0).

If this project leads to IP that is commercially exploitable, UMI3 Ltd will be consulted regarding routes to commercialisation such as patents or licensing.

[1] R.W. Moskowitz, I. Ziv, C.W. Denko, B. Boja, P.K. Jones, J.H. Adler, Spondylosis in sand rats: a model of intervertebral disc degeneration and hyperostosis, Journal of Orthopaedic Research 8(3) (1990) 401-411.